ARCHIVES OF ACOUSTICS
24, 3, 251–253 (1999)

PROFESSOR ZENON JAGODZIŃSKI

in memoriam

Professor Zenon Jagodziński was born in Samcieszynek, district Bydgoszcz, on April 5, 1913. He began his study at the Faculty of Architecture of the Technical University of Lvov in 1934. Four years later, he moved to Warsaw, when he specialised in radio engineering at the Technical University of Warsaw. The outbreak of World War Two interrupted his study. During the September Campaign he served as officer of artillery in the Polish army. After the battle by the river Bzura, he was taken captive. Until the very end of the war, he was in captivity. After liberation by the Allies, he stayed in Grate Britain, where he continued his study at the Polish University College that was established at the Imperial Institute of Science and Technology in London. In 1947 he completed his study in the field of telecommunication and took his M.Sc. degree at the Faculty of Electrical Engineering. At the end of this year, he came back to Poland and

started to work at the Naval Radio Service that was founded in that time at the Faculty of Engineering of the Technical University of Gdańsk. There he constructed in 1950 the first polish echo sounder. In 1952 he was appointed lecturer at the newly established Faculty of Telecommunication of the Technical University of Gdańsk. Prof. Jagodziński organised the Department of Radio Navigation at this faculty in 1953. Beside his didactic and scientific activities, he was engaged simultaneously in research concerning hydroacoustic constructions. In his department there were constructed echo sounders and sonars for the search of wrecks on the Polish shelf, as well as an ultrasound telephone for communication between frogmans ands submarines.

In 1960 Prof. Jagodziński took his doctor's degree in technical science at the Faculty of Telecommunication of the Technical University of Warsaw. His dissertation dealt with echo ranging systems. In 1964 he was appointed associate professor.

In 1969 he organised a specialisation in hydroacoustics that was unique in Poland; the staffs of the Department of Hydroacoustics and the Department of Electro-Acoustics at then Faculty of Electronics of the Technical University of Gdańsk were involved in it. The specialisation, founded and managed by Prof. Jagodziński, was attended and graduated by about 200 students. He was supervisor of 10 completed postgraduate studies. Five of his postgraduate students were qualified as assistant professors. He is the author of two monographs and about 70 scientific publications and of many patents and studies concerning radio navigation and hydroacoustic constructions.

Prof. Jagodziński performed many important faculty and university duties. He was subdean of the faculty for two terms. He is member of the Committee of Acoustics and the Committee of Sea Research of the Polish Academy of Sciences. He has organised the Polish Acoustical Society and was member of the management of this society for many years and its president from 1981 to 1987. He was member of the scientific council of the Research Centre of the Navy and the Naval Fishing Institute.

Prof. Zenon Jagodziński was awarded the Chivalry Cross of the Order of the Rebirth of Poland, the Medal of the National Education, the Bronze and Silver Medals of Merits to the Country's Defensive System, the Honourable Distinction of Merits to the District of Gdańsk and the Golden Distinction Worker of Merit of the Telecommunication. He also received awards of the President of the Committee of Science and Technology, of the Minister of National Defence, of the General Staff of the Polish Army, of the Commander of the Navy and many others.

Prof. Jagodziński retired in 1983. He left behind a group of mature scientists in the Department of Hydroacoustics (that has been called the Department of Acoustics since 1993). This is where theoretical and applied research in the field of hydroacoustics has been continued.

On December 9, 1994 the honorary doctorate was given to Prof. Jagodziński by the University of Surrey, Guilford, that is the heir of the tradition of the Imperial Institute. This honourable title was awarded Prof. Jagodziński as an outstanding scientist who, according to the idea of the founders of the Polish University College, returned after graduation to his ruined and vandalised country in order to organise a reputable scientific centre that has effectively co-operated with the British acousticians in the field of hydroacoustics and ultrasonics.

Prof. Jagodziński has two desirable but seldom features: the ability of a creative application of theoretical achievements in practice and, first of all, the ability to stimulate a creative climate of friendly co-operation.

The first one bore fruit in the forms of two monographs: the *Radio Navigation Systems*, that appeared in 1969 (and disappeared a long time ago, not only from the bookstores but also from librairies from which it has been appropriated by fan-readers) and another one entitled *Ultrasonic Transducers* that appeared in 1998 year and is hust vanishing from the bookstors. The respect of Prof. Jagodziński for practice manifested itself in the obligation, and pleasure, of each of his students to participate under the Professor's supervision in the field laboratories installed on lakes (hydroacoustics) and airports (radio navigation). In this way the students was given a chance to get a knowledge of problems appearing in real systems and centres and to gain in engineering intuition indispensable in the designing of hydroacoustics and navigation devices.

The second one has born fruit in the creation of a stable and strong team of a recognised scientific and didactic position; this team has tried to continue and develop the style of activities of Prof. Jagodziński.

Professor Zenon Jagodziński died in January 22, 1999.

Professor Jagodziński will always remain in the memory of all those who had the privilege to meet Him on the way of their lives.

ARCHIVES OF ACOUSTICS
24, 3, 255–267 (1999)

COMPLETE CHARACTERIZATION OF ULTRASOUND TRANSDUCERS THROUGH THE "FIELD II" SIMULATION PROGRAM

G. GUIDI and S. FALTERI

Electronic Engineering Department
University of Florence
(3–50139 Florence, Via S. Marta, Italy)
e-mail: g.guidi@ieee.org

Acoustic field characterization is usually limited to the measurement of the field amplitude, and employs well-known investigation methods. However, it is known that in many applications an important role is played by the phase field distribution. For example, a complete acoustic field characterization (i.e. the determination of both the amplitude and phase field distributions), results very useful for the correct interpretation of the Doppler signals detected by such a transducer. In this paper a technique for the measurement of the complex field (phasor) produced by single element transducers is presented. It is based on the time domain analysis of the RF pressure signals produced in front of the transducer. The technique, proposed as a general experimental procedure for the concurrent measurement of phase and amplitude fields, is here applied to fields synthesized with the "Field II" simulation program. Simulation results are compared with field distributions both available in the literature in analytic form, or derived experimentally.

1. Introduction

Important issues, like the quantitative assessment of pressure impinging on human tissues or the estimation of transducers' focusing properties, are yielded by estimating the field amplitude in front of the transducer face.

As known, such evaluation can be made with direct measurement, by scanning with hydrophones the volume of interest, or indirectly, by measuring the signal backscattered toward the transducer from a point-like target located at different places.

The former method is usually considered the "gold standard" for any quantitative estimation of pressure levels, while focusing properties, providing a target small enough to be considered like a point, can be detected with the latter too.

In any case the quantity to be measured is always the field amplitude, while little emphasis is given to the phase field distribution.

As a matter of fact, the phase can be neglected in imaging systems characterization, where the lateral resolution — or the capability to distinguish two near details along a line perpendicular to the beam axis at a certain range — is determined by the beam Full

Width at Half Maximum (FWHM), given as the intersection between the field *amplitude* at the range of interest, and a -6 dB threshold level [1].

When a beam has to be characterized for a Doppler equipment rather than an imager, *phase* field distribution becomes important [2, 3]. A scatterer traveling across an acoustic field, whose phase distribution differs from plane wave conditions, originates a frequency modulation in the backscattered signal which broadens the Doppler Spectrum with respect to the simple theoretical predictions associated to the transit-time only.

Beam characterization of transducers to be coupled to Doppler flowmeters should therefore take into account not only the amplitude but also the phase distribution with proper measurement techniques [4, 5].

In this paper a method for calculating the complex (amplitude and phase) spatial field from the time domain RF signals, as those detected from hydrophones, is presented. Despite of the fact that it was proposed as a general technique, it has been verified here on simulated RF signals. A comparison between simulated and experimental intensity beamplots, for two differently focused circular transducers, is finally shown.

2. Methods

The tool used for simulating the complex field distribution is the "Field II" program, developed by JENSEN [6], which employs the spatial impulse response method proposed by TUPHOLME and STEPHANISHEN [7, 8].

The original method requires to know the spatial impulse response of the transducer geometry; in order to reduce the analytic complexity involved, the simulation program provides the subdivision of the transducer surface in small squares, whose impulse response is known, and evaluates the global field by summing the response of each elementary radiator. The calculation time is kept low considering the small elementary square aperture, and using for this reason far-field approximation for each transducer element.

The simulator inputs define the transducer geometry as aperture shape and dimensions, focusing properties, possible presence of apodization, and the excitation signal applied to the transducer. As output it supplies the space-time properties of the pressure field $u(x, y, z, t)$ resulting from a known velocity $v(x, y, z, t)$ over the transducer surface. Such output is analogous to the RF signal displayed by an oscilloscope connected to an hydrophone located at the points of simulation.

In our experiments a spherically focused circular transducer was used, as the one sketched in Fig. 1, where the cartesian reference is also shown.

The excitation was chosen as a burst at frequency f_0 made by an integer number of pulses. The velocity distribution was supposed uniform over the whole transducer and given in the form:

$$v(t) = v_0 e^{i\omega_0 t}, \qquad \omega_0 = 2\pi f_0 \tag{1}$$

with v_0 unknown and set to an arbitrary value. However, since the scope of the work was not to simulate a transducer in order to guess an absolute amplitude value, but just for having a relative amplitude beam plot and the absolute phase distribution, the

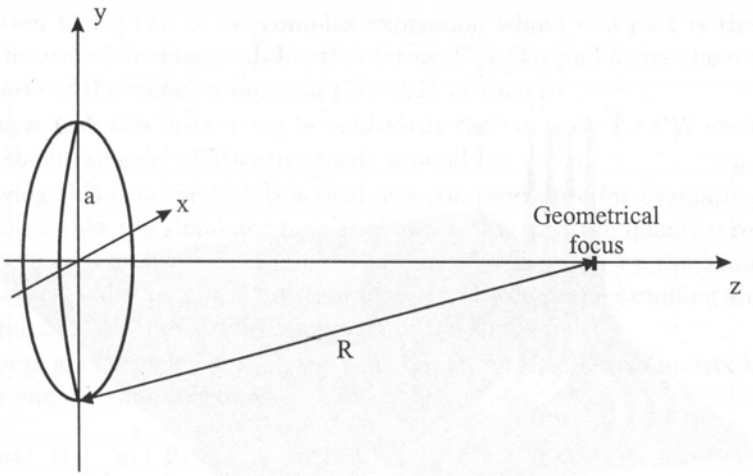

Fig. 1. Spherically focused circular transducer and reference system.

knowledge of v_0 was actually not required. For a quantitative simulation v_0 should be estimated, as for example in the work of MAIONE *et al.* [9], starting from the knowledge of the exciting amplitude, and simulating with PSpice and a proper electro-mechanical model the actual transducer vibration.

Figure 2 shows one of the typical outputs of the program. It was originated by simulating a circular transducer with a diameter of $2a = 8\,\text{mm}$, radius of curvature $R = 30\,\text{mm}$ (geometrical focus), operating at $f_0 = 8\,\text{MHz}$ with no apodization. The excitation signal was a narrowband pulse composed by 4 sinusoid cycles. The display shows the behavior in time of the field at 30 mm from the aperture, for several off-axis displacements. The time axis starts from an offset, supplied as output by the simulator, which represents the global delay of this space-time distribution respect to the application of the excitation to the transducer. By looking at the figure, it can be identified the pulse train proceeding and, for different time instants, it is possible to see the growing of sidelobes as the time passes.

A field representation in the time domain, as this one described above, is doubtlessly the best one for analyzing the effect of a transient excitation. On the other hand, when a beamplot have to be calculated, the most convenient representation is that where the time dependent term is separated by the space varying one. Indicating with $u(x, y, z, t)$ the behavior in time of the acoustic field at the spatial point $\{x, y, z\}$, for a CW excitation or a steady period of a pulsed excitation, the field can be expressed as:

$$u(x, y, z, t) = \text{Re}\left\{\underline{U}(x, y, z)e^{j\omega_0 t}\right\}, \tag{2}$$

where $\underline{U}(x, y, z)$ is the complex function obeying to the Helmoltz equation, which defines the spatial varying part of the field [10], having its own modulus and phase:

$$\underline{U}(x, y, z) = U(x, y, z)e^{j\phi(x,y,z)}. \tag{3}$$

Looking at $u(x, y, z, t)$ as the projection on the real axis of a rotating phasor with angular velocity ω_0, if we consider a specific point $\{\tilde{x}, \tilde{y}, \tilde{z}\}$ at two specific times $\tilde{t}$ and $\tilde{t} - \Delta\tilde{t}$,

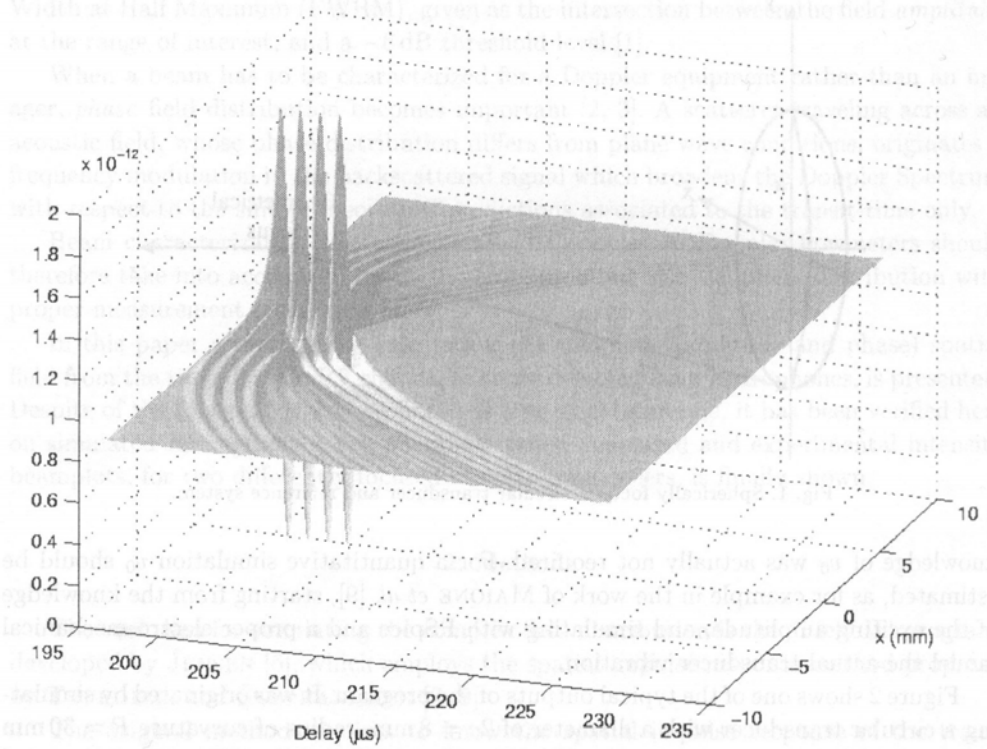

Fig. 2. Typical output of the "Field II" program, obtained for a Spherically focused circular transducer with $a = 4\,\text{mm}$ and $R = 30\,\text{mm}$, simulating the field generated at 30 mm from the transducer, for $y = 0$ and x ranging from -10 and 10 mm.

the field can be written as:

$$\begin{aligned} u(\tilde{x},\tilde{y},\tilde{z},\tilde{t}) &= U(\tilde{x},\tilde{y},\tilde{z})\cos\left[\omega_0\tilde{t}+\phi(\tilde{x},\tilde{y},\tilde{z})\right], \\ u(\tilde{x},\tilde{y},\tilde{z},\tilde{t}-\Delta\tilde{t}) &= U(\tilde{x},\tilde{y},\tilde{z})\cos\left[\omega_0\tilde{t}-\omega_0\Delta\tilde{t}+\phi(\tilde{x},\tilde{y},\tilde{z})\right]. \end{aligned} \tag{4}$$

If $\Delta\tilde{t}$ is chosen such as:

$$\omega_0\Delta\tilde{t} = \frac{\pi}{2},$$

the expression $(4)_2$ becomes:

$$\begin{aligned} &u(\tilde{x},\tilde{y},\tilde{z},\tilde{t}-\Delta\tilde{t}) \\ &\quad = U(\tilde{x},\tilde{y},\tilde{z})\cos\left[\left(\omega_0\tilde{t}+\phi(\tilde{x},\tilde{y},\tilde{z})\right)-\frac{\pi}{2}\right] = U(\tilde{x},\tilde{y},\tilde{z})\sin\left[\omega_0\tilde{t}+\phi(\tilde{x},\tilde{y},\tilde{z})\right]. \end{aligned} \tag{5}$$

Hence combining Eq. $(4)_1$ and 5 as the real and imaginary part of a complex number, we have:

$$\begin{aligned} &u(\tilde{x},\tilde{y},\tilde{z},\tilde{t})+ju(\tilde{x},\tilde{y},\tilde{z},\tilde{t}-\Delta\tilde{t}) \\ &\qquad = U(\tilde{x},\tilde{y},\tilde{z})\cos\left[\omega_0\tilde{t}+\phi(\tilde{x},\tilde{y},\tilde{z})\right]+jU(\tilde{x},\tilde{y},\tilde{z})\sin\left[\omega_0\tilde{t}+\phi(\tilde{x},\tilde{y},\tilde{z})\right] \\ &\qquad = U(\tilde{x},\tilde{y},\tilde{z})e^{j\left[\omega_0\tilde{t}+\phi(\tilde{x},\tilde{y},\tilde{z})\right]} = \underline{U}(\tilde{x},\tilde{y},\tilde{z})e^{j\omega_0\tilde{t}} \end{aligned}$$

that, as written in Eq. (2), is the complex expression whose real part is the quantity hydrophone measured or simulated. In other terms, Eqs. $(4)_1$ and 5 give the real and the imaginary parts of the complex function $\underline{U}(\tilde{x}, \tilde{y}, \tilde{z})$ at time $\tilde{t}$.

Operating in CW this instant can be arbitrarily chosen, while for PW excitation the spatial field should remain sufficiently steady around $\tilde{t}$.

For applying this concept in a practical numeric procedure for evaluating $\underline{U}(\,)$, we have to consider that the simulator output shown in Fig. 2 is the quantity represented by Eq. (2) for $y = \tilde{y}$ and $z = \tilde{z}$. The resulting set of data given by the simulator is a sampling in space and time of the function $u(x, \tilde{y}, \tilde{z}, t)$, where the sampling steps over x and t, Δx and Δt_s, are user defined as inputs of the simulator.

The outputs are the delay d of all the time-lines, and the 2D real matrix $\mathbf{u}$, with M (space) rows and N (time) columns:

$$\mathbf{u} = \begin{bmatrix} u(1,1) & u(1,2) & \dots & u(1,N) \\ u(2,1) & u(2,2) & \dots & u(2,N) \\ \vdots & \vdots & \vdots & \vdots \\ u(M,1) & u(M,2) & \dots & u(M,N) \end{bmatrix}$$

$$= u\left[\left(m - \frac{M}{2}\right)\Delta x, \tilde{y}, \tilde{z}, d + n\Delta t_s\right] \quad \text{for} \quad m = 1, 2, ..., M, \quad n = 1, 2, ..., N. \tag{6}$$

In order to smoothly extract from such matrix only the complex array, representing the spatial field distribution along x, we have to chose a time sampling frequency $f_s = 1/\Delta t_s$ equal to an integer multiple of $4f_0$. This condition is required because if:

$$f_s = 4kf_0, \qquad \text{and} \qquad \Delta t_s = \frac{1}{f_s} = \frac{1}{4kf_0} \tag{7}$$

then for each x, the time instants where the field is sampled, are $t_n = n\Delta t_s$, so that the "in phase" and "in quadrature" components have phases given by:

$$\omega_0 t_n = \frac{2\pi f_0 n}{4kf_0} = \frac{2\pi}{4k} n \qquad \text{(Phase)},$$

$$\omega_0 t_n - \frac{\pi}{2} = \frac{2\pi}{4k}(n-k) \qquad \text{(Quadrature)}$$

or, with reference to matrix $\mathbf{u}$, for a specific (space) row m, the time components corresponding to indexes n and $n - k$.

Therefore, once a starting time $\tilde{t} = \tilde{n}\Delta t_s$ is chosen such that the field amplitude remains sufficiently steady in the previous $k\Delta t_s$ seconds, we evaluate the complex field at $y = \tilde{y}$ and $z = \tilde{z}$ through the complex array $\mathbf{U}$ whose components are:

$$U(m) = u(m, \tilde{n}) + ju(m, \tilde{n} - k) \qquad \text{for} \quad m = 1, 2, ..., M. \tag{8}$$

By repeating this procedure for several depth, a 2D complex representation of the field in space (e.g. xz scan), can be extracted by the time domain data.

3. Results

The field distribution obtained with the method described above was first compared with the approximated expression of the space field distribution produced in the focal plane by a spherically focused circular transducer that can be found in the literature [11, 1, 12]. It is proportional to the so-called Airy distribution, given by:

$$u_{\text{Airy}} = \rho c \frac{u_0}{\lambda} \frac{\pi a^2}{R} \frac{2J_1(\xi)}{\xi}, \qquad \xi = \frac{2\pi a \rho'}{\lambda R}, \tag{9}$$

where J_1 indicates the first order Bessel function, and the meaning of the symbols is the following one:

- ρ density of the propagating medium (Kg/m^3),
- c sound velocity in the propagating medium (m/s),
- λ wavelength in the propagating medium (m),
- a aperture radius (m),
- R geometrical focus (m),
- ρ' radial distance off-axis (m).

As specified in the previous section, since we do not have a quantitative value of the transducer velocity, our interest is for the qualitative field distribution. Therefore only a normalized version of Eq. (9) can be considered and compared with the corresponding normalized field obtained from the simulation procedure. With reference to the cartesian reference shown in Fig. 1:

$$u'_{\text{Airy}}(x,y) = \frac{J_1(\xi(x,y))}{\xi(x,y)}, \qquad \xi(x,y) = \frac{2\pi a}{\lambda R}\sqrt{x^2+y^2}. \tag{10}$$

The data used for the comparison were the same as indicated for Fig. 2 ($a = 4\,\text{mm}$, $R = 30\,\text{mm}$, $c = 1500\,\text{m/s}$, $\lambda = c/f_0 = 1500/8 \cdot 10^6 = 187.5\,\mu\text{m}$) over the x axis.

This expression is valid for CW excitation, hence the simulation procedure was performed with an excitation pulse long enough to produce a steady field after a transition period. In Fig. 3 a a gray level image of the transient field at $z = 30\,\text{mm}$ is shown, where two lines indicate the phase and quadrature times, chosen after nine burst pulses, in order to have a fully developed spatial field.

In Fig. 3 b the function represented by Eq. (10) has been plotted (dotted line) for $y = 0$ and x ranging from -6 to 6 mm. In the same figure the continuous line indicates the normalized field amplitude obtained by processing the time domain data of Fig. 3 a. The strong agreement between the two curves make them almost not distinguishable.

The phase behavior obtained from the analytical Airy distribution is shown in Fig. 3 c with a dotted line. It exhibits a flat null behavior with alternate jumps from 0 to π for each zero of the field amplitude. Differently from the extremely good agreement between the simulated and analytical amplitudes, the phase variation originated by the simulation differs evidently from the analytical one. The geometrical focus, where such behavior has been calculated, is in fact farer from the aperture respect to the true focus F, where the maximum amplitude holds and the phase distribution is flat. In general [5, 13] the phase plot of a focused beam is concave with concavity oriented away from the transducer

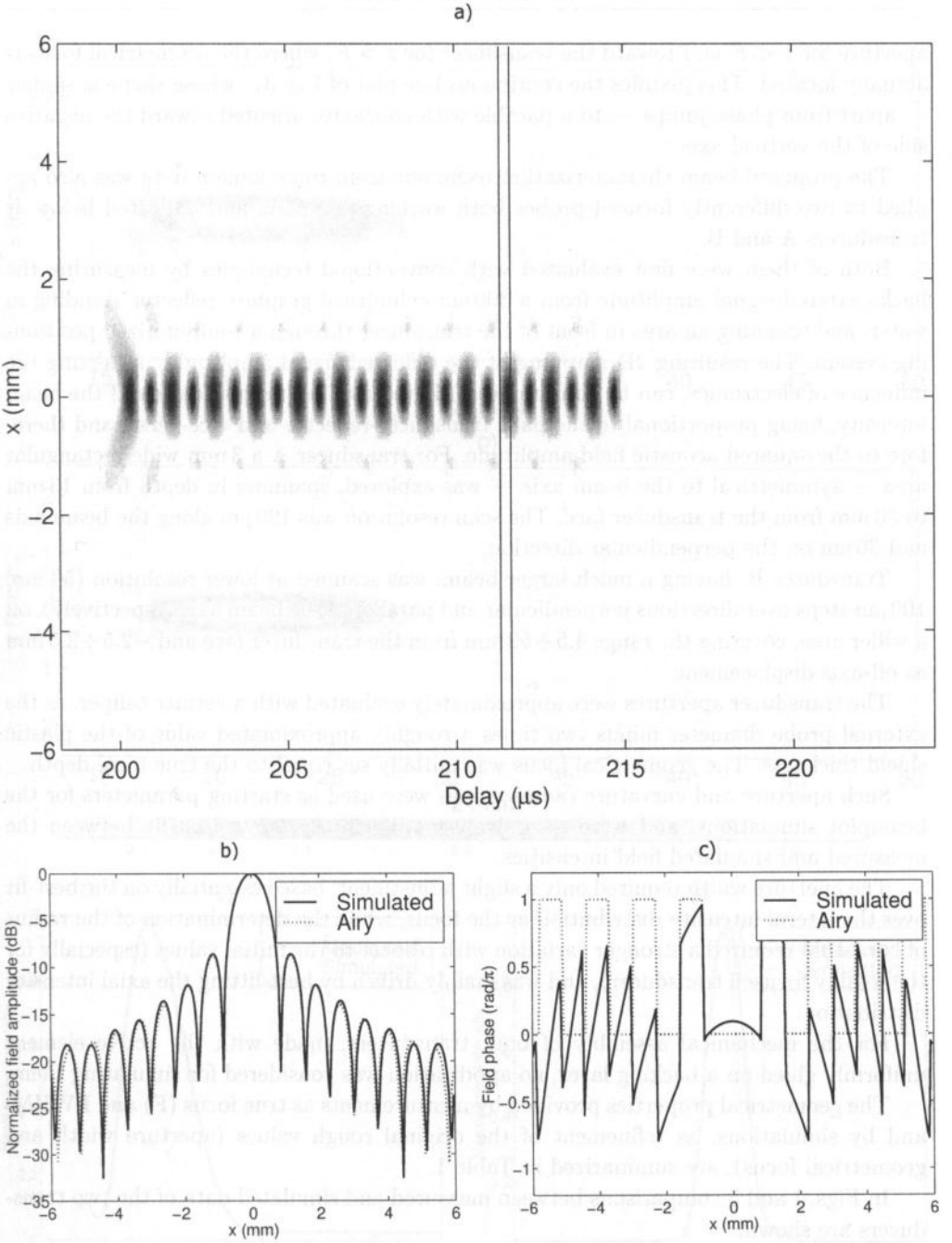

Fig. 3. Simulation of the field generated at $z = 30$ mm by the same transducer of Fig. 2 excited with an 8 MHz burst composed by 12 cycles; a) time-space representation of the field. The vertical lines represent the Phase and Quadrature sampling instants. b) Field amplitude module. c) Field phase.

aperture for $z < F$ and toward the transducer for $z > F$, where the geometrical focus is actually located. This justifies the continuous line plot of Fig. 3 c, whose shape is similar — apart from phase jumps — to a parable with concavity oriented toward the negative side of the vertical axis.

The proposed beam characterization technique from time-domain data was also applied to two differently focused probes both working at 8 MHz and indicated below as transducers A and B.

Both of them were first evaluated with conventional techniques by measuring the backscattered signal amplitude from a 300 μm cylindrical graphite reflector standing in water, and scanning an area in front of the transducer through a computerized positioning system. The resulting 2D mapping of the reflected signal amplitude, neglecting the influence of electronics, can be considered as the normalized representation of the beam intensity, being proportional to the path transducer-reflector and vice-versa, and therefore to the squared acoustic field amplitude. For transducer A a 3 mm wide rectangular area — symmetrical to the beam axis — was explored, spanning in depth from 13 mm to 50 mm from the transducer face. The scan resolution was 100 μm along the beam axis and 30 μm on the perpendicular direction.

Transducer B, having a much larger beam, was scanned at lower resolution (50 and 100 μm steps over directions perpendicular and parallel to the beam axis respectively), on a wider area, covering the range $4.5 \div 50$ mm from the transducer face and $-2.5 \div 2.5$ mm as off-axis displacement.

The transducer apertures were approximately evaluated with a vernier caliper, as the external probe diameter minus two times a roughly approximated value of the plastic shield thickness. The geometrical focus was initially set equal to the true focal depth.

Such aperture and curvature radius values were used as starting parameters for the beamplot simulations, and were recursively modified to reach a best-fit between the measured and simulated field intensities.

The aperture width required only a slight adjustment, based essentially on the best-fit over the lateral intensity distribution at the focus, while the determination of the radius of curvature required a stronger variation with respect to the initial values (especially for the weakly focused transducer), and was mainly driven by best-fitting the axial intensity distribution.

For the mechanical assembly of both transducers, made with the active element uniformly glued on a backing layer, no apodization was considered for simulating them.

The geometrical properties provided by measurements as true focus (F) and FWHM, and by simulations, as refinement of the original rough values (aperture width and geometrical focus), are summarized in Table 1.

In Figs. 4 and 5 comparisons between measured and simulated data of the two transducers are shown.

Figure 4 reports data related to the transducer A. The measured and simulated 2D beam intensity plot after normalization have been reported (Fig. 4 a and 4 b, respectively). The strong qualitative agreement between them is confirmed by the variation of the normalized field with distance on the beam axis (Fig. 4 c), and with lateral displacement at the true focus (Fig. 4 d).

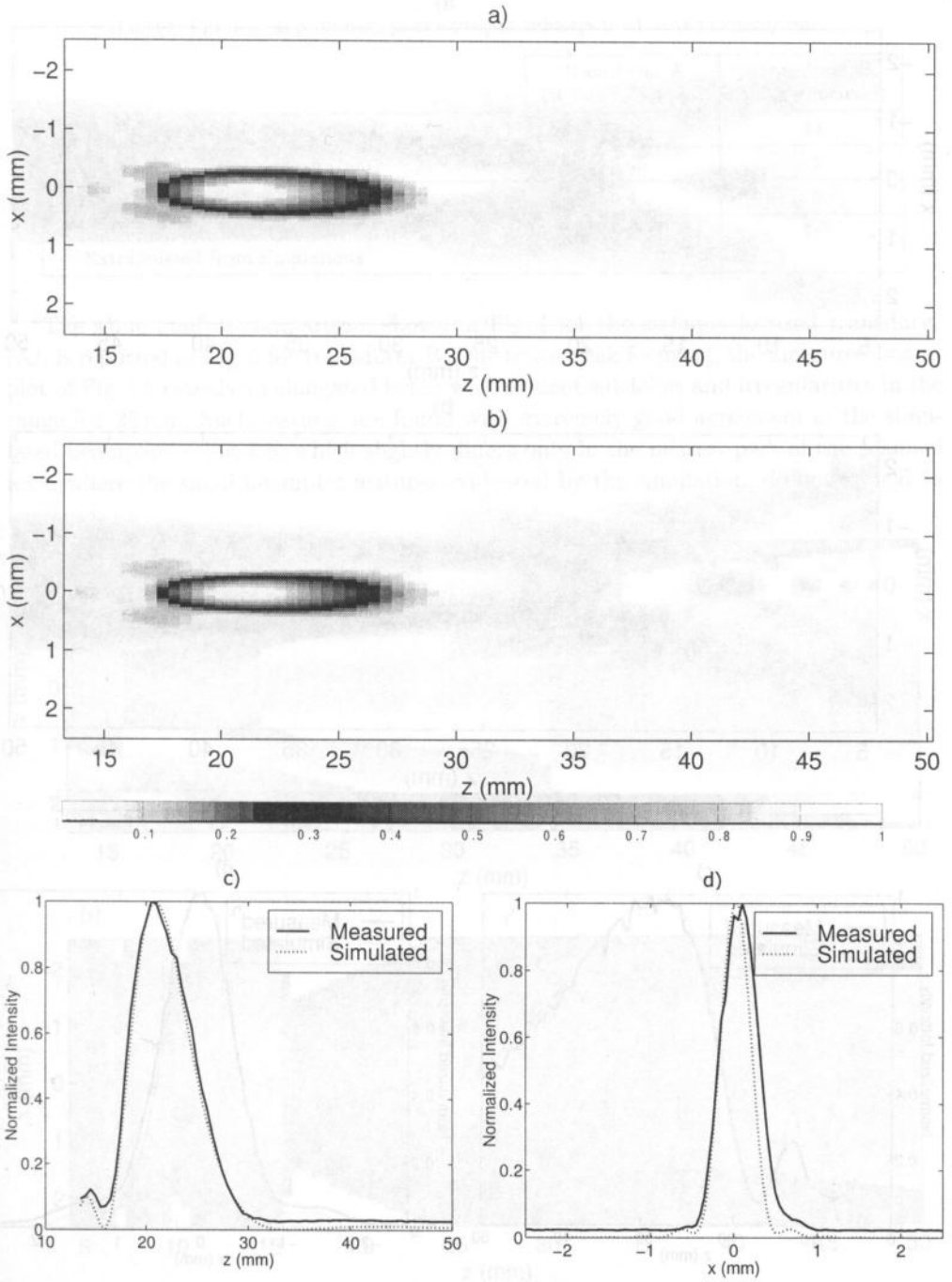

Fig. 4. Transducer A (strongly focused). 2D plot of the beam intensity a) measured; b) simulated; beam intensity along the z axis (c), and along the x axis at the focus (d).

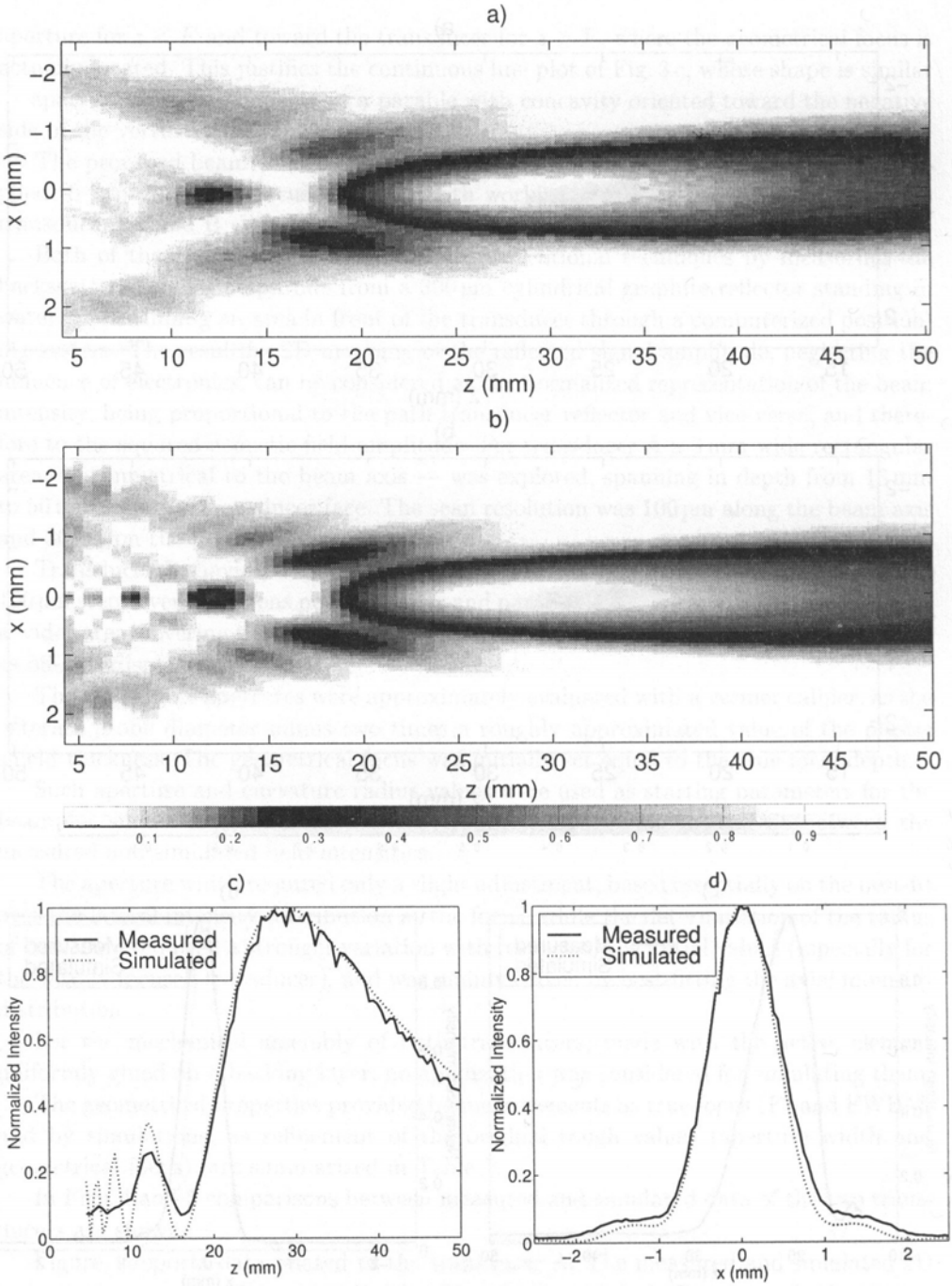

Fig. 5. Transducer B (weakly focused). 2D plot of the beam intensity a) measured; b) simulated; beam intensity along the z axis (c), and along the x axis at the focus (d).

Table 1. Parameters summary of the two transducers used in the experiments.

	Transducer A (strongly focused)	Transducer B (weakly focused)
F or True focus (mm) — Measured	20.75	30
FWHM or −6 dB beamwidth (mm) — Measured	0.45	1
Diameter (mm) — Extrapolated from simulations	9.4	6
Radius of curvature or Geometrical focus (mm) — Extrapolated from simulations	21.6	46

The same kind of comparison, shown in Fig. 4 for the strongly focused transducer (A), is reported in Fig. 5 for transducer B. Due to its weak focusing, the measured beamplot of Fig. 5 a reveals an elongated beam with evident sidelobes and irregularities in the range $5 \div 25$ mm. Such features are found with extremely good agreement in the simulated beamplot of Fig. 5 b, which slightly differs only in the nearest part of the scanned area, where the small beamplot features evidenced by the simulation, do not appear in

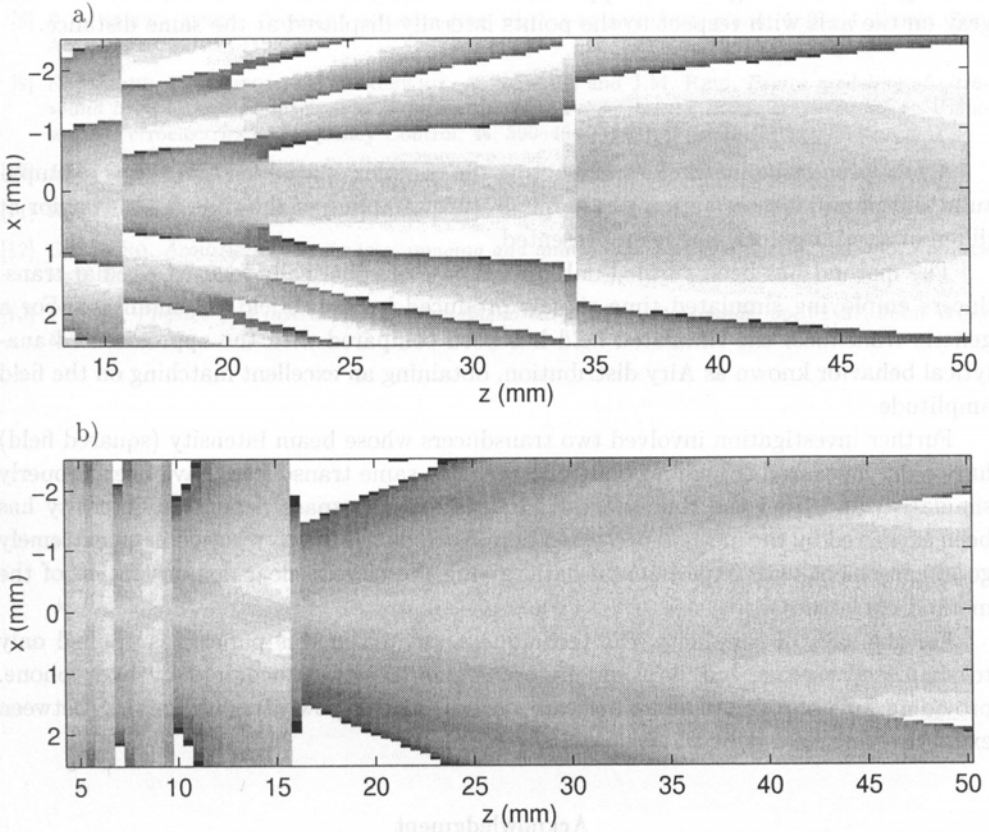

Fig. 6. Phase distributions of both transducers from the complete fields originating Figs. 4 b and 5 b; a) Transducer A, $F = 20.75$ mm; b) Transducer B, $F = 30$ mm. In the gray level scale $-\pi$ corresponds to white and $+\pi$ to black. The absence of any phase unwrapping involves abrupt white-to-black transitions.

Fig. 5 a. This might be due to the 300 μm echogenic target used to obtain the measured beamplot. It was wider than λ (187.5 μm in 20° pure water), being actually a reflector rather than a scatterer, and therefore capable of producing an intrinsic smoothing of the beamplot which could have hidden some tiny details. The qualitative agreement of the two beamplots of Figs. 5 a and 5 b is confirmed by the simulated and measured behaviors of the field intensity along z-axis (Fig. 5 c), and along x-axis at the focal distance (Fig. 5 d).

From the complete fields originating such nicely matched beamplots, the phase fields were calculated and shown in Fig. 6 with a gray level scale where $-\pi$ corresponds to white and π to black. The absence of any phase unwrapping involves abrupt white-to-black transitions visible in both images of Fig. 6.

Transducer A (Fig. 6 a) exhibits a stronger phase bending in comparison with transducer B (Fig. 6 b) as shown by the higher number of white-to-black transitions present in Fig. 6 a. In both cases near the beam axis the phase curvature is positive for $z < F$ as shown for a given distance by a gray level lighter on the axis rather than off-axis. Looking at the two figures the opposite situation is evident for $z > F$, with a darker gray on the axis with respect to the points laterally displaced at the same distance.

4. Conclusions

A new processing method for extracting the complex spatial field, in terms of amplitude and phase, from a proper phase-quadrature sampling of the time field behavior at different spatial points, has been presented.

The method has been verified only in the case of spherically focused circular transducers employing simulated time signals produced by the "Field II" simulator. For a generic transducer the simulated field has been compared with the approximated analytical behavior known as Airy distribution, obtaining an excellent matching on the field amplitude.

Further investigation involved two transducers whose beam intensity (squared field) have been measured trough a point-reflector. The same transducers have been properly simulated, and from the time-space field variation, the space dependent intensity has been extracted by the method presented here. Such distributions resulted in an extremely good agreement with experimental data, giving therefore a clear demonstration of the method correctness.

For the sake of simplicity, the technique presented in this paper was applied only to simulated signals, but it would be applicable to signals acquired by hydrophone, providing an appropriate sampling rate, and a precise (low-jitter) triggering between excitation and field data acquisition.

Acknowledgment

The authors wish to thank Professor PIERO TORTOLI, from the Electronic Engineering Dept. of the University of Florence, for useful discussions.

References

[1] J.W. HUNT, M. ARDITI and F.S. FOSTER, *Ultrasound transducers for pulse echo medical imaging*, IEEE Trans. on Biomed. Eng., **30**, 453–481 (1983).

[2] P.J. FISH, *Doppler methods*, [in:] Physical Principles of Medical Ultrasonics, 350–363, C.R. HILL [Ed.], Ellis Horwood, Chichester, UK 1986.

[3] O.W. ATA and P.J. FISH, *Effect of deviation from plane wave conditions on the Doppler spectrum from an ultrasonic blood flow detector*, Ultrasonics, **29**, 395–403 (1991).

[4] J.D. AINDOW and R.C. CHIVERS, *Measurement of the phase variation in an ultrasonic field*, J. Phys. E: Sci. Instrum., **15**, 83–86 (1982).

[5] G. GUIDI and S. FALTERI, *Phase measurement of acoustic fields based on a moving target*, IEEE Transactions on Ultrasonics, Ferroelectrics & Frequency Control, **46**, 679–689 (1999).

[6] J.A. JENSEN and N.B. SVENDSEN, *Calculation of pressure fields from arbitrarily shaped, apodized, and excited ultrasound transducers*, IEEE Transactions on Ultrasonics, Ferroelectrics & Frequency Control, **39**, 262–267 (1992).

[7] G.E. TUPHOLME, *Generation of acoustic pulses by baffled plane pistons*, Matematika, **16**, 209–224 (1969).

[8] P.R. STEPHANISHEN, *Transient radiation from pistons in an infinite planar baffle*, J. Acoust. Soc. Am., **77**, 1629–1638 (1971).

[9] E. MAIONE, P. TORTOLI, G. ŁYPACEWICZ, A. NOWICKI and J.M. REID, *Pspice modeling of ultrasound transducers: comparison of software models to experiments*, IEEE Transactions on Ultrasonics, Ferroelectrics & Frequency Control, **46**, 399–406 (1999).

[10] J.W. GOODMAN, *Introduction to Fourier optics*, pp. 33–34, McGraw-Hill, New York 1968.

[11] H.T. O'NEIL, *Theory of focusing radiators*, J. Acoust. Soc. Am., **21**, 126–516 (1949).

[12] G.S. KINO, *Acoustic waves: devices, imaging and analog signal processing*, pp. 182–186, Prentice Hall, Englewood Cliffs, 1987.

[13] P. FISH, *Physics and instrumentation of diagnostic medical ultrasounds*, pp. 32–37, John Wiley & Sons, 1990.

ARCHIVES OF ACOUSTICS
24, 3, 269–288 (1999)

COMPUTING AND MEASURING NONLINEAR AND LINEAR PROPAGATION BY TWO INDEPENDENT METHODS

L. FILIPCZYŃSKI, T. KUJAWSKA, W. SECOMSKI, R. TYMKIEWICZ and J. WÓJCIK

Polish Academy of Sciences
Institute of Fundamental Technological Research
Department of Ultrasound
(00-049 Warszawa, Świętokrzyska 21, Poland)

Nonlinear effects, caused by propagation of ultrasonic pulses with finite amplitudes, were computed and measured in water in the case of pulses with pressures up to 1.5 MPa_{pp} used in diagnostic devices. An electronic transmitter generated high (280 V_{pp}) and low (47 V_{pp}) voltages, applied to a plane PZT transducer causing in this way nonlinear and linear propagation effects. The carrier frequency of the pulse was 2 MHz, while its time duration was 2.5 ms. The measurements were carried out by means of a typical calibrated PVDF membrane hydrophone and by an electromagnetic (EM) hydrophone, prepared for this study. The pulse measurements by means of the PVDF hydrophone showed a higher number of spectral components than those by means of the EM hydrophone. This effect was explained by sensitivity characteristics that increased in the PVDF and decreased in the EM hydrophone as a function of frequency. Previously, it was shown that the effective frequency band used in measurements by means of the PVDF hydrophone is situated below the resonance, on the increasing slope of the resonanse curve. The properties of the EM hydrophone were analysed on the basis of the plane wave assumption. A procedure was developed to correct distortions of the pulse spectrum and its pressure measured by PVDF and EM hydrophones. In the first case the maximum peak-to-peak pulse pressure should be decreased by 27%, while in the second case it should be increased by only 0.7%, and by 3% if an additional amplifier was used. The sensitivities of PVDF and EM hydrohones were very different and equal for the frequency of 2 MHz to 28 mV/MPa and 0.10 mV/MPa, respectively. The calibration of the EM hydrophone was carried out by means of only two simple: electrical and magnetic independent measurements, although in the EM hydrophone there occured external interferring signals. For the theoretic-numerical detemination of the acoustic fields and their spectra generated in the case of nonlinear and linear propagation the numerical procedure called the WJ Code was applied. It was developed recently by the last-named author of this paper. In calculations absorption in water was taken into account. The critical distance, where distortions caused by nonlinear propagation in water were maximum, was determined by a number of computations of the ultrasonic field as a function of the distance from the transducer. A good agreement between computed results and those measured by two different methods, showing the pulse pressure distribution along the whole beam axis, was confirmed. In this case it was shown that the $\lambda/4$ matching layer covering the transducer surface influenced the edge wave radiated by the transducer.

Keywords: ultrasound, nonlinear propagation, pulses, diagnostics, hydrophone

1. Introduction

When investigating nonlinear effects caused by propagation of finite amplitude disturbances in fluids and in soft tissues, it is sometimes necessary to measure pressure pulses with spectral distributions up to frequences of 20 MHz or, even, higher. This is the case typical of ultrasonography where the pulses of short time duration, in the MHz range, with amplitudes equal or higher than 1 MPa, are sometimes applied [3]. The problem of exact measurements of nonlinear distortions is crucial for nonlinear acoustics, so we decided to investigate this problem in more detail. The purpose of this paper is to show and to discuss distortions of nonlinear effects caused by measurements with PVDF hydrophones and to present a different measurement method by means of an electromagnetic (EM) hydrophone that seems to be more exact. At the same time, we would like to compare the experimental results with numerical ones obtained by means of the WJ Code developed recently by the last-named author [19].

2. Experimental equipment

The principle of the experimental system used in measurements is shown in Fig. 1. In these experiments we used a 2 MHz PZT plane transducer, 1 cm in radius, coated with a $\lambda/4$ matching layer. To obtain nonlinear propagation we applied a pulse transmitter with an output of 280 V_{pp} while for linear propagation a voltage of 47 V_{pp} was ued. The measurements during nonlinear and linear propagation were carried out by switching the transmitter without changing the probe. In this way it was possible to compare directly the nonlinear and linear effects in the same medium, on the same wave path and almost at the same time. The pulse duration time equaled 2.5 μs.

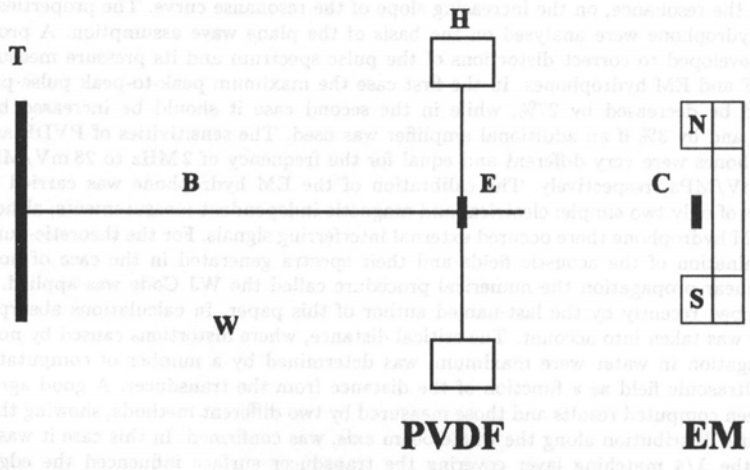

Fig. 1. The system used in measurements: T — transmitting PZT transducer, W — water, H — PVDF hydrophone, E — its active electrode, EM — electromagnetic hydrophone, C — its sensitive gold conductor, B — ultrasonic beam axis.

All the measurements were carried out at a temperature of 22°C, in a water container connected to a microscopic positioning table. The electronic equipment consisted of a switchable pulse transmitter and an additional calibrated amplifier. The output signals from hydrophones were recorded by the LeCroy 9450A digital storage oscilloscope. It allowed up to 50000 points with 400 MHz sampling frequency to be recorded. Data was stored in the memory of the RAM card. The single shot data was recorded to a 8 bit accuracy. Averaged data and FFT frequency spectrum of the signal were stored with a 16 bit accuracy. After measurements data stored in the memory card was transferred into the PC computer via the GP-IB interface (General Purpose Interface Bus). Data was converted in the computer from the LeCroy binary format (type × dkb) to the text format and was converted by the software written in the Turbo Pascal language.

For first, approximate pressure measurements a laboratory made PVDF hydrophone was used with the sensitivity of 18 mV/MPa. However, for exact pressure measurements the PVDF bilaminar membrane hydrophone (Model 804-041 without preamplifier) was used. It was produced by Sonic Technology (Hatboro, USA) and calibrated at the National Physical Laboratory (Teddington, England). Its active gold electrode was 0.6 mm in diameter and the sensitivity equaled 28 mV/MPa at a frequency of 2 MHz. The calibrated sensitivity characteristic is shown in Table 1 as a function of frequency.

Table 1. Calibrated sensitivity of the PVDF hydrophone.

Frequency	[MHz]	2	4	6	8	10	12	14	16	18	20
Sensitivity	[mV/MPa]	28	33	37	41	44	47	50	53	55	56

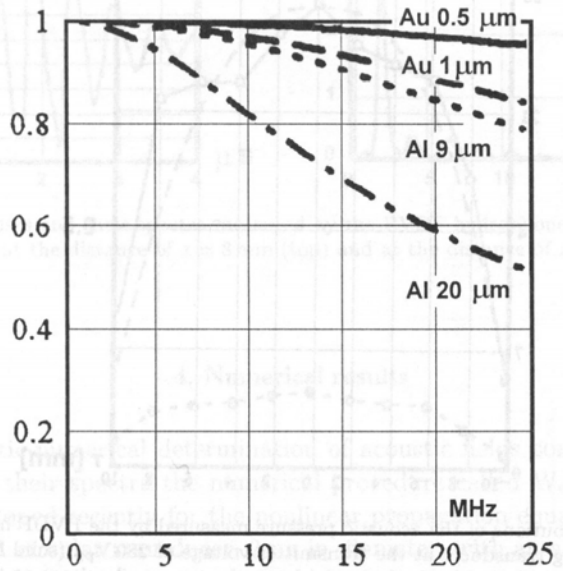

Fig. 2. The calculated modulus of the frequency characteristic of the system water — gold layer — perspex for various thickness of gold (Au) and aluminium (Al).

To obtain independent information about pressure pulses measurements were also carried out by means of an EM hydrophone [13]. This type of the hydrophone was used for absolute measurements of ultrasonic pulses [8], then for diagnostic ultrasound [4], and also recently for shock wave measurements [6]. For the present study a special EM hydrophone was prepared with a gold conductor, 0.3 mm in width, 1.3 mm in length, and 0.5 μm thick. For such a case frequency characteristics of the system composed of water-gold conductor-perspex block, used in this hydrophone, were computed in the plane wave approximation [6], giving the result shown in Fig. 2.

3. Pressure at the source

The crucial problem of our investigations was the determination of the pressure amplitude at the surface near the front surface of the radiating transducer. Its value is decisive for the numerical description of nonlinear distortions in the acoustic field. In Fig. 3 are presented distributions of the peak-to-peak pressure measured by the PVDF hydrophone in water at the distance of $z = 8$ mm from the transducer. These distributions show some irregularities that may be partially caused by vibrations of several modes of the piezoelectric ceramic transducer [14]. Knowing the maximum measured pressure near the transducer equal to $p_0 = 0.97\,\mathrm{MPa_{pp}}$ and its distribution across the beam it was possible to determine boundary conditions of the acoustic pressure at the transducer surface (see the next section).

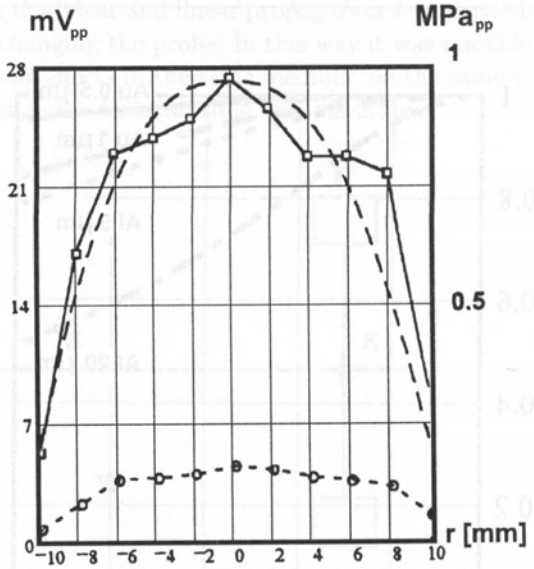

Fig. 3. Radial distributions of the acoustic pressure measured by the PVDF hydrophone in water in front of the radiating transducer at the transmitter voltage of 280 V_{pp} (solid line and points) and of 47 V_{pp} (dashed line and points). Vertical axis shows the measured voltage at the hydrophone output and calulated pressures. The dashed line represents an approximate curve $f(r) = p_0[1 - 0.8(|r|/a)^{2.5}]$ used in calculations.

Near the transducer surface no nonlinearities caused by propagation effects in water were expected. However, we observed in our case at the transducer surface a fundamental frequency of 2 MHz and additionally the third harmonic which was generated by the transmitter-transducer set (Fig. 4, top). Due to the improper frequency characteristic of the PVDF hydrophone the measured amplitude of the third harmonic was inreased by about 30% (see Table 1). It was interesting to notice that the third harmonic decreased with the distance z, for example at $z = 50$ cm the measured amplitude was already comparable with other harmonics which were generated due to nonlinear propagation in water (Fig. 4, bottom). Therefore, in the first approximation the third harmonic at source was neglected.

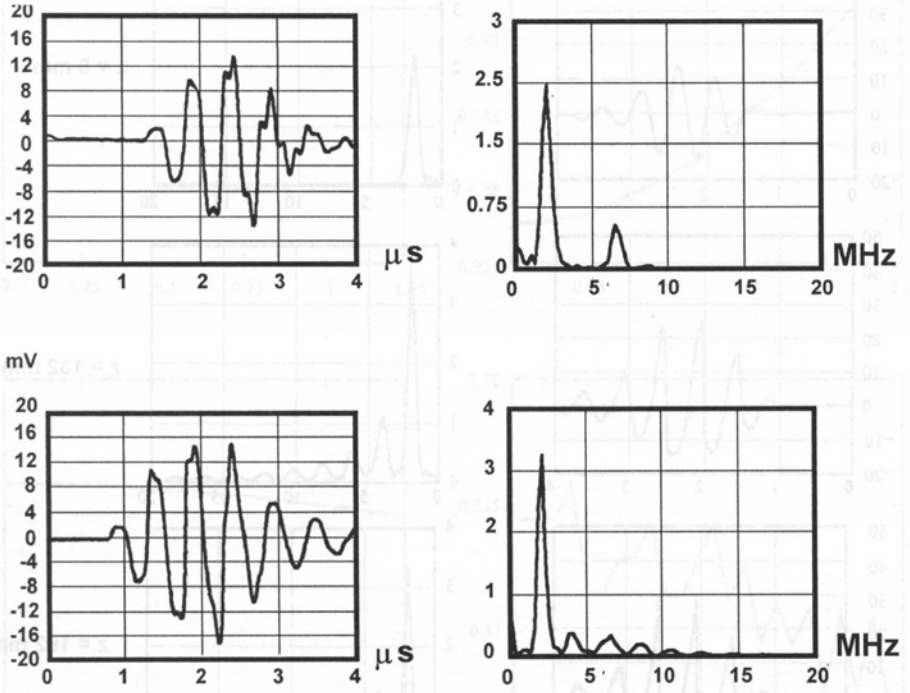

Fig. 4. Pressure pulses and their spectra measured by the PVDF hydrophone for the transmittter voltage of 280 V_{pp} at the distance of $z = 8$ mm (top) and at the distance of $z = 50$ mm (bottom).

4. Numerical results

For the theoretic-numerical determination of acoustic fields connected with propagating pulses and their spectra the numerical procedure called WJ Code [19] was applied. It was developed recently for the nonlinear propagation equation (24) published by WÓJCIK [18]. A circular transducer, 2 cm in diameter, with an aproximate parabolic pressure distribution on its surface (see Fig. 3) was assumed as the wave source. Boundary conditions for a plane transducer were assumed as in the paper [12]. One should

notice that the matching layer on the transducer surface was ignored in numerical calculations. Absorption coefficient for water $\alpha = 28 \cdot 10^{-5}$ Np/cm MHz^2 [2] was applied in calculations.

To determine the critical distance, where distortions caused by nonlinear propagation in water were maximum, a number of measurements were carried out by means of the PVDF hydrophone. Figure 5 shows the pulse shapes and their spectra obtained on

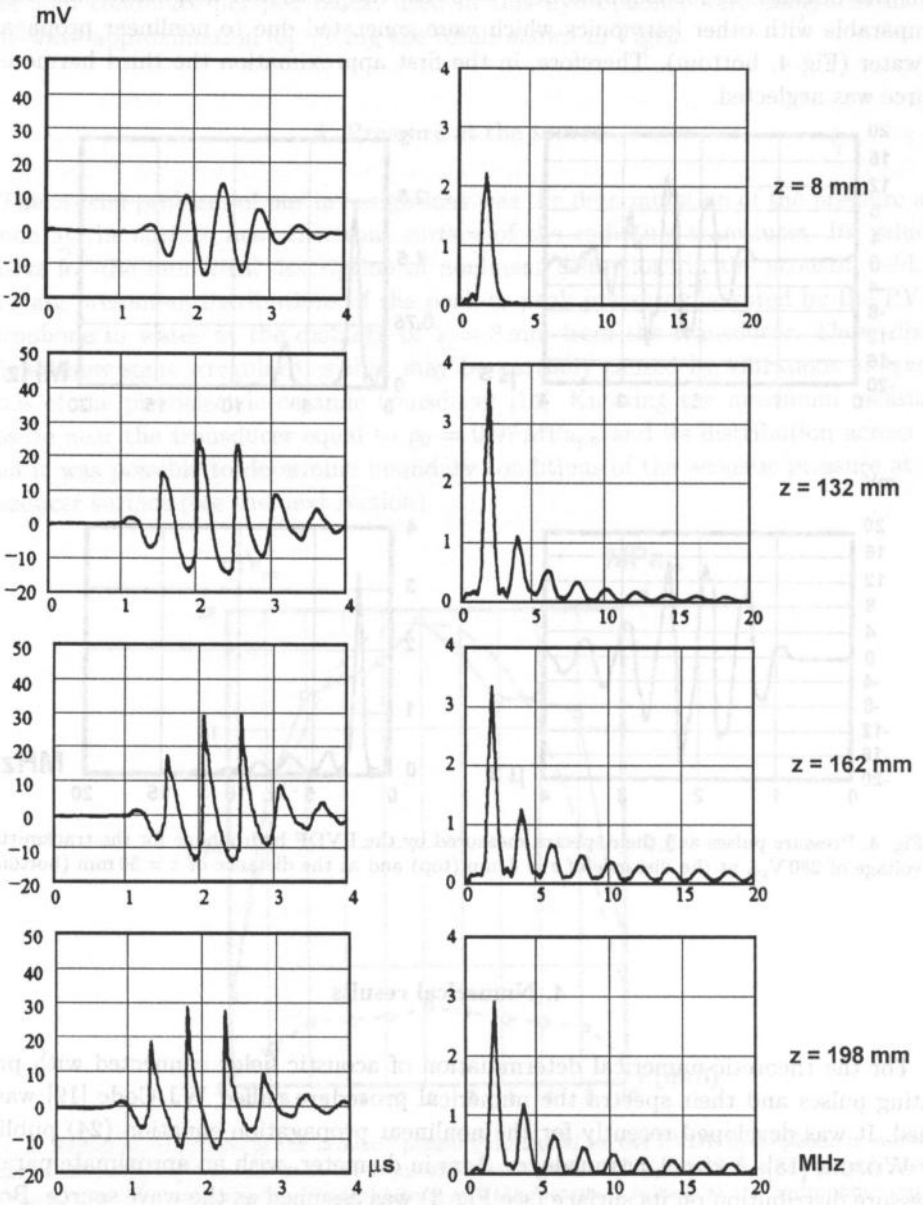

Fig. 5. Pressure pulses and their spectra at various distances z measured with the PVDF hydrophone.

the beam central axis, very near to the transducer at a distance $z = 8\,\text{mm}$, then at $z = 132\,\text{mm}$, $162\,\text{mm}$ and $198\,\text{mm}$. It is evident that the highest number of harmonics arose for distances $z > 160\,\text{mm}$ (see also Fig. 7). The second and third harmonics which have the highest amplitudes among other harmonics attained maximum values at this distance. So, we assumed that at this distance maximum distortions, caused by nonlinear propagation, were expected.

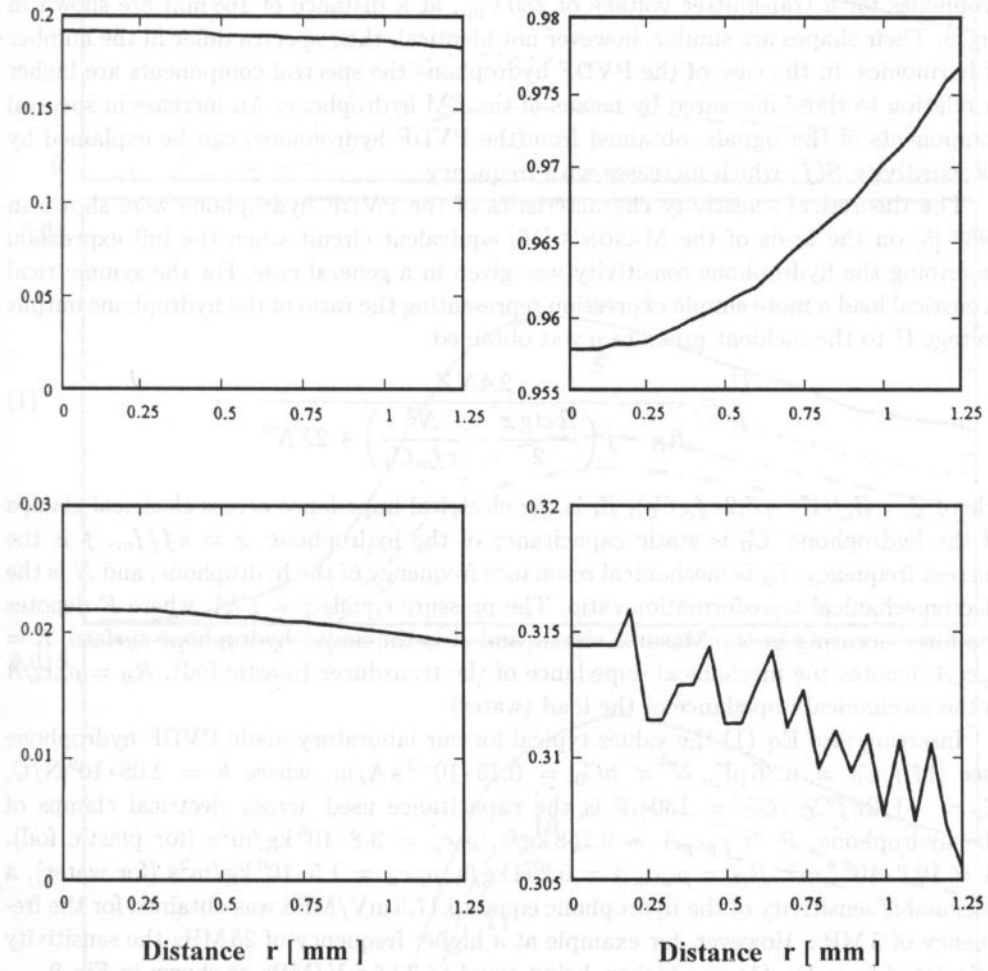

Fig. 6. The distribution of the pressure in the ultrasonic pulse as a function of the distance from the central beam axis computed for the carrier frequency (top) and for the 5-th harmonic (bottom). Moduli in relative units (left) are shown and phases in radians (right). The distance $z = 168\,\text{mm}$.

Figure 6 demonstrates, as an example, of the distribution of the pressure as a function of the distance r from the central beam axis for the distance of $z = 168\,\text{mm}$ computed for the carrier frequency and for the 5-th harmonic. Taking into account the length of the gold conductor equal to $1.3\,\text{mm}$, which is evaporated on the surface of the perspex block, it was observed that at the distance $r = 0.65\,\text{mm}$ the amplitude drop equaled 0.5%

and the phase change equaled only 0.35° while for the 5-th overtone the corresponding values were 2.5% and 1.7°, respectively. Therefore, the generated wave was considered to be practically plane.

Also the corresponding distributions of the first 11 harmonics of the nonlinear pulse were computed along the beam central axis (Fig. 7).

Pressure pulses and their spectra computed and measured by PVDF and EM hydrophones for a transmitter voltage of 280 V_{pp}, at a distance of 168 mm are shown in Fig. 8. Their shapes are similar, however not identical, their spectra differ in the number of harmonics. In the case of the PVDF hydrophone the spectral components are higher in relation to those measured by means of the EM hydrophone. An increase in spectral components of the signals, obtained from the PVDF hydrophone, can be explained by its sensitivity $S(f)$ which increases with frequency.

The theoretical sensitivity characteristics of the PVDF hydrophone were shown in 1988 [5] on the basis of the MASON'S [16] equivalent circuit when the full expression describing the hydrophone sensitivity was given in a general case. For the symmetrical acoustical load a more simple expression representing the ratio of the hydrophone output voltage U to the incident pressure p was obtained

$$\frac{U}{p} = \frac{2ANZ}{R_B - j\left(\dfrac{R \operatorname{ctg} x}{2} - \dfrac{N^2}{x f_m C_0}\right) + 2ZN^2} \tag{1}$$

where $Z = Z_i/(1 + jZ_i 2x f_m C_0)$, Z_i is the electrical impedance across electrical clamps of the hydrophone, C_0 is static capacitance of the hydrophone, $x = \pi f/f_m$, f is the current frequency, f_m is mechanical resonance frequency of the hydrophone, and N is the elecromechanical transformation ratio. The pressure equals $p = F/A$, where F denotes the force occuring in the Mason's circuit and A is the active hydrophone surface, $R = \rho_p c_p A$ denotes the mechanical impedance of the transducer (plastic foil), $R_B = \rho_w c_w A$ is the mechanical impedance of the load (water).

Inserting into Eq. (1) the values typical for our laboratory made PVDF hydrophone (see [17]) $C_0 = 0.36\,\text{pF}$, $N = hC_0 = 0.75 \cdot 10^{-3}\,\text{s A/m}$, where $h = 2.08 \cdot 10^9\,\text{N/C}$, $Z_i = -1/2\pi f C_C$, $C_C = 130\,\text{pF}$ is the capacitance used across electrical clamps of the hydrophone, $R = \rho_p c_p A = 0.758\,\text{kg/s}$, $\rho_p c_p = 3.8 \cdot 10^6\,\text{kg/m}^2\text{s}$ (for plastic foil), $A = 19.6 \cdot 10^{-8}\,\text{m}^2$, $R_B = \rho_w c_w A = 0.294\,\text{kg/s}$, $\rho_w c_w = 1.5 \cdot 10^6\,\text{kg/m}^2\text{s}$ (for water), a reasonable sensitivity of the hydrophone equal to 17.5 mV/MPa was obtained for the frequency of 3 MHz. However, for example at a higher frequency of 25 MHz the sensitivity calculated from Eq. (1) was higher, being equal to 22.5 mV/MPa as shown in Fig. 9.

The mechanical resonance frequency $f_m = 43\,\text{MHz}$ corresponded to the plastic foil 25 μm thick. However, the gold layers of electrodes, covering the plastic foil, can decrease considerably the resonance frequency to a value of about 30 MHz [7, 9]. So, the effective frequency band, used in the measurements, is situated on the increasing slope of the resonance curve, below the resonance, and therefore the hydrophone sensitivity increases considerably with frequency.

The PVDF bilaminar membrane hydrophone (Model 804-041) which was used in course of this work for exact measurements was much more sensitive than our laboratory

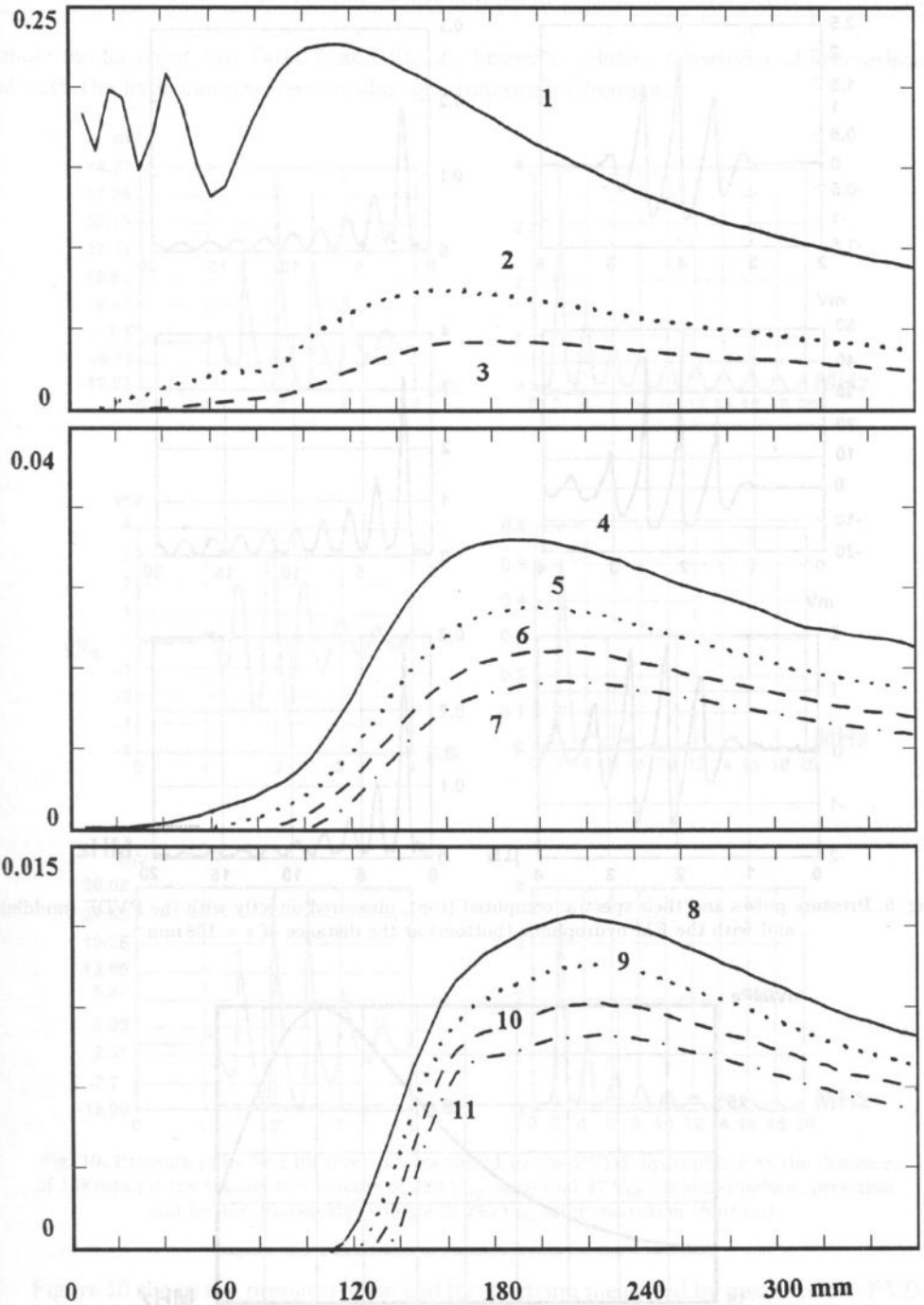

Fig. 7. The modulus of the first 11 harmonics as a function of the distance z from the transducer. The numbers of harmonics are given at the corresponding curves.

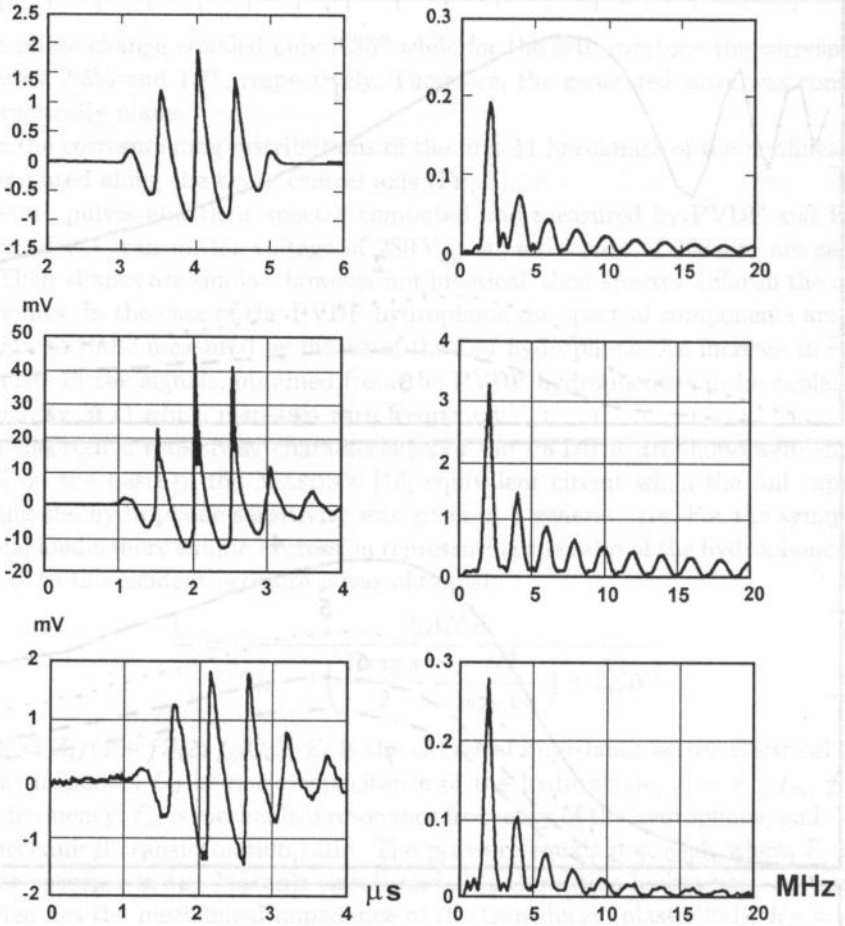

Fig. 8. Pressure pulses and their spectra: computed (top), measured directly with the PVDF (middle) and with the EM hydrophone (bottom) at the distance of $z = 168\,\mathrm{mm}$.

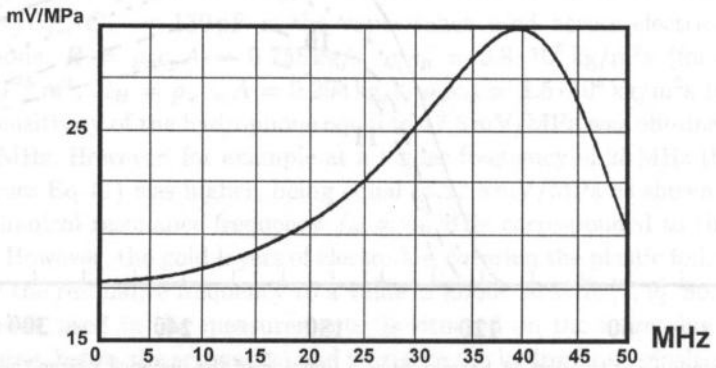

Fig. 9. Sensitivity of the PVDF hydrophone calculated from Eq. (1).

made model (compare Table 1 and Fig. 9), however, relative sensitivity characteristics of both the hydrophones were similar as a function of frequency.

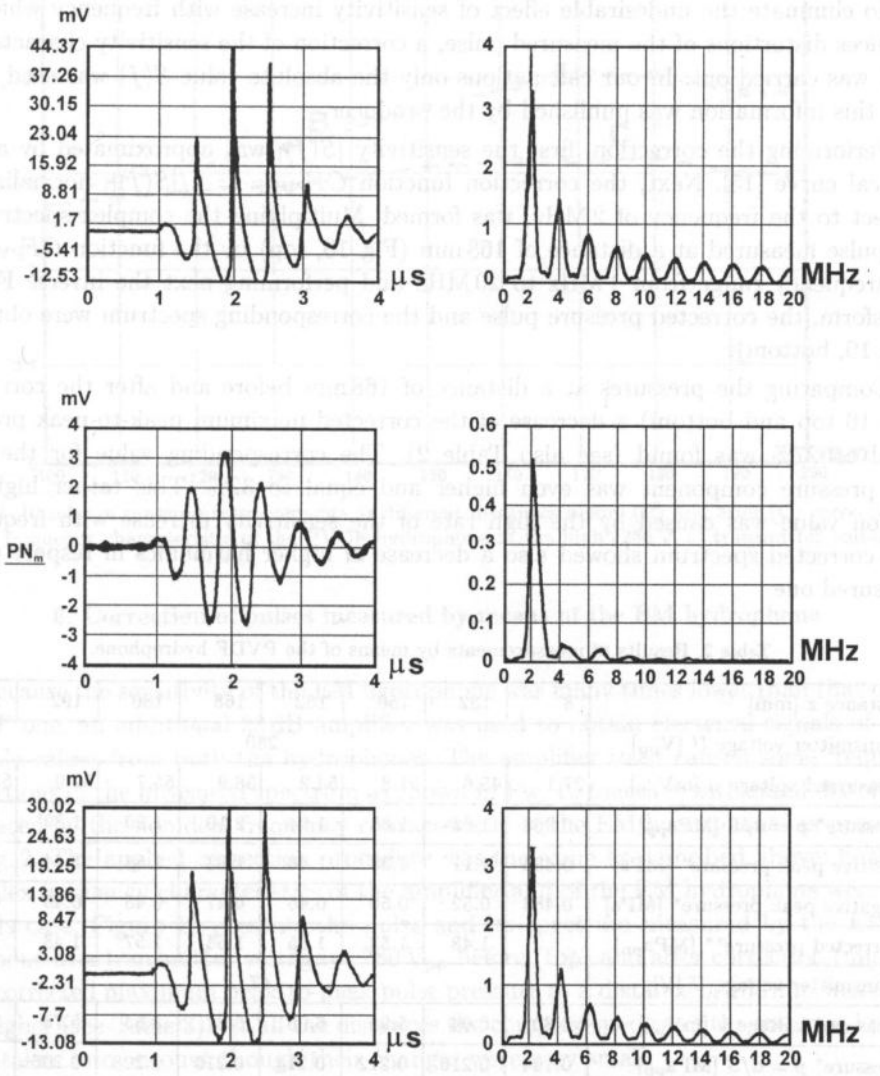

Fig. 10. Pressure pulse and its spectrum measured by the PVDF hydrophone at the distance of 168 mm for the transmitter voltage of 280 V_{pp} (top) and 47 V_{pp} (middle) before correction and for the transmitter voltage of 280 V_{pp} after correction (bottom).

Figure 10 shows the pressure pulse and its spectrum measured by means of the PVDF hydrophone at a distance of 168 mm for transmitter voltages of 280 V_{pp} (top) and 47 V_{pp} (middle). Higher harmonics obtained in the second case were much lower. For example, the 5-th overtone was relatively 15 times lower. This case showing a rather quasi-linear pulse propagation in water was called a linear case in the first approximation.

5. Correction of pulses measured by means of the PVDF hydrophone

To eliminate the undesirable effect of sensitivity increase with frequency which introduces distortions of the measured pulse, a correction of the sensitivity characteristic $S(f)$ was carried out. In our calculations only the absolute value $S(f)$ was used, since only this information was published by the producer.

Performing the correction, first the sensitivity $|S(f)|$ was approximated by an analytical curve [15]. Next, the correction function $CF_{\mathrm{PVDF}} = 1/|S(f)|$, normalized in respect to the frequency of 2 MHz, was formed. Multiplying the complex spectrum of the pulse measured at a distance of 168 mm (Fig. 10, top) by the function CF_{PVDF} in the frequency range from 1 MHz to 20 MHz and performing next the inverse Fourier transform, the corrected pressure pulse and the corresponding spectrum were obtained (Fig. 10, bottom).

Comparing the pressures at a distance of 168 mm before and after the correction (Fig. 10 top and bottom) a decrease of the corrected maximum peak-to-peak pressure equal to 27% was found (see also Table 2). The corresponding value for the positive pressure component was even higher and equal to 32%. This rather high correction value was caused by the high rate of the sensitivity increase with frequency. The corrected spectrum showed also a decrease of higher harmonics in respect to the measured one.

Table 2. Results of measurements by means of the PVDF hydrophone.

Distance z [mm]	8	132	150	162	168	180	192	198
Transmitter voltage U [V_{pp}]	280							
Measureed voltage u [mV_{pp}]	27.1	45.6	51.8	54.2	58.9	55.7	52.9	53.2
Pressure* $p = u/S$ [MPa_{pp}]	0.968	1.63	1.85	1.94	2.10	1.99	1.89	1.90
Positive peak pressure* [MPa]	0.484	1.11	1.35	1.48	1.63	1.54	1.44	1.48
Negative peak pressure* [MPa]	0.484	0.52	0.50	0.46	0.47	0.45	0.45	0.42
Corrected pressure** [MPa_{pp}]		1.43	1.53	1.55	1.54	1.57	1.48	1.47
Transmitter voltage U [V]	47							
Measured voltage u [mV_{pp}]	4.60	6.04	5.95	6.00	5.87	5.83	5.78	5.75
Pressure* $p = u/S$ [MPa_{pp}]	0.164	0.216	0.212	0.214	0.210	0.208	0.206	0.205

* Calculated for the sensitivity of $S = 28$ mV/MPa corresponding to the frequency of 2 MHz.
** After correction of the sensitivity characteristic of the PVDF hydrophone.

Figure 11 presents the pressures measured on the beam axis by means of the PVDF hydrophone at the high (280 V_{pp}) voltage as a function of distance, before and after the correction. In all the cases the complex spectrum of the measured pulse was taken into account. At low transmitter voltage (47 V_{pp}) the correction was not necessary, since the pulses had a narrow band spectrum with a practically constant sensitivity.

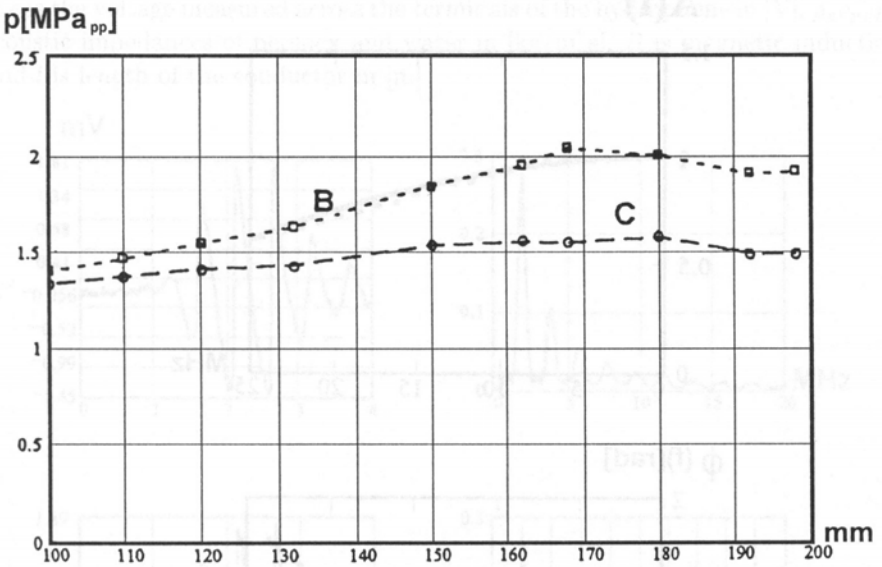

Fig. 11. Results of pressure measurements at different distances before (B) and after (C) correction of the frequency characteristic of the PVDF hydrophone at the high (280 V_{pp}) transmitter voltage.

6. Correction of pulses measured by means of the EM hydrophone

Because the sensitivity of the EM hydrophone was many times lower than that of the PVDF one, an additional 28 dB amplifier was used to obtain electrical signals of comparable values from both the hydrophones. The amplifier itself caused some frequency distortions of the measured spectrum as shown in Fig. 12 together with small distortions produced by the nonideal frequency characteristic of the EM hydrophone, as presented in Fig. 2. The applied correction procedure was the same as described above; however, complex frequency characteristics of the amplifier and of the EM hydrophone were used in this case. Figure 13 presents the pulse and its spectrum measured by the EM hydrophone at a transmitter voltage of 280 V_{pp} before (top) and after correction (middle). The corrected maximum peak-to-peak pulse pressure at a distance of 168 mm was about 3% higher (see Table 3). At all the distances the complex spectra of the measured pulses were taken into account though their changes were very small.

However, when using a perfect amplifier with a constant frequency response characteristic of up to 20 MHz the corrected pulse pressure measured by the EM hydrophone should be increased by 0.7% only. The very low value of the correction is caused by the almost constant sensitivity of the EM hydrophone as a function of frequency up to 20 MHz.

The pulse pressure measured by means of the EM hydrophone is given in [Pa] by the formula [8]

$$p = \frac{e(\rho_p c_p + \rho_w c_w)}{2Bl}, \tag{2}$$

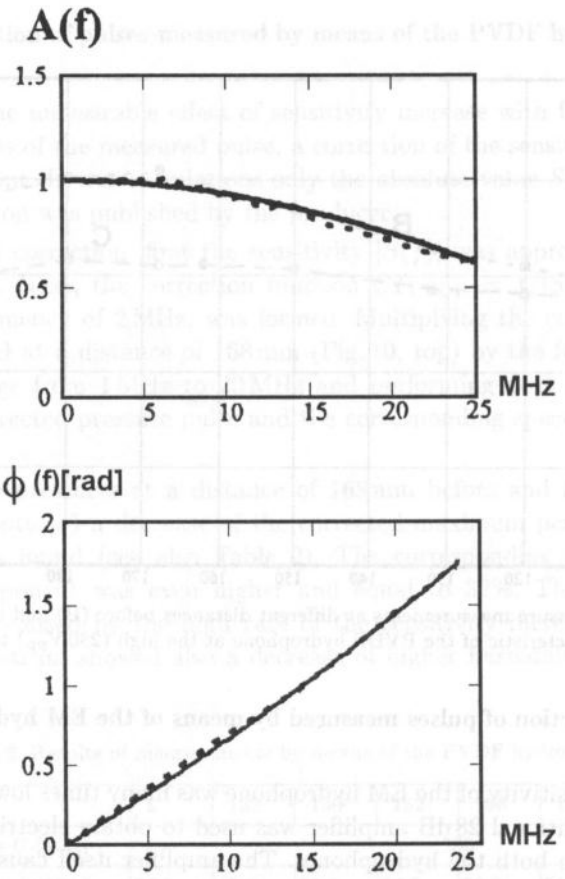

Fig. 12. Modulus A and phase ϕ of an additional amplifier as a function of frequency. Measurements — dotted lines, analytical approximating curves — solid lines.

Table 3. Results of measurements by means of the EM hydrophone.

Distance z [mm]	132	150	162	168	180	192	198
Transmitter voltage U [V_{pp}]	280						
Measured voltage u [mV_{pp}]	3.39	3.49	3.31	3.27	3.07	3.19	3.03
Corrected voltage*** u [mV_{pp}]	3.42	3.51	3.38	3.36	3.15	3.30	3.14
Pressure p**** [MPa_{pp}]	1.37	1.41	1.36	1.35	1.27	1.33	1.26
Tansmitter voltage U [V_{pp}]	47						
Measured voltage u [mV_{pp}]	0.43	0.44	0.40	0.43	0.41	0.39	0.36
Corrected voltage*** u [mV_{pp}]	0.44	0.44	0.41	0.43	0.43	0.40	0.38
Pressure p**** [MPa_{pp}]	0.215	0.215	0.20	0.21	0.195	0.19	0.18

*** After correction of frequency characteristics of the amplifier and of the EM hydrophone.
**** Calculated from Eq. (1).

where e is the voltage measured across the terminals of the hydrophone in [V], $\rho_p c_p$, $\rho_w c_w$ are acoustic impedances of perspex and water in [kg/m^{2}s], B is magnetic induction in [T], and l is length of the conductor in [m].

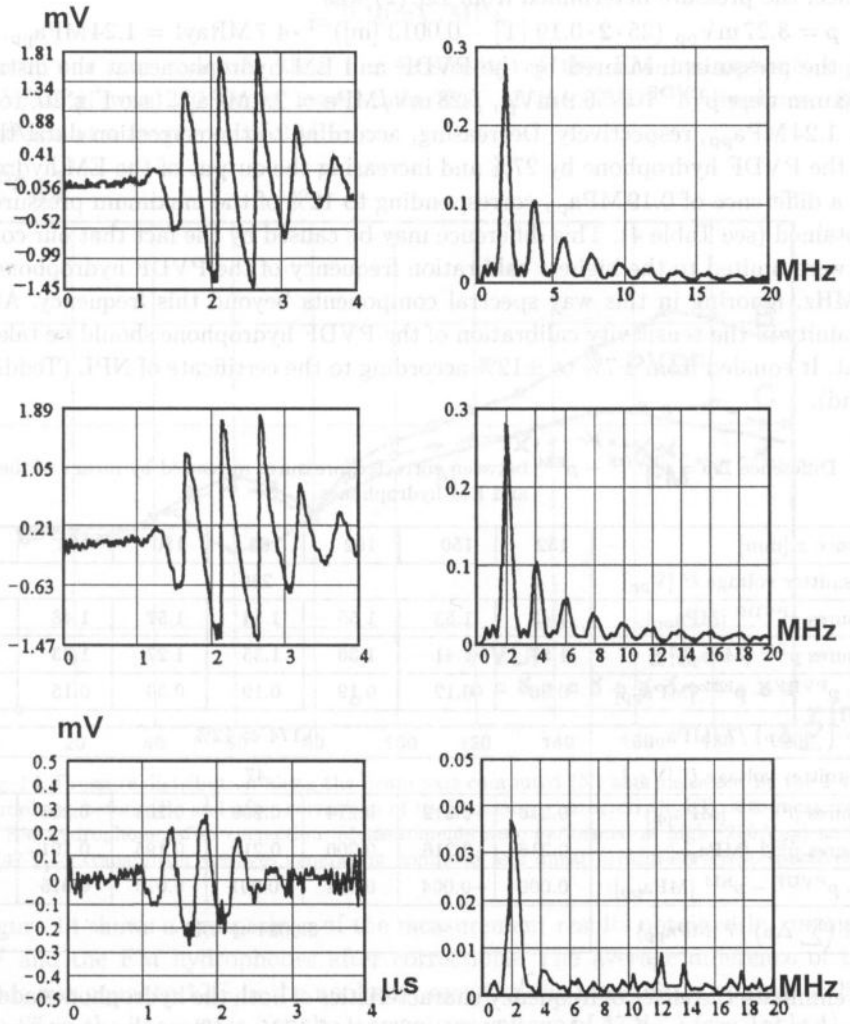

Fig. 13. The pressure pulse and its spectrum measured with the EM hydrophone at a distance of $z = 168$ mm for the transmitter voltage of 280 V_{pp} before (top), after correction (middle) and for the transmitter voltage of 47 V_{pp} (bottom).

7. Comparison of corrected PVDF and EM measurements

Applying the EM hydrophone under the same conditions as those for the PVDF hydrophone (Fig. 1) at a distance of $z = 168$ mm, the value $e = 3.27\,\mathrm{mV_{pp}}/25$ was

obtained for the transmitter voltage of $280\,V_{pp}$ (Fig. 13, top). The number 25 in the denominator was equal to the additional amplification used in this case, the other values being: $B = 0.19\,T$, $l = 0.0013\,m$, $\rho_p c_p = 3.2 \cdot 10^6\,kg/m^2s$ and $\rho_w c_w = 1.5 \cdot 10^6\,kg/m^2s$.

Hence, the pressure determined from Eq. (2) was

$$p = 3.27\,mV_{pp}\ (25 \cdot 2 \cdot 0.19\ [T]\ \cdot\ 0.0013\ [m])^{-1} \cdot 4.7\,MRayl = 1.24\,MPa_{pp}.$$

So, the pressures measured by the PVDF and EM hydrophones at the distance of $z = 168\,mm$ were $p^{PVDF} = 56.9\,mV_{pp}\ /\ 28\,mV/MPa = 2.0\,MPa_{pp}$ (see Fig. 10, top) and $p^{EM} = 1.24\,MPa_{pp}$, respectively. Decreasing, according to the correction data, the output of the PVDF hydrophone by 27% and increasing the output of the EM hydrophone by 3% a difference of $0.19\,MPa_{pp}$ corresponding to 12% of the maximum pressure value was obtained (see Table 4). This difference may be caused by the fact that our considerations were limited to the highest calibration frequency of the PVDF hydrophone equal to 20 MHz, ignoring in this way spectral components beyond this frequency. Also the uncertainity in the sensitivity calibration of the PVDF hydrophone should be taken into account. It equaled from ±7% to ±12% according to the certificate of NPL (Teddington, England).

Table 4. Difference $\Delta p = p^{PVDF} - p^{EM}$ between corrected pressures measured by means of the PVDF and EM hydrophones.

Distance z [mm]	132	150	162	168	180	192	198
Transmitter voltage U [V_{pp}]	280						
Pressures p^{PVDF} [MPa_{pp}]	1.43	1.53	1.55	1.54	1.57	1.48	1.47
Pressures p^{EM} [MPa_{pp}]	1.37	1.41	1.36	1.35	1.27	1.33	1.26
$\Delta p = p^{PVDF} - p^{EM}$ [MPa_{pp}]	0.06	0.12	0.19	0.19	0.30	0.15	0.21
Mean $\left(\sum \Delta p\right)/7$ [MPa_{pp}]	0.174 ⇔ 12%						
Transmitter voltage U [V_{pp}]	47						
Pressures p^{PVDF} [MPa_{pp}]	0.216	0.212	0.214	0.209	0.208	0.206	0.205
Pressures p^{EM} [MPa_{pp}]	0.216	0.216	0.200	0.210	0.195	0.191	0.183
$\Delta p = p^{PVDF} - p^{EM}$ [MPa_{pp}]	0.000	−0.004	0.014	−0.001	0.013	0.015	0.022
Mean $\left(\sum \Delta p\right)/7$ [MPa_{pp}]	0.0084 ⇔ 4%						

To eliminate the effect of frequency characteristics of both the hydrophones additional measurements were performed at a lower voltage of $47\,V_{pp}$. Then the spectrum of the pulse corresponded to a narrow frequency band around a carrier frequency of 2 MHz. The pressure measured by the PVDF hydrophone at the distance of $z = 168\,mm$ was equal to $p^{PVDF} = 5.89\,mV_{pp}\ /\ (28\,mV/MPa) = 0.21\,MPa_{pp}$. Figure 13 (bottom) shows the same pulse and its spectrum measured by means of the EM hydrophone. One can observe here a high level of interferring signals arising from other electrical equipment situated near-by. The voltage value obtained in this case equaled $0.55\,mV_{pp}$, hence the same pressure, namely $p^{EM} = 0.21\,MPa_{pp}$ was calculated from Eq. (2). Almost the same pressure was measured with PVDF and EM hydrophones at distances of 132, 150, 162, 168,180, 192 and 198 mm (see Table 4).

From Eq. (2) it was possible to determine directly the sensitivity of the EM hydrophone in the case of linear propagation, namely:

$$e/p = 2Bl(\rho_p c_p + \rho_w c_w)^{-1} = 2 \cdot 0.19\,[\mathrm{T}]1.3 \cdot 10^{-3}\,[\mathrm{m}]\{(3.2 + 1.5) \cdot 10^6\,[\mathrm{kg/m^2 s}]\}^{-1}$$
$$= 0.10\,\mathrm{mV/MPa}. \tag{3}$$

Hence, one can conclude that the sensitivity of the EM hydrophone, equal to 0.10 mV/MPa, was 280 times lower than that of the PVDF hydrophone equal to 28 mV/MPa at a frequency of 2 MHz.

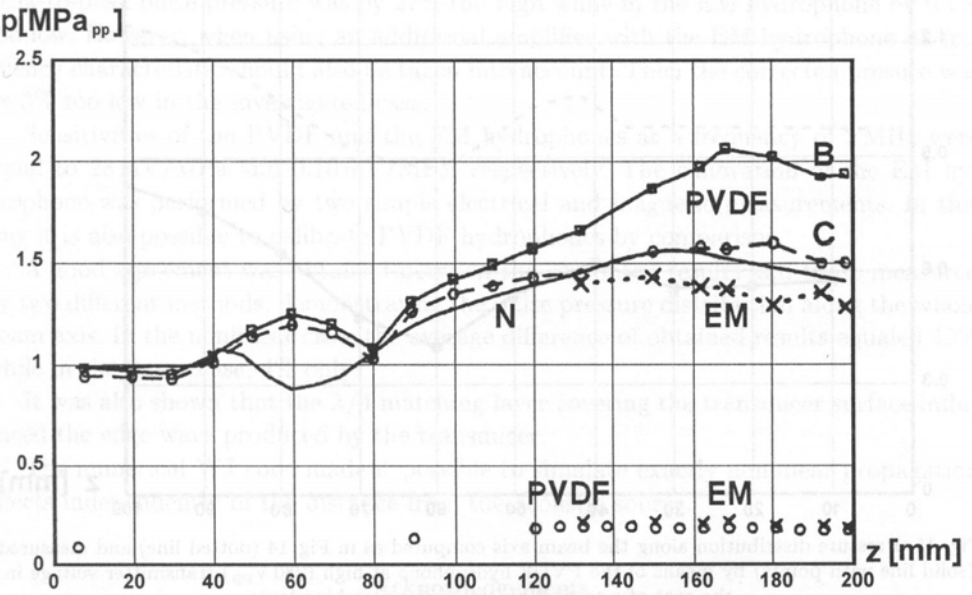

Fig. 14. Pressure distribution along the beam axis computed (N) and measured by the PVDF hydrophone before (B) and after correction of its frequency characteristic (C), also measured by the EM hydrophone, after correction. Measurements were performed at high (280 V_{pp}) and low (47 V_{pp}) transmitter voltages generating nonlinear and linear pressure levels, respectively.

Figure 14 shows a comparison of the measurement results obtained by means of the PVDF and the EM hydrophones after corrections. The average difference of the two methods was equal to 12% in the nonlinear case (for the transmitter voltage of 280 V_{pp}) and to 4% in the linear case (for the transmitter voltage of 47 V_{pp}) (see Table 4). Hence, one can conclude that our EM hydrophone measured the pressures correctly.

The agreement between the computed and measured pressure distributions along the beam axis is fairly good with the exception of the distance $z = 30\,\mathrm{mm} - 90\,\mathrm{mm}$, which corresponded to the region of interference between the central axial wave and the edge wave [1]. This effect was caused by the $\lambda/4$ matching layer covering the radiating transducer that changed the edge wave. To verify this supposition measurements were performed by means of the PVDF hydrophone along the beam axis with an ultrasonic transducer radiating directly a pressure pulse without a matching layer. Figure 15 shows the obtained computed and measured distributions of the pulse pressure at the distance

of $z = 0 - 100$ mm. The measured pressures are lower than in Fig. 14 due to the lack of the matching layer; however, the shapes of the measured and computed curves are almost identical. In this way the agreement between the computed and measured curves showing the pulse pressure distribution along the whole beam axis was confirmed.

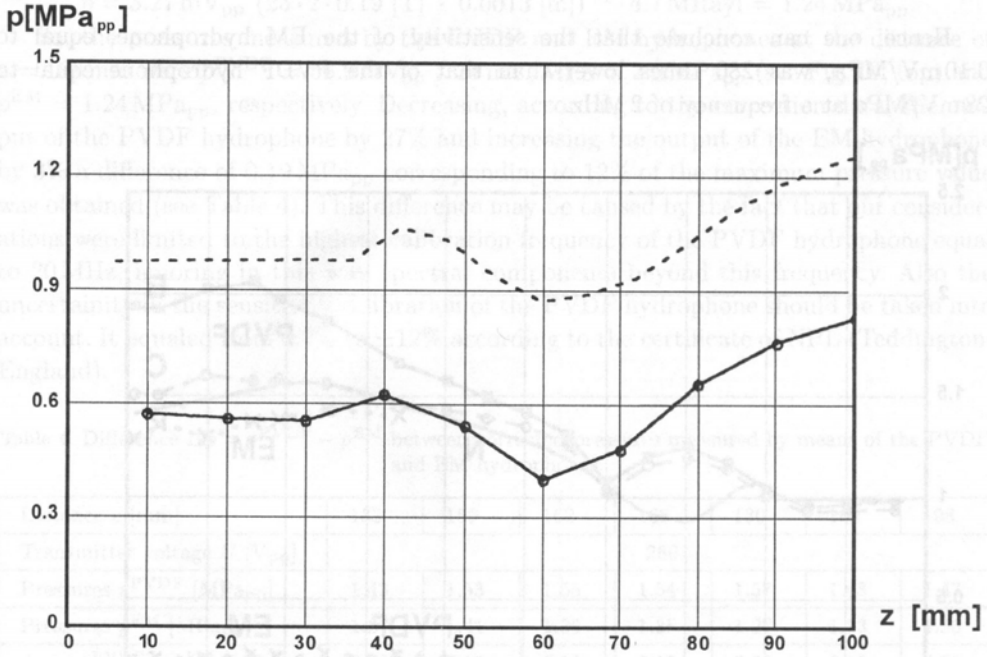

Fig. 15. Pressure distribution along the beam axis computed as in Fig. 14 (dotted line) and measured (solid line with points) by means of the PVDF hydrophone at high (280 V_{pp}) transmitter voltage in the case of a transducer without a matching layer.

However, it arises a question if the hydrophones used in measurements were linear, otherwise one could expect serious distortions of the obtained data. The linearity of the PVDF hydrophone was shown up to pressures of 2.3 MPa by means of a newly developed multilayer method [10]. The EM hydrophone is linear in its principle. However, it was also necessary to demonstrate that the acoustic impedances in the formula (2) are practically not dependent on the nonlinearity of the measured pulses. This was already shown by the formula (7) in the paper [6] devoted to the EM hydrophone used for shock wave measurements, and derived in a previous publication [11].

8. Conclusions

Nonlinear propagation effects of short finite amplitude pulses radiated by a plane transducer with pressures of about 1.5 MPa_{pp} and a carrier frequency of 2 MHz were computed by the numerical code recently developed by the last-named author and were measured in a water tank. Measurements by means of a calibrated PVDF hydrophone

showed a higher number of spectral components (harmonics) than those by an electromagnetic (EM) hydrophone due to sensitivity characteristics, increasing in the PVDF hydrophone and decreasing in the EM hydrophone as a function of frequency, as shown by analysis.

Measurements were performed at several distances from the wave source at high and low transmitter voltages corresponding to nonlinear and linear propagation. Corrections of the distortions caused by frequency characteristics of both the hydrophones demonstrated that in the investigated PVDF hydrophone, the maximum measured peak-to-peak pulse pressure was by 27% too high while in the EM hydrophone by 0.7% too low. However, when using an additional amplifier with the EM hydrophone its frequency characteristic should also be taken into account. Then the corrected presure was by 3% too low in the investigated case.

Sensitivities of the PVDF and the EM hydrophones at a frequency of 2 MHz were equal to 28 mV/MPa and 0.10 mV/MPa, respectively. The calibration of the EM hydrophone was performed by two simple electrical and magnetic measurements. In this way it is also possible to calibrate PVDF hydrophones by comparison.

A good agreement was obtained between the computed results and those measured by two different methods, demonstrating the pulse pressure distribution along the whole beam axis. In the nonlinear case, the average difference of obtained results equaled 12% while in the linear case, 4% only.

It was also shown that the $\lambda/4$ matching layer covering the transducer surface influenced the edge wave produced by the transducer.

The numerical WJ code made it possible to simulate exactly nonlinear propagation effects independently of the distance from the acoustic source.

Acknowledgements

The first author of this paper learned with sorrow of the death of Professor Z. JAGODZIŃSKI, a woderful man, who was his first chief at the MORS Comp. in Gdynia, teaching him radio-communication sea service in 1948. Then, he became his close friend cooperating in many fields of ultrasonic problems.

The authors thank the Committee of Scientific Research, Warsaw, for the financial grant support (Grant nr 7T07B03414).

References

[1] M. AVERKIOU and M. HAMILTON, *Nonlinear distortion of short pulses radiated by plane and foused circular pistons*, J. Acoust. Soc. Am., **102**, 2539–2548 (1997).

[2] A. BRIGGS, *Acoustic microsopy*, Clarendon Press, Oxford, UK 1992, 35.

[3] F. DUCK and K. MARTIN, *Exposure values for medical devices in ultrasonic exposimetry*, M. ZISKIN, P. LEVIN [Eds.], CRC Press, Boca Radon, Florida 1993, 329, 333.

[4] J. ETIENNE, L. FILIPCZYŃSKI, A. FIREK *et al.*, *Intensity determination of ultrasonic focused beams used in ultrasonography in the case of gravid uterus*, Ultrasound in Med. and Biol., **2**, 119–122 (1976).

[5] J. ETIENNE, L. FILIPCZYŃSKI, A. GRABOWSKA and T. WASZCZUK, *Pressure measurements by means of foil and capacitance hydrophones in nonlinear acoustics*, Proc. of the XXXV Open Acoustic Seminar, Białowieża – Warszawa, Institute of Fundamental Technological Research, Vol. I, 266–271 (1988).

[6] J. ETIENNE, L. FILIPCZYŃSKI, T. KUJAWSKA and B. ZIENKIEWICZ, *Electromagnetic hydrophone for determination of pressures of shock wave pulses*, Ultrasound in Med. and Biol., **23**, 747–754 (1997).

[7] B. FAY, P.A. LEWIN, G. LUDWIG, G.M. SESSLER and G. YANG, *The influence of spatial polarization distribution on spot poled PCDF membrane hydrophones performance*, Ultrasound in Med. and Biol., **18**, 625–635 (1992).

[8] L. FILIPCZYŃSKI, *Absolute measurements of particle velocity, displacement or intensity of ultrasonic pulses in liquids and solids*, Acustica, **21**, 173–180 (1969).

[9] L. FILIPCZYŃSKI, J. ETIENNE, G. ŁYPACEWICZ and T. WASZCZUK, *Merasurement technique of shock wave pulses at extremely high pressures*, Archives of Acoustics, **21**, 37–51 (1996).

[10] L. FILIPCZYŃSKI, J. ETIENNE, T. KUJAWSKA, R. TYMKIEWICZ and J. WÓJCIK, *A multilayer method for linearity determination of the PFDV hydrophone pressures up to 2.3 MPa*, Archives of Acoustics, **23**, 513–520 (1998).

[11] L. FILIPCZYŃSKI and A. GRABOWSKA, *Deviation of the acoustic pressure to particle velocity ratio from the ρc value in liquids and solids at high pressures*, Archives of Acoustics, **14**, 173–179 (1989).

[12] L. FILIPCZYŃSKI, T. KUJAWSKA, R. TYMKIEWICZ and J. WÓJCIK, *Nonlinear and linear propagation of diagnostic ultrasound pulses*, Ultrasound in Medicine and Biology, **25**, 285–299 (1999).

[13] L. FILIPCZYŃSKI, T. KUJAWSKA, R. TYMKIEWICZ and J. WÓJCIK, *Computing and measuring of nonlinear propagation effects by means of PVDF and EM hydrophones*, Paper presented at the 15 International Symposium on Nonlinear Acoustics (15 ISNA), Goettingen, Germany, 1-4 September 1999.

[14] G. ŁYPACEWICZ and L. FILIPCZYŃSKI, *Measurement method and experimental study of ceramic transducer vibrations*, Acustica, **25**, 1, 64–68 (1972).

[15] G. ŁYPACEWICZ, A. NOWICKI, R. TYMKIEWICZ, P. KARŁOWICZ and W. SECOMSKI, *Acoustic field measurements using a PVDF foil hydrophone*, Archives of Acoustics, **21**, 361–369 (1996).

[16] W.P. MASON, *Electromechanical transducers and wave filters*, Van Nostrand, 1948.

[17] J. SOMER, J. CORSEL and H. VAN DER VOORT, *Evaluation of a computer-model for PVDF transducers of arbitrary configuration*, Archives of Acoustics, **13**, 127–135 (1988).

[18] J. WÓJCIK, *Conservation of energy and absorption in acoustic fields*, J. Acoust. Soc. Am., **104**, 2654–2663 (1998).

[19] J. WÓJCIK, see the section *Basis of numerical procedures* in the reference 12.

ARCHIVES OF ACOUSTICS
24, 3, 289–302 (1999)

MEASUREMENTS OF THE NONLINEARITY PARAMETER B/A OF SEAWATER

E. KOZACZKA

Naval Academy,
(81-919 Gdynia, Smidowicza 71, Poland)
and
Technical University of Koszalin,
(75-620 Koszalin, Racławicka 13-17, Poland)

G. GRELOWSKA

Naval Academy,
(81-919 Gdynia, Smidowicza 71, Poland)

The application of modern hydroacoustic systems making use of the phenomenon of the nonlinear wave propagation is the object of interest in the sphere of basic scientific research as well as solving construction problems. The problem of particular importance for practical application is the knowledge of nonlinear properties of the medium in which propagate the finite amplitude waves. This is why the research in the sphere of space distribution of the nonlinear parameter of the medium becomes so important. The work contains the description of principal relations which make it possible to delineate the parameter of the nonlinearity of the medium B/A. Apart from that method has been proposed to delineate that parameter on the basis of the results obtained from maritime research. For that purpose a measurement set up has been constructed which makes it possible to obtain the measurement of nonlinearity parameter *in situ*. Results are also presented of the maritime research in the shape of distribution of the parameter B/A for the region of the Southern Baltic.

1. Introduction

The nonlinearity parameter B/A, defined as a ratio of coefficients in a Taylor series expansion of the isentropic equation of state [17], is a material constant which characterizes a phenomenon of distortion of a finite amplitude wave during its propagation in fluids.

There are two principal methods for determining the nonlinearity parameter B/A: the finite amplitude method and the thermodynamic method. The thermodynamic method is based on measurements of changes in thermodynamic parameters of medium caused

by finite amplitude wave [7, 9]. The value of the nonlinearity parameter B/A is usually obtained using the following formula introduced by R.T. BEYER [3]:

$$\frac{B}{A} = 2\varrho_0 c_0 \left(\frac{\delta c}{\delta p}\right)_{T,\varrho=\varrho_0} + \frac{2c_0 \alpha T}{C_p}\left(\frac{\delta c}{\delta T}\right)_{p,\varrho=\varrho_0}, \tag{1}$$

where ϱ_0 — the equilibrium density of medium, c_0 — the infinitesimal amplitude sound wave speed, T — the absolute temperature, C_p — the specific heat capacity at constant pressure, $\alpha = (1/V)(\delta V/\delta T)_p$ — the volume coefficient of thermal expansion, $(\delta c/\delta p)_T$ — change of the sound speed with pressure at constant temperature, $(\delta c/\delta T)_p$ — change of the sound speed with temperature at constant pressure.

In the finite amplitude method the nonlinearity parameter B/A is determined by means of measurement of nonlinear wave distortion. That method is based on the investigation of changes in spectrum due to distortion of the propagating sinusoidal wave [6, 10, 15].

The nonlinearity parameter B/A of seawater is obtained mainly for high-salinity seawater [8]. Low-salinity of the Baltic Sea are the fundamental reason of our interest in the nonlinear properties of the low-salinity water.

The results obtained by means of the thermodynamic method for several points of the South Baltic Sea were presented in papers [14, 15]. This method is based on the thermodynamic equation of the medium and measurements of temperature and salinity as a function of depth (static pressure).

The acoustical method based on measurements of distortion of the finite amplitude wave was applied too. The results received in preliminary measurements encouraged us to advance the acoustical method. A special device for measurements of the nonlinearity parameter B/A *in situ* was designed and used in practice.

2. Method of measurements

The method of determination of the nonlinearity parameter B/A of seawater is an adaptation of the one proposed by W.N. COBB [6] for sea conditions [13]. The main idea of that method is using a receiver of the same area as a transmitter and evaluating the parameter B/A by means of measurement of the second harmonic component of the wave. The value of the nonlinearity parameter B/A is obtained using the formula [6]:

$$\frac{B}{A} = 2\left(\frac{|\langle p_2(z)\rangle|}{p_0^2}\frac{\varrho_0 c_0^3}{\pi f |I_1 - I_2|} - 1\right), \tag{2}$$

where $|\langle p_2(z)\rangle|$ denotes the amplitude of the second harmonic of the pressure averaged over the receiver's area measured at the distance z from the transmitter, p_0 — pressure at the transmitter surface, f — frequency. The term I_1 is a factor describing the influence of attenuation on the amplitude of the second harmonic pressure component:

$$I_1 = \frac{e^{2\alpha_1 z} - e^{\alpha_2 z}}{\alpha_2 - 2\alpha_1}, \tag{3}$$

where α_1 and α_2 are the fundamental wave and the second harmonic component attenuation coefficients, respectively.

Because of diffraction, sources for which the quantity ka is much greater than 1 (a is the radius of the piston) have a fine structure in the nearfield. The term I_2 introduces a correcting element. It takes into account the diffraction spreading and phase cancellation over the receiver.

$$I_2 = Q\left(\int_{z/2}^{z} e^{2\alpha\Theta}\left[(\Theta^2+4a^2)^{1/2}-\Theta\right]^{-1/2} d\Theta - \frac{1}{8a^2}\int_{z/2}^{z} e^{2\alpha\Theta}\left[(\Theta^2+4a^2)^{1/2}-\Theta\right]^{3/2} d\Theta\right), \tag{4}$$

where

$$Q = \frac{8e^{i\pi/4}}{(\pi k)^{1/2}} e^{-2(\alpha_2-\alpha_1)z} \tag{5}$$

and

$$\alpha = \alpha_2 - 2\alpha_1 . \tag{6}$$

An acoustic part of the device for measurements of the nonlinearity parameter B/A of seawater consists of a piston circular source of 46 mm diameter driven at its central frequency equal to 1 MHz corresponding to $ka = 96$ (k is a wave number, a is the transmitter radius). For pseudo CW measurements a sinusoidal tone burst of about 50 cycles is applied to the device. The pressure is measured using a receiver of the same area as the transmitter placed coaxial with the source of the wave. Its receiving characteristic covers the frequency range from up to 5 MHz. The distance between transducers can be changed up to 251 mm.

The distortion of an electrical signal obtained from the receiver depends on the nonlinearity parameter B/A of water. The value of the amplitude of the second harmonic component is extracted in two independent ways, by means of the analog filtering and applying the Fourier analysis. In the second method the digital storage oscilloscope is used as a digitizer. An example of changes in a wave spectrum with the distance between the transmitter and the receiver is presented in Fig. 1.

The assumed arrangement of the device causes that the receiver is placed in the nearfield area of the transmitter. It means that measurements are done in the area of pressure field of fine structure. The changes in pressure distribution along the axis of the system are shown in Fig. 2. They are obtained theoretically by means of linear approximation [18] and using parabolic approximation [1]. In the Fig. 3 a, b are shown transverse pressure distributions of the first and the second pressure harmonic components at the distance of 251 mm from the source of the wave determined theoretically by means of parabolic approximation and experimentally using needle 1 mm-diam PVdF hydrophone.

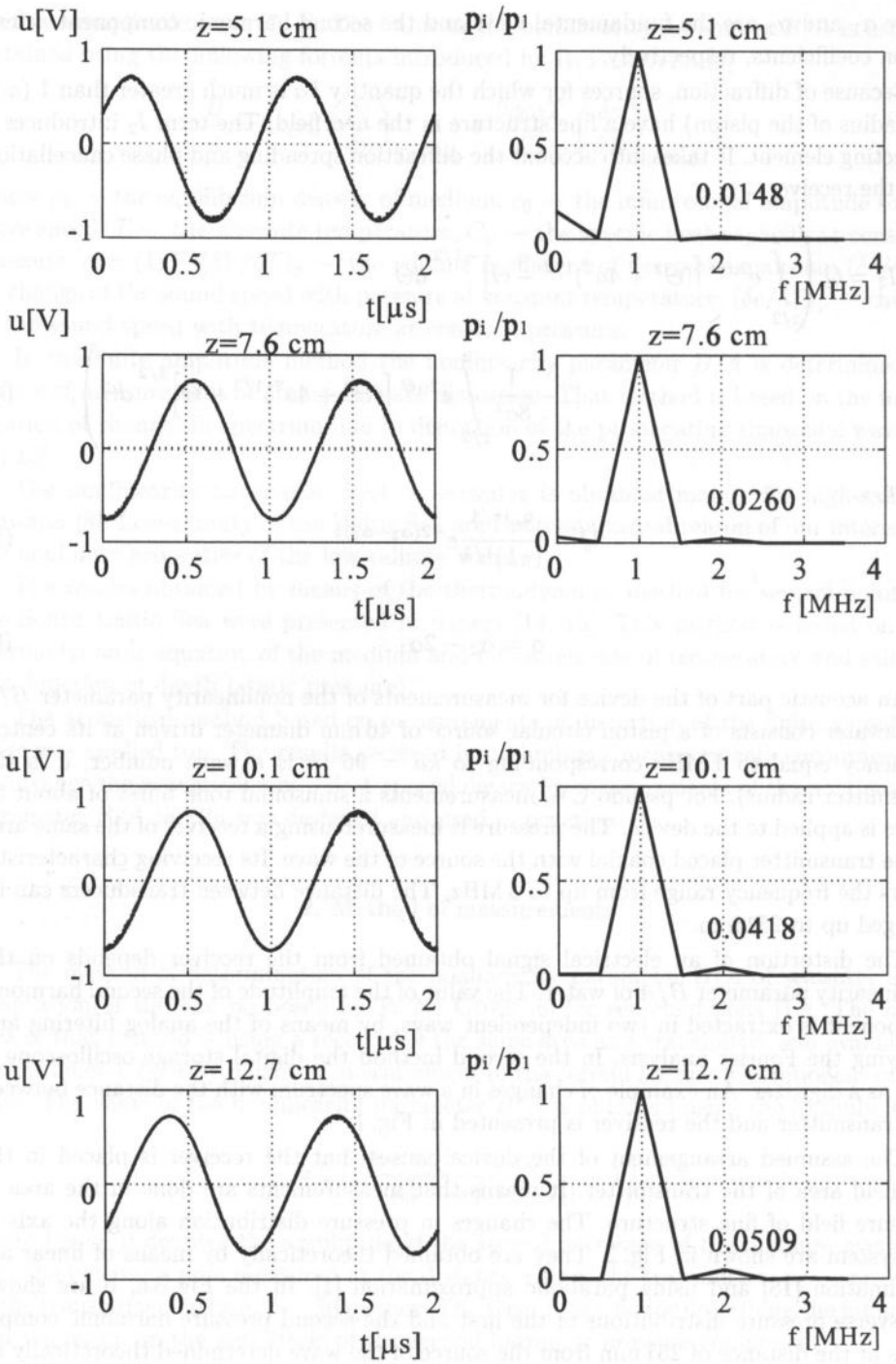

Fig. 1. a. Changes in the wave spectrum with the increasing distance between the transmitter and the receiver.

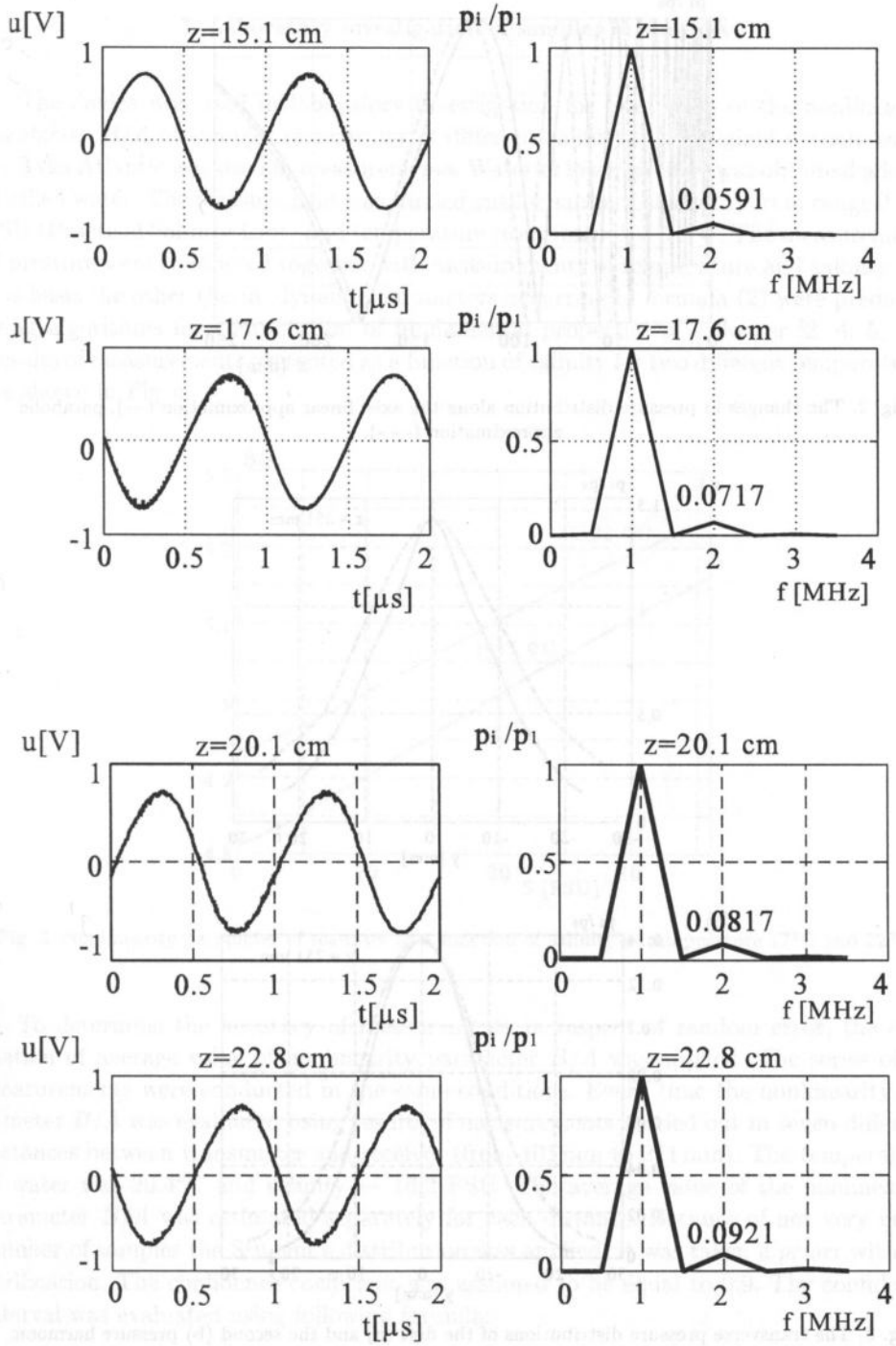

Fig. 1. b. Changes in the wave spectrum with the increasing distance between the transmitter and the receiver.

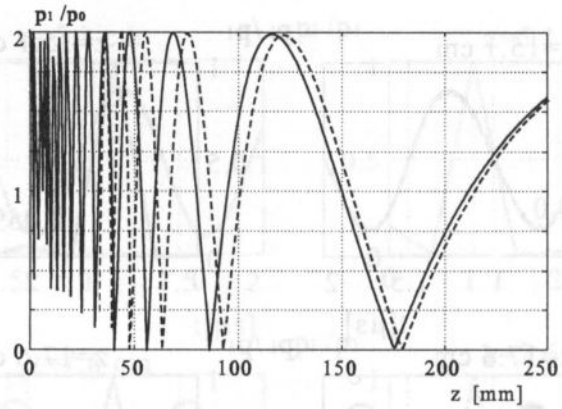

Fig. 2. The changes in pressure distribution along the axis: linear approximation (—), parabolic approximation (- - -).

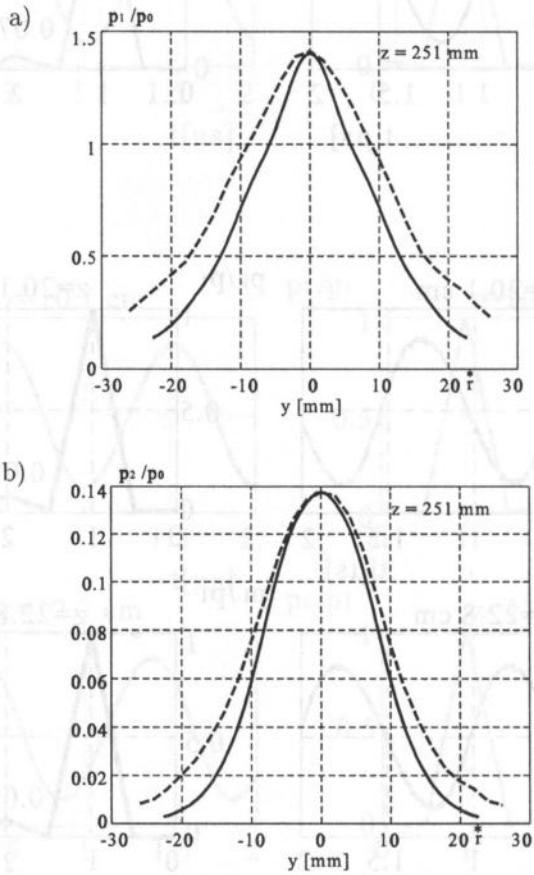

Fig. 3. The transverse pressure distributions of the first (a) and the second (b) pressure harmonic components at the distance of 251 mm from the source (—) parabolic approximation, (- - -) results of measurement.

3. Laboratory investigation of samples of seawater

The device was used in laboratory investigation for evaluation of the nonlinearity parameter B/A of samples of seawater of different salinity. The original oceanic water from the Atlantic was used in measurements. Water of lower salinity was obtained adding distilled water. The measurement was carried out for samples of salinity from range 0 – 36 PSU (Practical Salinity Unit) and temperature from range 15 – 25°C. The measurements of pressure were conducted together with measurements of temperature and salinity. On this basis the other thermodynamic parameters occurring in formula (2) were predicted using algorithms for computation of fundamental properties of seawater [2, 4, 5, 16]. Results of measurements presented as a function of salinity for two different temperatures are shown in Fig. 4.

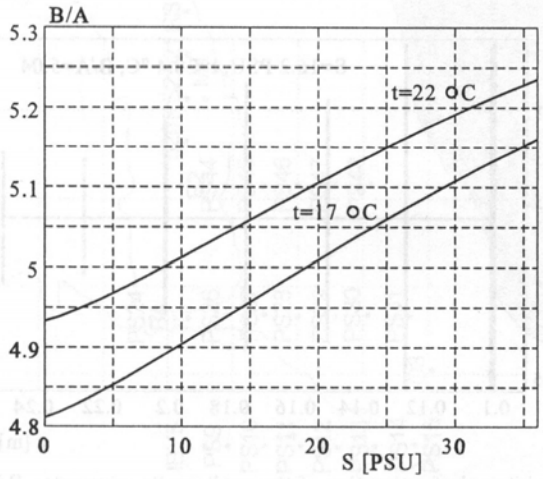

Fig. 4. Nonlinearity parameter of seawater as a function of salinity in temperature 17°C and 22°C.

To determine the accuracy of measurements in respect of random error, the estimation of average value of nonlinearity parameter B/A was applied. The series of 20 measurements were conducted in the same conditions. Every time the nonlinearity parameter B/A was evaluated using results of measurements carried out in seven different distances between transmitter and receiver (from 101 mm to 251 mm). The temperature of water was 20.4°C and salinity — 16.2 PSU. The average value of the nonlinearity parameter B/A was estimated separately for each distance. Because of not very great number of samples the Student's distribution was applied. It was taken *a priori* without verification. The confidence coefficient was assumed to be equal to 0.9. The confidence interval was evaluated using following formula:

$$p\left(\frac{\overline{B}}{A} - t_\alpha S < \frac{B}{A} < \frac{\overline{B}}{A} + t_\alpha S\right) = 1 - \alpha, \tag{7}$$

where $\overline{B/A}$ denotes the average value of the nonlinearity parameter at fixed distance:

$$\frac{\overline{B}}{A} = \frac{1}{n}\sum_{i=1}^{n}\left(\frac{B}{A}\right)_i \tag{8}$$

and S denotes the error meansquare of measurement:

$$S = \sqrt{\frac{1}{n(n-1)}\sum_{i=1}^{n}\left(\frac{B}{A} - \frac{\overline{B}}{A}\right)^2}. \tag{9}$$

For a sample size $n = 20$ the value of parameter t_α equals 1.752 [11]. The confidence interval determined for each of measurement distances are shown in Fig. 5. The average value of the parameter B/A equals 5.04. The results of estimation indicate the higher accuracy of measurements at greater distances between transducers.

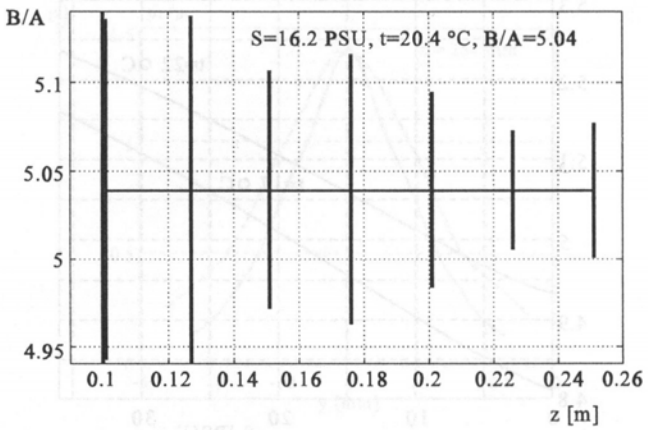

Fig. 5. The confidence interval of estimation of the nonlinearity parameter B/A at various distances between transmitter and receiver obtained for the confidence coefficient assumed to be equal to 0.9.

4. Investigation of the nonlinear parameter B/A in chosen points of the South Baltic Sea

The device verified in laboratory investigations was next used in measurement carried out *in situ* in the Baltic Sea. The investigations were done in April 1994 in stations marked in Fig. 6. The measurements of the nonlinearity parameter B/A were conducted together with the measurements of changes in pressure and salinity as a function of the depth using the STD sounder produced by Guideline.

For each station the vertical distribution of the nonlinearity parameter B/A was determined based on results of measurements of the second harmonic component of the pressure. The receiver was most often placed at the distance greater then 200 mm from transmitter (226 mm or 251 mm). Sometimes measurements at the same station were carried out twice applying two different distances between transducers.

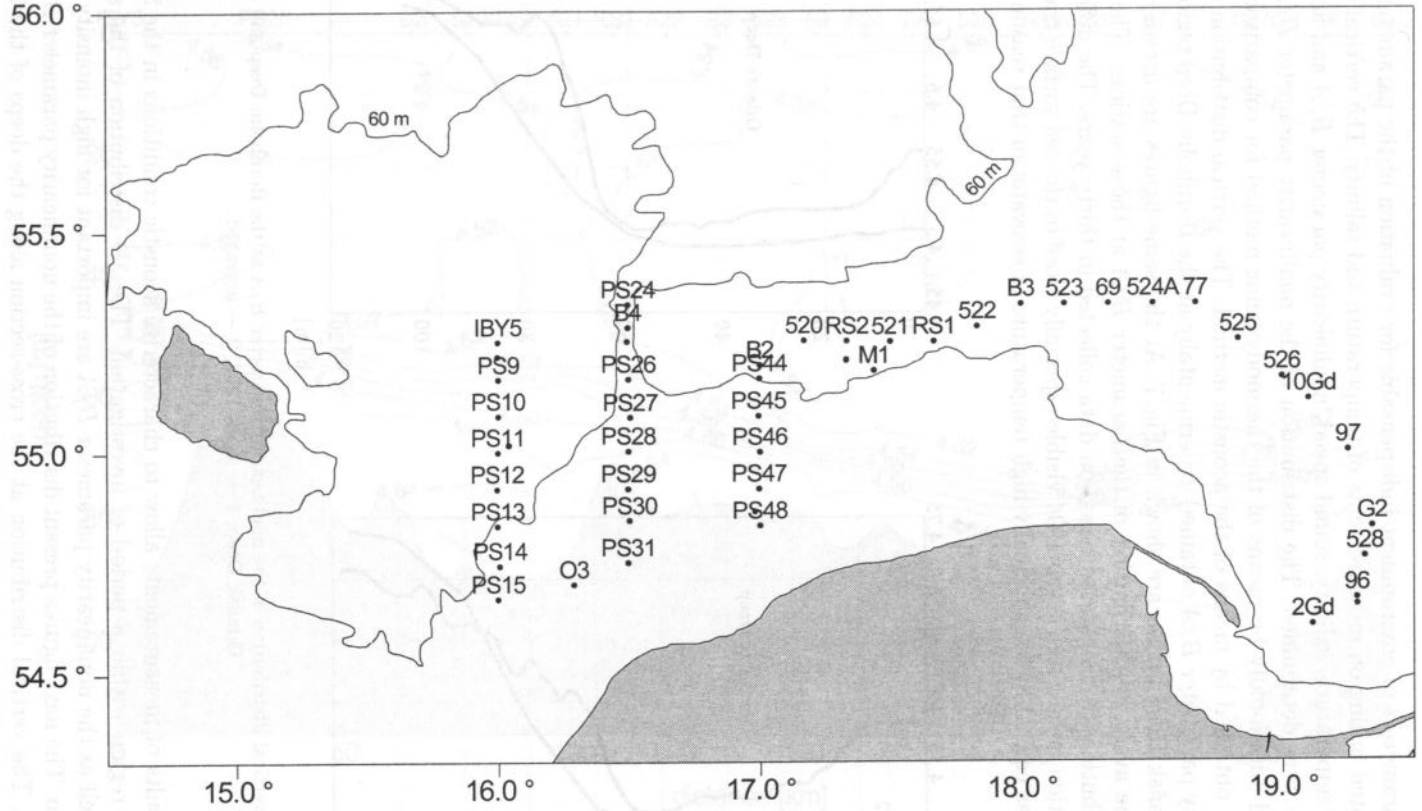

Fig. 6. Localization of the measurement stations.

The parameters of environment indispensable for evaluation of the parameter B/A are calculated basing on measurements of temperature and salinity. The vertical distribution of temperature, salinity, sound speed, nonlinearity parameter B/A and acoustic impedance were determined. The distribution of the nonlinearity parameter B/A was determined additionally by means of the thermodynamic method for comparison with the results obtained by means of the acoustic method. The vertical distribution of the nonlinearity parameter B/A obtained experimentally at the Bornholm Deep region and at the Gdańsk Deep region are shown in Fig. 7. At the same figures are drown curves showing the averaged distribution of the parameter B/A at those stations. The averaged distribution are calculated based on data collected in thirty years. The difference in distribution obtained in April 1994 visible especially close to the sea surface could be explained as caused by exceptionally high temperature of seawater in that season.

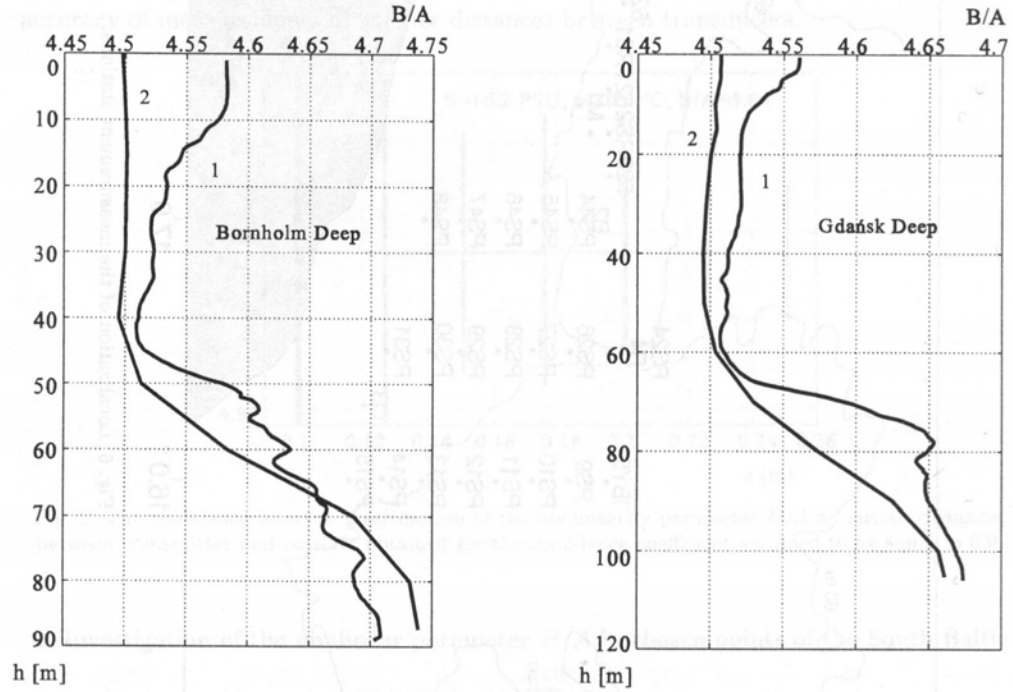

Fig. 7. The vertical distribution of the nonlinearity parameter B/A at the Bornholm Deep and at the Gdańsk Deep: 1 — April 1994, 2 — averaged.

The results of measurements allow to characterize acoustic conditions in the South Baltic Sea region within a period of investigation. The 3D distribution of the sound speed as well as the nonlinearity parameter B/A are important for high intensity wave propagation. The next figures present distribution of the nonlinearity parameter B/A in April 1994. The vertical distribution at the cross-section along the deeps of the South Baltic is shown in Fig. 8 while the horizontal distribution at the sea surface and at depth of 20 m are presented in Fig. 9.

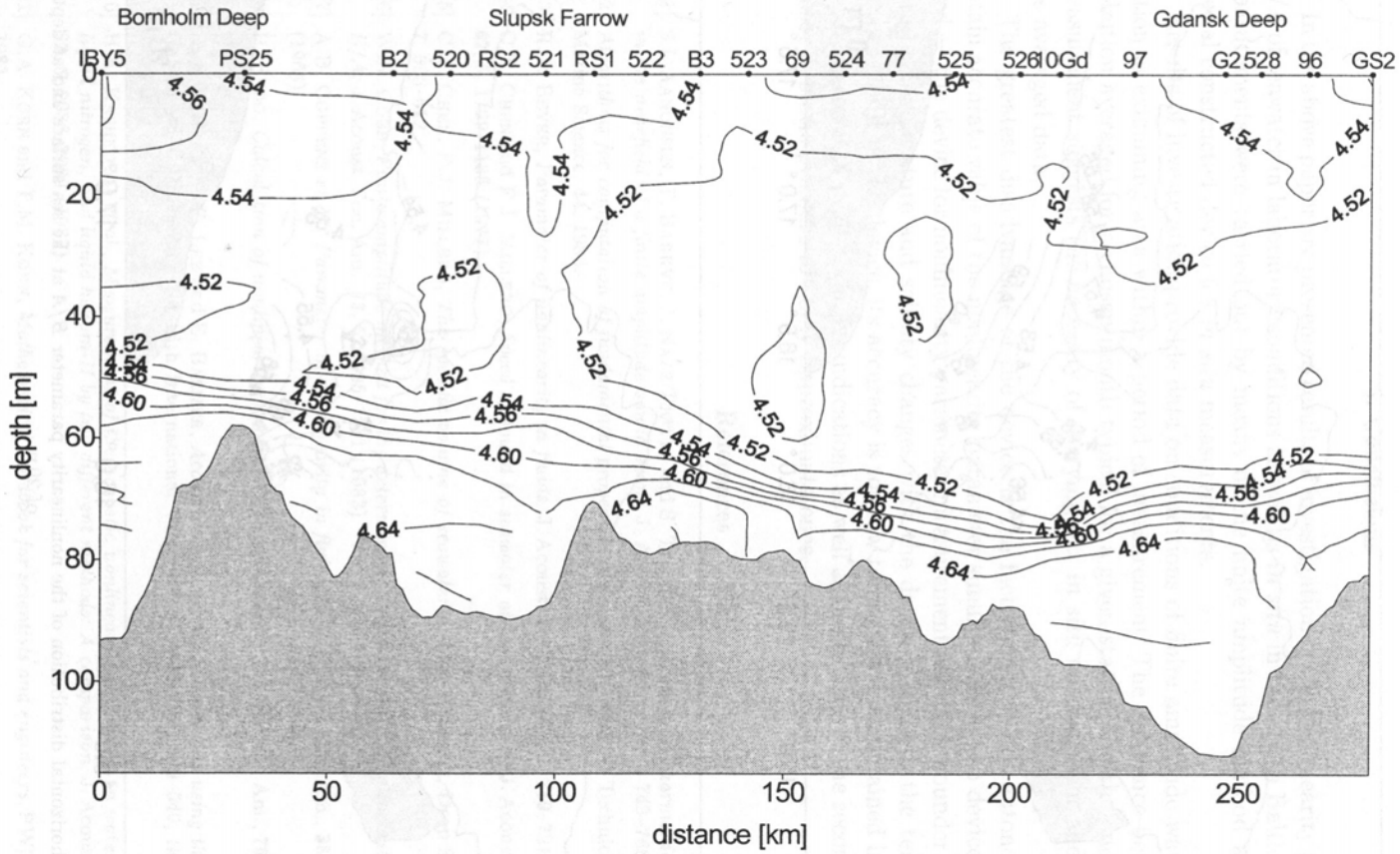

Fig. 8. The vertical distribution of the nonlinearity parameter B/A in the cross-section along the deeps of the South Baltic Sea.

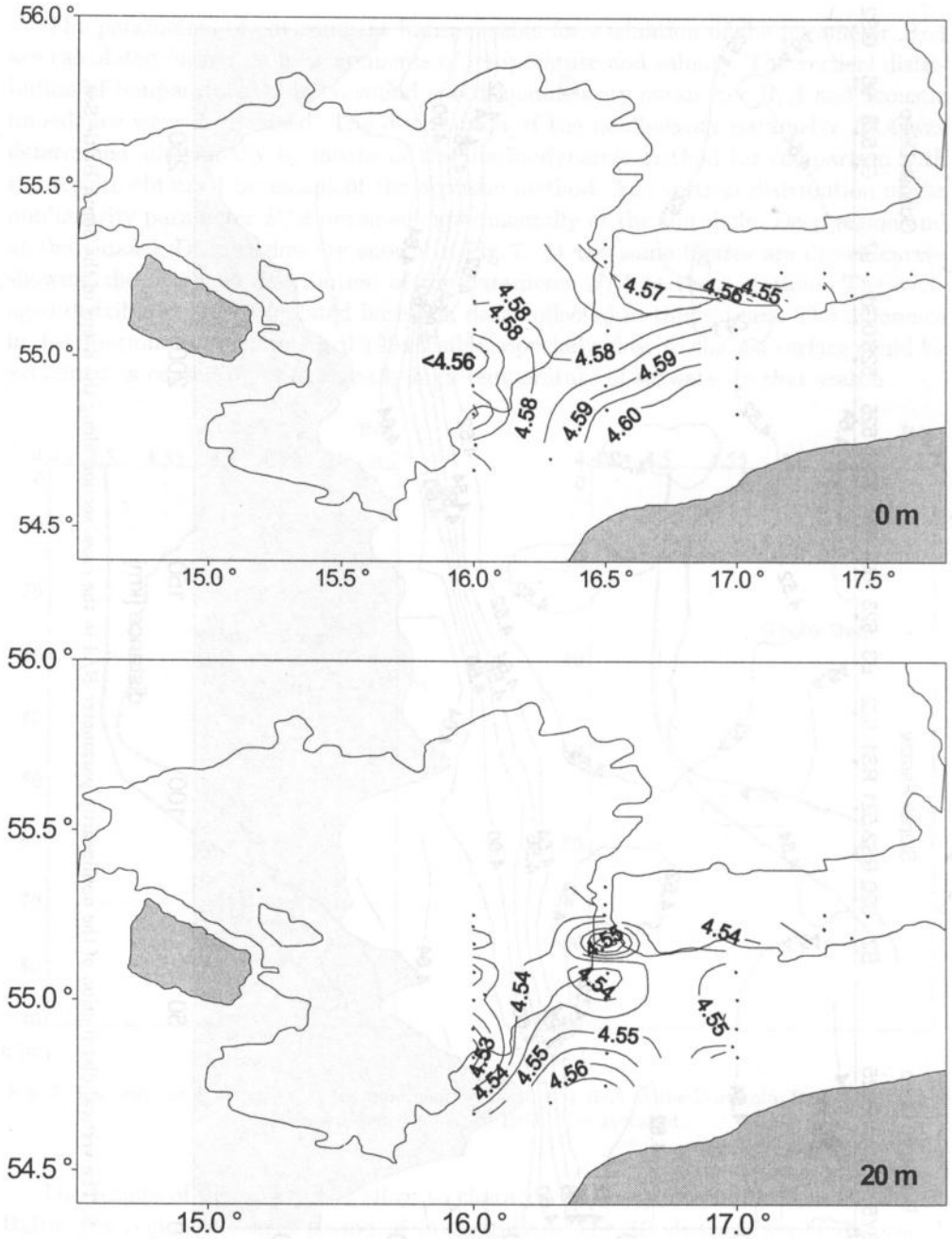

Fig. 9. The horizontal distribution of the nonlinearity parameter B/A at the sea surface and at depth of 20 m.

5. Conclusions

In the above paper are presented results of investigation of the nonlinearity parameter B/A of seawater in laboratory conditions as well as *in situ* in the South Baltic Sea. The measurements were carried out by means of the finite amplitude method applying a special constructed device for *in situ* measurements.

Results of investigation provide data on conditions of finite amplitude waves propagation in examining area within a period of measurement. The difference between distribution averaged for a chosen month typical for a given station and the one based on measurement suggests the necessity of carrying out *in situ* measurement and verifying the averaged data.

The greatest disadvantage of the device is the fact that it is not autonomous. To obtain accurate value of the nonlinearity parameter simultaneously two devices must be used — the device for nonlinearity parameter measurement and STD sounder to sample data on temperature and salinity changes with the depth. Although the temperature sensor is built in the device, its accuracy is too low to use the data obtained in this way in parameter B/A evaluation. Its indications as well as indications of the second built-in sensor of static pressure are only approximate ones.

References

[1] S.I. AANONSEN, T. BARKVE, J. NAZE TJØTTA and S. TJØTTA, *Distortion and harmonic generation in the nearfield of a finite amplitude sound beam*, J. Acoust. Soc. Am., **75**, 3, 749–768 (1984).

[2] *Algorithms for computation of fundamental properties of seawater*, UNESCO Technical Papers in Marine Science, 44, 1983.

[3] R.T. BEYER, *Parameter of nonlinearity in fluids*, J. Acoust. Soc. Am., **32**, 2, 719–721 (1960).

[4] C.T. CHEN and F.J. MILLERO, *Speed of sound in seawater at high pressures*, J. Acoust. Soc. Am., **62**, 5, 1129–1135 (1977).

[5] C.T. CHEN, F.J. MILLERO, *The specific volume of seawater at high pressures*, Deep Sea Res., **23**, 7, 595–612.

[6] W.N. COBB, *Finite amplitude method for the determination of the acoustic nonlinearity parameter B/A*, J. Acoust. Soc. Am., **73**, 5, 1525–1531 (1983).

[7] A.B. COPPENS *et al.*, *Parameter of nonlinearity in fluids*, II, J. Acoust. Soc. Am., **38**, 5, 797–804 (1965).

[8] H. ENDO, *Calculation of nonlinearity parameter for seawater*, J. Acoust. Soc. Am., **76**, 1, 274–279 (1984).

[9] B. HARTMANN, G.F. LEE and E. BALIZER, *Acoustic nonlinearity calculations using the Tait equation of state*, Proceedings of 16th International Congress on Acoustics, 539–540, Seattle 20–26 June 1998.

[10] H.A. KASHKOOLI *et al.*, *Measurement of the acoustic nonlinearity parameter in water, methanol, liquid nitrogen, and liquid helium-II by two different methods: A comparison*, J. Acoust. Soc. Am., **82**, 6, 2086–2089 (1987).

[11] G.A. KORN and T.M. KORN, *Mathematical handbook for scientists and engineers*, PWN, Warszawa 1983.

[12] E. KOZACZKA and G. GRELOWSKA, *Nonlinearity parameter B/A of the low-salinity seawater*, Archives of Acoustics, **19**, 2, 259–269 (1994).

[13] E. KOZACZKA and G. GRELOWSKA, *Investigation of the nonlinearity parameter B/A in the south Baltic Sea*, Nonlinear acoustics in perspective, 14-th International Symposium on Nonlinear Acoustics, Nanjing University Press, 88–93, 1996.

[14] E. KOZACZKA, G. GRELOWSKA, P. BITTNER and A. GRELOWSKI, *The influence of Vistula water on the thermodynamic and acoustic parameters of the Gulf of Gdańsk*, Oceanologia, **37**, 2, 227–248 (1995).

[15] W.K. LAW, L.A. FRIZZELL and F. DUNN, *Ultrasonic determination of the nonlinearity parameter B/A for biological media*, J. Acoust. Soc. Am., **69**, 4, 1210–1212 (1981).

[16] F.J. MILLERO, G. PERRON and J.F. DESNOYERS, *Heat capacity of seawater solutions from 5° to 35° C and 0.05 to 22‰ chlorinity*, J. Geophys. Res., **78**, 21, 4499–4506.

[17] D.V. RUDENKO and S.I. SOLUAN, *A theoretical introduction to nonlinearity acoustics*, Nauka, Moscow 1975.

[18] J. ZEMANEK, *Beam behavior within the nearfield of a vibrating piston*, J. Acoust. Soc. Am., **49**, 1(2), 181–191 (1971).

ARCHIVES OF ACOUSTICS
24, 3, 303–317 (1999)

STUDYING THE ACOUSTIC EMISSION OF THE TEMPOROMANDIBULAR JOINT

W. LIS, R. SALAMON

Department of Acoustics
Technical University of Gdańsk
(80-052 Gdańsk, ul. G. Narutowicza 11/12, Poland)
e-mail: wall@eti.pg.gda.pl

J. ZIENKIEWICZ

Department and Clinic of Maxillofacial Surgery
Medical Academy in Gdańsk
(ul. Dębinki 7, Poland)

The method of acoustic emission is widely used for testing the strength of materials and in passive underwater acoustics. Recently in the field of medicine, acoustic emission signals received in the traditional phonendoscope method are recorded and processed using advanced electronic technology. Presented in this paper is an example of this work. It is a system that tests the acoustic emission of the temporomandibular joint which when in a pathological state seriously impairs important physiological functions of man. The presented system receives and records acoustic signals emitted by the joint. This is synchronised with the registration of the jaw displacement. Based on that, parameters and characteristics of acoustic emission signals which could indicate a specific disease of the joint are determined. In the research to date the focus has been on determining the statistical distributions of root-mean-square and maximal values of the signals and the current spectrums linked to the movement of the mandible. Clinical tests carried out at the Clinic of Maxillofacial Surgery at the Medical Academy of Gdańsk have provided preliminary confirmation of the usefulness of the system for diagnostic functions. The tests are being continued and are systematically contributing to the collection of signals and cases. This in turn is the condition of progress of continued work on the use of acoustic emission in diagnosing the temporomandibular joint.

1. Introduction

The phenomenon of acoustic emission is widely used in science and technology, in particular for testing the strength of materials and in passive underwater acoustics. For many years now attempts have been made to put this phenomenon to work in medical diagnosing. The research focuses on those sounds emitted by the human body which the physician cannot hear directly because of their volume or high frequency or which he disregards on grounds of interpretative problems. These sounds include acoustic signals

which are produced by the movement of the joints. One of such joints that the medical world shows special interest in is the temporomandibular joint. What sets it apart from other joints is its complex anatomic structure and its exceptional susceptibility to injury plus the intense suffering it causes to the patients once dysfunctional.

The first mention on the use of the acoustic emission of the temporomandibular joint that the authors know of comes from D. WATT [11] who observed the correlation between the nature of audible sounds generated by the joint and malocclusion. The first application of technical means (a microphone and graphic recorder) for the purpose of testing the joint's acoustic emission was described by E. WEGGEN and K.H. GUNTHER [12], and soon afterwards by J. and Z. KRASZEWSCY in Poland [5]. Further work in this area was aimed at improving the technology of sound recording, and in particular the methods of processing acoustic emission signals. The mid eighties saw the beginning of a widespread use of digital and computer technologies in this area. The mainstream works include those of L. HEFFEZ and D. BLAUSTEIN [4] (spectral analysis using the FFT method), L. CHRISTENSEN [2] (statistical methods) and R. BADWAL [1] (fractal method). It was probably because of the high hopes scientists had in the processing of signals that the problem of sensors for the reception of these signals has been disregarded, as well as, although not entirely, the issue of correlation between the signals emitted and the movements of the joint (CH. OSTER *et al.* used X rays to do that [9]).

Systematic research on the acoustic emission of the temporomandibular joint was begun in 1994 at the Department and Clinic of Maxillofacial Surgery at the Medical Academy of Gdańsk and the Department of Acoustics at the Technical University of Gdańsk [6, 13]. The research covered the development of a special sensor for the reception of the signals emitted by the joint [6], design of a system to record and process these signals and clinical testing on a large group of patients. The article will present the design of the system, signal processing methods used and the results of the clinical testing to date.

2. Design of the system

The system for examining the acoustic emission of the temporomandibular joint consists of two channels, as shown in Fig. 1.

The first (acoustic) channel receives and records acoustic signals emitted by the joint, the second measures mandible displacement. Acoustic signals emitted by the joint are transformed into electric signals in a specially designed piezoceramic transducer [6]. The electric signal from the transducer goes through an amplifier and a low-pass filter of upper cut-off frequency of about 10 kHz, and next is sampled at a frequency of 22050 Hz in a 16 bit analogue to digital converter. This converter is a component of a computer stereo audio card. The recorded files are processed and analysed in the computer, mainly using the MATLAB 5-3 programme. The calibration generator is switched on to replace the transducer in order to test and adjust the system's parameters periodically.

The second channel registers the state of jaw opening. To do that a tensometric sensor is used, coupled through a lever with the movements of the jaw (mandible) of the

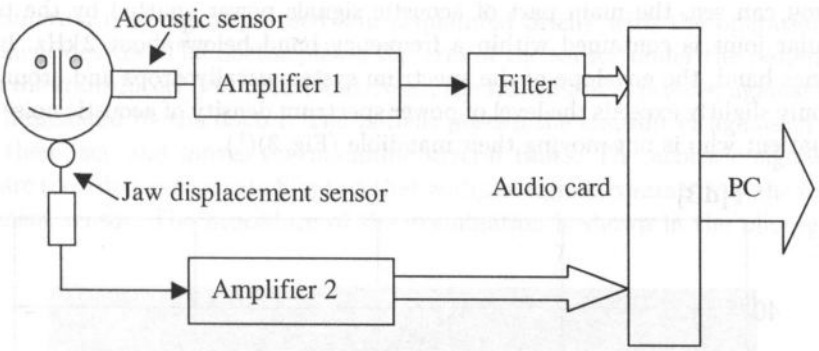

Fig. 1. Block diagram of the system for examining the acoustic emission of the temporomandibular joint.

patient. The electric signal coming from the sensor is amplified and given to the input of the second channel of the stereo audio card. Sampling of this signal is also done at a frequency of 22050 Hz, and the resulting digital signal is recorded synchronously with the acoustic signal in computer memory.

The transfer bandwidth of the acoustic channel was chosen based on the available literature on the spectrum width of signals emitted by the temporomandibular joint [3, 4] and on our own measurements of the spectrum. To take the measurements we used a transducer with upper cut-off frequency of 25 kHz, a broad-band amplifier and an A/D converter with sampling frequency of 41100 Hz. A typical power spectrum density F of a digital signal generated in this way is shown in Fig. 2.

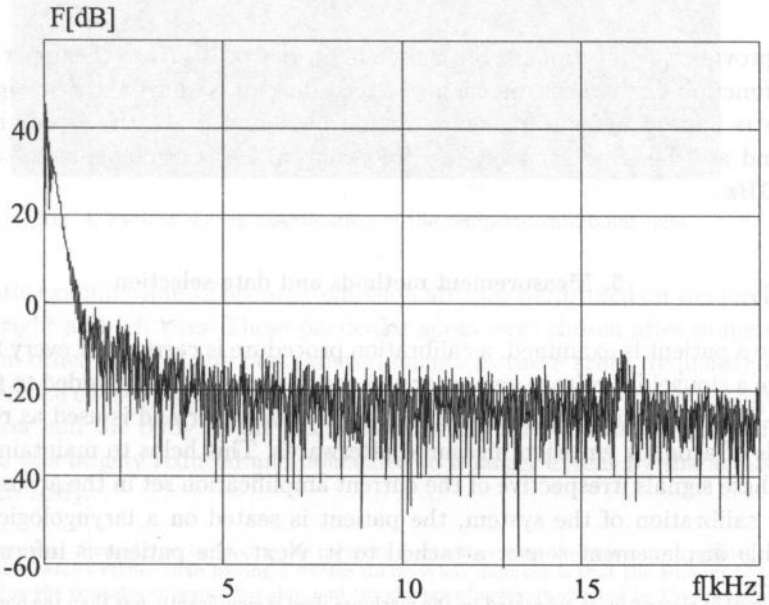

Fig. 2. Typical power spectrum density of an acoustic emission signal.

As you can see, the main part of acoustic signals power emitted by the temporo-mandibular joint is contained within a frequency band below about 2 kHz. In higher frequencies band, the envelope of the spectrum systematically drops and around about 10 kHz only slightly exceeds the level of power spectrum density of acoustic noise emitted by the patient who is not moving their mandible (Fig. 3)([1]).

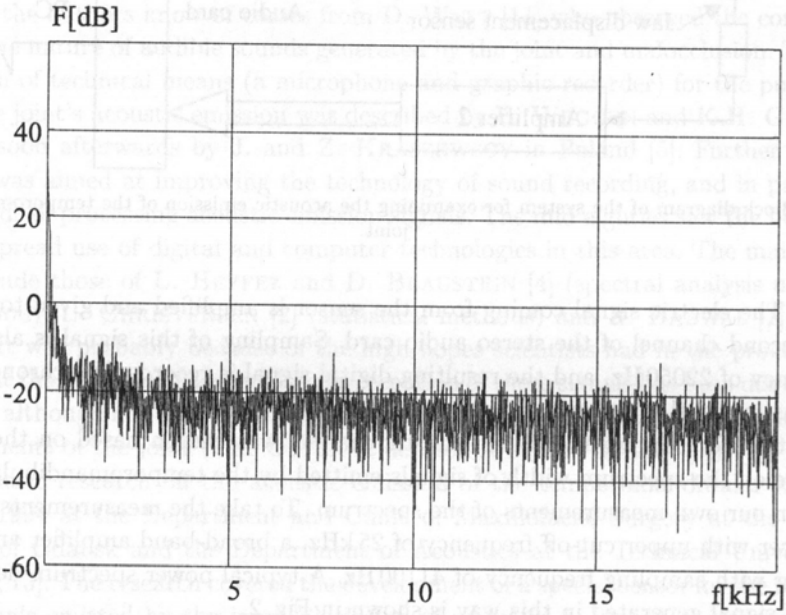

Fig. 3. Spectrum of interference emitted by the patient's body and measurement devices.

This provides justification for the chosen frequency of 10 kHz as the upper limit of the transfer function of the acoustic channel. According to Nyquist theorem signals whose spectrum is limited by this frequency should be sampled at a frequency higher than 20 kHz and are therefore sampled at a frequency which is available in the audio card, i.e. 22050 Hz.

3. Measurement methods and data selection

Before a patient is examined, a calibration procedure is carried out every time. In the procedure a sinusoidal voltage generator of a constant amplitude is added to the acoustic channel. The calibration signal is recorded in the computer and is used as reference for all signals of acoustic emission measured afterwards. This helps to maintain a constant scale of these signals irrespective of the current amplification set in the acoustic channel.

After calibration of the system, the patient is seated on a laryngologic chair with a mandible displacement sensor attached to it. Next, the patient is informed on how

([1]) The level of electric noise generated by the machines used is significantly less than the observed acoustic noise.

the examination is going to proceed and acquainted briefly with the operation of the measurement devices. The doctor places the arm of the sensor under the patient's chin and puts the transducer([2]) in their hand. Next, the transducer is pressed against areas of the face designated by the doctor. The patient presses the transducer against a specific spot on their face and moves the mandible several times. The acoustic signals being emitted are recorded as separate files together with the signals coming from the mandible displacement sensor. The procedure of the examination is shown in the photograph in Fig. 4.

Fig. 4. Patient during examination of the temporomandibular joint.

Systematic examinations of acoustic emission are now performed on the forehead and around the right and left ears. These particular spots were chosen after numerous tests performed on other parts of the face. Measurements in these areas frequently carried a lot of interference caused by the fact that it is difficult to maintain in a constant contact the transducer and the body as the mandible is being moved. Also the level of noise of these signals was largely reduced and concealed to a larger extent by the acoustic noise of the human body.

([2]) The experiment showed that by having the patients themselves press the transducer against the selected spots gives better results rather than having a doctor do it. What happens is that the amount of interference caused by moving the transducer across the skin and the change of pressure exerted by the transducer against the body is reduced. In general, one can say that the patient has a better control of the examination, can select the transducer's pressure against their body easier and performs fewer unnecessary moves.

Typical signals recorded in one spot that the transducer is placed against are shown in Fig. 5.

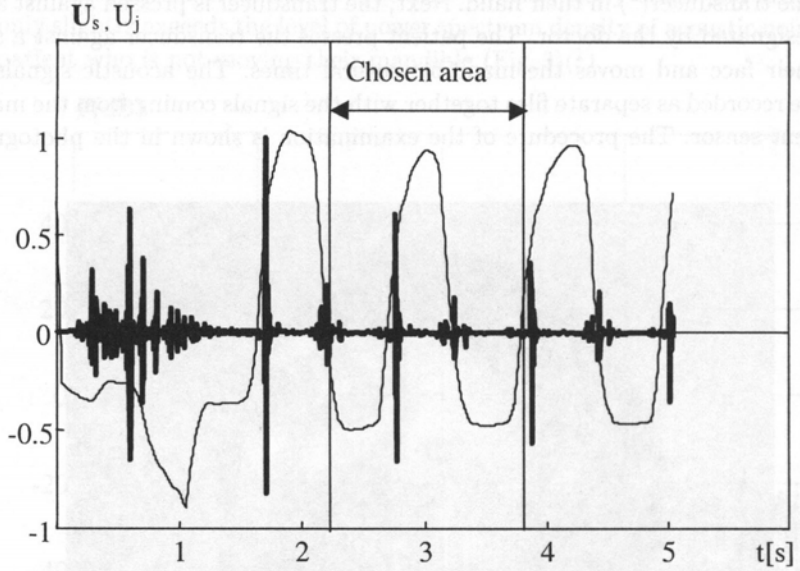

Fig. 5. Acoustic emission signal (thick line) against the signal from the mandible displacement sensor. ($\mathbf{U}_s$ – acoustic signal, U_j — relative value of jaw displacement).

The signal coming from the mandible displacement sensor encompasses four cycles of opening and closing of the mouth. Its minimal value is for a closed mouth while the maximal value signifies a full opening of the mandible. In the background of this signal, the signal of the acoustic emission of the temporomandibular joint is clear. It exhibits characteristic short lasting "pulses" of high values and other more equal fragments of smaller amplitudes.

This type of signal presentation has the enormous advantage of allowing each fragment of the acoustic emission signals to be linked to the current phase of mandible opening. When the doctor is interpreting the recorded signals (including the results of the processing), he can easily determine at which point of mandible movement specific acoustic signals are emitted.

Observation of acoustic emission signals and of mandible movement makes the following findings possible:

- in an acoustic emission signal some elements are repeated in some of the opening and closing cycles of the mandible,
- the movement of the mandible in the consecutive cycles is not identical,
- the full amplitude of the mandible movement gives strong acoustic emission,
- the intensity of acoustic emission depends on how quickly the mandible moves observed as a slope of the curve which describes the mandible's path.

These observations lead to the conclusion that from the entire recording we can select the most interesting fragments or at best one fragment which gives the most complete

insight into the joint's acoustic emission. A fragment representative of the phenomenon should include the whole cycle of mandible movement — from the closed state through full opening to a repeated closure. In the fragment chosen, the mandible movement should be complete, quick and possibly uniform. It is the role of the operator to get the patient to perform movements like these. The choice of the appropriate fragment is made subjectively by the doctor based on an overview of all the signals recorded.

The need for selection of the recorded signals is also the result of the need to limit the number of measurement data. The effective time of examining one patient lasts a few dozen seconds which given the relatively high sampling frequency provides more than 2 million samples as the end result of the examination. Looking through such files is very time consuming and occupies a large portion of computer memory. As an example Fig. 6 shows the result of a signal selection from a single measurement point made by the doctor.

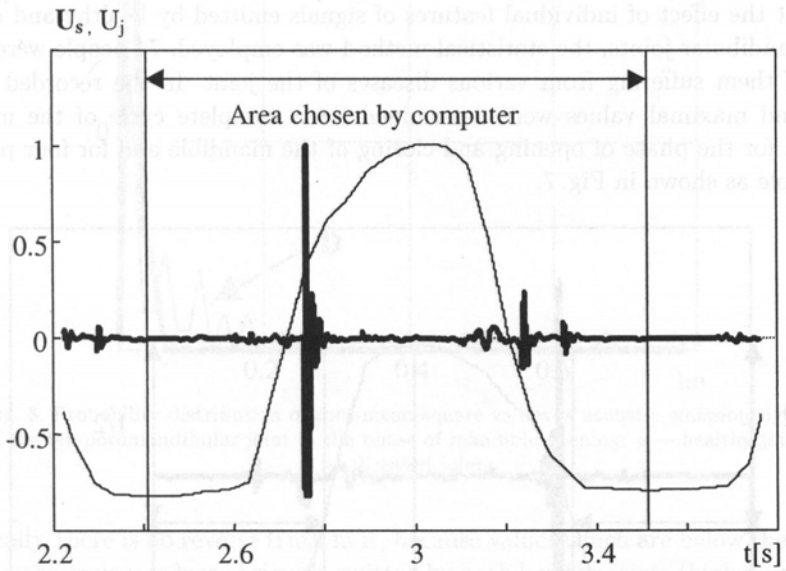

Fig. 6. Fragment of the signal from Fig. 5 chosen by the doctor with one cycle of mandible movement marked, automatically chosen by the computer.

Next, the computer programme determines the accurate limits of the selected fragment starting from the closed state of the mandible to its maximal opening and repeated closure. In this way, the selected signals are saved in computer memory as archive data and used for various analyses which primarily aim at determining the type of pathological state of the joint.

4. Analysis of the acoustic emission signal in the time domain

The literature as well as our own experiments show a lot of discrepancy observed in the signals emitted by the temporomandibular joint in healthy as well as in sick patients.

This is due to the differences in the anatomic structure of the joint and the surrounding osseous and muscular system, pathological states and lack of a complete repeatability of the results of the measurements. For this reason, one cannot expect to obtain a model acoustic emission signal, characteristic of specific diseases or of a healthy joint. The only thing an analysis of acoustic emission signals can do is help to select some characteristic features which can be linked to specific illnesses with a certain degree of probability.

The first step in this direction is to identify those features of signals which will help to distinguish between signals emitted by healthy joints and those emitted by diseased joints. In a recently started new stage of the research, the project concentrates on identifying features that are characteristic of certain pathological states. The results of an analysis of acoustic emission signals presented further on come from the first stage of the research only, because the material gathered on the basis of clinical tests to date is insufficient and does not allow the formulation of conclusions on the particular illnesses.

To limit the effect of individual features of signals emitted by healthy and diseased temporomandibular joints, the statistical method was employed. 74 people were tested, with 33 of them suffering from various diseases of the joint. In the recorded signals, effective and maximal values were determined for a complete cycle of the mandible movement, for the phase of opening and closing of the mandible and for four phases of the mandible as shown in Fig. 7.

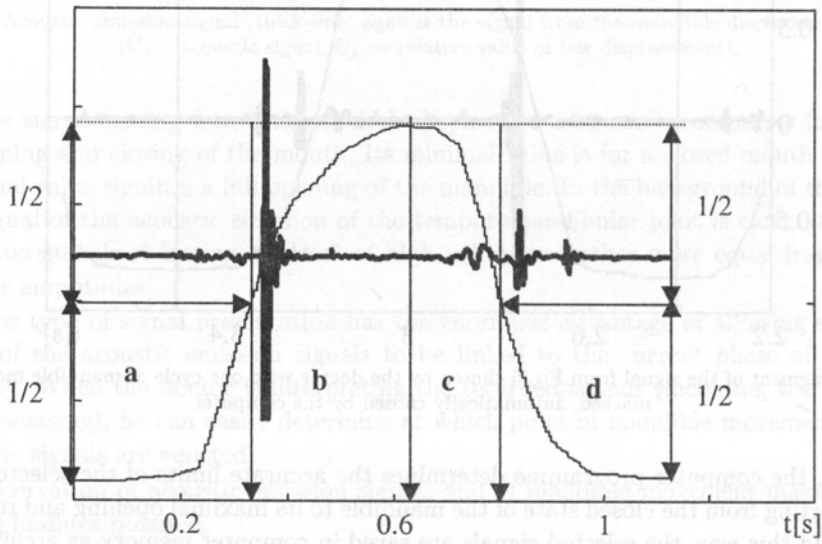

Fig. 7. Phases of mandible movement: **a** — early opening phase, **b** — final opening phase, **c** — early closing phase, **d** — final closing phase.

The results of the measurements are depicted in the form of probability distribution ϕ of root-mean-square lm and maximal values U for the entire mandible cycle and for its particular phases. From among all the determined probability distributions in the figures given further on, the ones shown are those exhibiting distinct differences between the levels of signals emitted by healthy and diseased joints. The probability distributions

of the root-mean-square value of signals referring to the opening phase of the mandible (Fig. 8) show that when this value exceeds a specific threshold set for the experiment, it is highly likely that the signal comes from a diseased temporomandibular joint.

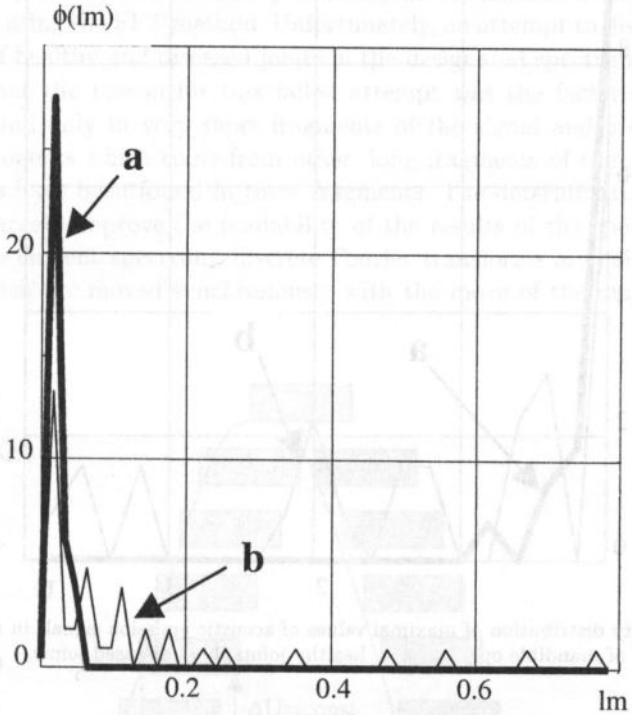

Fig. 8. Probability distribution of root-mean-square values of acoustic emission signals of the temporomandibular joint in the phase of mandible opening: **a** — healthy joints, **b** — diseased joints.

Basically, there is no reverse truth in it, because values which are below the threshold are root-mean-square values of signals emitted by both healthy joints (higher probability) and diseased joints (lower probability). A good separation of probability distribution of maximal values of the signals is observed in the second phase of mandible opening. Figure 9 shows clearly that high values of signal maximums in the phase of the mandible's movement are characteristic of diseased temporomandibular joints.

The measurements were used as a basis for determining average values and variances of root-mean-square and maximal values of signals in all the phases of the mandible's movement for both healthy and diseased joints. The results are listed in Table 1 which in clinical practice is used for diagnosing individual cases. The results of measurements taken for each patient are placed in the first column of the table and compared with the mean values obtained during the examination of the 74 people. High dispersions of mean and maximal values make this method of diagnosing unreliable. As a result, other features of the signals have to be found, ones that will provide a better distinction between healthy and diseased joints.

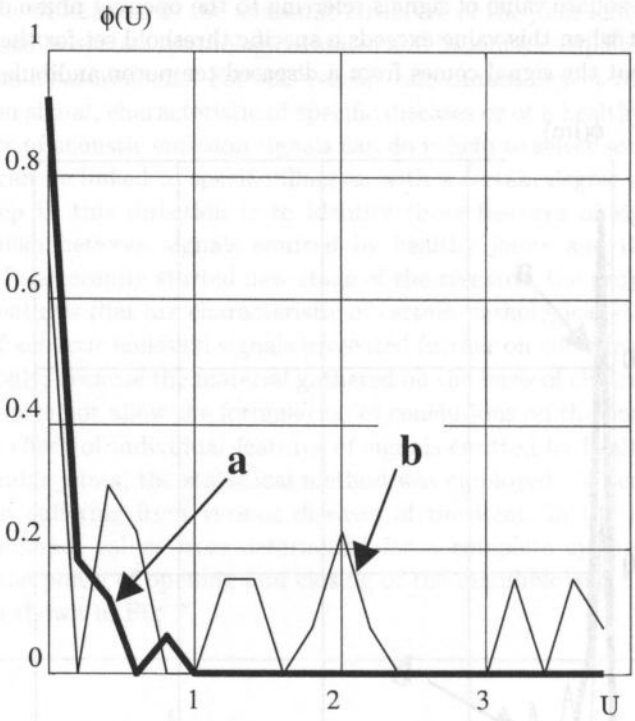

Fig. 9. Probability distribution of maximal values of acoustic emission signals in the final phase of mandible opening: **a** — healthy joints, **b** — diseased joints.

Table 1.

Number of examination	023		Full name of patient		
Place of examination	Left ear		Jan Kowalski		
	Result of examination	Sick patients		Healthy patients	
Parameter		Mean value	Dispersion	Mean value	Dispersion
Root-mean square values					
Early opening phase	**0.014**	**0.027**	0.040	**0.018**	0.009
Final opening phase	**0.008**	**0.111**	0.225	**0.022**	0.016
Early closing phase	**0.057**	**0.073**	0.116	**0.045**	0.039
Final closing phase	**0.036**	**0.070**	0.101	**0.048**	0.046
Maximal values					
Early opening phase	**0.041**	**0.164**	0.371	**0.066**	0.052
Final opening phase	**0.020**	**0.611**	1.062	**0.085**	0.117
Early closing phase	**0.262**	**0.461**	0.780	**0.243**	0.278
Final closing phase	**0.137**	**0.301**	0.465	**0.191**	0.196

5. Analysis of signals in the frequency domain

Analysis of acoustic emission signals of the temporomandibular joint began with determining the power spectrum density of all signals recorded in a complete movement of the mandible using the FFT method. Unfortunately, an attempt to distinguish features characteristic of healthy and diseased joints in the designated spectrums failed. Further tests showed that the reason for this failed attempt was the fact that characteristic features are found only in very short fragments of the signal and are masked by the spectrum components which come from other, long fragments of the signal. So far, no specific features have been found in these fragments. The determination of the current spectrum did largely improve the readability of the results of the spectral analysis. In determining the current spectrum, discrete Fourier transforms are calculated in about 80 windows which are moved synchronously with the move of the mandible, as shown in Fig. 10.

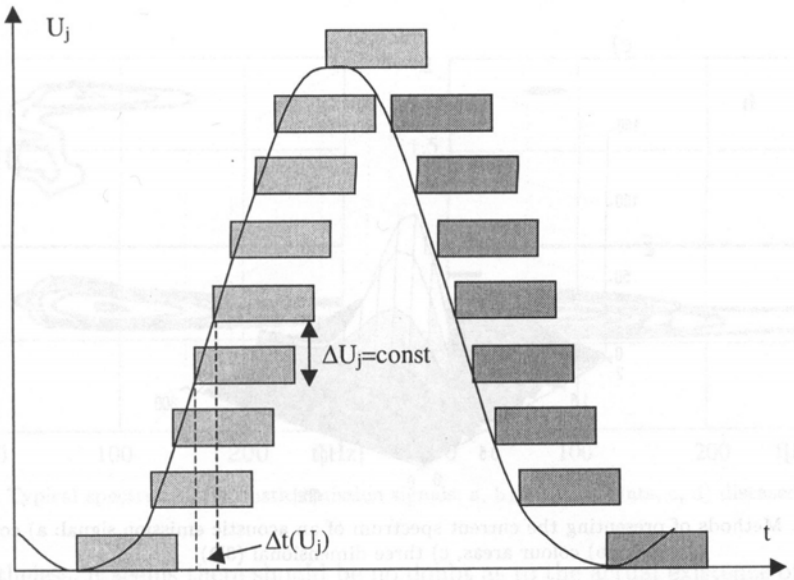

Fig. 10. Illustration of how the window movement is synchronised with the mandible movement.

In each window, the discrete Fourier transform is calculated from 1024 samples of acoustic emission signal. To reduce false spectral lines which are the result of the finite number of samples a typical Blackman window was used [10]. A natural effect of the shortening of the window is a deteriorated frequency resolution which at this point amounts to about 22 Hz. When the entire movement of the mandible was being sampled it amounted to about 1 Hz. Figure 11 shows three ways of presenting the current spectrum used in the system. In the original 12 colours of lines and areas are used to mark the level of the spectrum which greatly facilitates the interpretation of spectrograms. The move of the mandible is described on a scale of 0 to 2 with 0 as the closing of the mandible, 1 — full opening and 2 — repeated closure.

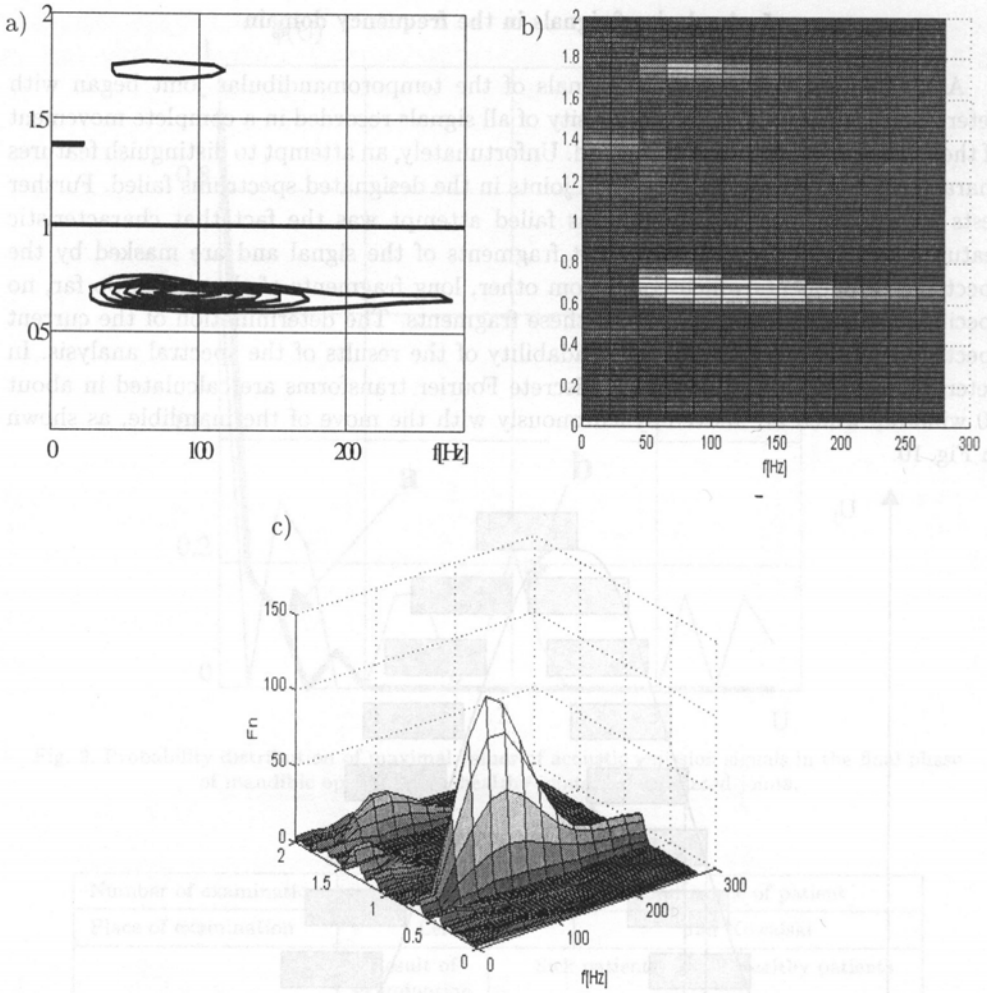

Fig. 11. Methods of presenting the current spectrum of an acoustic emission signal: a) contour, b) colour areas, c) three dimensional (3D).

Following the determination of the spectra of acoustic emission signals of the joints of 74 patients, the spectra were then analysed. The analysis has led to these conclusions:

- the presence of spectrum components exhibiting a high value and a broad band in the phase of mandible opening is typical of numerous pathological states of the temporomandibular joint,
- the presence of spectrum components in the phase of mandible closing only is typical of healthy temporomandibular joints.

Typical spectra of acoustic emission signals of healthy and diseased joints are shown in Fig. 12. The sad thing is that in a few cases of healthy and diseased joints some deviations from these rules were spotted which means that the method cannot be recognised as a valid diagnostic method.

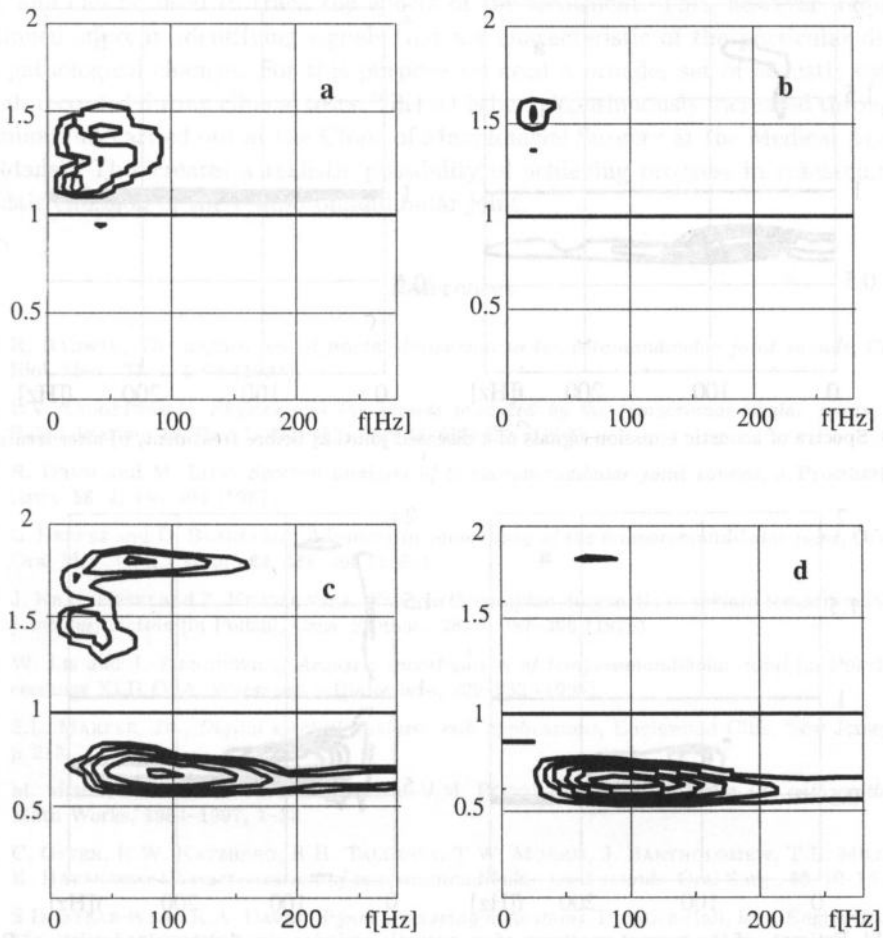

Fig. 12. Typical spectrums of acoustic emission signals: a, b) healthy joints, c, d) diseased joints.

Nonetheless, it seems there should be no doubt as to the actual existence of a correlation between the joint's pathological states and the shape of the spectrum of acoustic emission signals. A proof of that is provided, among other things, by comparing spectrums emitted during the treatment of a diseased joint, shown in Fig. 13. It is true that the shape of the spectrum after a completed treatment continues to be different from one that is typical of healthy joints, however, the features that are characteristic of diseased joints have retreated, too.

The deteriorated resolution following a reduction of the window is especially negative in the range of low frequencies. This can be eliminated though by using one of the parametric methods of spectrum estimation [7]. To illustrate the positive effects of such methods, Fig. 14 a shows a spectrum that has been determined using Burg algorithm. This spectrum was calculated on the basis of a number of samples in a window reduced to 64 and assuming a filter model of the 4-th order.

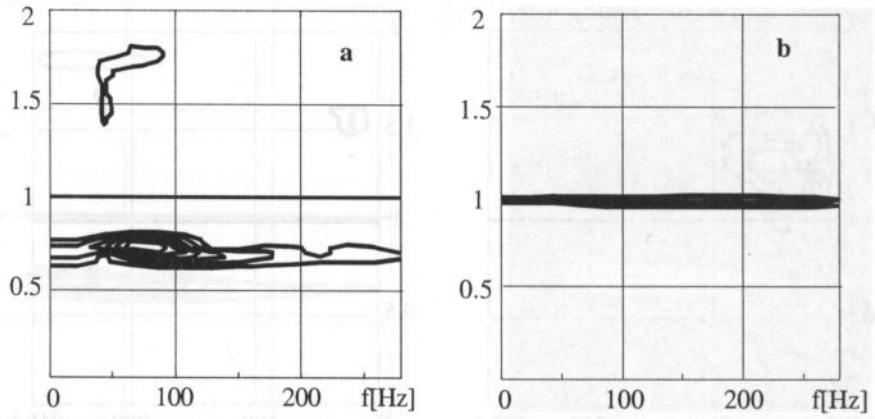

Fig. 13. Spectra of acoustic emission signals of a diseased joint: a) before treatment, b) after treatment.

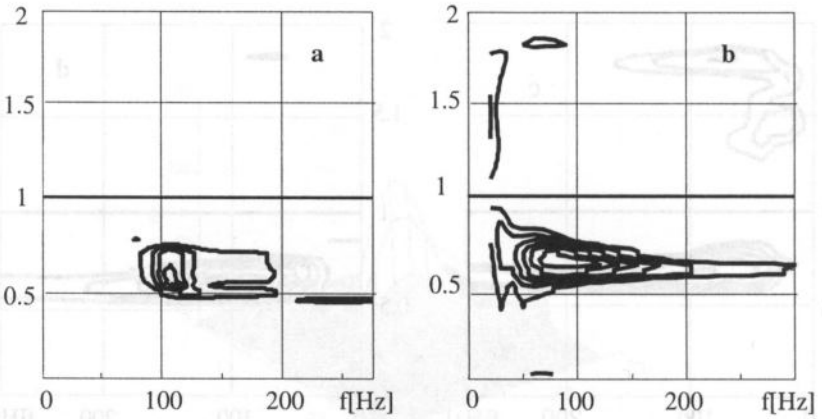

Fig. 14. Estimate of the current spectrum of an acoustic emission signal determined using: a) Burg method, b) wavelet method. (The spectrum of the same signal determined using the FFT method is shown in Fig. 12 d).

Attempts were made to improve the resolution in the time domain (of the mandible movement). To do that wavelet transformation was applied, using Morlet and Coiflet wavelets [8]. The resolution of the current spectrum in the time domain improved only slightly in the range of higher frequencies, as illustrated in Fig. 14 b.

Therefore, "wavelet" transformation can be treated only as a supplement to Fourier transformation with mobile window.

6. Conclusions

The clinical tests to date have shown that analysis of acoustic emission signals can prove a useful tool in the future for diagnosing the diseases of the temporomandibular

joint and can be used to track the effects of the treatment. This, however, requires a continued effort in identifying signals that are characteristic of the particular diseases and pathological changes. For this purpose we need a broader set of acoustic emission signals recorded during clinical tests. This set is being continuously increased through the examinations carried out at the Clinic of Maxillofacial Surgery at the Medical Academy of Gdańsk. This creates a realistic possibility of achieving progress in researching the acoustic emission of the temporomandibular joint.

References

[1] R. BADWAL, *The application of fractal dimension to temporomandibular joint sounds*, Comput. Biol. Med., **23**, 1, 1–14 (1993).

[2] L.V. CHRISTENSEN, *Physics and the sounds produced by the temporomandibular joints*, J. Oral Rehabilitation, **19**, Part I. 471–483, Part II. 615–627 (1992).

[3] R. DRUM and M. LITT, *Spectral analysis of temporomandibular joint sounds*, J. Prosthetic Dentistry, **58**, 4, 485–494 (1987).

[4] L. HEFFEZ and D. BLAUSTEIN, *Advances in sonography of the temporomandibular joint*, Oral Surg. Oral Med. Oral Pathol., **62**, 486–495 (1986).

[5] J. KRASZEWSKI and Z. KRASZEWSKA, *Phonoarthrographic diagnostic in certain temporomandibular joint dysfunction* [in Polish], Czas. Stomat., **28**, 4, 387–396 (1975).

[6] W. LIS and J. ZIENKIEWICZ, *Acoustic investigation of temporomandibular joint* [in Polish], Proceedings XLII OSA, Warszawa – Białowieża, 229–232 (1995).

[7] S.L. MARPLE, JR., *Digital spectral analysis with applications*, Englewood Clifs, New Jersey 1987, p. 213.

[8] M. MISITI, Y. MISITI, G. OPPENHEIM and J.M. POGGI, *Wavelet toolbox for use with matlab*, The Math Works, 1984–1997, 1–33.

[9] C. OSTER, R.W. KATZBERG, R.H. TALLENTS, T.W. MORRIS, J. BARTHOLOMEW, T.L. MILLER and K. HAYAKAWA, *Characterization of temporomondibular joint sounds*, Oral Surg., **58**, 10–16 (1984).

[10] S.D. STEARNS and R.A. DAVID, *Signal processing algorithms*, Prentice-Hall, Inc., Englewood Cliffs, New Jersey 1988, p. 167.

[11] D.M. WATT, *Clinical applications of gnathosonics*, Prosthetic Department, School of Dental Surgery, University of Edinburgh, Scotland, I-II, 16, 83–95 (1966).

[12] E. WEGGEN and K.H. GUNTHER, *Phonognathographie. Eine Methode zur Registrierung und Beurteilung von Schallphanomenen, die durch den Kaumechanismus hervorgerufen werden*, Dtsch. Stomat., **20**, 575 (1970).

[13] J. ZIENKIEWICZ and W. LIS W, *A new method of examining phenomena in temporomandibular joint* [in Polish], Czas. Stom., **49**, 10, 710–716 (1996).

ARCHIVES OF ACOUSTICS
24, 3, 319–329 (1999)

DETECTION OF MICELLAR STRUCTURES IN OIL-WATER-SURFACTANT SYSTEMS WITH A PHOTOACOUSTIC METHOD

S.J. POGORZELSKI, J. SZURKOWSKI and A. ŚLIWIŃSKI

Institute of Experimental Physics,
University of Gdańsk
(80-952 Gdańsk, Wita Stwosza 57, Poland)
e-mail: fizas@univ.gda.pl

Model studies were performed with a layered system consisting of thin olive oil layers (25 – 250 μm in thickness) spread over the water surface using a photoacoustic method. Significant variations in the signal phase and amplitude found out at the interfaces (air/oil and oil/water) as well as at a depth of 9 – 13 μm beneath the oil surface point to the formation of organized clathrate molecular structures under the film-covered surfaces and micellar structures of surfactants if present in a bulk oil phase at an appropriate concentration (above CMC) and temperature (Krafft point). Such organized structures have different thermodynamic properties (like specific heat or thermal diffusivity, discussed in terms of classical thermodynamics of thin surface layers) that is supposed to affect the photoacoustic effect used for depth profiling.

1. Introduction

Shallow coastal marine waters are enriched in a wide variety of oil and surface-active substances (surfactants) being a result of pollutant organic slicks from petroleum spills or municipal effluents containing: detergents, fertilizers, washing agents, chemicals etc.

At an appropriate concentration of surfactants (above CMC — critical micellar concentration) and temperature (Krafft point) they form compact monomolecular diffusion-controlled layers at interfaces and organized molecular aggregates (micelles) in the bulk water beneath the adsorbed film [8].

Surface film studies performed in coastal regions of the Baltic and Mediterranean Seas on the film material directly sampled pointed to the vertically segregated film structure forming nearly separate layers at the interface with the most insoluble surfactant compound on the top of this layered system [9, 12 – 14].

In model laboratory investigations organic materials of similar physico-chemical properties as found in nature were spread over the water surface and studied with a photoacoustic method to determine their mechano-thermal parameters. Amplitude and phase dependences of the photoacoustic signal, as a function of sample layer thickness, demonstrate step changes corresponding to interfacial regions (air/oil and oil/water) and seen

at a certain depth (about 9 – 13 μm) in the bulk oil phase. The observed signal features are expected to be useful in detection of the film-induced clathrate organized water molecules in the subsurface water layer (about 190 μm in thickness) and in studies of mechano-thermal irregularities in the liquid bulk attributed to the formation of surfactant micellar structures.

The aim of the paper is an attempt to interprete the observed signal variations in terms of the ordering water molecules effect (of negative entropy with a certain loss of the molecules degrees of freedom) taking place under the film covered surface and the occurrence of different quasi-crystal micellar structures of surfactant molecules different in their elasto-thermal parameters than the surrounding liquid phase.

2. Measuring system and theoretical principles

A block diagram of the measuring photoacoustic (PA) system is shown in Fig. 1.

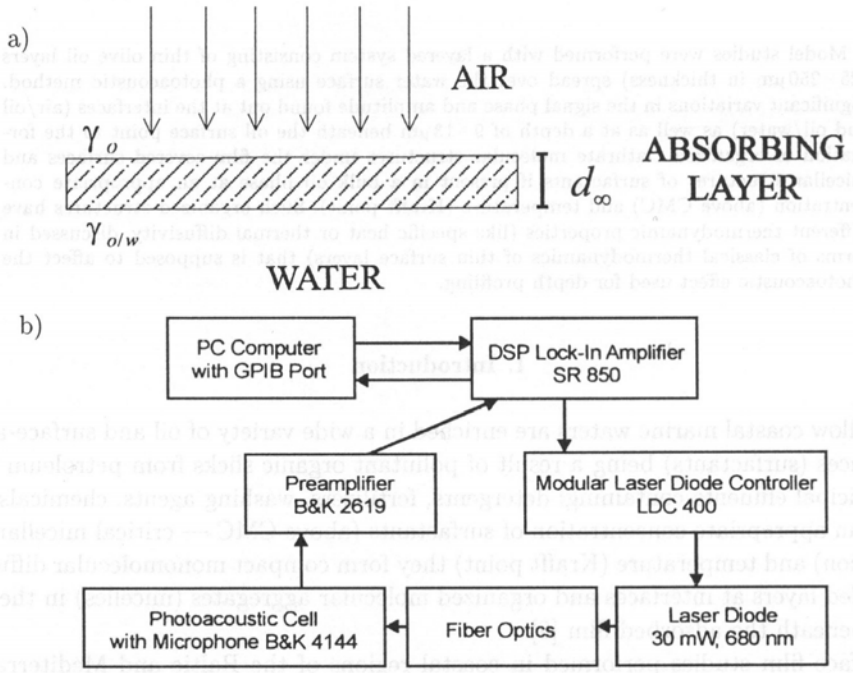

Fig. 1. A block diagram of the measuring set-up, for details see text. a) An open-type photoacoustic cell filled with a layered oil-on-water system of the equilibrium thickness d_∞, irradiated with a laser beam. γ_o, $\gamma_{o/w}$ — surface tension of oil, and oil-water interfacial tension, respectively. b) The associated electronic units for data collection and measurement control with laser beam guiding fiber wires and signal sensors.

In the presented studies, a novel experimental set-up based on a lock-in amplifier SR 850 was used, which not only measured the signal but also controlled operation of the laser diode being a source of modulated light. A laser diode (type SDL-73311) is

a source of modulated light of the wavelength 680 nm. The laser beam is, by a fiber wire, provided to the measuring cell of author's construction. The photoacoustic signal received by a microphone is phase-sensitive detected using a lock-in amplifier (type SR 850). An internal generator of the amplifier is also used for operating the laser diode controller (LPC 400). All data collection and further processing is realized by a PC computer working in the GPIB standard. The introduction of a laser diode and electronic light modulation system allowed receiving a higher signal to noise ratio in reference to its mechanical analogue. The modulation frequency of the light was varied from 1 to 1000 Hz. The adopted modulation frequency range allowed the depth distribution of signal response to be determined for all the studied layers. The PA signals were analysed using the depth profiling in terms of one-dimensionally inhomogeneous materials theory.

Interpretation of our data is based on the results originating from a classical Rosencweig–Gersho model [16]. In particular, a one dimensional heat flow in the sample is assumed, and in the framework of the model the thermal diffusion length μ (a certain sample thickness which affects the signal magnitude at a fixed modulation frequency) can be written:

$$\mu = \sqrt{\frac{\alpha}{\pi f}} \tag{1}$$

and

$$\alpha = \frac{k}{\delta c}, \tag{2}$$

where α is the thermal diffusivity, f the frequency of light modulation, k — the thermal conductivity, c — the heat capacity, δ — the medium density.

Such a dependence was adopted in our measurements to derive the thermal diffusivity of the studied samples.

In studied model layered oil-water system, thin layers of olive oil (from 25 to 250 μm in thickness) were formed onto the clean water surface by spreading from a solution of oil dissolved in ethyl ether. After evaporating the solvent, the olive oil layer was formed of equilibrium thickness d_∞ determined by the spreading coefficient and density difference of the liquids in contact [1].

Homogeneity of the formed oil layers were checked by comparing photoacoustic spectra (PAS) (obtained for different modulation frequencies) with those measured with a Fourier Transform Infrared Reflection Spectroscopy (FTIRS) system supplemented with a photoacoustic cell.

3. Results and discussion

In Fig. 2 amplitude and phase dependences of the photoacoustic signal for the studied samples are presented against the square root of the light modulation frequency [17]. They demonstrate significant variations at the interfacial regions certainly correlated with a step character of the thermodynamic properties changes in the liquid layer at a certain depth.

In order to describe the results let us perform the following consideration.

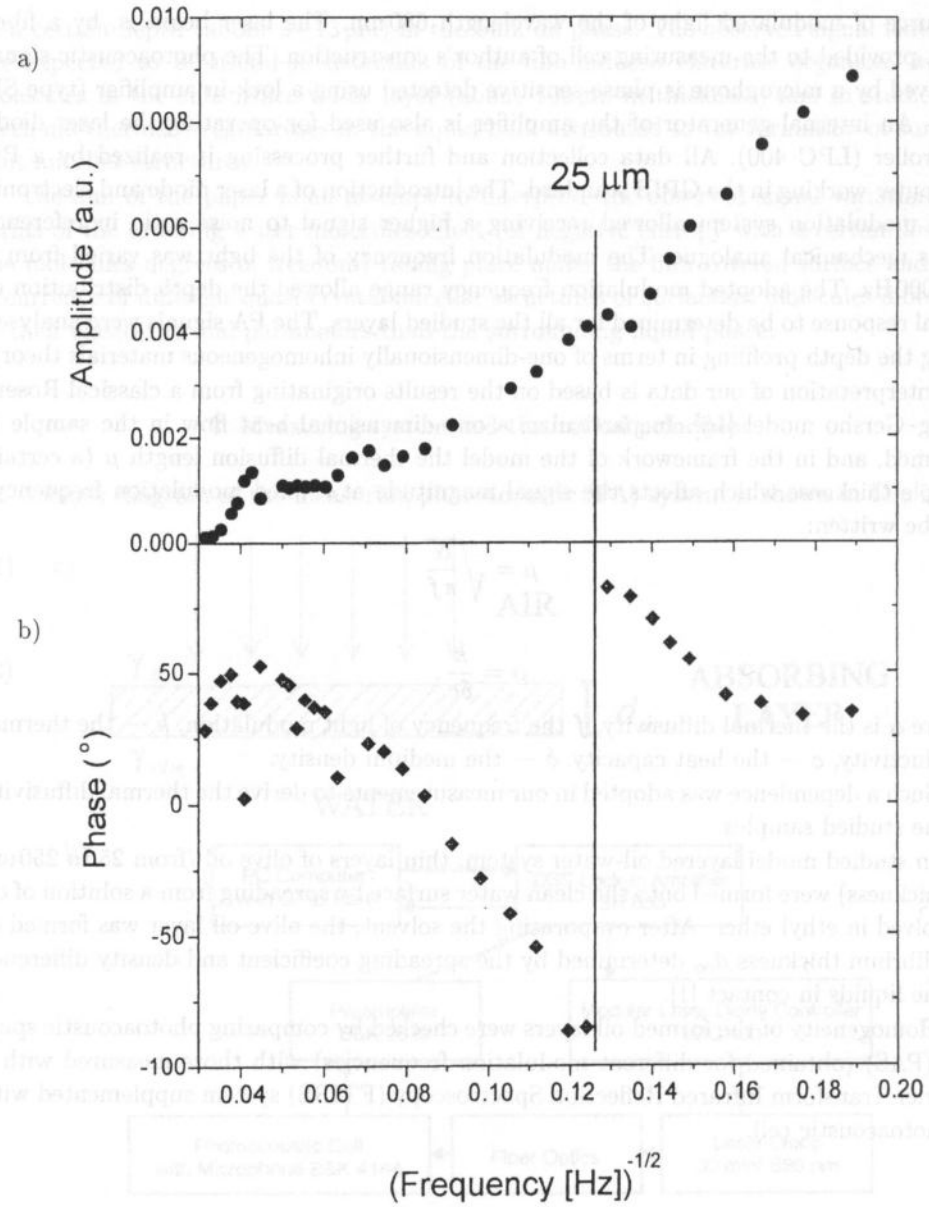

Fig. 2. Photoacoustic signal amplitude (a) and phase (b) as a function of sample depth, for a layered olive oil-water system.

3.1. Surfactant monolayers adsorbed at interfaces

Surface-active substances present in both polar (hydrophilic) and nonpolar (hydrophobic) solvents form at interfaces (air/oil or oil/water) a monolayer, as a result

of surface adsorption described by the Gibbs' equation [1]:

$$\Gamma = -\frac{c}{RT}\frac{d\gamma}{dc} \tag{3}$$

with the thickness δ:

$$\delta = \frac{\Gamma_\infty \cdot M}{\rho}, \tag{4}$$

where Γ, Γ_∞ is the Gibbs' excess (adsorption) and its saturation value, respectively, c — the surfactant bulk concentration in the solution, γ — the surface or interfacial tension, T — absolute temperature, R — the gas constant, M — molecular weight, and ρ — density of the dissolved surface-active substance.

Values of δ, for lipid substances, are of the order of 10–25 Å[1] that is comparable to the intermolecular distance between the water molecules in the surface layer (= 5.8 Å, [2]). In the presence of a monomolecular surface film intensive hydrophobic and hydrophilic interactions with the adjacent water layer occur [11, 18]. Various spectroscopic studies [6] have shown that the effect of a surface film is largely to hinder the rotational motion and the mobility of the water molecules and enhance the degree of the 0–H...0 hydrogen bonding between water molecules [10].

The reduction in mobility of the water molecules is associated with a decrease of the diffusion coefficient D_o of pure water. If it is assumed that a surface film induced (potential) activition energy ΔE of the order of 5.53 kJ/mol, and the thermal energy kT govern the energy distribution of the water molecules, Boltzmann statistics can be applied to this system and the diffusion coefficient D_s of a surface film covered water surface can be expressed by [7]:

$$D_s = D_o \exp[-\Delta E/kT]. \tag{5}$$

Often the diffusional properties are expressed in terms of a relaxation time τ which is linearly correlated with the surface viscosity of the monolayer [7]. The viscosity increases with increasing alkyl chain length as shown in the homologous series of alkanols and carboxylic acids. Note that in both cases the hydrophilic group of the surfactant was kept constant and only the alkyl chain length of the hydrophobic group was varied.

The modification of the relaxation time by the adsorbed film is given by:

$$\tau_s = \tau_o \exp[\Delta E/kT] \tag{6}$$

(for pure water $\tau_o = 1.19 \times 10^{-11}$ s).

Microwave radiometer measurements at $f = 1.43$ GHz over a sea surface covered with a monomolecular 9-octadecen-1-ol, Z isomer (oleyl alcohol), surface film lead to the value of τ_s equal to 1.11×10^{-10} s. The thickness of the emitting surface layer d, i.e., the penetration depth at which the surface film induced activation energy ΔE decreased to $1/e$ (37%) is $\leq 1.9 \times 10^{-4}$ m [4]. It is concluded from the obtained values that icelike clathrate structures are induced by the surface film in a water layer of underneath the surface that is schematically illustrated in Fig. 3.

At first glance the obtained value appears to be surprisingly high. However, an extensive evaluation of the literature showed an evidence of long-range effects within interfacial

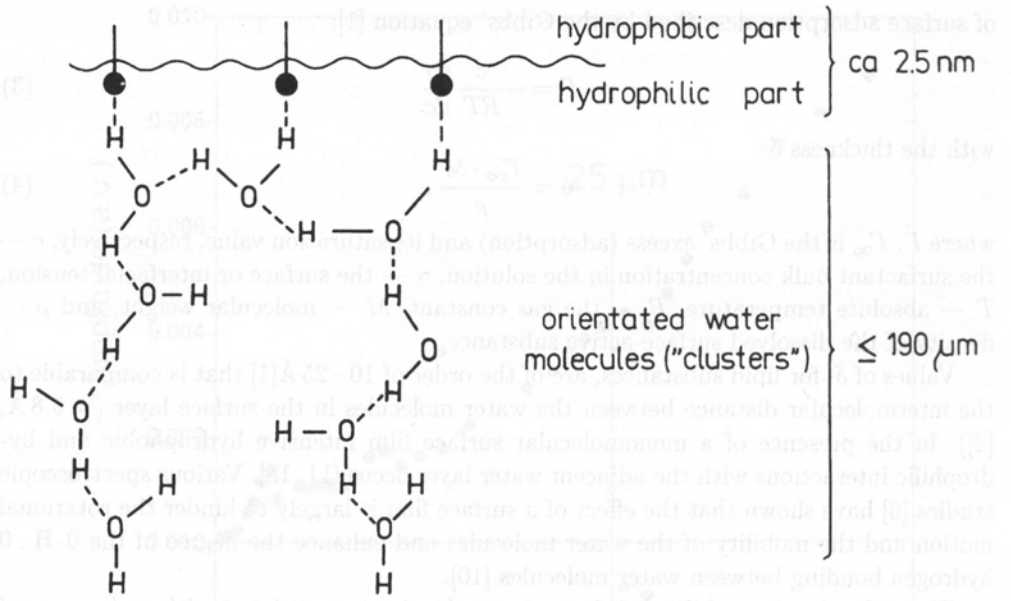

Fig. 3. Interaction of the film-forming molecules of a surfactant with the water molecules in the subsurface region [7].

water layers at the boundary water organic substance (as summarized in Tab. 1 of [7]). The obtained values are as follows: 25 – 200 μm (fatty acids), 2.2 – 190 μm (long-chain alcohols), 0.1 – 19 μm (polymeric macromolecules) and originate from a variety of different measurements and methods.

Note, that "classical" theories include penetration depths of only 10^{-9} m due to direct interactions between the hydrophilic group of the surface-active compound and adjacent water molecules by forming "shells" of structured water [6, 18]. The results cited above however, give experimental evidence for the penetration depth, which are 10^2 – 10^5 times larger.

From a thermodynamic point of view, the surface activation energy ΔE ought to be substituted by the term "free activation enthalpy" ΔG. In the upper water layer, which is influenced by the surface film, the activation enthalpy ΔH is connected with the free activation enthalpy ΔG by the Gibbs–Helmholtz equation [7].

$$\Delta G = \Delta H - T\Delta S, \tag{7}$$

where ΔS is the entropy change in the surface layer due to the surface film, ΔG can be expressed by using relaxation frequencies f_o and f_s corresponding to the mentioned relaxation times τ_o and τ_s measured for clean and film-covered water surfaces, respectively in the following form [7]:

$$\Delta G = kT \ln(f_o/f_s). \tag{8}$$

The enthalpy change per mole is, $\Delta G = 2.32\,RT = 5.53\,\mathrm{kJ/mol}$.

It can be deduced that clathrate-type arrangements of the water molecules are formed, which implies changes of the specific volume. Therefore, in the presence of

surface film the energy term associated with volume changes has to be added and we thus obtain the activation enthalpy ΔH.

Since different arrangements of molecules must be concerned with the entropy, the hysteresis of the compression/dilatation surface film isotherms is presumably correlated with the change of entropy ΔS of the interfacial system. Consequently, the well-known negative entropy effect — ΔS, of a regular monomolecular surface film on the adjacent water layer was observed by several authors [10, 11, 18], which reflects the formation of the organized water molecules and a certain loss of the system degrees of freedom.

Values of ΔS, obtained for natural marine films from surface isotherm hysteresis measurements, are ranging from -36 to $-133\,\mathrm{J/mol\,K}$ [13].

As a consequence, the thermodynamic parameters (specific heat, thermal conductivity) exhibit a step change in the air/liquid interfacial region. Thermal properties affect to a great extent the photoacoustic effect used to the layered air/water system sensing.

3.2. Organized surfactant structures in water-oil-surfactant systems

Moreover, amplitude and phase dependences of the photoacoustic signal clearly demonstrate rather rapid changes at a certain depth ($h \sim 9 - 13\,\mu\mathrm{m}$) underneath the oil phase surface. As mentioned above, that fact could result from the formation of 3-dimensional molecular structures at that oil layer having different thermo-mechanic properties than the surrounding oil.

Surface-active substances (surfactants) occurring in the oil phase at the critical micellar concentration (CMC) and appropriate temperature (so-called Krafft point) form aggregates or micelles [8, 15]. In such a state of the surfactant solution many physico-chemical parameters (surface tension, density, electric and thermal conductivity etc.) demonstrate rapid changes arround CMC [1]. For the same homologous series of surface active substances, CMC decreases with increasing the hydrocarbon chain length as well as with the addition of electrolytes (for ionic surfactants). At first, an increase in the surfactant concentration (above CMC) leads to the creation of spherical then rod-like, and finally lamellar micelles. These molecular structures possess an apparent anisotropy with a tendency for a long-range order similar to found in liquid crystals.

In apolar (oil) solvents a degree of aggregation in the micelle (e.q. a number of molecules therein) is much lower than in the polar (aqueous) surfactant solutions [8, 15].

For a particular water-oil-surfactant system, the phase diagrams determining concentration ranges of the compounds corresponding to the presence of the particular kind of micelles are created [8]. It must be pointed out that in the case of our particular oil-water-surfactant system we are concerned with very low concentrations of surfactants and oil fractions in water. Moveover, natural systems are composed of a mixture of different surface-active compounds of differentiated surface activities which likely form various mixed micelles. As a result, micellar structures to be found in the studied system may differ in their structure and thermodynamics if compared to these predicted in an idealised 3-compound surfactant solution. An exemplary phase diagram for a 3-compound surfactant system is reproduced in Fig. 4 [5].

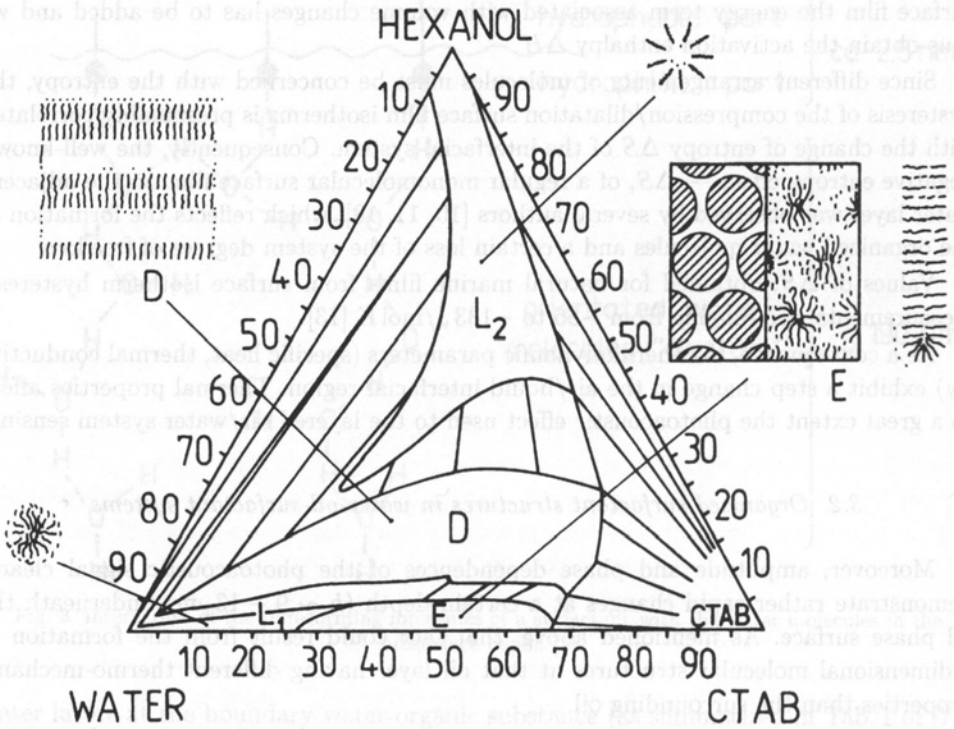

Fig. 4. Phase diagram of the 3-compound system (hexanol-water-CTAB; CTAB — cationic surface-active substance [5]. The specified areas correspond to the presence of: spherical micelles (L_1), inverted micelles sorrounded with oil (L_2), rod-like micelles (E) and lamellar, liquid crystal-like micelles (D).

In such a system we are concerned with a micellar solubilization phenomenon understood as solubilization of insoluble substances in the solution of surface-active substances (above CMC) (for instance, water in oil in our experiment). This effect takes place above CMC, and the mass of the dissolved substance increases proportionally to the concentration of micelles. In oil solvents (apolar media), the inverted micelles are formed with head groups of the surfactant in contact with dissolved water molecules occupying an interior of the micelle whereas the surrounding oil remains in contact with the hydrocarbon chains of the surfactant (as shown schematically in Fig. 5) [5, 8].

In our experiment the small dimensions of the photoacoustic cell lead through the spreading effect on the walls, to the particular shape of the layered oil-water interfaces in the form of a concave meniscus. The additional surface pressure resulted from the surface curvature apparently promotes a horizontal orientation of micellar structures situated close to the air/oil interface. Such an orientation is followed by rod-like and lamellar (plate-like) micelles under the condition of no intensive convection and mixing motions. The place of the micelles residence (depth) beneath the air/oil interface results from the balance between the surface tension and gravity (related to the actual density of the micellar solution) forces.

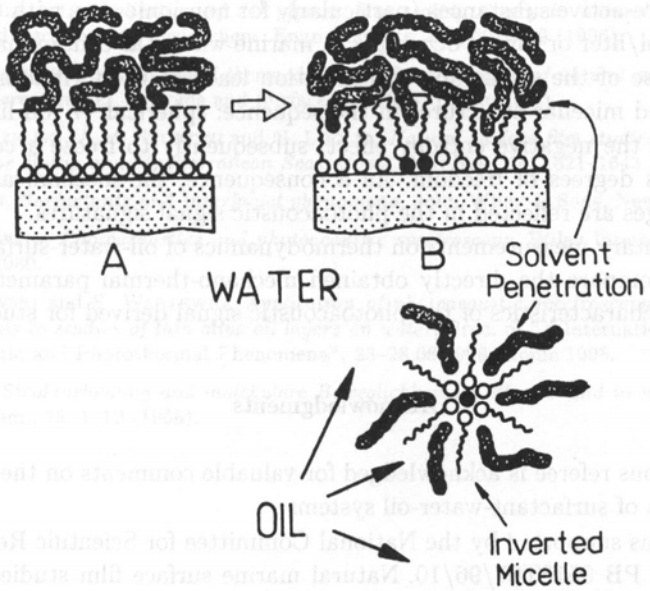

Fig. 5. Organized structures of a surfactant at an oil/water interface (A), and in a bulk oil phase (B). A general picture of micellar solubilization of water in inverted micelles formed in oil.

More compact liquid crystal-like micellar phases have mechano-thermal properties significantly different than the surrounding oil which can be reflected in the photoacoustic signal signatures noticed at the particular layer depth.

Moreover, it has been shown that the acoustic absorption measurements clearly reveal the several structural transitions occurring in the system (see Fig. 2 in [3]).

4. Conclusions

1. Ealier studies on the structure of marine organic films performed in the Baltic and Mediterranean Seas pointed to the complex vertically layered structure of a surfactant mixture consisting of several compounds differentiated in surface activity, solubility and physico-chemical structure [12–14]. Photoacoustic investigations were carried out on the physico-chemical model material similar to found in nature and demonstrated that photoacoustic spectroscopy is useful in detection of their formation.

2. Amplitude and phase changes of the photoacoustic signal attributed to a long-range ($d \leq 190\,\mu m$) organization phenomenon of water molecules in the subsurface region for film-covered surfaces orginate from the thermo-mechanical parameter (mainly in compressibility and specific heat) variations of the formed micellar structures.

Such a local properties variability can be explained in the framework of classical thermodynamics of thin layers.

3. Formation of micellar structures in surfactant solutions at concentrations C > CMC and appropriate temperature (Krafft point) is a common phenomenon observed

for several surface-active substances (particularly for non-ionic ones with CMC very low $10^{-8} \div 10^{-12}$ mol/liter or lower) occurring in marine waters as contaminants [9].

4. An increase of the surfactant concentration leads to the formation of more and more complicated micellar structures in the sequence: spherical → rod-like → lamellar micelles, and to the negative entropy effect, subsequently to freeze a certain number of the molecules degrees of freedom. As a consequence, the mechanical and thermal parameter changes are reflected in the photoacoustic signal signatures.

5. Supplementary measurements on thermodynamics of oil-water-surfactant systems make possible compare the directly obtained mechano-thermal parameters of layered structures with characteristics of the photoacoustic signal derived for studied layers.

Acknowledgments

An amonymous referee is acknowledged for valuable comments on the structure and thermodynamics of surfactant-water-oil systems.

The study was supported by the National Committee for Scientific Research (KBN) under the grant PB 0518T07/96/10. Natural marine surface film studies were carried out in the framework of scientific activity of the University of Gdańsk (supported from DS/5200-4-0024-8).

References

[1] A.W. ADAMSON, *Physical chemistry of surfaces*, Wiley, New York 1982.

[2] W. ALPERS, H.-J. BLUME, W.D. GARRETT and H. HÜHNERFUSS, *The effect of monomolecular surface films on the microwave brightness temperature of the sea surface*, Int. J. Remote Sens., **3**, 457–463 (1982).

[3] S. BALLARO, F. MALLAMACE and F. WANDERLINGH, *Ultrasonic attenuation in microemulsions and structural transitions*, Phys. Letters, **70A**, 497–499 (1979).

[4] G.P. DE LOOR, [in:] Remote Sensing for Environmental Studies, E. SHADA [Ed.], Springer, Berlin 1976.

[5] P. EKWALL, *A phase diagram of a water-surfactant-oil system*, Adv. Liquid Cryst., **1**, 1–12 (1975).

[6] F. FRANKS, *Water — A comprehensive treatise*, Vol. 4, Plenum, New York 1975.

[7] H. HÜHNERFUSS and W. ALPERS, *Molecular aspects of the system water/monomolecular surface film and the occurrence of a new anomalous dispersion regime at* 1.43 GHz, J. Phys. Chem., **87**, 5251–5258 (1983).

[8] B. LINDMAN [Ed.], *Micelles* (*Topics in current chemistry*), Vol. 87, Springer-Verlag, New York 1980.

[9] P.S. LISS, *Chemistry of the sea surface microlayer*, [in:] Chemical Oceanography, Vol. 2, J.P. RILEY and G. SKIRROW [Eds.], Academic Press, New York 1975.

[10] G. NEMETHY, *Hydrophobe Wechselwirkungen*, Angewandte Chemie, **79**, 260–271 (1967).

[11] G. NEMETHY and H.A. SCHERAGA, *The structure of water and hydrophobic bonding in proteins. III. The thermodynamic properties of hydrophobic bonds in proteins*, J. Phys. Chem., **66**, 1773–1789 (1962).

[12] S.J. POGORZELSKI, *Application of 2D plymer film scaling theory to natural sea surface films*, Colloids and Surfaces A: Physicochem. Engn. Aspects, **114**, 297–309 (1996).

[13] S.J. POGORZELSKI, *Structural and thermodynamic characteristics of natural marine films derived from force–area studies*, Colloids and Surfaces A (1998) (submitted).

[14] S.J. POGORZELSKI, A.M. STORTINI and G. LOGLIO, *Natural surface film studies in shallow coastal waters of the Baltic and Mediterranean Seas*, Cont. Shelf Res., **14**, 1621–1643 (1994).

[15] M.J. ROSEN, *Surfactants and interfacial phenomena*, John Wiley & Sons, New York 1978.

[16] A. ROSENCWAIG, *Photoacoustics and photoacoustic spectroscopy*, Wiley Interscience Publication, New York 1980.

[17] J. SZURKOWSKI and S. WARTEWIG, *Application of photoacoustic spectroscopy in visible and infrared regions to studies of thin olive oil layers on water*, Proc. of "X International Conference on Photoacoustic and Photothermal Phenomena", 23–28.08.1998, Rome 1998.

[18] E. WICKE, *Strukturbildung und molekulare Beweglichkeit im Wasser und in waßrigen Losungen*, Angew. Chem., **78**, 1–19 (1966).

ARCHIVES OF ACOUSTICS
24, 3, 331–364 (1999)

ULTRASONIC TRANSDUCER FOR THE RECEPTION OF ACOUSTIC EMISSION SIGNALS OF THE TEMPOROMANDIBULAR JOINT

R. SALAMON, W. LIS

Department of Acoustics
Technical University of Gdańsk
(80-052 Gdańsk, ul. G. Narutowicza 11/12, Poland)
e-mail: wall@eti.pg.gda.pl

J. ZIENKIEWICZ

Department and Clinic of Maxillofacial Surgery
Medical Academy in Gdańsk
(ul. Dębinki 7, Poland)

Auscultation and analysis of acoustic signals emitted by the human body are widely used in medical diagnosing. Acoustic signals are also emitted by joints, including the temporomandibular joint, which is the subject of this paper. A system was developed to receive, record, process and display the signals emitted by this particular joint. The article presents an essential fragment of the system, namely a special ultrasonic transducer designed to receive acoustic signals emitted by the temporomandibular joint. At first, the particular requirements were established in the area of the parameters and functions of the transducer. Following that, a technological solution was proposed. Next, a model of the transducer was analysed using the difference equation method with continuous time. The solution of these equations is the pulse response of the transducer and in the frequency domain, it is the shift function. These functions were used for an in-depth analysis of the effects of the transducer's construction on its parameters and values. Based on these findings, a methodology of the design of the transducer was developed. The transducer was designed and built according to the methodology. It was subsequently studied in detail. The results of the study have confirmed that the method of the analysis and the design were correct. Finally, the article presents some examples of real signals of acoustic emission of the temporomandibular joint as they were received by the ultrasonic transducer built in the course of the work.

1. Introduction

As we know, the human system is a source of numerous acoustic signals among which the speech signal is the most important and best-researched one. These signals are generated by the movements of muscles and joints and by the flow of blood and air. Since long ago auscultation of the signals made by the human body has been one of

medicine's basic methods of diagnosing. Usually a diagnosis is made based on a subjective assessment of the acoustic signal with the credibility of the diagnosis largely depending on the experience and predisposition of the doctor. This method of using acoustic signals proves successful in the diagnosis of lungs and heart diseases but is of little use in the diagnosis of muscles and joints. Acoustic signals that are emitted by muscles and joints usually feature an uncomplicated course and are not intense enough for an auscultation with a phonendoscope to be efficient. Additionally, the phonendoscope method does not allow for a signal recording and further analysis, which consequently makes the diagnosis' objectivity impossible.

One of the joints that deserves special attention is the temporomandibular joint which when diseased causes severe impairment of man's important functions such as speaking, eating and facial expression. The acoustic emission evoked by the movement of this joint, can be easily observed especially by the person setting the mandible in motion. Signals generated by the joint can also be heard using a phonendoscope. This was observed and used in the studies of the occlusion by D. WATT already in the sixties, [20]. First attempts to record the signals emitted by the temporomandibular joint were made in the seventies by, among others, YOWELOW [22] and J. and Z. KRASZEWSCY [9–10]. They would use a microphone to receive acoustic signals and a tape recorder or an electrocardiograph to record them. In the following years the technique of signal recording was improved as were the methods of processing these signals, [1–4, 6, 7, 11, 12, 16, 21]. A general and important result of these and later studies is the estimation of the width of the spectrum of acoustic emission signals. It matches the band of audiofrequencies. When, however, the frequency is more than several kilohertz the spectrum level quickly drops and reaches the level of noise. The least attention was given to the electroacoustic transducer even though its parameters largely determine the quality of the whole diagnostic apparatus. The authors are unaware of any reports in the literature on the optimisation of the construction of transducers in terms of adjusting their parameters to the specific requirements of reception of acoustic signals emitted by the temporomandibular joint. The article presents the results of a theoretical analysis, the construction and results of studies on a special transducer built to record and process acoustic emission signals made by the temporomandibular joint.

2. Mathematical model of the transducer receiving acoustic emission signals made by the temporomandibular joint

Studies on acoustic emission of the temporomandibular joint made so far used various types of microphones or less often accelerometers as electroacoustic transducers. Since the structure of all microphones is made to receive acoustic waves in the air, there is a concern whether the microphone is the appropriate device to measure waves propagated within the human body, especially those observed in the soft tissues surrounding the joint itself and the adjacent bone structure. The reason for this concern is that the acoustic properties of air and tissues are completely different which is expressed, among other things, by the big difference in acoustic impedance of both media. Acoustic impedance of

soft tissues is 5000 times greater than the impedance of air. Consequently, microphones operating in the air are activated by acoustic waves with high deflections and small pressures whereas when used in soft tissues they are activated by waves of high pressures and small deflections. Therefore, what we are dealing here with is a situation that is more typical for ultrasonic medical diagnosis or hydroacoustics rather than for audioacoustics. In both fields piezoceramic transducers are used commonly both for transmission and reception of acoustic waves.

To obtain better results than those produced by microphones one should turn to broadband ultrasonic transducers. Transducers like these are made as piezoceramic transducers with matching layers [15], as composite transducers [14] and accelerometers [17]. The first two types of transducers have a broad transmitted frequency band, however, it is located around a certain relatively high mid-band frequency. Therefore, it does not include very low audio-frequencies, which are included in the spectrum of acoustic emission signals of the temporomandibular joint. Accelerometers are used commonly in measurements of mechanical vibrations and their band covers the desired range of frequencies. However, the medium that the accelerometer is in contact with is usually a solid body whose characteristic acoustic impedance is greater than the soft tissue impedance, however, the disproportion in this case is not as big as between the tissues and air. Despite that, direct attempts to use standard accelerometers to receive acoustic emission signals coming from a patient's body are not without a doubt. The vibrations of the accelerometer are usually enforced by the vibrations of a big mass (e.g. the steel body of a machine or vehicle). Because of the significantly smaller mass and geometric dimensions of the accelerometer, it does not affect the distribution of vibrations of the measured object and the whole object-accelerometer system does not have to be seen in wave terms. This simplification is not justified when the accelerometer is in contact with a soft tissue where the acoustic wave propagates similarly to its propagation in liquids. Nonetheless, the very idea of using a piezoelectric transducer that constitutes an active element of the accelerometer and the use of a big mass to weight it on the back side seems to deserve a thorough analysis.

Following the above notions, a system was selected to act as a simplified theoretical model of an electroacoustic transducer. The system consisted of a piezoceramic transducer in the shape of an extended rectangular prism with a metal cylinder as its weighting placed on the back surface. It was assumed that the activation would originate from a plane acoustic wave, which propagates in a liquid inorganic medium and is perpendicular to the front surface of the piezoceramic transducer. The electrical signal is observed on electrodes attached to the front and back surface of the piezoceramic transducer. The piezoceramic transducer is polarised perpendicularly to the electrodes. Figure 1 shows a simplified form of the transducer.

At the output of the transducer the electrical signal in question can be determined using numerical methods (e.g. the finite elements methods) or analytical methods. Since the objective is not to analyse a singular case but to define some general relations, which could describe the operations of the transducer, in this case we decided to use the analytical method. The principles of this method were developed for designing broadband transducers with matching layers [15, 17–19].

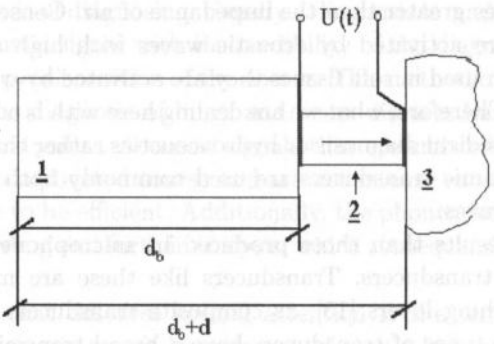

Fig. 1. A simplified form of the transducer receiving acoustic emission signals.

Let us assume that in a piezoceramic transducer and in the metal cylinder only the plane acoustic wave propagates perpendicularly to the electrodes. Let us also assume that mechanical and electrical loss in both elements is negligibly small and that the back surface of the metal cylinder is weighted with an unlimited medium — the air. Given such assumptions the vibrations of the whole system can be described using the velocities shown in Fig. 2.

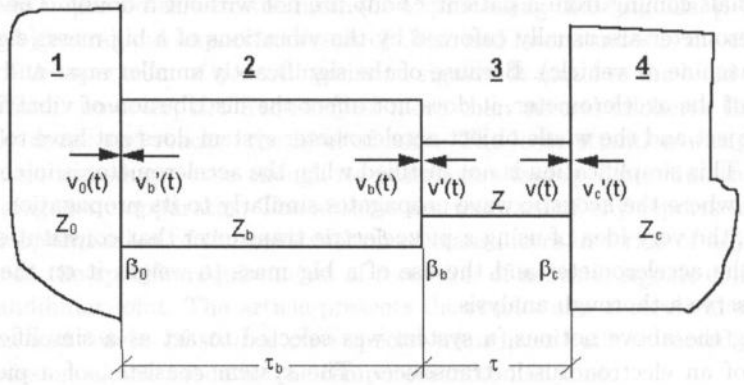

Fig. 2. Physical model of the transducer.

The symbols seen in the figure have the following physical interpretation:

• acoustic velocities $v_o(t)$, $v_b(t)$, $v_b'(t)$, $v(t)$, $v'(t)$ and $v_c'(t)$ are courses of component velocities of waves that are incident to the boundaries of the media,

• delays $\tau = d/c$ and $\tau_b = d_b/c_b$ are the duration of propagation of the longitudinal acoustic wave respectively between the electrodes of the piezoceramic plate and base of the metal cylinder (d — length of the piezorceramic transducer, c — velocity of the longitudinal wave in the piezoceramic transducer, d_b — length of the metal cylinder, c_b — velocity of the longitudinal wave in the metal cylinder),

• reflection coefficients β_0, β_c, and β_b, are mechanical coefficients of reflection on the boundaries of the respective media, defined for the forces ($\beta_0 = (Z_b - Z_0)/(Z_b + Z_0)$, $\beta_b = (Z - Z_b)/(Z + Z_b)$, $\beta_c = (Z_c - Z)/(Z_c + Z)$, where $Z_b = A_b\rho_b c_b$ is the mecha-

nical impedance of the base of the metal cylinder with surface A_b, density volume ρ_b and velocity of the longitudinal acoustic wave c_b, $Z_0 = A_b\rho_0 c_0$ which is the mechanical impedance of the medium on the left side of the cylinder's base, $Z = A\rho c$ is the mechanical impedance of the transducer and $Z_c = A_c\rho_c c_c$ is the mechanical impedance of tissues).

Our task is to determine the voltage $U(t)$ on open electrodes of the piezoceramic transducer as a function of acoustic velocity $v_c'(t)$ of a wave which is incident perpendicularly to the surface of the transducer from the direction of the tissues. If we assume that the shape of the transducer is close to that of a thin rod, voltage $U(t)$ can be described using the following relation, [5, 8]:

$$U(t) = Y_3^D g_{33} \int_0^t [V_b(t) - V_c(t)]\, dt, \tag{1}$$

where Y_3^D is the Young's modulus elasticity given a constant induction D, and g_{33} — a piezoelectric constant, and $V_b(t)$ and $V_c(t)$ the velocities of vibrations of the back and front surface of the piezoelectric transducer respectively.

The velocities of vibrations of the surfaces $V_c(t)$ and $V_b(t)$ are the sums of acoustic waves that are incident to, reflected from and going across the boundaries of the medium on the left or right side of the boundary. They can be easily determined using Fig. 2 and the functional diagram of the wave system in question as shown in Fig. 3.

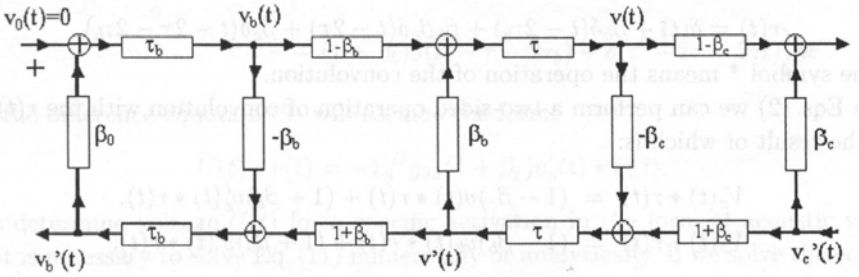

Fig. 3. Functional diagram of the transducer.

They are described with the following relations:

$$\begin{aligned} V_c(t) &= (1-\beta_c)v(t) + (1+\beta_c)v_c'(t), \\ V_b(t) &= (1-\beta_b)v_b(t) + (1+\beta_b)v'(t). \end{aligned} \tag{2}$$

As you can see, to calculate the velocity of vibrations of the transducer's surface it is necessary to know the velocity components $v(t)$, $v_b(t)$, $v'(t)$. These velocities can be determined using the below system of equations put together on the basis of the functional diagram from Fig. 3.

$$\begin{aligned} v_b(t) &= (1-\beta_0)v_o(t-\tau_b) + \beta_0 v_b'(t-\tau_b), \\ v_b'(t) &= (1+\beta_b)v'(t-\tau_b) - \beta_b v_b(t-\tau_b), \\ v(t) &= (1-\beta_b)v_b(t-\tau) + \beta_b v'(t-\tau), \\ v'(t) &= (1+\beta_c)v_c'(t-\tau) - \beta_c v(t-\tau). \end{aligned} \tag{3}$$

To solve this system of equations, first we need to notice that the characteristic acoustic impedance of the base of the metal cylinder is much bigger than the acoustic impedance of air. This makes the reflection coefficient β_0 practically equal to one. The equations (3) are then simplified to obtain the form of:

$$\begin{aligned} v_b(t) &= v_b'(t-\tau_b), \\ v_b'(t) &= (1+\beta_b)v'(t-\tau_b) - \beta_b v_b(t-\tau_b), \\ v(t) &= (1-\beta_b)v_b(t-\tau) + \beta_b v'(t-\tau), \\ v'(t) &= (1+\beta_c)v_c'(t-\tau) - \beta_c v(t-\tau). \end{aligned} \tag{4}$$

The above equations contain four unknown functions; they are $v_b(t)$, $v_b'(t)$, $v(t)$, $v'(t)$. Function $v_c'(t)$ is the activation that we know from the assumption. This means that this system of equations can be solved and each of the velocities that we are looking for can be determined as a function of activation. The solution to this untypical system of equations is given in the Appendix. Below we are presenting the result of the solution only:

$$\begin{aligned} v_b(t) * r(t) &= (1+\beta_b)(1+\beta_c)v_c'(t-\tau-2\tau_b), \\ v'(t) * r(t) &= (1+\beta_c)\left[v_c'(t-\tau) + \beta_b v_c'(t-\tau-2\tau_b)\right], \\ v(t) * r(t) &= (1+\beta_c)\left[v_c'(t-2\tau-2\tau_b) + \beta_b v_c'(t-2\tau)\right]. \end{aligned} \tag{5}$$

where

$$r(t) = \delta(t) + \beta_b\delta(t-2\tau_b) + \beta_b\beta_c\delta(t-2\tau) + \beta_c\delta(t-2\tau-2\tau_b), \tag{6}$$

and the symbol * means the operation of the convolution.

On Eqs. (2) we can perform a two-sided operation of convolution with the $r(t)$ function, the result of which is:

$$\begin{aligned} V_c(t) * r(t) &= (1-\beta_c)v(t) * r(t) + (1+\beta_c)v_c'(t) * r(t), \\ V_b(t) * r(t) &= (1-\beta_b)v_b(t) * r(t) + (1+\beta_b)v'(t) * r(t). \end{aligned} \tag{7}$$

On the right-hand side of Eqs. (7) there are convolutions of the velocities with the $r(t)$ function which we can see on the left-hand side of the equations, too (5). Therefore, we can make the appropriate substitutions as a result of which we get:

$$\begin{aligned} V_c(t) * r(t) &= (1+\beta_c)\left[v_c'(t-2\tau-2\tau_b) + \beta_b v_c'(t-2\tau)\right] + v_c'(t) + \beta_b v_c'(t-2\tau_b), \\ V_b(t) * r(t) &= (1+\beta_b)(1+\beta_c)\left[v_c'(t-\tau-2\tau_b) + v_c'(t-\tau)\right]. \end{aligned} \tag{8}$$

The equation we have been looking for which contains only activation $v_c'(t)$ and response in the form of voltage $U(t)$ is obtained by performing on Eq. (1) the operation of convolution with the $r(t)$ function and by substituting Eqs. (8). As a result, we get:

$$\begin{aligned} U(t) * r(t) = -Y_3^D g_{33}(1+\beta_c)v_c'(t) * \int_0^t \Big[&\delta(t') - (1+\beta_b)\delta(t'-\tau) + \beta_b\delta(t'-2\tau) \\ &+ \beta_b\delta(t'-2\tau_b) - (1+\beta_b)\delta(t'-\tau-2\tau_b) + \delta(t'-2\tau-2\tau_b)\Big]dt'. \end{aligned} \tag{9}$$

In this way the voltage in question $U(t)$ has been described using a *non-homogenous difference equation* with a continuous duration in which on the left-hand side is a convolution of voltage $U(t)$ with function $r(t)$, and on the right-hand side a convolution of activation $v_c'(t)$ with a function written down in the above equation as an integral. Equation (9) can be treated as a mathematical model of the transducer. It can be used to analyse it in the time domain and also — after the necessary transformations — to analyse it in the frequency domain.

3. Analysis in the time domain

Analysis in the time domain is usually used to determine the response of a linear system to specific activation we are investigating. This method is less frequently used to research the general properties of a system. To that end the analysis in the frequency domain gives more insight and is therefore more frequently used. Nonetheless from the theoretical standpoint both methods are equivalent and will be presented below.

To simplify the notation of the equations let us mark the integral expression in Eq. (9) as:

$$w(t) = \int_0^t \Big[\delta(t') - (1+\beta_b)\delta(t'-\tau) + \beta_b\delta(t'-2\tau) + \beta_b\delta(t'-2\tau_b) - (1+\beta_b)\delta(t'-\tau-2\tau_b) + \delta(t'-2\tau-2\tau_b)\Big]dt'. \tag{10}$$

Then the difference equation (9) will assume the form:

$$U(t) * r(t) = -Y_3^D g_{33}(1+\beta_c)v_c'(t) * w(t). \tag{11}$$

To determine voltage $U(t)$ for a specific activation in the form of acoustic velocity $v_c'(t)$ it is necessary to solve Eq. (11) numerically or analytically. If we solve the equation directly, then for each activation we have to repeat all calculations, which are not always simple. This inconvenience can be eliminated by using *pulse responses*. To that end, let us introduce the term of a *homogenous difference equation* of the considered system. It can be noted as:

$$k(t) * r(t) = \delta(t), \tag{12}$$

or in the full form as:

$$k(t) + \beta_b k(t-2\tau_b) + \beta_b\beta_c k(t-2\tau) + \beta_c k(t-2\tau-2\tau_b) = \delta(t), \tag{13}$$

where $\delta(t)$ is Dirac's function, and $k(t)$ — *pulse response of a homogenous equation.*

Now let us write the difference equation (11) as a convolution with pulse response $k(t)$:

$$U(t) * r(t) * k(t) = -Y_3^D g_{33}(1+\beta_c)v_c'(t) * w(t) * k(t). \tag{14}$$

Using Eq. (12), we get:

$$U(t) = -Y_3^D g_{33}(1+\beta_c)v_c'(t) * w(t) * k(t). \tag{15}$$

As you can see, voltage $U(t)$ can be calculated as a convolution of activation $v_c'(t)$ with pulse response $k(t)$ and function $w(t)$. The saving in the computation is that both pulse response $k(t)$ and function $w(t)$ are dependent solely on the parameters of the analysed system. Therefore, they can be computed once and then used multiple times to determine response $U(t)$ to random activation $v_c'(t)$.

Pulse response $k_u(t)$ of the analysed system according to the theory of linear systems is equal to the system's response to activation in the form of Dirac's pulse. That's why by adding $v_c'(t) = \delta(t)$ to Eq. (15) we get:

$$k_u(t) = -Y_3^D g_{33}(1 + \beta_c)w(t) * k(t) \tag{16}$$

and

$$U(t) = k_u(t) * v_c'(t). \tag{17}$$

The result of the transformations we have applied is the following procedure of determining the voltage on open electrodes of the sensor's piezoceramic plate:

- by solving the homogenous difference equation (12) we determine the $k(t)$ pulse response,
- we determine the $w(t)$ function from relation (10),
- from Eq. (16) we calculate pulse response $k_u(t)$,
- we calculate voltage $U(t)$ as a convolution of activation $v_c'(t)$ with pulse response $k_u(t)$ (Eq. (17)).

The only, slightly less frequent mathematical problem that is present in this computational method is the solution of the difference equation with a continuous time

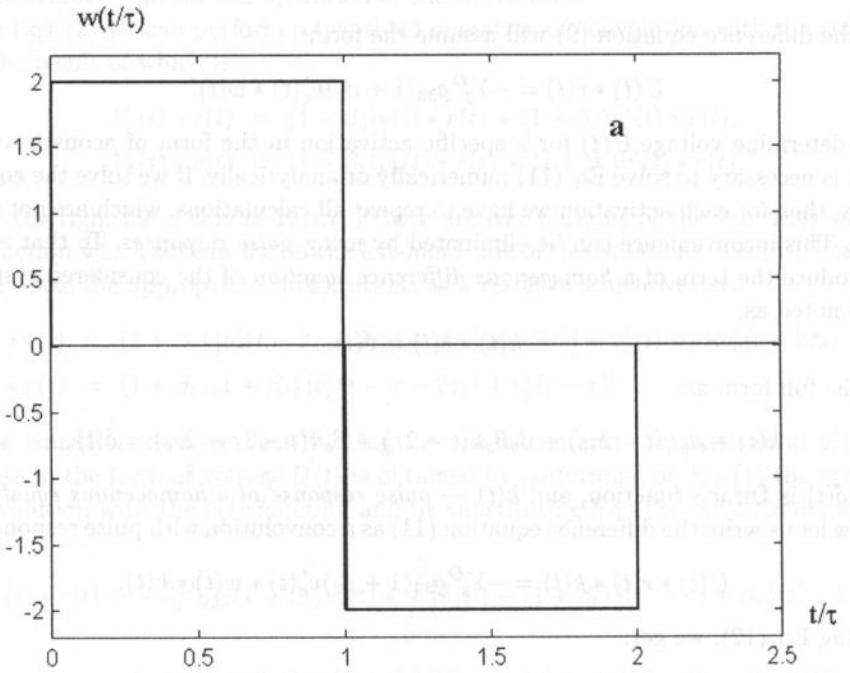

[FIG. 4 a]

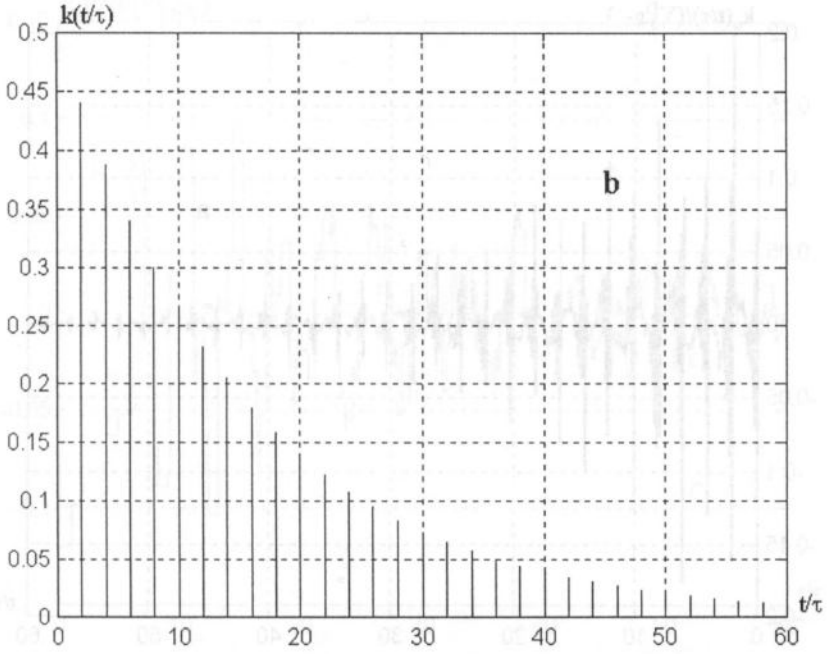

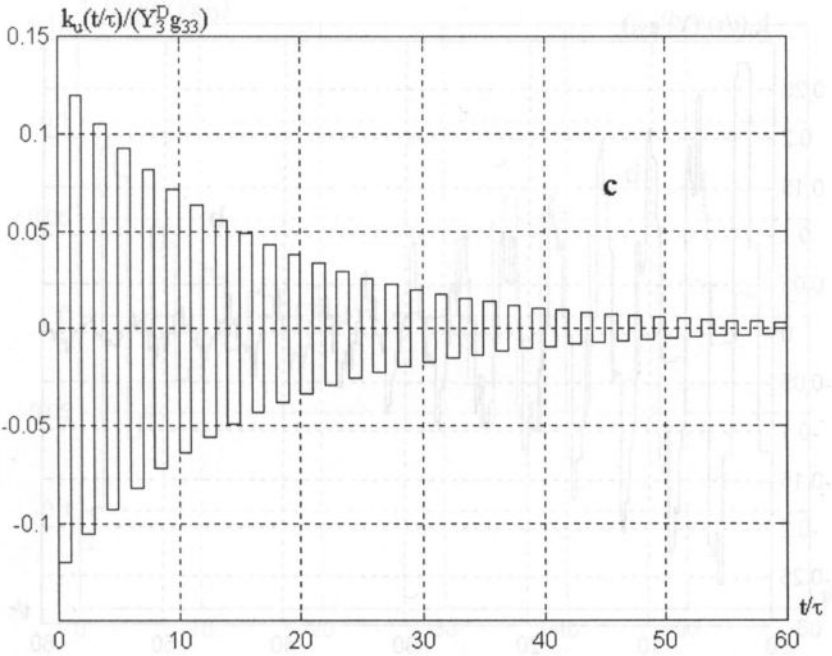

Fig. 4. The forming of the transducer's pulse response without the metal cylinder ($\beta_b = 1$, $\beta_c = -0.88$): a) function $w(t)$, b) auxiliary function $k(t)$, c) pulse response of the transducer.

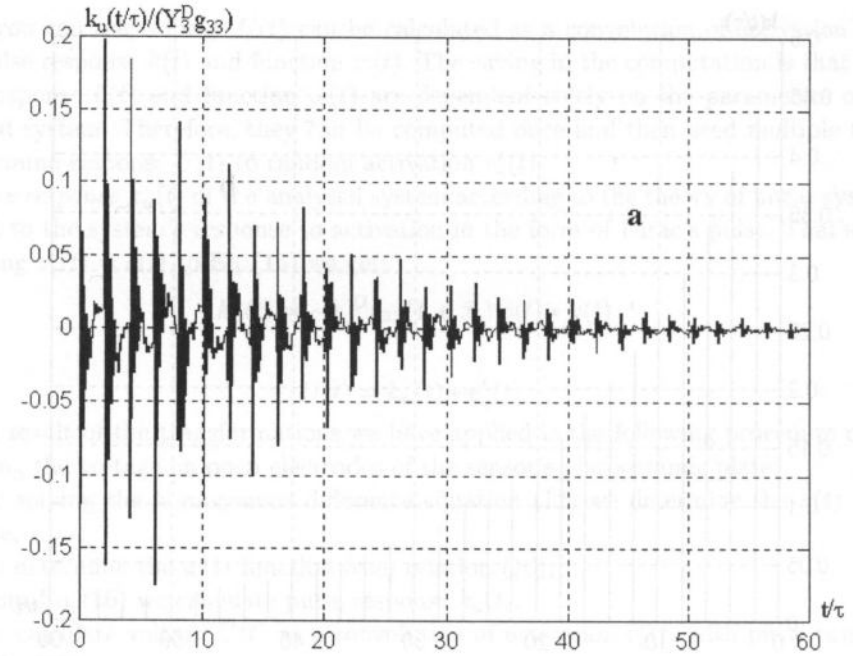
$k_u(t/\tau)/(Y_3^D g_{33})$
0.2
0.15
0.1
0.05
0
-0.05
-0.1
-0.15
-0.2
a
0
10
20
30
40
50
60
t/τ

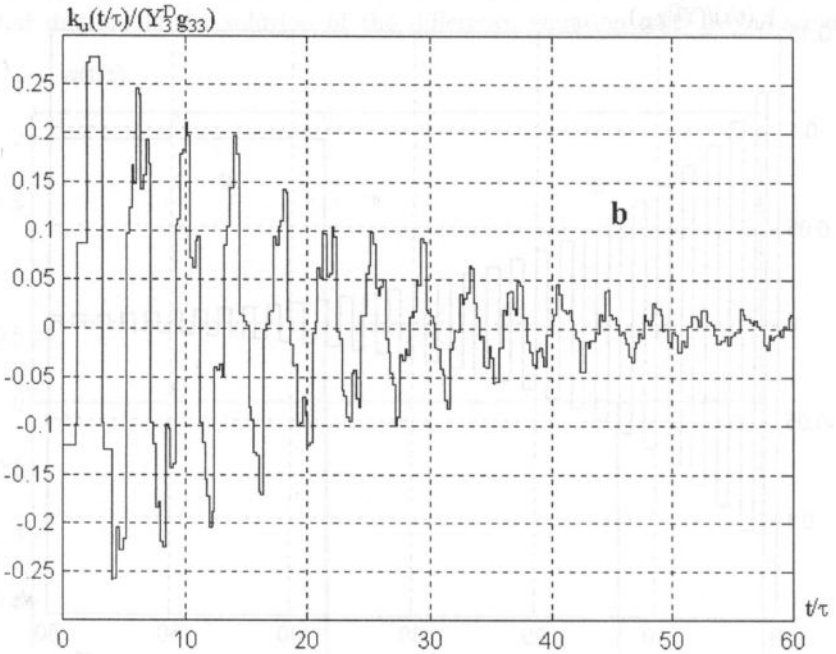
$k_u(t/\tau)/(Y_3^D g_{33})$
0.25
0.2
0.15
0.1
0.05
0
-0.05
-0.1
-0.15
-0.2
-0.25
b
0
10
20
30
40
50
60
t/τ

[FIG. 5 a, b]

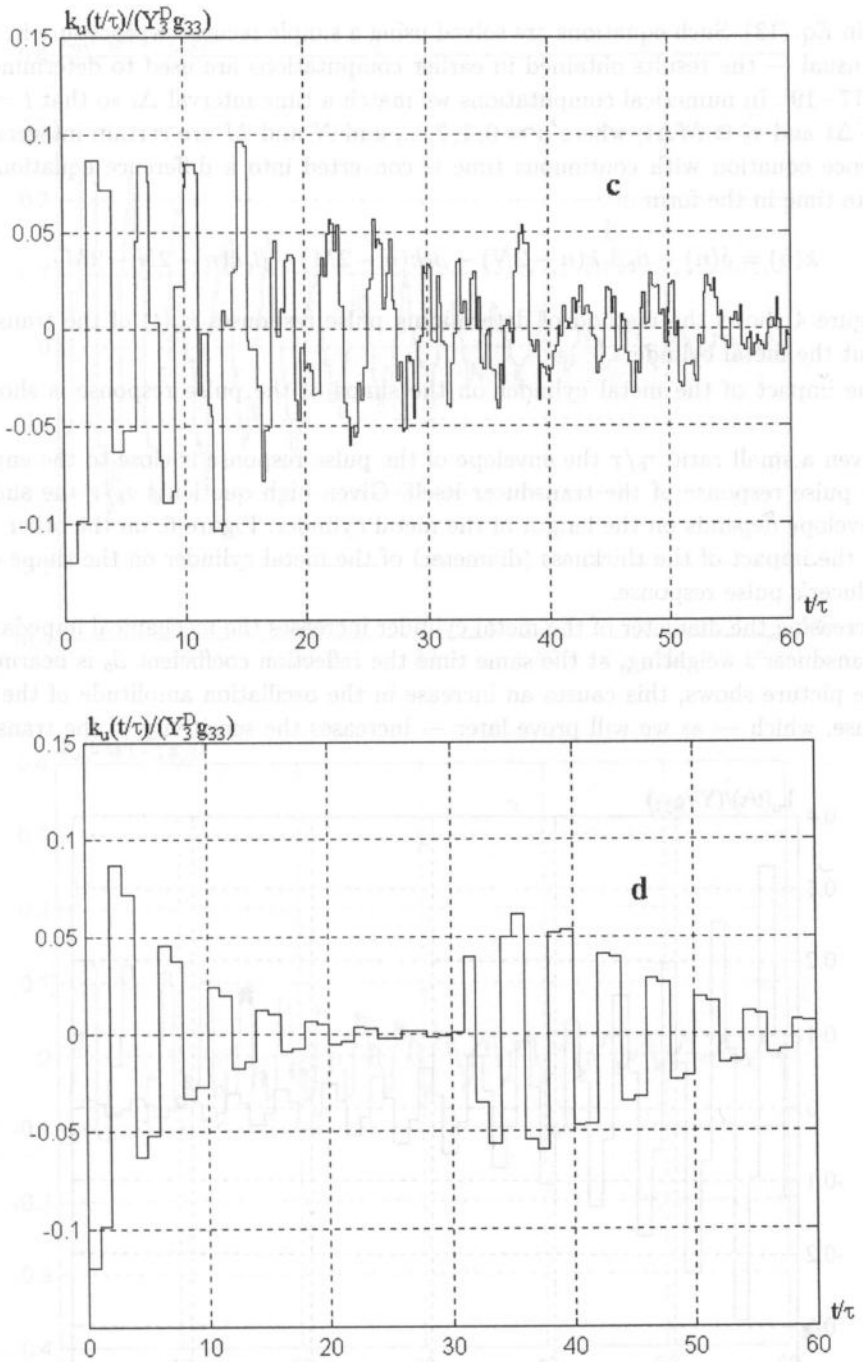

Fig. 5. The effects of the length of the metal cylinder on the pulse response of the transducer ($\beta_b = -0.823$, $\beta_c = -0.88$): a) $\tau_b/\tau = 0.05$, b) $\tau_b/\tau = 0.6$, c) $\tau_b/\tau = 2.6$, d) $\tau_b/\tau = 15$.

given in Eq. (13). Such equations are solved using a simple recurrent procedure in which — as usual — the results obtained in earlier computations are used to determine new ones [17–19]. In numerical computations we match a time interval Δt so that $t = n\Delta t$, $\tau \cong N\Delta t$ and $\tau_b \cong M\Delta t$, where $n = 0, 1, 2, ...$, and N and M are certain integers. The difference equation with continuous time is converted into a difference equation with discrete time in the form of:

$$k(n) = \delta(n) - \beta_b\beta_c k(n - 2N) - \beta_b k(n - 2M) - \beta_c k(n - 2N - 2M). \tag{18}$$

Figure 4 shows the method of determining pulse responses $k_u(t)$ of the transducer without the metal cylinder.

The impact of the metal cylinder on the shape of the pulse response is shown in Fig. 5.

Given a small ratio τ_b/τ the envelope of the pulse response is close to the envelope of the pulse response of the transducer itself. Given high quotients τ_b/τ the shape of the envelope depends on the length of the metal cylinder. Figure 6, on the other hand, shows the impact of the thickness (diameter) of the metal cylinder on the shape of the transducer's pulse response.

Increasing the diameter of the metal cylinder increases the mechanical impedance of the transducer's weighting, at the same time the reflection coefficient β_b is nearing -1. As the picture shows, this causes an increase in the oscillation amplitude of the pulse response, which — as we will prove later — increases the sensitivity of the transducer

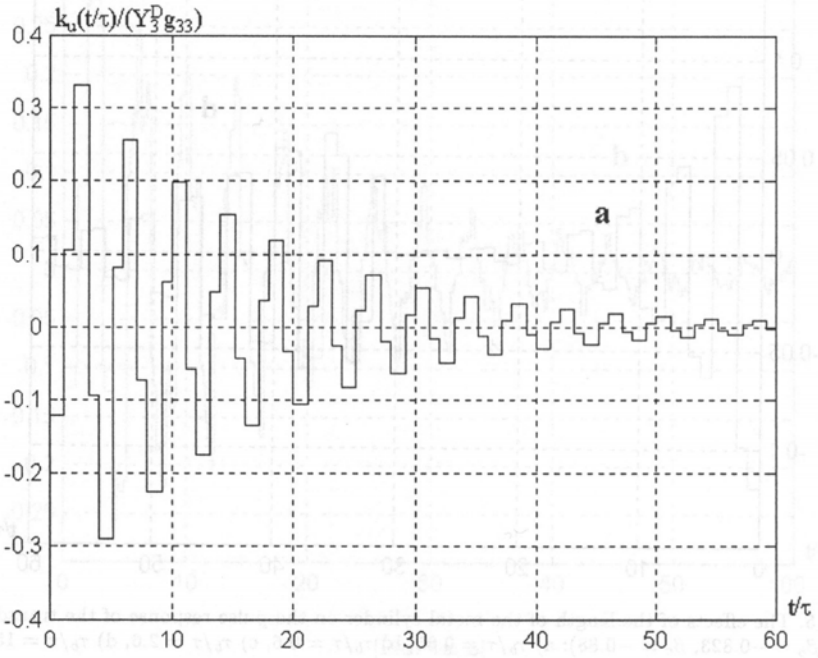

[FIG. 6 a]

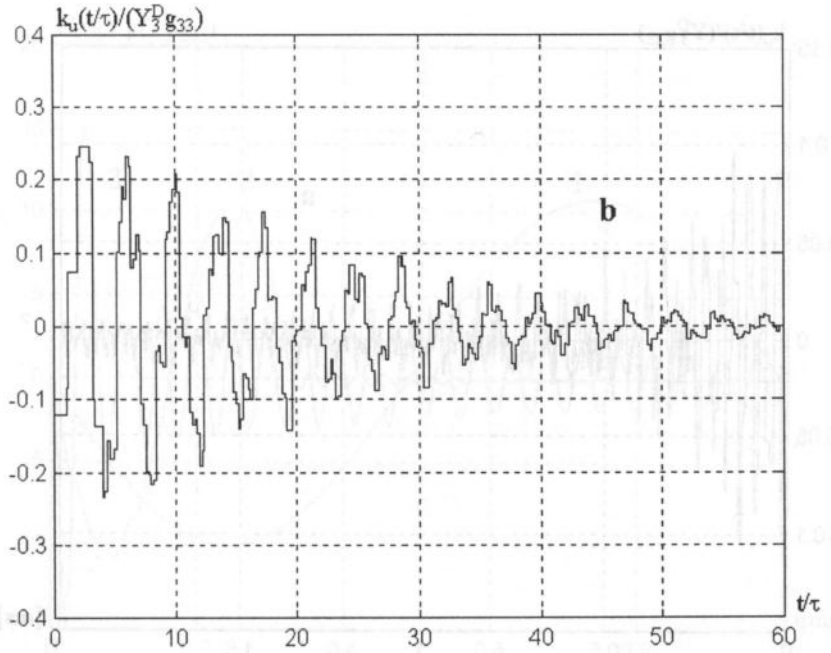

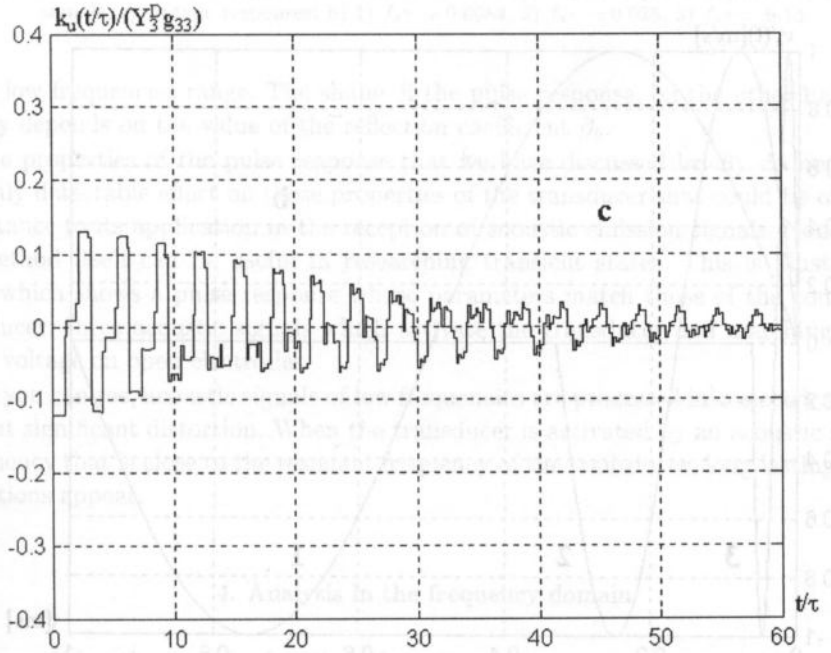

Fig. 6. The effects of the diameter of the metal cylinder on the pulse response of the transducer ($\tau_b/\tau = 0.6$, $\beta_c = -0.88$): a) $\beta_b = -1$, b) $\beta_b = -0.7$, c) $\beta_b = -0.1$.

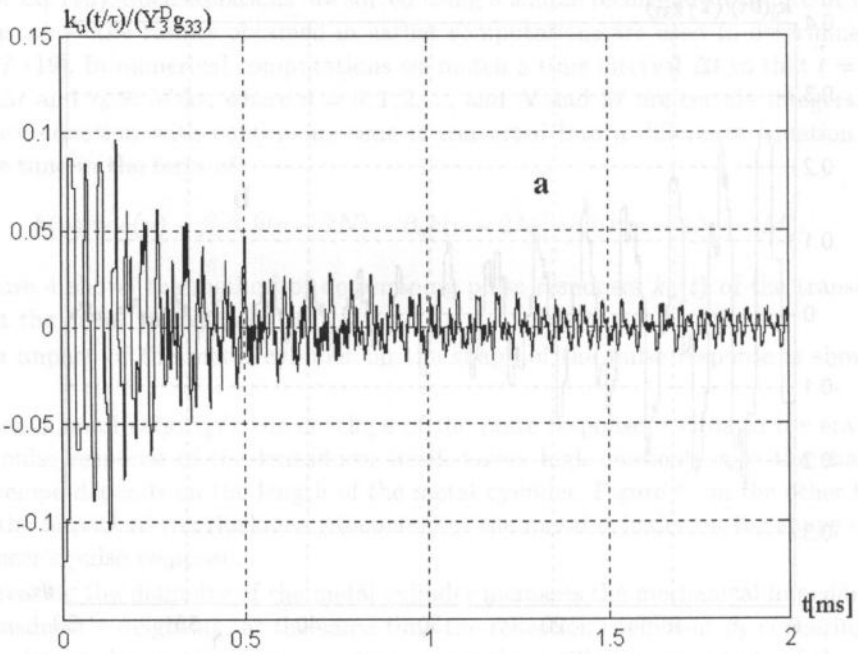
$k_a(t/\tau)/(Y_3^D g_{33})$
0.15
0.1
0.05
0
-0.05
-0.1
a
0
0.5
1
1.5
2
t[ms]

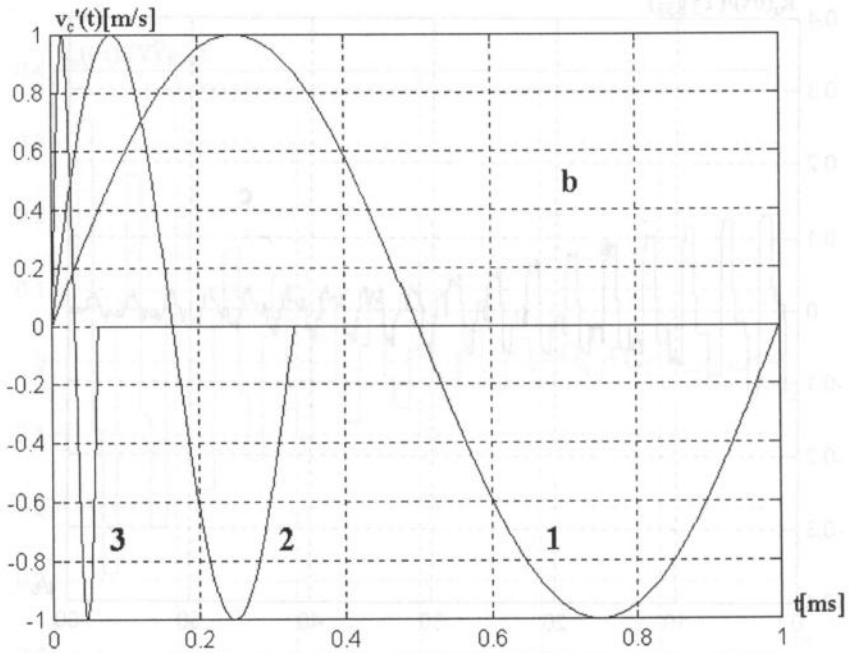
$v_c'(t)$[m/s]
1
0.8
0.6
0.4
0.2
0
-0.2
-0.4
-0.6
-0.8
-1
b
3
2
1
0
0.2
0.4
0.6
0.8
1
t[ms]

[FIG. 7 a, b]

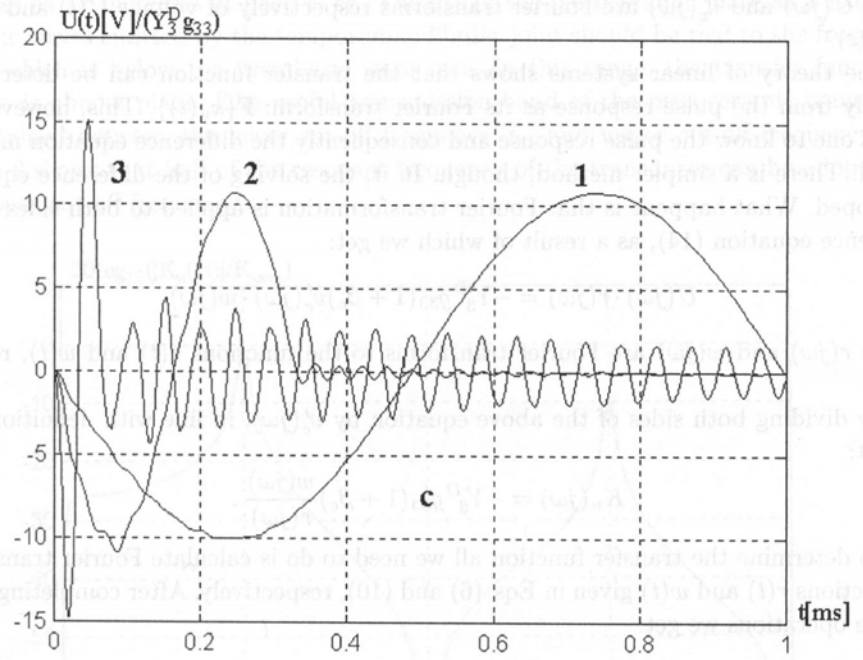

Fig. 7. Pulse responses of the designed transducer after computation: a) pulse response, b) activating signals, c) voltage responses: b) 1) $f_s\tau = 0.0083$, 2) $f_s\tau = 0.025$, 3) $f_s\tau = 0.13$.

in the low frequencies range. The shape of the pulse response, on the other hand, only slightly depends on the value of the reflection coefficient β_b.

The properties of the pulse response that we have discussed briefly do not exhibit an easily detectable effect on those properties of the transducer that could be of critical importance to its application in the reception of acoustic emission signals. Nonetheless, the method itself can be useful in researching transient states. This is illustrated in Fig. 7 which shows a pulse response whose parameters match those of the constructed transducer, three acoustic signals which activate the transducer and matching courses of the voltage on open electrodes.

As you can see, acoustic signals of low frequencies are processed into electrical signals without significant distortion. When the transducer is activated by an acoustic signal of a frequency that is close to the resonant frequency of the transducer, long lasting voltage oscillations appear.

4. Analysis in the frequency domain

Let us define the transfer function of the transducer as:

$$K_u(j\omega) = \frac{U(j\omega)}{v_c'(j\omega)}, \tag{19}$$

where $U(j\omega)$ and $v_c'(j\omega)$ are Fourier transforms respectively of voltage $U(t)$ and velocity $v_c'(t)$.

The theory of linear systems shows that the transfer function can be determined directly from the pulse response as its Fourier transform: $\mathbf{F}\{k_u(t)\}$. This, however, requires one to know the pulse response and consequently the difference equation must be solved. There is a simpler method, though. In it, the solving of the difference equation is skipped. What happens is that Fourier transformation is applied to both sides of the difference equation (14), as a result of which we get:

$$U(j\omega)\cdot r(j\omega) = -Y_3^D g_{33}(1+\beta_c)v_c'(j\omega)\cdot w(j\omega), \tag{20}$$

where $r(j\omega)$ and $w(j\omega)$ are Fourier transforms to the functions $r(t)$ and $w(t)$, respectively.

By dividing both sides of the above equation by $v_c'(j\omega)$, in line with definition (19) we get:

$$K_u(j\omega) = -Y_3^D g_{33}(1+\beta_c)\frac{w(j\omega)}{r(j\omega)}. \tag{21}$$

To determine the transfer function all we need to do is calculate Fourier transforms of functions $r(t)$ and $w(t)$ given in Eqs. (6) and (10), respectively. After completing these simple operations we get:

$$K_u(j\omega) = j\frac{Y_3^D g_{33}(1+\beta_c)}{\omega} \cdot \frac{1-(1+\beta_b)e^{-j\omega\tau}+\beta_b e^{-j2\omega\tau}+\left[\beta_b-(1+\beta_b)e^{-j\omega t}+e^{-j2\omega\tau}\right]e^{-j2\omega\tau_b}}{1+\beta_b e^{-j2\omega\tau_b}+\beta_b\beta_c e^{-j2\omega\tau}+\beta_c e^{-j2\omega(\tau+\tau_b)}}. \tag{22}$$

Using the above formula, we can study the effects of the particular parameters of the transducer on the course of its transfer function. We will begin this study by determining the transfer function of the piezoceramic transducer weighted with air from the backside. It will be a good model for defining the effects of the parameters of the metal cylinder on the performance of the whole transducer. To that end we add to Eq. (22) $\beta_b = 1$ and get:

$$K_u(i\omega) = j\frac{Y_3^D g_{33}(1+\beta_c)}{\omega}\cdot\frac{1-2e^{-j\omega\tau}+e^{-j2\omega\tau}}{1+\beta_c e^{-j2\omega\tau}}. \tag{23}$$

Figure 8 shows a module of the transfer function described with formula (23). On the X-axis the scale $f\tau$ was assumed, where $f = \omega/2\pi$. The same scale was maintained for the other pictures which makes interpretation easier. To obtain the real scale of frequencies, the numbers found on the adopted scale should be divided by the time of propagation of the longitudinal, plane acoustic wave τ along the thickness of the piezoceramic element. The adopted value of the reflection coefficient $\beta_c = -0.9$ matches approximately the real conditions that are present on the boundary between the soft tissue and an average ceramics PZT.

The above transfer function shows resonance of thickness vibrations of the transducer that appear at $f\tau = 0.5$ and $f\tau = 1.5$. The resonance also appears periodically in higher frequencies with period $f\tau = 1$, while the values of the transfer function's module

decrease as $f\tau$ increases at pace $1/f\tau$. The use of the piezoceramic plate as a sensor of acoustic waves emitted by the temporomandibular joint should be tied to the frequency range which is below the first basic resonance. In this range, the transfer function's module is almost plane. The useful transmission band of the piezoceramic transducer is contained between the lower cut-off frequency f_m and upper cut-off frequency f_M. Figure 8 shows that half of the resonant frequency of the transducer can be adopted as the upper cut-off frequency.

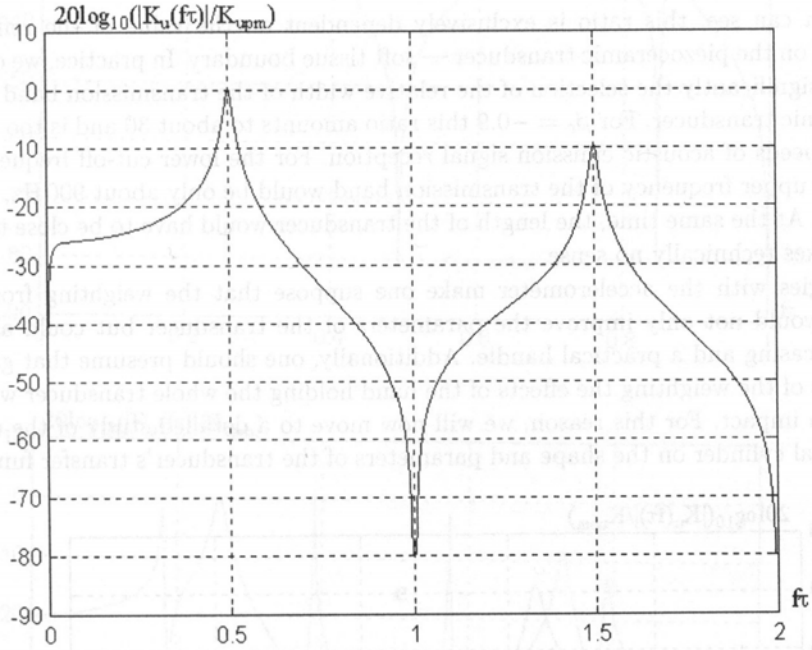

Fig. 8. Module of the shift function of the transducer without the metal cylinder: $\beta_b = 1$, $\tau_b/\tau = 0$, $K_{upm} = |K_u(0.5)|$, $\beta_c = -0.88$.

That's why, it is equal to approximately:

$$f_M = \frac{1}{4\tau} = \frac{c}{4d}. \tag{24}$$

The lower cut-off frequency can be determined from the transfer function (23) by using the approximation $\exp(-j\omega\tau) \cong 1 - j\omega\tau$, authorised for low frequencies. In this frequency range, the transfer function's module adopts the following form:

$$|K_u(j\omega)| = Y_3^D g_{33}\tau \cdot \frac{\omega\tau}{\sqrt{1+(\omega\tau)^2 A^2}}, \tag{25}$$

where

$$A = \frac{2\beta_c}{1+\beta_c}. \tag{26}$$

The lower cut-off frequency is determined from the condition $\omega_m \tau A = 2\pi f_m \tau A = 1$, and so:

$$f_m = \frac{1}{4\pi\tau} \frac{1+\beta_c}{\beta_c} = \frac{c}{4\pi d} \frac{1+\beta_c}{\beta_c}. \tag{27}$$

Equations (24) and (27) show that the relation between upper and lower cut-off frequency is approximately equal to:

$$\frac{f_M}{f_m} = \frac{\pi\beta_c}{1+\beta_c}. \tag{28}$$

As you can see, this ratio is exclusively dependent on the value of the reflection coefficient on the piezoceramic transducer — soft tissue boundary. In practice, we cannot influence significantly the selection of the relative width of the transmission band of the piezoceramic transducer. For $\beta_c = -0.9$ this ratio amounts to about 30 and is too low to meet the needs of acoustic emission signal reception. For the lower cut-off frequency of 30 Hz, the upper frequency of the transmission band would be only about 900 Hz, which is too low. At the same time, the length of the transducer would have to be close to 1 m, which makes technically no sense.

Analogies with the accelerometer make one suppose that the weighting from the backside would not only improve the parameters of the transducer but could also be used as a casing and a practical handle. Additionally, one should presume that given a large mass of the weighting the effects of the hand holding the whole transducer will not have much impact. For this reason, we will now move to a detailed study of the effects of the metal cylinder on the shape and parameters of the transducer's transfer function.

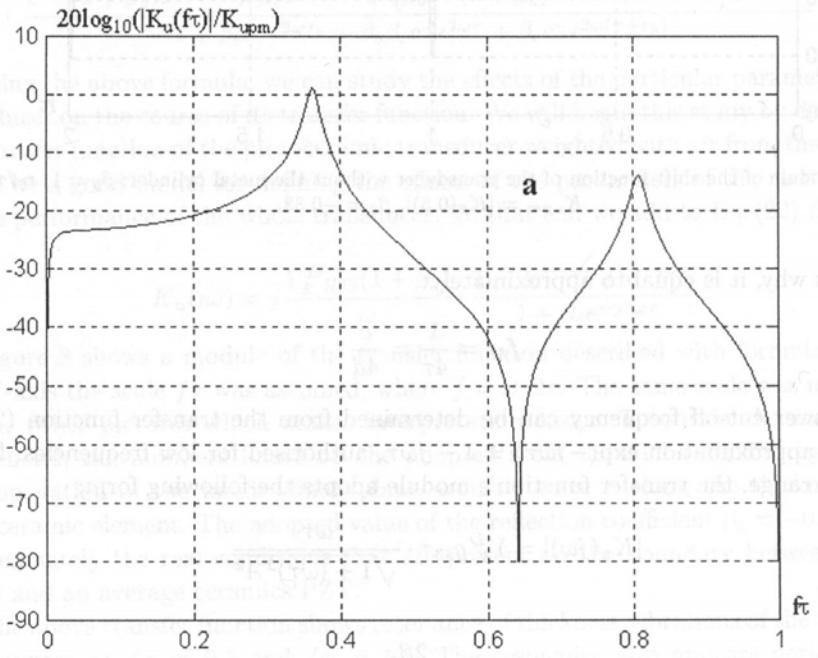

[FIG. 9 a]

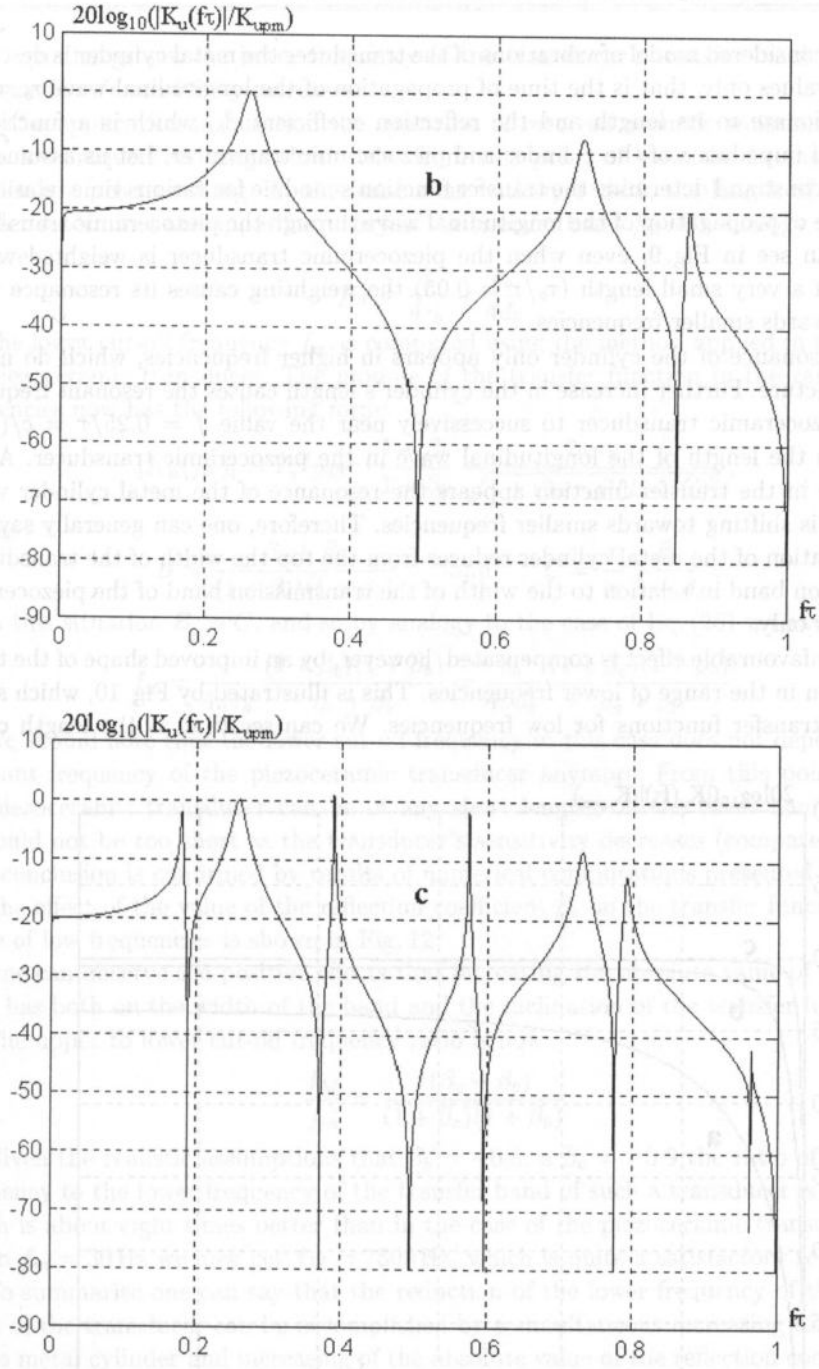

Fig. 9. The effects of the thickness of the cylinder on the module of the transducer's shift function ($\beta_b = -0.823$, $\beta_c = -0.88$, $K_{upm} = \max|Ku|$): a) $\tau_b/\tau = 0.05$, b) $\tau_b/\tau = 0.6$, c) $\tau_b/\tau = 2.6$.

In the considered model of vibrations of the transducer the metal cylinder is described with two values only, that is the time of propagation of the longitudinal wave τ_b, which is proportionate to its length and the reflection coefficient β_b, which is a function of mechanical impedance of the cylinder and piezoceramic transducer. Let us assume first that $\beta_b = \text{const}$ and determine the transfer function's module for various time relations τ_b to the time of propagation of the longitudinal wave through the piezoceramic transducer. As you can see in Fig. 9, even when the piezoceramic transducer is weighted with a cylinder of a very small length ($\tau_b/\tau = 0.05$) the weighting causes its resonance to be shifted towards smaller frequencies.

The resonance of the cylinder only appears in higher frequencies, which do not fit into the picture. Further increase in the cylinder's length causes the resonant frequency of the piezoceramic transducer to successively near the value $f = 0.25/\tau = c/(\lambda/4)$, where λ is the length of the longitudinal wave in the piezoceramic transducer. At the same time in the transfer function appears the resonance of the metal cylinder whose frequency is shifting towards smaller frequencies. Therefore, one can generally say that the application of the metal cylinder reduces from the top the width of the transducer's transmission band in relation to the width of the transmission band of the piezoceramic transducer only.

This unfavourable effect is compensated, however, by an improved shape of the transfer function in the range of lower frequencies. This is illustrated by Fig. 10, which shows the same transfer functions for low frequencies. We can see that as the length of the

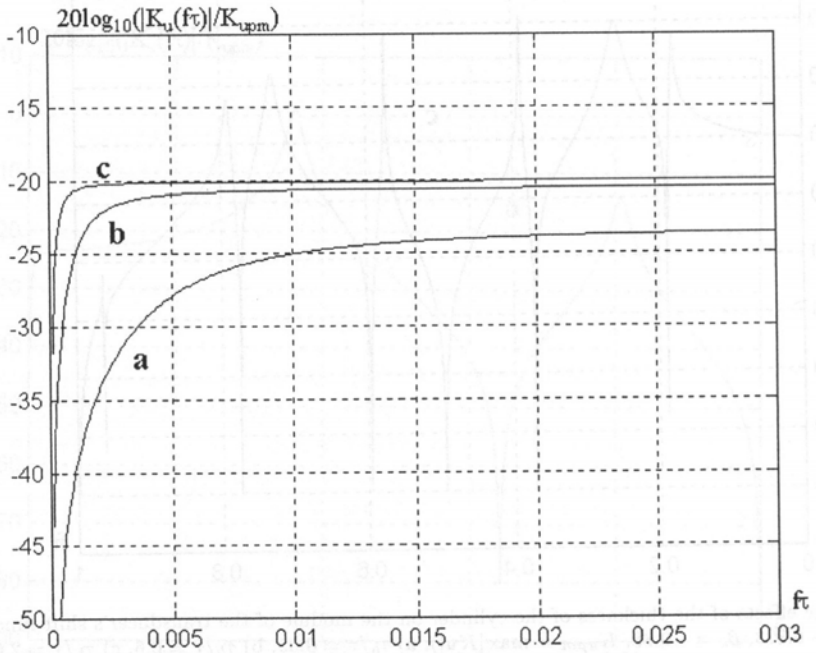

Fig. 10. Module of the transducer's shift function in the range of low frequencies ($\beta_b = -0.823$, $\beta_c = -0.88$, $K_{upm} = \max|K_u|$): a) $\tau_b/\tau = 0.05$, b) $\tau_b/\tau = 0.6$, c) $\tau_b/\tau = 2.6$.

metal cylinder grows, the lower frequency of the transducer's transfer band drops and the transducer's sensitivity increases.

In the application in question the spectrum of received acoustic emission signals is in the low frequencies range that's why from this point of view the extension of the cylinder is a positive thing. At the same time with $\tau_b/\tau \gg 1$, the length of the metal cylinder determines the upper frequency of the transfer band f_M. By analogy to Eq. (24) we have:

$$f_M = \frac{1}{4\tau_b} = \frac{c_b}{4d_b}\,. \tag{29}$$

The lower cut-off frequency f_m is computed using the method applied in the case of the piezoceramic transducer. The module of the transfer function in the range of low frequencies now has the following form:

$$|K_u(j\omega)| = Y_3^D g_{33}\tau \cdot \frac{1-\beta_b}{1+\beta_b} \frac{2\omega\tau_b}{\sqrt{1+(2\omega\tau_b)^2(B+C)^2}}\,, \tag{30}$$

where

$$B = \frac{\beta_c+\beta_b}{(1+\beta_c)(1+\beta_b)} \qquad \text{and} \qquad C = \frac{\tau}{\tau_b}\frac{\beta_c}{1+\beta_c}\,. \tag{31}$$

In this situation $B \gg C$, and so by analogy to the case of Eq. (25) we have:

$$f_m = \frac{1}{4\pi\tau_b}\frac{(1+\beta_c)(1+\beta_b)}{\beta_c+\beta_b} = \frac{c_b}{4\pi d_b}\frac{(1+\beta_c)(1+\beta_b)}{\beta_c+\beta_b}\,. \tag{32}$$

We should note that the lower cut-off frequency in this case does not depend on the resonant frequency of the piezoceramic transducer anymore. From this point of view the piezoceramic transducer can be of any short length, on the other hand however, it should not be too short as the transducer's sensitivity decreases (compare Eq. (30)). This conclusion is confirmed by results of numerical computations presented in Fig. 11.

The effect of the value of the reflection coefficient β_b on the transfer function in the range of low frequencies is shown in Fig. 12.

One can observe the positive effects that increasing the absolute value of this coefficient has both on the width of the band and the inclination of the transfer function.

The upper to lower cut-off frequency ratio is now:

$$\frac{f_M}{f_m} = \frac{\pi(\beta_c+\beta_b)}{(1+\beta_c)(1+\beta_b)}\,. \tag{33}$$

Given the realistic assumptions that $\beta_b = -0.8$, a $\beta_c = -0.9$ the ratio of the upper frequency to the lower frequency of the transfer band of such a transducer is about 250 which is about eight times better than in the case of the piezoceramic transducer only. Given $f_m = 30\,\text{Hz}$ we now get $f_M = 7500\,\text{Hz}$, which is quite a satisfactory result.

To summarise one can say that the reduction of the lower frequency of the transfer band of the transducer can be accomplished by a simultaneous increasing of the length of the metal cylinder and increasing of the absolute value of the reflection coefficient β_b. If the metal cylinder is made of a material of a specific acoustic impedance $\rho_b c_b$, the value of the reflection coefficient increases parallel to the increase in the surface of the cylinder's base. As a result, the combined increase in the cylinder's length and reflection coefficient is in this case equivalent to the increase in its mass.

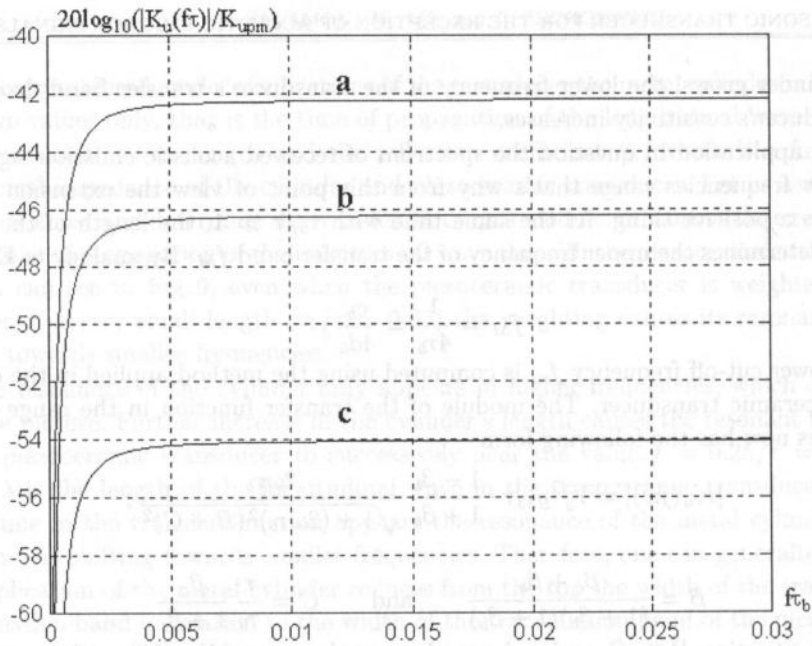

Fig. 11. Module of the transducer's shift function given a constant length of the metal cylinder — low frequencies range ($\beta_b = -0.823$, $\beta_c = -0.88$, $K_{upm} = \max|K_u|$): a) $\tau/\tau_b = 0.8$, b) $\tau/\tau_b = 0.5$, c) $\tau/\tau_b = 0.2$.

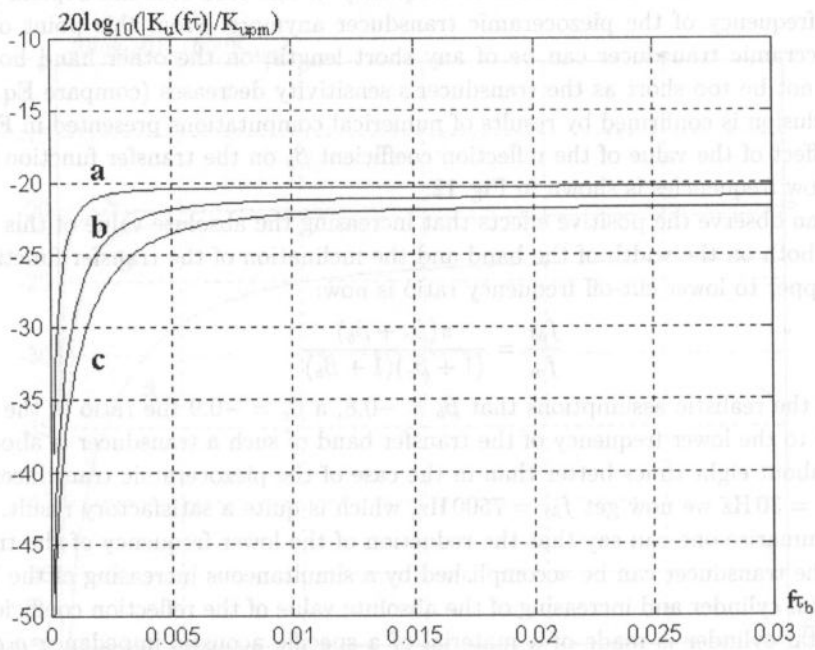

Fig. 12. The effects of the diameter of the metal cylinder on the module of the transducer's shift function within low frequencies range ($\beta_c = -0.88$, $\tau_b/\tau = 0.6$, $K_{upm} = \max|K_u|$): a) $\beta_b = -0.9$, b) $\beta_b = -0.7$, c) $\beta_b = -0.5$.

5. Design, construction and measurements of the transducer

The transducer was designed and later built on the basis of the following operating assumptions:

- effective transfer band of the transducer should be between app.10 Hz to about 10 kHz, which ensures a transfer without distortion of acoustic emission signals,
- considering the convenience of using the transducer its total length should not exceed 15 cm, with total mass less than 1 kg and diameter of the metal cylinder not to exceed 4 cm,
- the ratio of the surface of the metal cylinder to the surface of the piezoceramic transducer should not be greater than 10 which reduces the effects of transverse vibrations of the metal cylinder on the transducer's transfer function, [5].

Since the mass of the metal cylinder should be big, it was decided to make it of brass of density of $\rho_b = 8100\,\mathrm{kg/m^3}$. Elementary computations show that given the admissible mass and diameter of the cylinder, its length should not exceed 10 cm. By adding to Eq. (29) $d_b = 0.1\,\mathrm{m}$ and the velocity of the longitudinal wave in brass equal to approximately $c_b = 4000\,\mathrm{m/s}$ we get $f_M = 10\,\mathrm{kHz}$. This frequency is equal to the upper frequency of the required transfer band of the transducer.

By making the preliminary assumption that the lower cut-off frequency of the transducer $f_m = 10\,\mathrm{Hz}$ and that the reflection coefficient on the transducer-body boundary is equal to $\beta_c = -0.88$, from Eq. (33) we denote $\beta_b = -0.95$. Given this value of the reflection coefficient the ratio of the mechanical impedance of the brass cylinder Z_b to the mechanical impedance of the piezoceramic transducer would have to be 39. Given the similar values of acoustic impedance of both materials this would require a significant differentiation between the surface of the cylinder and the piezoceramic transducer. Because it is contrary to the above criterion, we are forced to abandon the assumption that $f_m = 10\,\mathrm{Hz}$. And so we are increasing the lower cut-off frequency to $f_m = 40\,\mathrm{Hz}$ and from Eq. (33) we denote the value of the reflection coefficient $\beta_b = -0.823$. As a result, the ratio Z_b/Z is now 10.3 and is acceptable.

If we assume that the radius of the surface of the metal cylinder is $r = 2\,\mathrm{cm}$ we compute the mechanical impedance $Z_b = \pi r^2 \rho_b$, $c_b = 40694\,\mathrm{kg/s}$ and mechanical impedance of the piezoceramic transducer $Z = Z_b/10.3 = 3951\,\mathrm{kg/s}$. The applied transducer is made of PZT ceramics of density $\rho = 7030\,\mathrm{kg/m^3}$, and velocity $c = 3480\,\mathrm{m/s}$. From the equation $A = Z/\rho c$ we compute the field of the surface of the piezoceramic transducer $A = 1.61\,\mathrm{cm^2}$.

The last value we are looking for is the length of the piezoceramic transducer d. It should be long enough for the transducer's resonant frequency to be higher than the resonant frequency of the metal cylinder which in this case is in excess of 20 kHz. The selected transducer's resonant frequency is 60 kHz with no acoustic weighting which is a frequency of $f_r = 30\,\mathrm{kHz}$ when weighted with a brass cylinder. The length of the transducer is $d = c/4f_4 = 2.9\,\mathrm{cm}$.

The theoretical transfer function in this design of the transducer denoted from Eq. (22) is shown in Fig. 13.

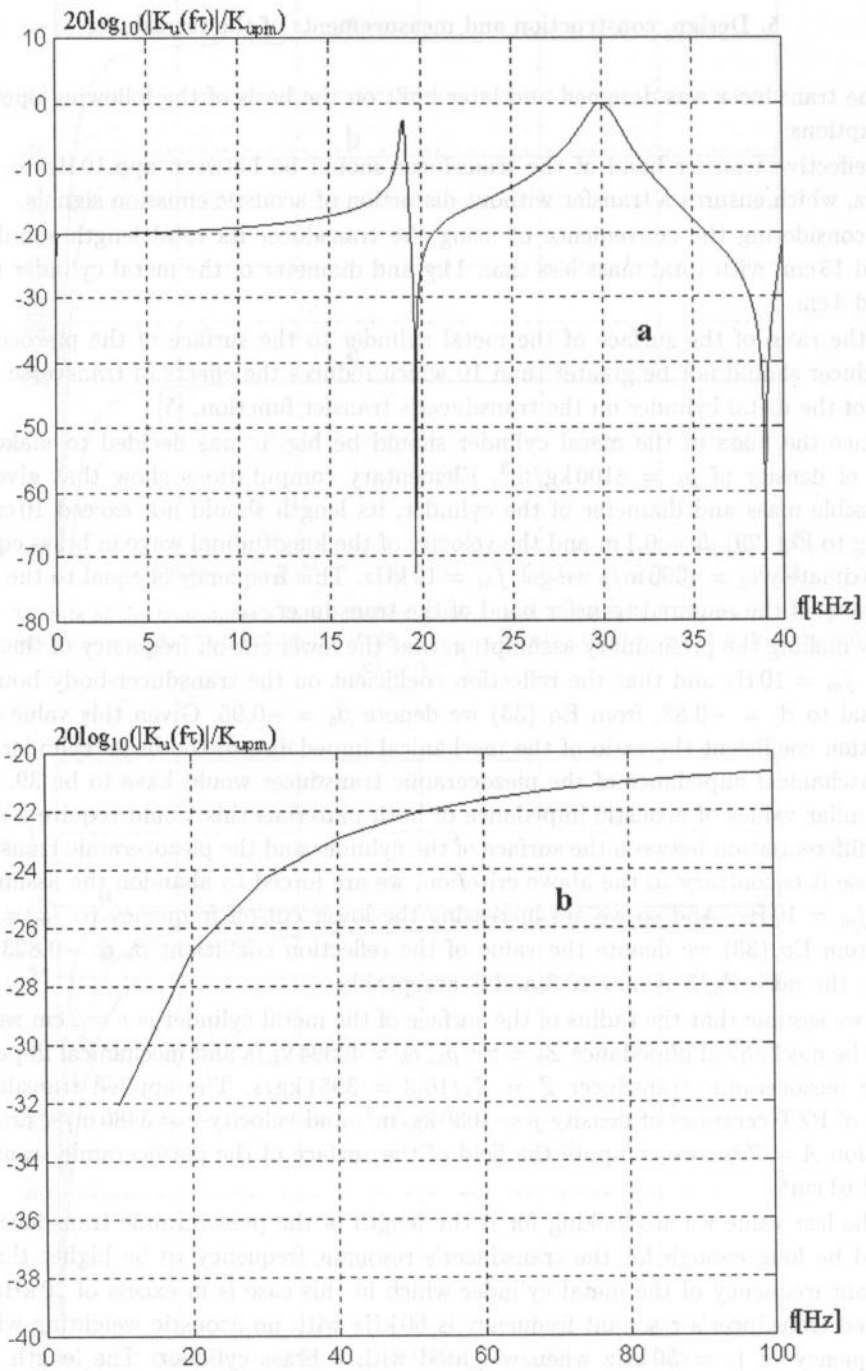

Fig. 13. Module of the shift function of the designed transducer.

As you can see, the location of the resonance meets the expectations. What is more important the transfer band in the low frequency range is almost plane up to frequency 40 Hz. Attenuation in this frequency is as little as 3 dB in relation to attenuation in the transfer band. At frequency of 10 Hz, the sensitivity of the transducer is smaller by 9 dB. Therefore, it is safe to say that the designed transducer transfers acoustic emission signals without significant distortion in the band from 40 Hz to 10 kHz. Attenuation of signals in the band from 10 Hz to 40 Hz is sufficiently small and does not exclude observation of the signals in this band.

The transducer was built based on the above design. Its construction is shown in Fig. 14.

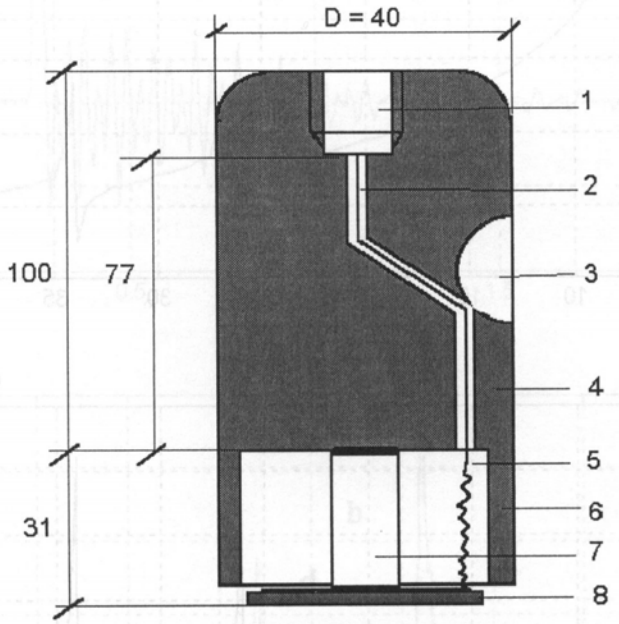

Fig. 14. The structure of the transducer — axial alignment: 1 – opening for the signal socket, 2 – duct for electrical wire, 3 – technological opening, 4 – brazen body (cylinder), 5 – niche, 6 – shielding of the ceramics, 7 – piezoelectric transducer, 8 – shielding and the active electrode.

To verify the theoretical and design computations its electrical impedance was measured $Z_e(f)$. The module of the impedance multiplied by the frequency should, according to the theory, describe the transducer's transfer function, [5, 13]. As is shown in Fig. 15 the transfer function of the transducer built is similar to the theoretical transfer function shown in Fig. 13.

The only variances apply to the placement of the resonance of the metal cylinder and the appearance of an additional resonance at the frequency of about 17 kHz. The increase in the resonant frequency of the brass cylinder is the result of the opening (1) lying opposite the piezoceramic transducer. The path between the bottom of the opening and the surface of the transducer is $d_b' = 77\,\text{mm}$ which at velocity of $c_b = 4000\,\text{m/s}$ gives the resonance frequency of 26 kHz. Lack of resonance at frequency of 20 kHz can

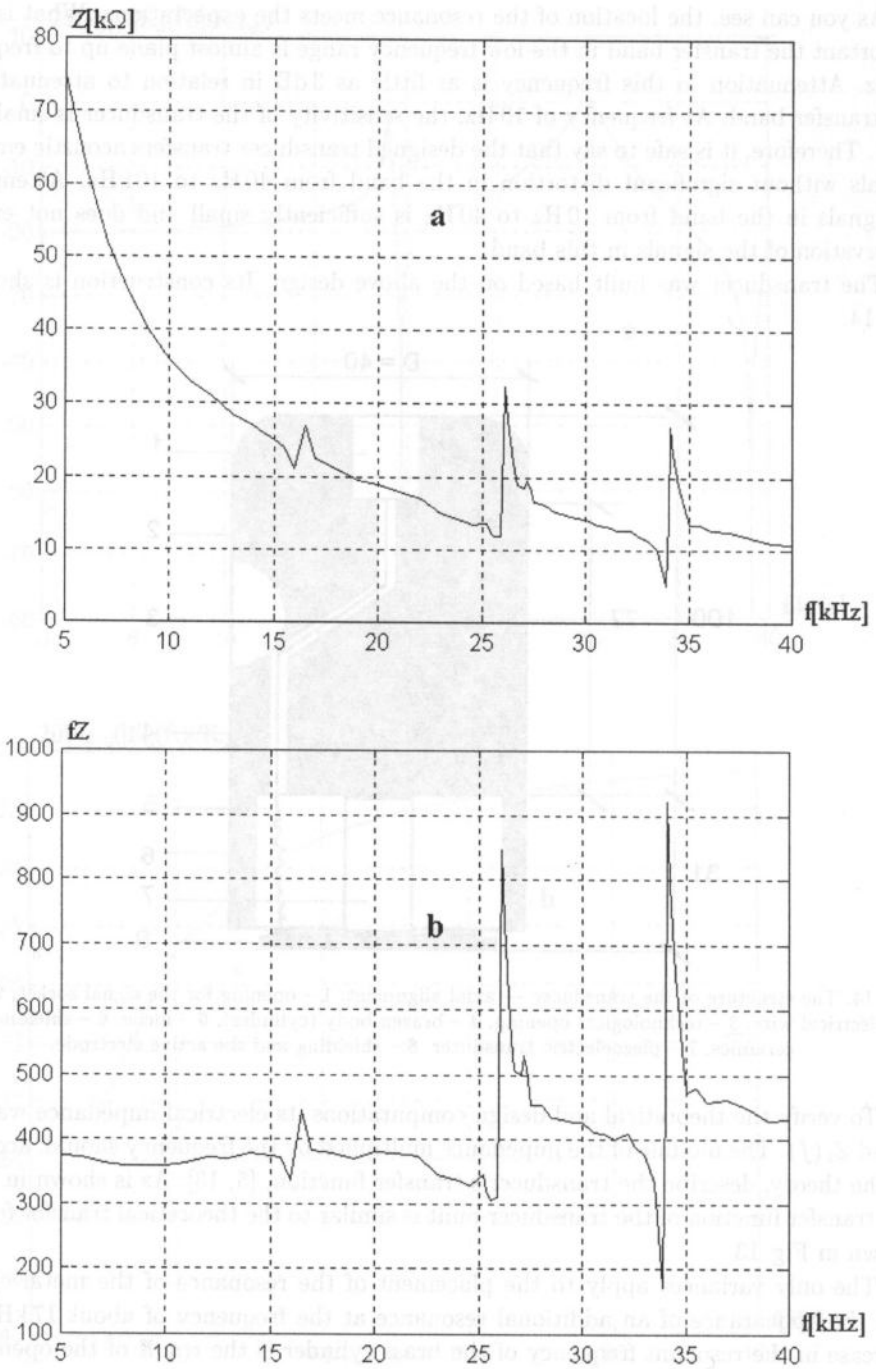

Fig. 15. Electric impedance of the transducer: a) module of electric impedance, b) product of the module of electric impedance and the frequency.

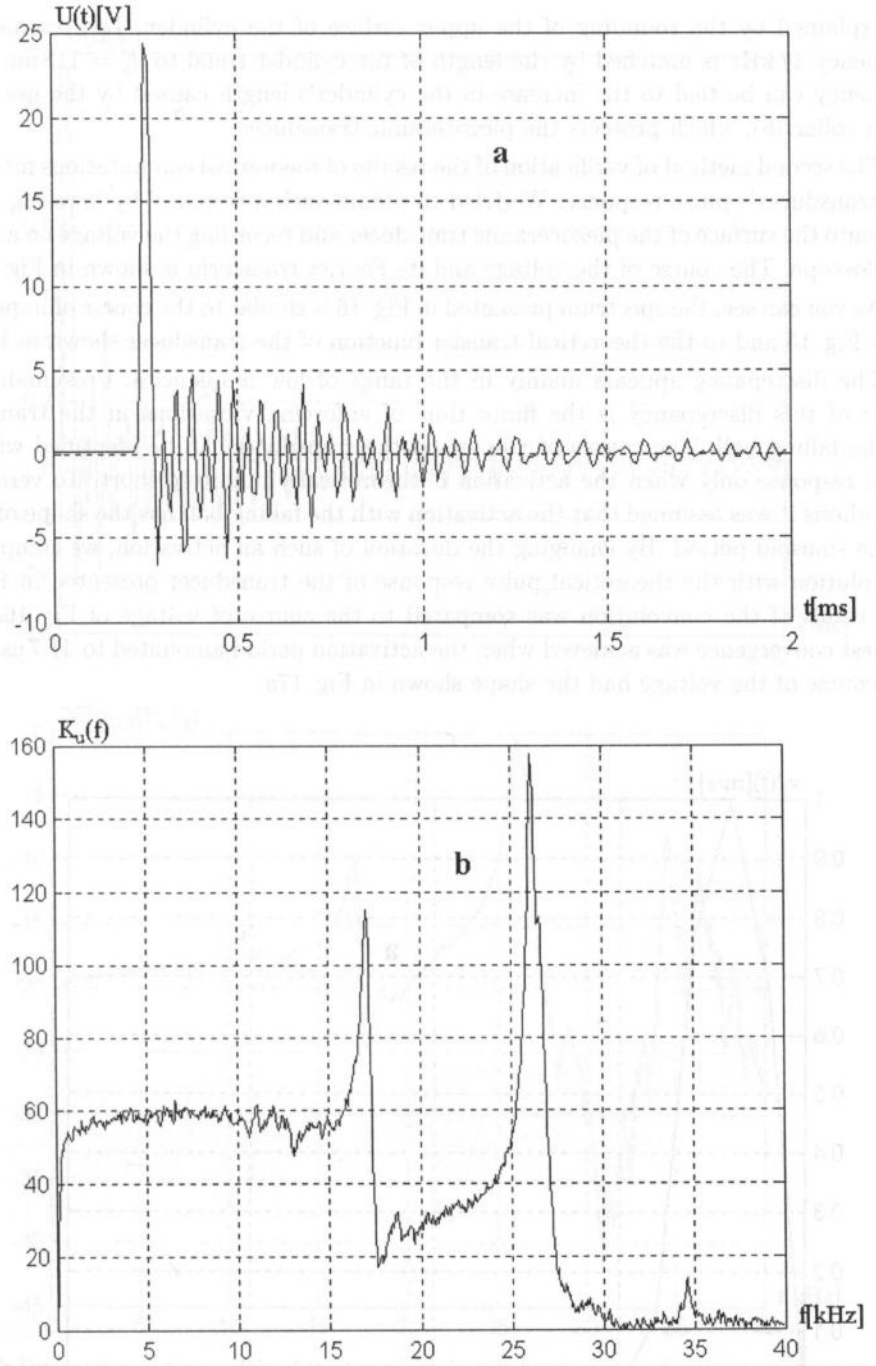

Fig. 16. Voltage response of transducer as it is hit with a metal ball a) transducer's response in time, b) module of the spectrum of the transducer's response.

be explained by the rounding of the upper surface of the cylinder. The resonance at frequency 17 kHz is matched by the length of the cylinder equal to $d_b'' = 118$ mm. This frequency can be tied to the increase in the cylinder's length caused by the use of the brass collar (6), which protects the piezoceramic transducer.

The second method of verification of the results of theoretical computations measured the transducer's pulse response. We tried to obtain such a response by lowering a steel ball onto the surface of the piezoceramic transducer and recording the voltage on a digital oscilloscope. The course of the voltage and its Fourier transform is shown in Fig. 16.

As you can see, the spectrum presented in Fig. 16 is similar to the course of impedance from Fig. 15 and to the theoretical transfer function of the transducer shown in Fig. 13.

The discrepancy appears mainly in the range of low frequencies. Presumably, the cause of this discrepancy is the finite time of enforcing vibrations in the transducer by the falling ball. The course of voltage on the transducer can be identified with the pulse response only when the activation is theoretically infinitely short. To verify this hypothesis it was assumed that the activation with the falling ball has the shape of a half of the sinusoid period. By changing the duration of such an activation, we compute its convolution with the theoretical pulse response of the transducer presented in Fig. 7a. The result of the convolution was compared to the course of voltage of Fig. 16a. The highest convergence was achieved when the activation period amounted to 41.7 μs. Then the course of the voltage had the shape shown in Fig. 17a.

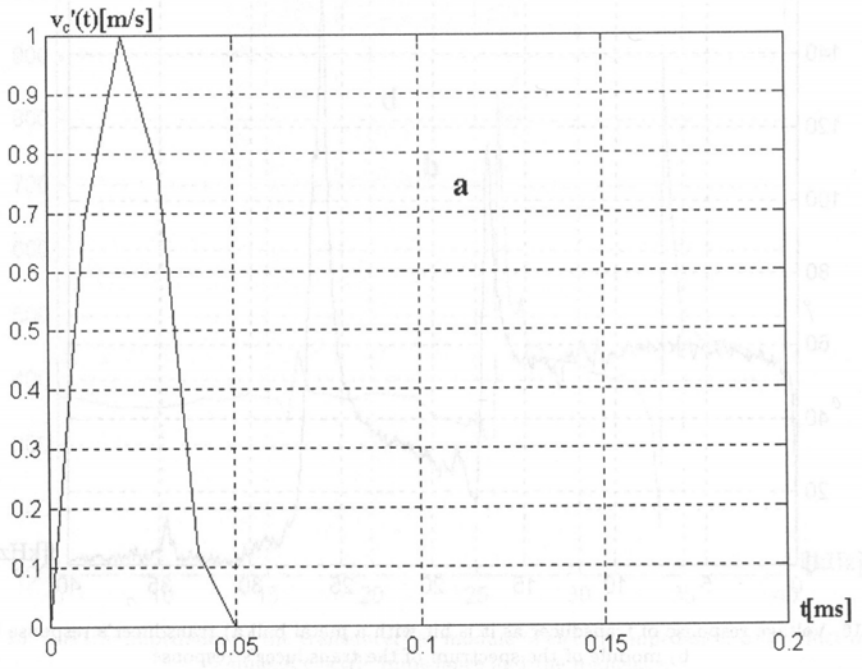

[FIG. 17a]

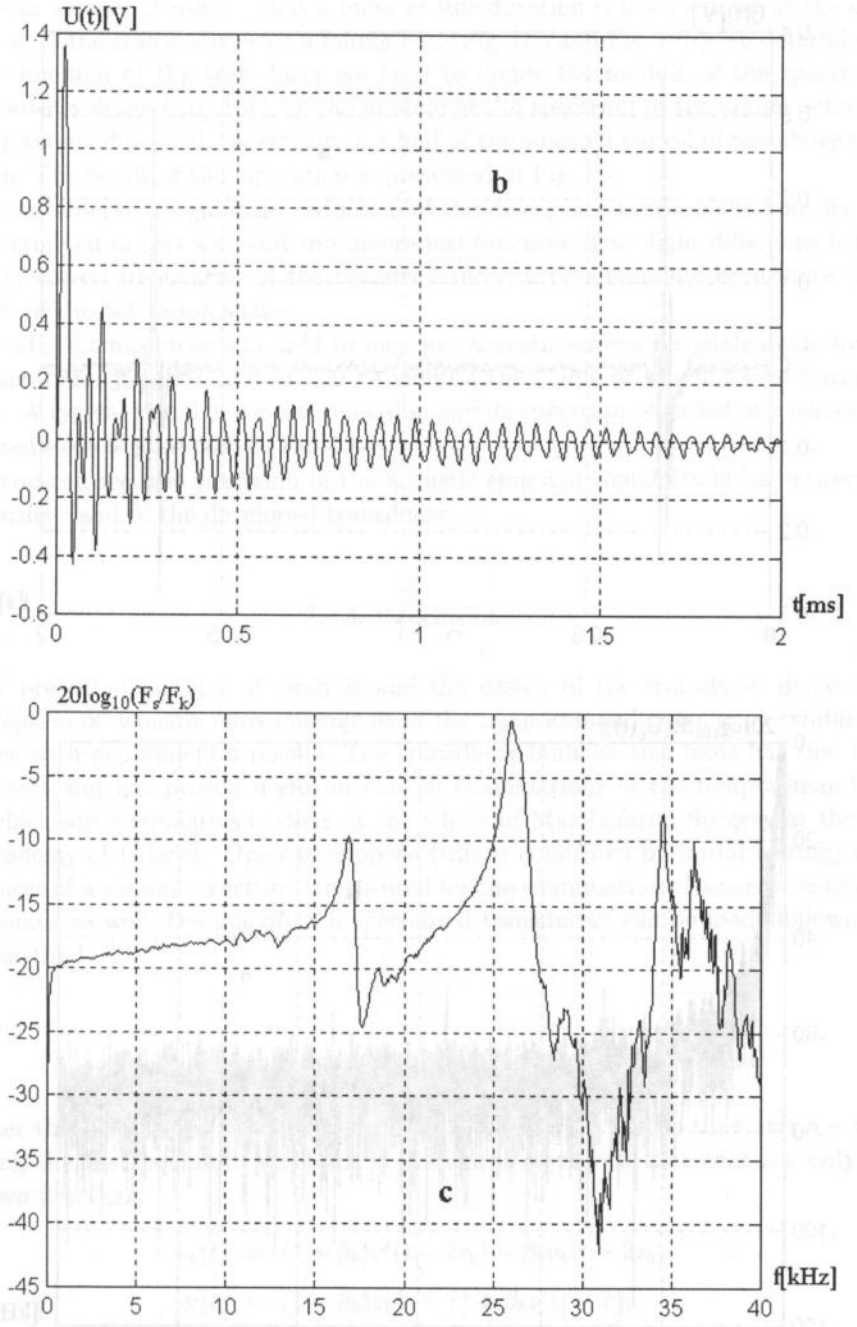

Fig. 17. Designation of the module of the transducer's shift function: a) activation imitating a falling ball, b) transducer's response — a convolution of the pulse response (Fig. 7 a) with the activation that imitates a falling ball, c) module of the shift function computed as the relation between the modules of the signal's spectra from Fig. 17 a and the module of the spectrum of the signal imitating the activation with the ball (half of the sinusoid).

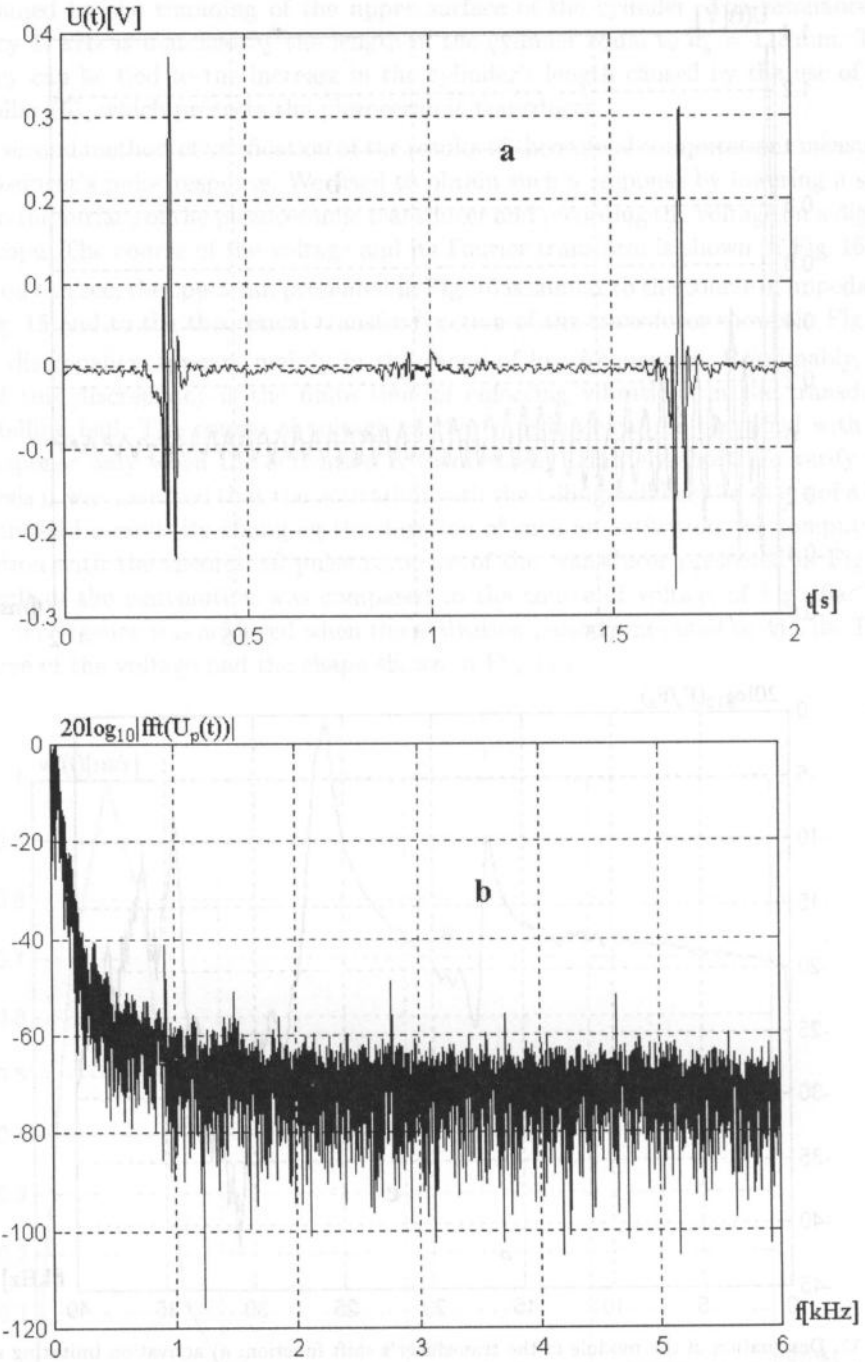

Fig. 18. A typical acoustic signal recorded in a patient: a) the time course, b) signal's spectrum.

We can assume therefore, that a pulse of this duration is most similar to the actual activation of the transducer with a falling ball (Fig. 16a and Fig. 17b). To determine the transfer function of the transducer we need to divide the module of the spectrum of the recorded voltage (Fig. 16b) by the module of the spectrum of the actual activation, meaning the module of the spectrum of a half of the sinusoid period of the above stated duration. The result of this operation is presented in Fig. 17c.

We can observe a significant reduction of the divergence between the transfer function determined in this way and the theoretical function. The slight difference between the lower cut-off frequencies of the transfer band can be eliminated by a more careful selection of the activation shape.

The above transducer was used to measure acoustic emission signals made by temporomandibular joints in almost 200 patients of the Clinic of Maxillofacial Surgery in Gdańsk. A typical signal of acoustic emission and its spectrum recorded in a person with a diseased joint is presented in Fig. 18.

As you can see, the spectrum of the acoustic emission signal fits in its entirety into the transfer band of the developed transducer.

6. Conclusion

The presented method of analysis and the design of the transducer dedicated to the reception of acoustic emission signals of the temporomandibular joint exhibits convergence with experimental results. The transducer built on this basis has the desired parameters and has proved useful in clinical examinations of the temporomandibular joint which are systematically done at the Clinic of Maxillofacial Surgery at the Medical Academy of Gdańsk. One can suppose (this is confirmed by initial testing) that a transducer of a similar structure can be used for the examination of acoustic emission of other joints, as well. Designs of such specialised transducers can be made following the above method.

Appendix

After the shift of functions that are present in Eq. $(4)_2$ on the time axis $o - \tau_b$ and inserting the first equation we obtain a system of equations that contains only three unknown functions.

$$\begin{aligned} v_b(t) &= (1+\beta_b)v'(t-2\tau_b) - \beta_b v_b(t-2\tau_b), \\ v(t) &= (1-\beta_b)v_b(t-\tau) + \beta_b v'(t-\tau), \\ v'(t) &= (1+\beta_c)v'_c(t-\tau) - \beta_c v(t-\tau). \end{aligned} \tag{A.1}$$

To further reduce the number of unknown functions we can eliminate velocity $v'(t)$. To that end we multiply the first equation by β_b and shift $o-\tau$, and multiply the second

equation by $(1+\beta_b)$ and shift $o-2\tau_b$. We then get:

$$\begin{aligned} \beta_b v_b(t-\tau) &= \beta_b(1+\beta_b)v'(t-2\tau_b-\tau) - \beta_b^2 v_b(t-2\tau_b-\tau), \\ (1+\beta_b)v(t-2\tau_b) &= (1-\beta_b^2)v_b(t-\tau-2\tau_b) + \beta_b(1+\beta_b)v'(t-\tau-2\tau_b). \end{aligned} \tag{A.2}$$

After subtracting the above equations by the sides and arranging the expressions we get:

$$\beta_b v_b(t-\tau) + v_b(t-\tau-2\tau_b) = (1+\beta_b)v(t-2\tau_b), \tag{A.3}$$

By applying the same operations to the first and third equation from the system of equations (A.1) we have:

$$v_b(t) + \beta_b v_b(t-2\tau_b) = (1+\beta_b)\Big[-\beta_c v(t-\tau-2\tau_b) + (1+\beta_c)v_c'(t-\tau-2\tau_b)\Big]. \tag{A.4}$$

Equations (A.3) and (A.4) contain two unknown functions, that is $v_b(t)$ and $v(t)$. Let us now multiply the equation (A.3) by β_c and shift $o-\tau$. This gives us:

$$\beta_c\beta_b v_b(t-2\tau) + \beta_c v_b(t-2\tau-2\tau_b) = (1+\beta_b)\beta_c v(t-\tau-2\tau_b). \tag{A.5}$$

After adding by the sides the equations (A.4) and (A.5) we get:

$$\begin{aligned} v_b(t) + \beta_b v_b(t-2\tau_b) + \beta_b\beta_c v_b(t-2\tau) + \beta_c v_b(t-2\tau_b-2\tau) \\ = (1+\beta_b)(1+\beta_c)v_c'(t-\tau-2\tau_b). \end{aligned} \tag{A.6}$$

Equation (A.6) is a non-homogenous difference equation with continuous time of the function $v_b(t)$. On the right side of the equation is as usual the activation — in our case it is velocity $v_c'(t)$. To simplify the notation of further equations let us introduce the following notation:

$$r(t) = \delta(t) + \beta_b\delta(t-2\tau_b) + \beta_b\beta_c\delta(t-2\tau) + \beta_c\delta(t-2\tau-2\tau_b), \tag{A.7}$$

where $\delta(t)$ is Dirac's distribution.

Using the above notation, the difference equation (A.6) can be written as:

$$v_b(t) * r(t) = (1+\beta_b)(1+\beta_c)v_c'(t-\tau-2\tau_b), \tag{A.8}$$

where symbol (*) means the convolution operation.

Let us now denote equations which describe the other wanted functions, that is velocities $v(t)$ and $v'(t)$. To that end, let us note the first of the equations (A.1) in the form of a convolution with the function $r(t)$:

$$v_b(t) * r(t) + \beta_b v_b(t-2\tau_b) * r(t) = (1+\beta_b)v'(t-2\tau_b) * r(t). \tag{A.9}$$

Next using the equation (A.8), we have:

$$(1+\beta_b)(1+\beta_c)\Big[v_c'(t-\tau-2\tau_b) + \beta_b v_c'(t-\tau-4\tau_b)\Big] = (1+\beta_b)v'(t-2\tau_b) * r(t). \tag{A.10}$$

After simplifications, the above equation assumes the following form:

$$v'(t) * r(t) = (1+\beta_c)\Big[v_c'(t-\tau) + \beta_b v_c'(t-\tau-2\tau_b)\Big]. \tag{A.11}$$

Similarly, the difference equation is obtained in relation to velocity $v(t)$:

$$v(t) * r(t) = (1-\beta_b)v_b(t-\tau) * r(t) + \beta_b v'(t-\tau) * r(t). \tag{A.12}$$

Equations (A.8), (A.11) and (A.12) are used in the main text of the article.

Acknowledgements

The authors wish to express their gratitude to Professor Tadeusz Korzon, at the time the head of the Department and the Clinic of Maxillofacial Surgery at the Medical Academy in Gdańsk for having initiated the acoustic examination of the temporomandibular joint, for the many years of support for the studies and for the inspiring discussions on the directions and methods of the studies. We wish to thank Professor Leszek Filipczyński — full member of the Polish Academy of Sciences and Andrzej Stepnowski from the Department of Acoustics of the Technical University of Gdańsk for the valuable comments on the theory and measurements of the transducer.

References

[1] R. BADWAL, *The application of fractal dimension to temporomandibular joint sounds*, Comput. Biol. Med., **23**, 1, 1–14 (1993).

[2] L.V. CHRISTENSEN, *Physics and the sounds produced by the temporomandibular joints*, Journal of Oral Rehabilitation, **19**, Part I. 471–483, Part II. 615–627 (1992).

[3] R. DOVE, R. FRIGHT, B. PRICE, K. SCALLY and R. TREMEWAN, *Tracking jaw movement*, Medical & Biological Engineeering & Computing, September 32, 584–588 (1994).

[4] R. DRUM and M. LITT, *Spectral analysis of temporomandibular joint sounds*, The Journal of Prosthetic Dentistry, **58**, 4, 485–494 (1987).

[5] L. FILIPCZYŃSKI, *Transients and the equivalent electrical circuit of piezoelectric transducer*, Acustica, **10**, 149–154 (1960).

[6] T. GAY and C.N. BERTOLAMI, *The spectral properties of temporomandibular sounds*, J. Dent., Res., **66**, 6, 1189–1194 (1987).

[7] L. HEFFEZ and D. BLAUSTEIN, *Advances in sonography of the temporomandibular joint*, Oral Surg. Oral Med. Oral Pathol., **62**, 486–495 (1986).

[8] H.W. KATZ, *Solid state magnetic and dielectric devices*, John Wiley & Sons, Inc., New York 1959, 120.

[9] J. KRASZEWSKI and Z. KRASZEWSKA, *Phonoarthographic diagnostics of temporomandibular joint* [in Polish], Czas. Stomat., **28**, 3, 279–285 (1975).

[10] J. KRASZEWSKI and Z. KRASZEWSKA, *Phonoarthographic diagnostic in certain temporomandibular joint dysfunction* [in Polish], Czas. Stomat., **28**, 4, 387–396 (1975).

[11] W. LIS, J. ZIENKIEWICZ and R. SALAMON, *Parameters of acoustic signal emitted by the temporomandibular joint* [in Polish], Proceedings XLIII OSA, Gliwice – Ustroń, 457–462 (1996).

[12] W. LIS and J. ZIENKIEWICZ, *The wavelet transform analysis of the temporomandibular joint acoustic emission* [in Polish], Proceedings XLIV OSA, Gdańsk – Jastrzębia Góra, 423–428 (1997).

[13] G. ŁYPACEWICZ and E. DURIASZ, *Compensating circuit of ultrasonic probe* [in Polish], Proceedings X Symposium on Hydroacoustics, Jurata May, 139–144 (1993).

[14] G. ŁYPACEWICZ, *Design of ultrasonic probes for medical diagnostics* [in Polish], Proceedings IX Symposium on Hydroacoustics, Gdynia – Jurata, 11–30 (1992).

[15] A. MARKIEWICZ and G. ŁYPACEWICZ, *Application of matching layers of ultrasonic probes to biological structures* [in Polish], Prace OSA XXI, Rzeszów, 139–141 (1974).

[16] C. OSTER, R.W. KATZBERG, R.H. TALLENTS, T.W. MORRIS, J. BARTHOLOMEW, T.L. MILLER and K. HAYAKAWA, *Characterization of temporomondibular joint sounds*, Oral Surg., **58**, 10–16 (1984).

[17] R. SALAMON, *Wellenmodell des Beschleunigungsmessers*, Fortschritte der Akustik Duisburg DAGA, 275–278 (1989).

[18] R. SALAMON and F. CHINCHURRETA, *Signalmodell des piezoelektrischen Schwingers*, Acustica, **66**, 247–257 (1988).

[19] R. SALAMON and F. CHINCHURRETA, *Analyse piezoelektrischer Breitbandschwinger mit Differenzengleichung*, Acustica, **67**, 19–29 (1988).

[20] D.M. WATT, *Clinical applications of gnathosonics*, Prosthetic Department, School of Dental Surgery, University of Edinburgh, Scotland, I-II, 16, 83–95 (1966).

[21] R.M. WILK and S.E. HARMS, *Temporomandibular joint: Multislab, threee-dimensional Fourier transformation MR imaging*, Radiology, **167**, 3, 861–863 (1988).

[22] I. YAVELOW and G.S. ARNOLD, *Temporomondibular joint clicking*, Oral Surg., **32**, 708–714 (1971).

ARCHIVES OF ACOUSTICS
24, 3, 365–378 (1999)

BOTTOM TYPE IDENTIFICATION USING COMBINED NEURO-FUZZY CLASSIFIER OPERATING ON MULTI-FREQUENCY DATA

A. STEPNOWSKI, J. MACIOŁOWSKA and TRAN VAN DUNG

Technical University of Gdańsk
Acoustics Department
(80-952 Gdańsk, Poland)
e-mail: astep@pg.gda.pl
joan@dolphin.eti.pg.gda.pl
dung@dolphin.eti.pg.gda.pl

The paper introduces a novel approach to acoustic methods of characterising the bottom type by using a neuro-fuzzy classifier which processes the bottom backscatter data collected with an echosounder on three different operating frequencies. The classifier combining fuzzy logic and artificial neural networks was created using NEFClass system. It constitutes a fuzzy system, which can be viewed as a special 3-layer feed-forward neural network architecture, where the nodes of the second layer represent fuzzy rules. These rules are derived from a set of training data separated into crisp classes. In training and testing stages, apart from using single-frequency data, sets of dual-frequency and triple-frequency data combined together were used in order to enhance the classifier's performance. The results show that combining dual-frequency, or moreover triple-frequency data, clearly improves the generalisation ability of the classifier. The bottom backscattered echoes were acquired from acoustic surveys carried out on Lake Washington using the single-beam digital echosounder working on three frequencies: 38 kHz, 120 kHz and 420 kHz.

1. Introduction

As being non-invasive and faster than other techniques, the hydroacoustic methods of sea-bottom characterisation and identification have gathered a lot of importance in the last two decades and they are still a subject of extensive research. Information retrieved from bottom echo about seabed type is especially useful in hydrography, environmental sciences, marine engineering etc. Among the various acoustic techniques, which have been developed in recent years for characterising and classifying the bottom type, methods of so-called vertical, or normal incidence — utilising backscattered data from a single-beam echosounder — have achieved special attention, due to their simplicity and versatility.

These methods can be roughly categorised as follows:

- measurement of energy ratio in the first and second bottom echo [2, 3];
- comparison of a shape of bottom echo with patterns obtained from backscatter theoretical models [9, 11];
- techniques using wideband (chirp) signals and parametric arrays [1, 4];

- fractal analysis of bottom echo envelope [6];
- analysis of bottom echo using neural networks and cluster analysis [11, 12].

Variety of sediments' types, geomorphologic forms and layer structures make it especially difficult to determine a type of seabed, when an identification process is based only on the acoustic backscatter from the seafloor. The relations between a type of sediment and parameters of the bottom echo sometimes might be ambiguous and vague, and even when found for the explored area they don't necessarily have to be valid when extrapolated on other regions.

Intending to build up a reliable classification system and being aware of the difficulty of the problem, we have commenced with creating a Fuzzy Inference System (FIS) [7]. This system, as based on fuzzy logic, is especially suited when dealing with data with not sufficient information *a priori*, what leads to ambiguous and partial knowledge about the bottom type. Although the achieved results — 62% to 67% of correct classification rate — were promising, the method itself had limitation, which implied turning our interest towards an Adaptive Neuro-Fuzzy Inference System (ANFIS) [5]. Unlike FIS, the neuro-fuzzy system has an ability to adapt itself i.e. to derive shapes of membership functions and fuzzy "*if-then*" rules from a learning data set. This property of ANFIS is especially attractive in situation, when after learning the neuro-fuzzy net must extrapolate its classification abilities to unknown data, even acquired on a region different to the area where the learning data set was collected.

2. Classification methods

In general, the classification problem can be characterised as a function F, assigning a new input $\mathbf{x}_i$ to one of the disjoint classes c_i from the set of all classes C:

$$F : \mathbf{x}_i \to c_i , \tag{1}$$

$$F = F(\mathbf{x}_i, \mathbf{w}), \tag{2}$$

where $\mathbf{w}$ — vector of the parameters, $\mathbf{x}_i$ — input vector, $\mathbf{x}_i = [x_1, ..., x_d] \in X$, X — set of all input vectors.

Very often an additional group — "unknown" — is added to the set of classes. An input vector is assigned to this class when it cannot be assigned to any other category.

Most classifiers do not operate on the space X in which the input vector is described, but rather on the space of descriptors $y(X)$, extracted from the input vector, as processing data of lower dimension requires less memory and less computation power. In most situations reduction of the dimensionality of input vectors results in loss of information. Therefore the main goal is to choose such a set of parameters that as much of the relevant information as possible is retained.

For each class c_i a set of representative data, called a *learning set* Z, $Z = \{(y(\mathbf{x}_i), c_i) \in Y \times C\}$ already classified by an observer, is needed. It is used in the learning process, in which the values of parameters of the function F are determined.

The system's ability to classify unknown data is confirmed on an independent data set called a *testing set*.

2.1. Fuzzy reasoning

Fuzzy classifiers are based on a notion of the fuzzy logic operating on fuzzy sets, which were introduced by L.A. ZADEH [13] and which offer a formal description of linguistic expressions.

The definition of a fuzzy set is fundamental for the fuzzy logic theory and can be expressed as below [10]:

A fuzzy set μ of X is a function that maps from the space X into the unit interval, i.e.

$$\mu : X \to [0.1].$$

The value of the function $\mu(x)$ denotes the membership degree of x to the fuzzy set μ and is called the membership function. The value zero is used to represent complete non-membership, the value one represents complete membership, while the values in between are used to represent degrees of membership. In practice, the terms: "membership function" and "fuzzy set" get used interchangeably [10].

Fuzzy logic can be viewed as an extension of the binary (Boolean) logic to multivalued logic, which handles the concept of partial truth by operating on fuzzy sets.

The foundation of the fuzzy reasoning lays in the "*if–then*" rules:

$$\begin{aligned} &\textbf{If } x_1 \text{ is } A_1 \text{ AND } x_2 \text{ is } B_1 \textbf{ Then } y \text{ is } C_1, \\ &\textbf{If } x_1 \text{ is } A_2 \text{ OR } x_2 \text{ is } B_2 \textbf{ Then } y \text{ is } C_2 \end{aligned} \tag{3}$$

"x_i is A_i AND x_i is B_i" is an antecedent and "y is C_i" is a consequent of the rule [10].

Usually, especially in the classification systems, a scalar or numeric output value is desired. Therefore, some sort of defuzzifying operation is needed to reduce the output fuzzy set to a single number, which represents a class. From numerous defuzzyfication methods [5] centroid of the set (4) technique was used in the carried-out investigation:

$$y_{COA} = \frac{\int\limits_{\gamma} y\mu_{C'}(y)\,dy}{\int\limits_{\gamma} \mu_{C'}(y)\,dy}, \tag{4}$$

where $\mu_{C'}(y)$ is the combined output membership function.

Classification system, which uses a collection of fuzzy membership functions and fuzzy rules to reason about data, called also the Fuzzy Inference System (FIS) is depicted in form of a block diagram in Fig. 1 and characterisation of its functional blocks is as below:

- **Fuzzyfication** — maps a point from the universe of descriptors to values from 0 to 1 interval using a set of input membership functions.
- **Knowledge base** — contains information about the domains of variables and the fuzzy sets associated with the linguistic terms and a set of "*if–then*" rules.
- **Decision logic** — determines the values of the output variables.
- **Defuzzyfication** — selects a single number to represent the fuzzy output set.

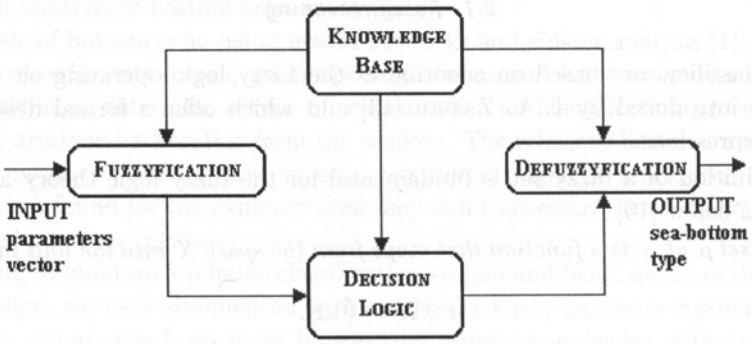

Fig. 1. Architecture of the fuzzy inference system.

2.2. Neuro-fuzzy classification system — NEFClass

The Adaptive Neuro-Fuzzy Inference Systems (ANFIS) are derived from the general architecture of FIS system, shown in Fig. 1. By employing artificial neural networks they are able to find optimal membership functions, optimal number and structure of "*if–then*" rules and defuzzyfication method in a given problem [5].

We applied the NEFClass fuzzy inference system [8] to build ANFIS classifier, which can be viewed as a special 3-layer feed-forward neural network architecture. The nodes of the first layer of the net represent input parameters, the nodes of the second layer represent fuzzy rules, and in the output layer one node indicates each class. The fuzzy sets are characterised by fuzzy weights on the connections from the input to the hidden layer. Fuzzy rules are derived from a set of training data separated into crisp classes. A schematic block-diagram of the NEFClass architecture is presented in Fig. 2.

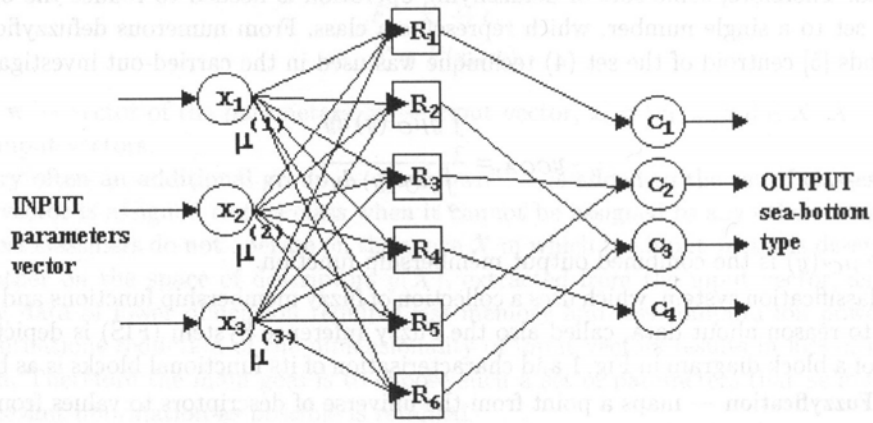

Fig. 2. Architecture of the neuro-fuzzy classification system.

Each connection between the output units and the units of the hidden layer is labelled with a linguistic term like *small, medium, large* etc. Connections coming from the same input unit x_i and having identical labels bear the same weight at all the time.

The task of NEFClass is to learn fuzzy rules and to learn shapes of the membership functions to determine the correct class category of a given unknown input pattern.

The learning algorithm of NEFClass, fully described in [8] can be summarised in the following steps:

1. **Initialization** — For each feature there is an input unit, and for each class there is one output unit designated. For each input unit an initial fuzzy partitioning is specified e.g. a number of equally distributed triangular membership functions is set.

2. **Rule Learning** — The system starts operation without any rules. The rules are inserted during the first run through the training data. A rule is created by finding, for a given input pattern, the combination of fuzzy sets, which gives the highest degree of membership for the respective input feature. If this combination is not identical to the already existing one, a new rule is added. In the second run the rules are evaluated and only the best are kept.

3. **Fuzzy Membership Shape Learning** — When the rule base is created, the learning algorithm adapts the membership functions μ of the antecedents. They are triangles defined by the function (5), where a, b and c are its parameters:

$$\mu : R \to [0,1], \qquad \mu(x) = \begin{cases} \dfrac{x-a}{b-a} & \text{if } x \in [a,b), \\ \dfrac{c-x}{c-b} & \text{if } x \in [b,c], \\ 0 & \text{otherwise.} \end{cases} \tag{5}$$

The back-propagation scheme is used for finding optimal shapes of the membership functions, by adjusting values of a, b and c parameters. The range of each parameter is limited to the space in which parameter x is defined and also depends on how much the membership functions can overlap, which can be set in the NEFClass options. Depending on the output error for each rule unit, a decision is undertaken whether the activation value has to be lower or higher. Each rule unit then changes its membership functions by changing their support (i.e. the base of a membership triangle).

3. Experiment and results

Experimental data was acquired during acoustic surveys using a single-beam digital echosounder DT4000. The echosounder was operating on frequencies of 38 kHz, 120 kHz and 420 kHz with the pulse duration of 0.4 ms. Backscattered bottom echoes sampling rate was 41.66 kHz. The surveys were carried out on Lake Washington. For the experiment only data from an anchored ship was used, as transects were not completely validated due to limited ground truth sampling. To make sure that data collected at different frequencies came from the same regions, so the echoes corresponded to identical types of sediment, the geographical position of the vessel recorded by GPS was checked carefully. Only echoes obtained from the ship anchored in the same location for each bottom type and each frequency were further investigated. The chart of Lake Washington with acoustic sampling sites for each bottom type is presented in Fig. 3.

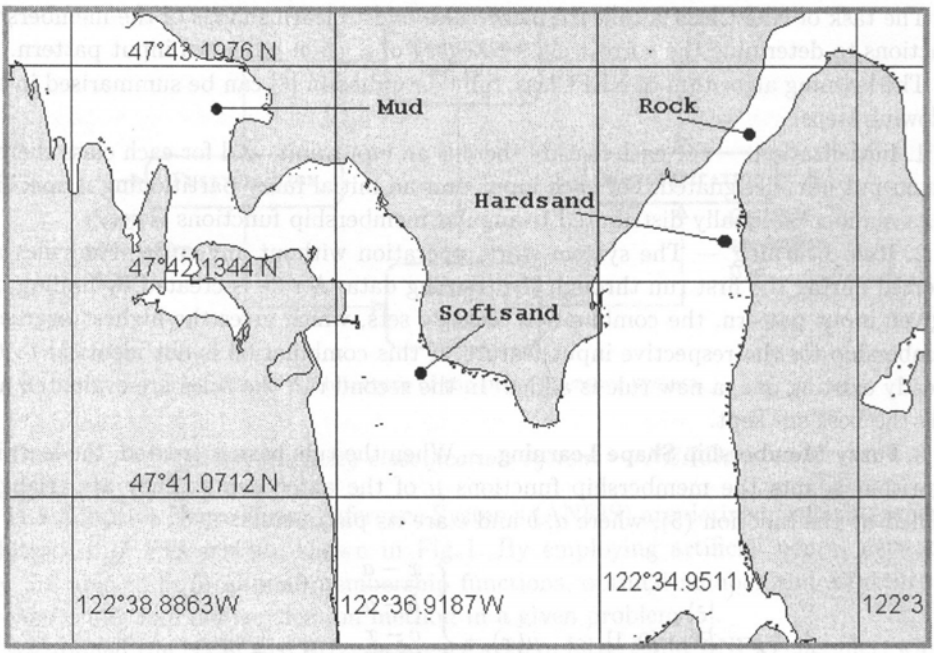

Fig. 3. Chart of Lake Washington with acoustic sampling sites marked.

Three types of classifiers were built. Firstly, two single-frequency classification systems working on 38 kHz or 120 kHz data sets were created. Consequently, these two data sets were combined for a dual-frequency classifying system. The third type of a system — triple-frequency classifier — was based on a set in which also 420 kHz data was combined with the previous two data sets.

3.1. Parameters extraction

Development process of each classifier is usually conducted in three steps. Firstly, a set of parameter must be extracted from a digitised echo. It was decided to use three echo parameters, which graphical representation is shown in a screen damp of the Visual Bottom Typer [11] in Fig. 4, and which are listed below:

- Energy of the leading part of the first echo (Bottom Hardness Signature)

$$E_1 = \sum_{i=n_1}^{n_M} a_i^2; \tag{6}$$

- Energy of the falling part of the first echo (Bottom Roughness Signature)

$$E_1' = \sum_{i=n_M}^{n_L} a_i^2; \tag{7}$$

- Amplitude of the secondary echo (Bottom Hardness Signature)

$$A_2 = \max_{i=m_1 \ldots m_L} a_i, \tag{6}$$

where a_i — quantized value of i-th sample of a digitised bottom echo signal, n_1 — number of the first sample in the first echo, n_M — number of the maximal sample in the first echo, n_L — number of the last sample in the first echo, m_1 — number of the first sample in the secondary echo, m_L — number of the last sample in the secondary echo.

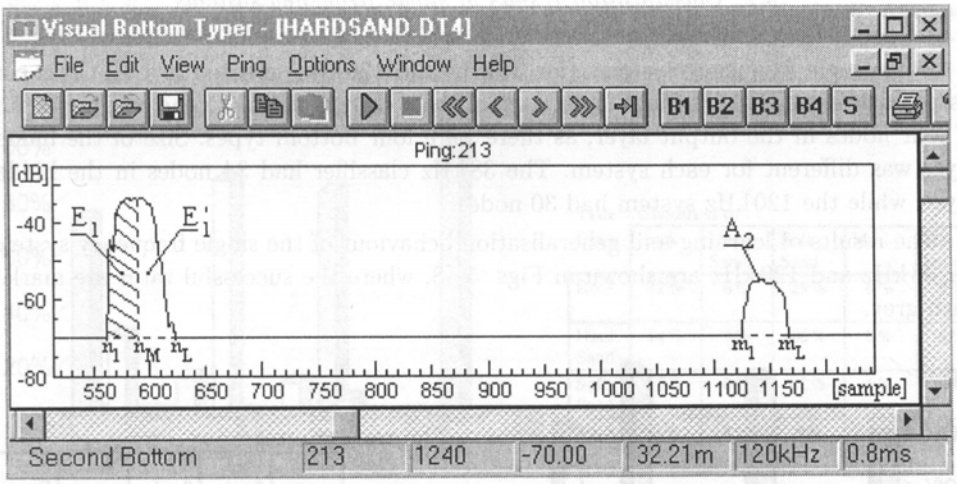

Fig. 4. Graphical interpretation of the parameters extracted from the bottom echo.

The bottom type in each data set was known. Four types of sediments were represented by data collected at 38 kHz and 120 kHz, and these were mud, soft sand, hard sand and rock. For 420 kHz data only three types of bottom data were collected, i.e.: mud, sand and rock.

The second step in creating a classifier is to train the system using the training data set. Then, the generalisation capacity of the systems must be checked on the testing data sets. Therefore, after computing parameters of each echo from all sets of data, they were divided into learning (training) and testing sets. For single-frequency systems, every second echo was chosen from the whole set of data and used for learning. For dual- and triple-frequency systems, the training set consisted of every third echo drawn from the whole set of data. Number of echoes in each of these sets for three operating frequencies is shown in Table 1.

The systems could learn only to some extend i.e. also in the learning phase some misclassifications occurred. Therefore the classification results are presented not only for the generalisation phase but also for the learning one.

Table 1. Amount of data used in the experiments.

Experiment		Echoes in training set	Echoes in testing set
single-frequency	38 kHz	200	220
single-frequency	120 kHz	395	666
dual-frequency	38 kHz + 120 kHz	200	645
triple-frequency	38 kHz + 120 kHz + 420 kHz	150	445

3.2. Classification results of single frequency systems

Both single frequency-systems (for 38 kHz and 120 kHz) created in NEFClass consisted of three nodes in the first layer, each of them corresponding to one parameter, and of four nodes in the output layer, as there were four bottom types. Size of the hidden layer was different for each system. The 38 kHz classifier had 34 nodes in the hidden layer, while the 120 kHz system had 30 nodes.

The results of learning and generalisation behaviour of the single frequency systems for 38 kHz and 120 kHz are shown in Figs. 5–8, where the successful rates are marked with grey.

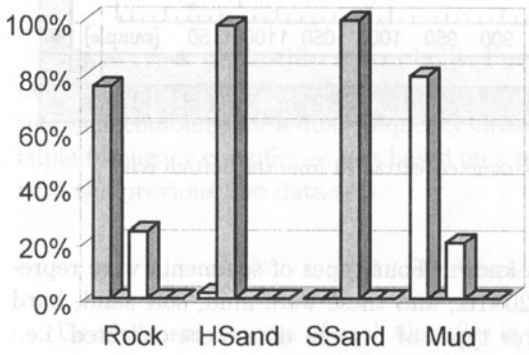

True Class	Classified to: Rock	Hard Sand	Soft Sand	Mud	Not Known
Rock	**76%**	**0%**	**24%**	**0%**	**0%**
Hard Sand	**2%**	**98%**	**0%**	**0%**	**0%**
Soft Sand	**0%**	**0%**	**100%**	**0%**	**0%**
Mud	**80%**	**0%**	**20%**	**0%**	**0%**

Fig. 5. Box diagram and confusion matrix showing the *learning* results of the 38 kHz frequency neuro-fuzzy classifier trained on a set of 200 echoes; percentage of echoes correctly classified in total is **68.5%**.

Summarising, although 38 kHz classifier behaved better during training stage, its generalisation behaviour gave low classification ratio of 56.95%. For this frequency the mud type of bottom was entirely misclassified.

More stable results, in the terms of a smaller variance between learning and generalising results, were obtained for the 120 kHz data i.e. the classification ratio during training and testing varied between 63.5% and 60%. Fewer misclassifications were encountered for the soft sand echoes but unfortunately hard sand correct classification rate dropped to zero.

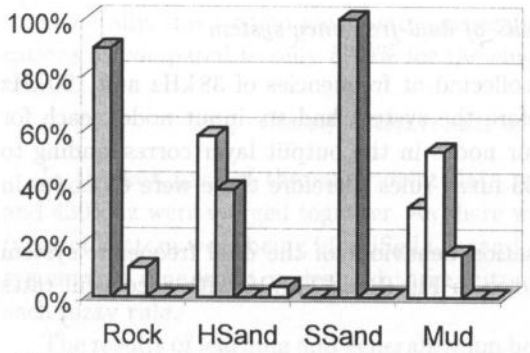

True Class	Classified to Rock	Hard Sand	Soft Sand	Mud	Not known
Rock	**89.3%**	**0.0%**	**10.7%**	**0.0%**	**0.0%**
Hard Sand	**57.7%**	**38.5%**	**0.0%**	**0.0%**	**3.8%**
Soft Sand	**0.0%**	**0.0%**	**100%**	**0.0%**	**0.0%**
Mud	**32.1%**	**52.4%**	**15.5%**	**0.0%**	**0.0%**

Fig. 6. Box diagram and confusion matrix showing the **generalisation** results of the 38 kHz frequency neuro-fuzzy classifier tested on a set of 220 echoes; percentage of echoes correctly classified in total is **56.95%**.

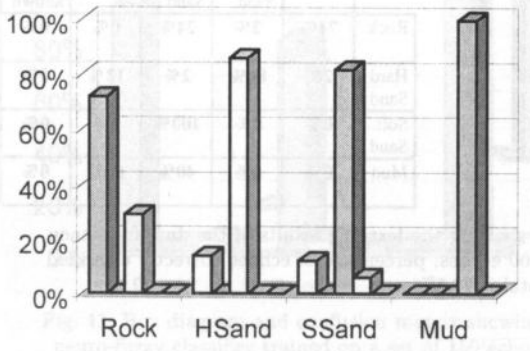

True Class	Classified to Rock	Hard Sand	Soft Sand	Mud	Not known
Rock	**72%**	**0%**	**29%**	**0%**	**0%**
Hard Sand	**14%**	**0%**	**86%**	**0%**	**0%**
Soft Sand	**12%**	**0%**	**82%**	**6%**	**0%**
Mud	**0%**	**0%**	**0%**	**100%**	**0%**

Fig. 7. Box diagram and confusion matrix showing the **learning** results of the 120 kHz frequency neuro-fuzzy classifier trained on a set of 395 echoes; percentage of echoes correctly classified in total is **63.5%**.

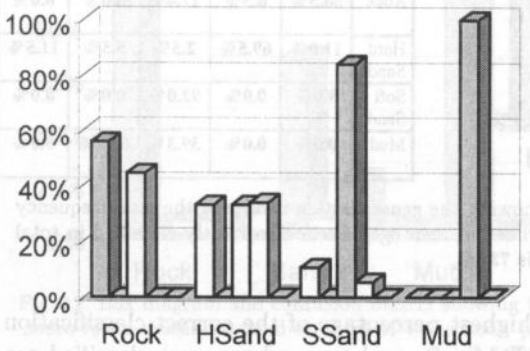

True Class	Classified to Rock	Hard Sand	Soft Sand	Mud	Not known
Rock	**55.6%**	**0.0%**	**44.4%**	**0.0%**	**0.0%**
Hard Sand	**33.1%**	**0.0%**	**33.1%**	**33.8%**	**0.0%**
Soft Sand	**10.7%**	**0.0%**	**84.0%**	**5.33%**	**0.0%**
Mud	**0.0%**	**0.0%**	**0.0%**	**100%**	**0.0%**

Fig. 8. Box diagram and confusion matrix showing the **generalisation** results of the 120 kHz frequency neuro-fuzzy classifier tested on a set of 666 echoes; percentage of echoes correctly classified in total is **59.9%**.

3.3. Classification results of dual-frequency system

In this part of the experiment data collected at frequencies of 38 kHz and 120 kHz was combined and used together. Therefore the system had six input nodes, each for one parameter of each frequency and four nodes in the output layer corresponding to each bottom type. The system created 66 fuzzy rules therefore there were 66 nodes in the hidden layer.

The results of learning and generalisation behaviour of the dual frequency system for combined 38 kHz and 120 kHz are shown in Fig. 9 and Fig. 10 with successful rates marked with grey.

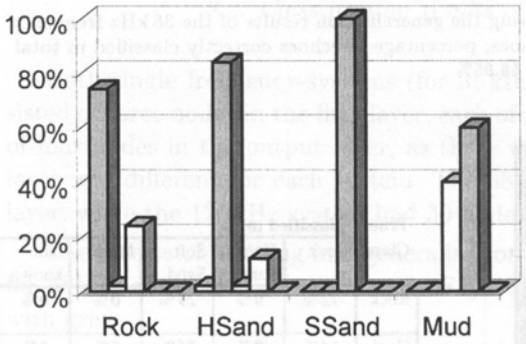

True Class	Classified to: Rock	Hard Sand	Soft Sand	Mud	Not known
Rock	74%	2%	24%	0%	0%
Hard Sand	2%	84%	2%	12%	0%
Soft Sand	0%	0%	100%	0%	0%
Mud	0%	0%	40%	60%	0%

Fig. 9. Box diagram and confusion matrix showing the **learning** results of the dual-frequency neuro-fuzzy classifier training on a set of 200 echoes; percentage of echoes correctly classified in total is **79.5%**.

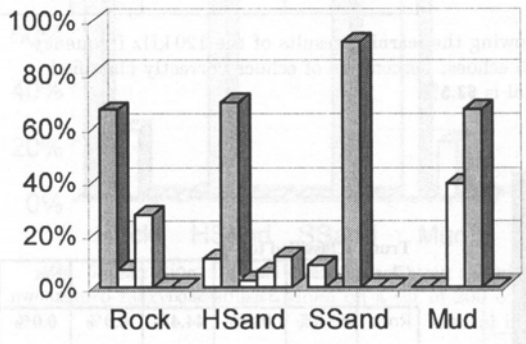

True Class	Classified to: Rock	Hard Sand	Soft Sand	Mud	Not known
Rock	66.3%	6.3%	27.4%	0.0%	0.0%
Hard Sand	11.0%	69.5%	2.5%	5.5%	11.5%
Soft Sand	8.0%	0.0%	92.0%	0.0%	0.0%
Mud	0.0%	0.0%	39.3%	66.7%	0.0%

Fig. 10. Box diagram and confusion matrix showing the **generalisation** results of the dual-frequency neuro-fuzzy classifier tested on a set of 645 echoes; percentage of echoes correctly classified in total is **73.6%**.

The soft sand bottom type had the highest percentage of the correct classification. During learning process as much as 100% of soft sand type echoes were classified correctly, while during testing only 8% of soft sand echoes were misclassified.

Unfortunately, also about 40% of the mud type echoes were misclassified and categorised to the soft sand type. Also the system was not able to assign over 11% of hard sand echoes to any of the classes.

Generally, this system gave better generalisation results of 73.6% of correct classifications as compared to only 59.9% for the single frequency system.

3.4. Classification results of triple-frequency system

In the last part of the experiment data sets for three frequencies 38 kHz, 120 kHz and 420 kHz were merged together. As there was no data for hard sand type, only three types of bottom were being identified i.e. sand, rock and mud. Therefore the neuro-fuzzy system had nine input nodes and three outputs. 45 hidden nodes were created one for each fuzzy rule.

The results of learning and generalisation behaviour of the triple-frequency system for combined 38 kHz, 120 kHz and 420 kHz are shown in Fig. 11 and Fig. 12 with successful rates marked with grey.

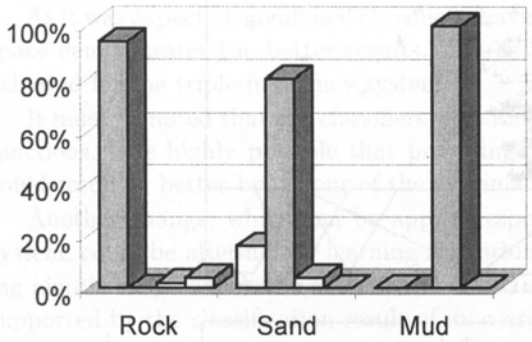

True Class	Classified to Rock	Sand	Soft Sand	Not Known
Rock	**94%**	**0%**	**2%**	**4%**
Sand	**16%**	**80%**	**4%**	**0%**
Mud	**0%**	**0%**	**100%**	**0%**

Fig. 11. Box diagram and confusion matrix showing the **learning** results of the triple-frequency neuro-fuzzy classifier trained on a set of 150 echoes; percentage of echoes correctly classified in total is **91.3%**.

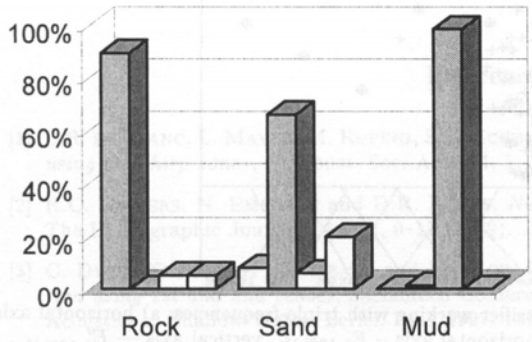

True Class	Classified to Rock	Sand	Mud	Not Known
Rock	**89.5%**	**0.0%**	**5.2%**	**5.3%**
Sand	**8.0%**	**66.0%**	**6.0%**	**20.0%**
Mud	**0.0%**	**1.3%**	**98.7%**	**0.0%**

Fig. 12. Box diagram and confusion matrix showing the **generalisation** results of the triple-frequency neuro-fuzzy classifier tested on a set of 445 echoes; percentage of echoes correctly classified in total is **84%**.

In general, the triple-frequency system gave better generalisation results of 84% of correct classifications as compared to only 59.9% for the single-frequency (120 kHz) system and 73.6% for the dual-frequency one. Unfortunately, the full comparison of these

classifiers is not possible as the single- and dual-frequency systems operated on four sediment types and the triple-frequency classifier only on three classes.

In Fig. 13, sample bottom classification results obtained from the triple-frequency ANFIS system are presented. The data is depicted in form of two-dimensional projection, where the membership functions of two different input parameters are also presented on X-axis and Y-axis. The nine-dimensional input vectors, i.e. vectors containing echoes' parameters are projected on the two-dimensional surface and it is clearly seen that they are not easily separable in the 2D space created in such a way.

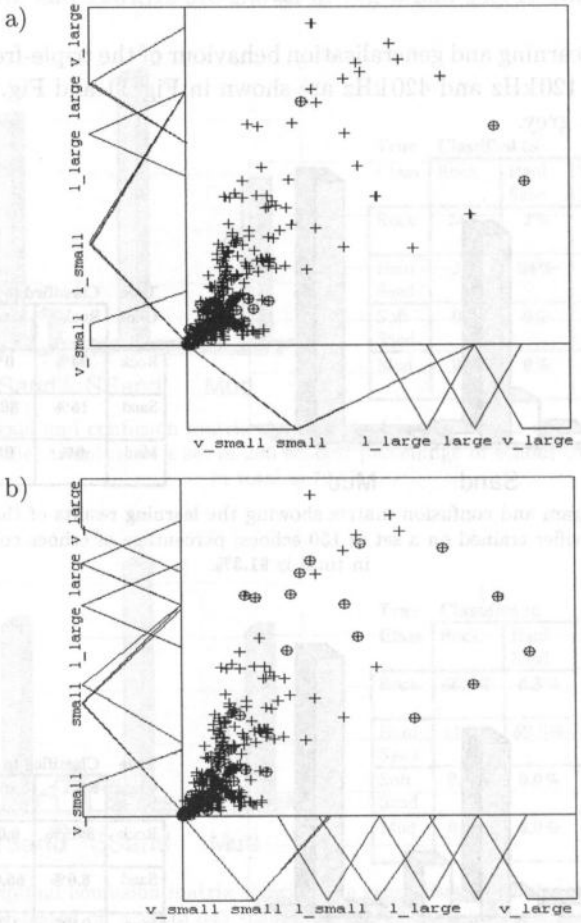

Fig. 13. 2D data projection in the case of classifier working with triple-frequencies: a) horizontal axis — $E_{1,420\text{kHz}}$, vertical axis – $A_{2,420\text{kHz}}$; b) horizontal axis – $E_{1,120\text{kHz}}$, vertical axis — $E'_{1,120\text{kHz}}$.

4. Conclusions

Neuro-fuzzy classifiers have been constructed in NEFClass system and tested on the hydroacoustics data i.e. bottom echoes acquired with a single-beam echosonder at

normal incidence. For each digitised echo's envelope a set of parameters was extracted, viz.: E_1 — energy of the leading part of the first echo, E_1' — energy of the falling part of the first echo, A_2 — amplitude of the second echo. These descriptors where used in the further classification process.

The system constitutes an adaptive three-layered neural network in which the hidden layer's nodes represent fuzzy rules and the weights between the input and second layer denote the membership functions of the input features. Depending on data the number and shape of membership functions and fuzzy rules were chosen and optimised in the process of learning.

Three different systems were created and investigated, starting from the single-frequency classifier (operating on 38 kHz or 120 kHz), then extending its function to the combined dual-frequency (38 kHz and 120 kHz) and triple-frequency (38 kHz, 120 kHz and 420 kHz) systems.

As it was expected, combined classifiers, having higher dimension of the input vector's space demonstrates the better results. The best correct classification rate of 84% was achieved for the triple-frequency system.

It must be noted that the classifiers were limited to have only triangular membership functions. It is highly possible that providing more complex shapes or smooth curves could result in better behaviour of the systems.

Another change, which can be applied especially to the combined multi-frequency system, could be altering the learning algorithm to use some kind of a reinforced learning algorithm, in which the classification decision about one frequency input sample is supported by the classification result of its corresponding sample collected on the other frequency.

Currently the authors are working on the multi-staged neural network architecture for a multi-frequency classifier, in which each single-frequency data are sequentially processed by the corresponding stage.

References

[1] L.R. LE BLANC, L. MAYER, M. RUFINO, S.G. SCHOCK and J. KING, *Marine Sediments classification using the chirp sonar*, J. Acoust. Soc. Am., **91**, 1, 107–115 (1992).

[2] R.C. CHIVERS, N. EMERSON and D.R. BURNS, *New acoustic processing for underway surveying*, The Hydrographic Journal, No. 56, 9–17 (1989).

[3] C. DYER, K. MURPHY, G. HEALD and N. PACE, *An experimental study of sediment discrimination using 1st and 2nd echoes*, Saclantcen Conference Proceedings Series CP-45, High Frequency Acoustics in Shallow Water, Lerici, Italy 1997, 139–146.

[4] M. GENSANE and H. TARAYRE, *Test of sea-bottom discrimination with a parametric array*, Acoustic Letters, **16**, 5, 110–115 (1992).

[5] J.-S.R. JANG, C.-T. SUN and E. MIZUTANI, *Neuro — Fuzzy and Soft Computing — A Computational Approach to Learning and Machine Intelligence*, Prentice-Hall International, Inc., 1997.

[6] Z. ŁUBNIEWSKI and A. STEPNOWSKI, *Sea Bottom Recognition Using Fractal Analysis and Scattering Impulse Response*, Proceedings of the Fourth European Conference on Underwater Acoustics, Rome 1998, 179–184.

[7] J. MACIOŁOWSKA, A. STEPNOWSKI and T.V. DUNG, *Fish Schools and Seabed Identification Using Neural Networks and Fuzzy Logic Classifiers*, Proceedings of the Fourth European Conference on Underwater Acoustics, Rome 1998, 275–280.

[8] D. NAUCK, U. NAUCK and R. KRUSE, *Generating Classification Rules with the Neuro-Fuzzy System NEFCLASS*, Proceedings of Biennial Conference of the North American Fuzzy Information Processing Society (NAFIPS'96), Berkeley, USA 1996.

[9] E. POULIQUEN and X. LURTON, *Seabed Identification Using Echosounder Signal*, European Conference on Underwater Acoustics, Elsevier Applied Science, London and New York 1992, 535.

[10] D. RUTKOWSKA, M. PILIŃSKI and L. RUTKOWSKI, *Sieci neuronowe, algorytmy genetyczne i systemy rozmyte*, Wydawnictwo Naukowe PWN, Warszawa – Lódź 1997.

[11] A. STEPNOWSKI, M. MOSZYŃSKI, R. KOMENDARCZYK and J. BURCZYŃSKI, *Visual Real-Time Bottom Typing System (VBTS) and neural networks experiment for seabed classification*, Proceedings of the Third European Conference on Underwater Acoustics, Heraklion, Crete 1996, 685–690.

[12] J. TĘGOWSKI, *Characteristic features of backscattering of the ultrasonic signals from the sea bottom at the Southern Baltic* [in Polish], Ph.D. Thesis, Institute of Oceanology of Polish Academy of Science, Sopot 1994.

[13] L.A. ZADEH, *Fuzzy sets*, Information and Control, **8**, 338–353 (1965).

ARCHIVES OF ACOUSTICS
24, 3, 379–390 (1999)

ELECTRO-ACOUSTIC TRANSDUCERS ON THE BASIS OF THIN PZT FILMS

Z. SUROWIAK, D. CZEKAJ

University of Silesia, Faculty of Engineering
Department of Materials Science
(41–200 Sosnowiec, 2, Śnieżna St., Poland)
e-mail:surowiak@us.edu.pl

A.A. BAKIROV and V.P. DUDKIEVICH

Rostov State University, Faculty of Physics
Department of Crystal Physics
(SU-344101 Rostov-on-Don, 194, Stachki Ave., Russia)

In the present work PZT-type thin films have been obtained by RF sputtering and electroacoustic transducers characterized by high sensitivity (γ), wide range of measured relative deformations (η) and high working frequencies (ω) were built. Polycrystalline ferroelectric thin films with the perovskite type structure and chemical composition $Pb(Zr_{0.53}Ti_{0.45}W_{0.01}Cd_{0.01})O_3$ have been fabricated by RF sputtering. The films exhibited slightly lower values of dielectric constant, residual polarization and piezoelectric coefficient $d_{33} = 80 \times 10^{-12}$ C/N, as compared with the ceramics of the same chemical composition. The thin films keep such a value of d_{33} up to the Curie point. On the basis of the PZT-type thin films the isotropic and anisotropic piezoelectric sensors were built and investigated. The electrical signal of the isotropic sensors is proportional to the sum of the main components of the relative deformation tensor whereas the signal of the anisotropic sensors depends on the angle ϕ between the sensor axis and the main axis of the deformation tensor of the sample under investigation. The sensors are characterized by high stability of the generated signal.

1. Introduction

There are several reasons for the increasing importance of ferroelectric thin films. Firstly, the trend toward miniaturisation of electronic components has led to the development of thin-film ferroelectric devices performing the same electronic functions, with only a fraction of the volume of devices based on bulk ceramics or single-crystal elements. Secondly, ferroelectric thin films are fast replacing expensive single crystal ferroelectrics. Thin films have the additional designing advantages of a small volume and a large geometrical flexibility over single crystals. Thirdly, new areas of application are being identified that utilise new device concepts, exploiting properties that are unique to both thin films and ferroelectric materials.

It is a common knowledge that for applications of ferroelectric thin films in electronics and optical devices, bulk ferroelectric properties must be achieved in thin films.

Therefore, a high-quality ferroelectric thin film should possess these properties: a stoichiometric composition, a dense and crystalline microstructure, a single-crystal or, at least, a preferentially oriented polycrystalline structure and uniformity over large areas.

Ferroelectric thin films of different chemical composition (e.g. $BaTiO_3$, $PbTiO_3$, $Pb(Zr,Ti)O_3$, $(Pb,La)(Zr,Ti)O_3$, $KNbO_3$, $LiNbO_3$, $(Sr,Ba)TiO_3$, $Bi_4Ti_3O_{12}$, and an organic polymer polyvinylidene fluoride) have been extensively studied for a wide variety of electrical and optical applications. Let us mention a few of them, namely: high dielectric capacitors [1, 2] and nonlinear capacitors [3], piezoelectric sensors of dynamical deformation [3–5], electroacoustic transducers [6], high-frequency surface acoustic wave (SAW) devices [7, 8], ultrasonic sensors [9], pyroelectric sensors and sensor arrays [3, 10–12], ferroelectric memory cells [13–17], optical waveguide devices or optical modulators [17], ferroelectric gates (FETs) [18], metal/insulator/semiconductor transistors (MIST) devices and many others [e.g. 19–22]. However, lead zirconate — titanate (PZT) — type thin films have received the most intensive study and will be emphasized in this article.

The reported methods to produce PZT films include, among others, various vapour-phase deposition techniques such as plasma and ion-beam sputter deposition, pulsed laser-ablation deposition, electron-beam or oven-induced evaporation for molecular-beam epitaxy, sol-gel process, metallorganic decomposition, and metallorganic chemical vapour deposition. However, additional research is still necessary to optimize the techniques to produce device-quality films on large semiconductor substrates in a way that is fully compatible with existing semiconductor process technology. Of all the reported techniques, the radio frequency (RF) sputtering technique appears to be promising because it offers the advantages of high deposition rates, film uniformity, composition control, high film densities and compatibility with integrated circuit technology [23, 24].

In the present work the lead-zirconate titanate (PZT)-type thin films have been obtained by RF sputtering. The sputtering parameters have been optimised in order to assure the composition transfer between the target and the film. Piezoelectric characteristics of the films were measured and electroacoustic transducers characterized by high sensitivity (γ), wide range of measured relative deformations (η) and high working frequencies (ω) were built.

2. Technology of the thin film preparation

The thin PZT films were obtained by RF sputtering. Two sputtering systems were used for the thin film preparation. A system I made it possible to sputter powdered target obtained from crushed ceramics of the chemical composition $Pb(Zr_{0.53}Ti_{0.45}W_{0.01}Cd_{0.01})O_3$. The coarse-grained powder was placed in the quartz vessel of 0.1 m in diameter and 5 mm high and covered the bottom of the vessel with a 2–5 mm thick layer. The RF generator was operating in the continuous mode during deposition.

A system II made it possible to sputter a disk target of $Pb(Zr_{0.53}Ti_{0.45}W_{0.01}Cd_{0.01})O_3$ ceramics obtained by hot pressing. Water-cooling of the cathode and the pulse operation mode of the RF generator avoid overheating of the target during sputtering.

Table 1. Technological conditions of the thin film preparation.

	SYSTEM I	SYSTEM II
material	coarse-grained powder of $Pb(Zr_{0.53}Ti_{0.45}W_{0.01}Cd_{0.01})O_3$ ceramics; 0.15 – 0.40 mm	hot-pressed disk target of $Pb(Zr_{0.53}Ti_{0.45}W_{0.01}Cd_{0.01})O_3$
heating	electron-ion bombardment; $T_s = 600 - 1073$ K	resistance heater $T_s = 600 - 1073$ K
generator	continuous mode of operation: $f = 13.6$ MHz; $U_a = 5$ kV; $i_a = 0.8$ A; $N = 2.5$ kW	pulse mode of operation: pulse duration $\tau = 0.1 - 1.2$ ms; pulse period to pulse length ratio $\gamma = 2 - 7$
working gas	oxygen; $p = 30 - 80$ Pa	oxygen; $p = 20 - 180$ Pa
substrates	metal foils and dielectric plates $20 \times 30 \times 0.1$ mm^3	platinum, stainless steel, monocrystalline mica, polycor
substrate-to-target distance	8 – 16 mm	8 – 16 mm

More detailed technological conditions used for the thin film preparation are presented in Table 1.

3. Chemical composition

Homogeneity check and investigation of the thin film composition have been performed by X-ray micro-probe analysis. The results are shown in Fig. 1 [25].

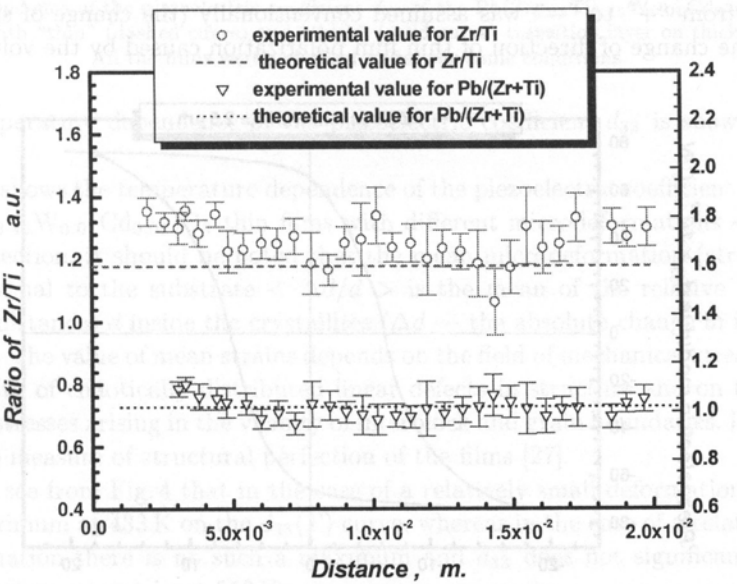

Fig. 1. Results of the analysis of homogeneity of the chemical composition of the PZT-type thin film (a probe was moved along a straight line parallel to an edge of the film): 1 – Zr/Ti; 2 – Pb/(Zr + Ti). Stoichiometric ratios of suitable components in the target are marked by dashed lines.

The stoichiometric ratio of the metallic components in the target is shown by dotted lines. As an indication of the measuring error the maximal deviations from the average value of 10 measurements are marked in the figure. As can be seen from Fig. 1 the thin PZT films obtained under optimal technological conditions are characterized by high homogeneity of the chemical composition and stoichiometry close to that of the target.

4. Piezoelectric characteristics

To obtain a piezoelectric effect one has to polarize thin films in an external electric field. The most stable polarization state was achieved by polarising them with the following conditions: sawtooth voltage with $E = 8 \times 10^7$ V/m, pulse arising time $t_1 = 5$ s, pulse decreasing time $t_2 = 5$ s and filling factor $k = 2$ (k is a ratio of the pulse period to pulse duration) was applied to the samples; at the same time the samples were heated to $T = 573$ K (in $t = 20$ minutes) and then cooled to room temperature in the same time so the total time of heat treatment was 40 min.

Piezoelectric properties are often described in terms of piezoelectric charge coefficients. The piezoelectric coefficient d_{ijk} is a third-rank tensor that relates a strain of a piezoelectric ceramic sample to an externally applied electric field. A contracted notation is often used so that tensor components may be written more easily. In the present study, the component d_{33} of the piezoelectric coefficient of the thin film was measured by a quasi-static method described in detail elsewhere [26].

Figure 2 shows the dependence of the piezoelectric coefficient d_{33} on the voltage U_0 which changes linearly with time at a rate of ± 0.003 V/s. A change of sign of piezoelectric coefficient from "+" to "−" was assumed conventionally (the change of sign of d_{33} is given by the change of direction of thin film polarization caused by the voltage $\pm U$).

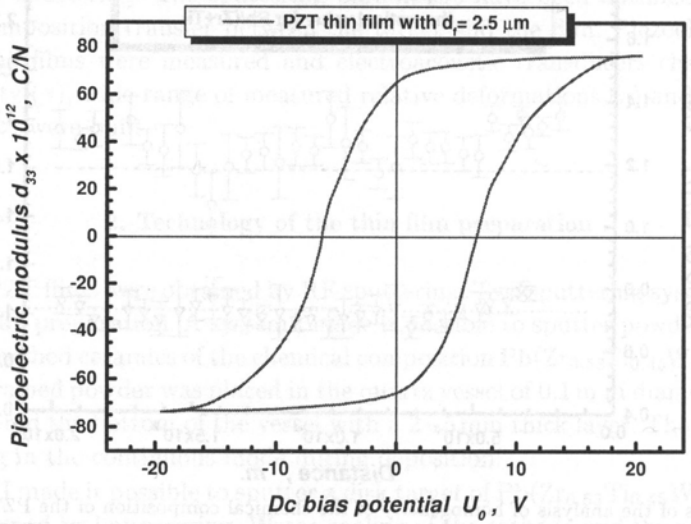

Fig. 2. Dependence of the piezoelectric coefficient d_{33} on the voltage U_0 for a PZT-type thin film with a thickness of 2.5 μm.

It has been stated that the d_{33} value changes with the thickness of the film and that the saturation of the dependence is achieved for the thin film thickness of about 2.5 – 3.0 μm at the level of $d_{33} = 80 \times 10^{-12}$ C/N ("thin" transition layer films, stainless-steel substrates; the films were polarized under the same conditions), whereas for the 5 – 6 μm thick PZT films the saturation is achieved at the level of $d_{33} = 25 - 30 \times 10^{-12}$ C/N ("thick" transition layer; measuring field $E_0 = 25 \times 10^6$ V/m). To illustrate the above mentioned effects the thickness dependencies of the component d_{33} of the piezoelectric coefficient are shown in Fig. 3.

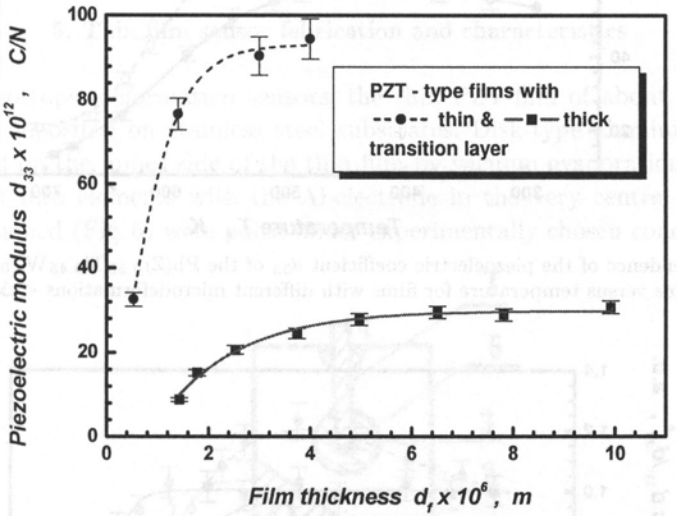

Fig. 3. Dependence of the piezoelectric coefficient d_{33} of the $Pb(Zr_{0.53}Ti_{0.45}W_{0.01}Cd_{0.01})O_3$ thin films with "thin" (dashed curve) and "thick" (solid curve) transition layer on thickness. All the films were polarized under the same conditions.

The temperature dependence of the piezoelectric coefficient d_{33} is shown in Fig. 4 and Fig. 5.

Figure 4 shows the temperature dependence of the piezoelectric coefficient d_{33} for the $Pb(Zr_{0.53}Ti_{0.45}W_{0.01}Cd_{0.01})O_3$ thin films with different microdeformations $< \Delta d/d >$. In this connection, it should be noted that the mean microdeformation (strain) in the direction normal to the substrate $< \Delta d/d >$ is the mean of the relative changes in interplanar distances d inside the crystallites (Δd — the absolute change in interplanar distances d). The value of mean strains depends on the field of mechanical stresses arising in the vicinity of chaotically distributed linear defects in structure and on the field of mechanical stresses arising in the vicinity of interblock and grain boundaries. It is usually taken as the measure of structural perfection of the films [27].

One can see from Fig. 4 that in the case of a relatively small deformation there is a diffused maximum at 433 K on the $d_{33}(T)$ curve, whereas in the case of a relatively large microdeformation there is no such a maximum and d_{33} does not significantly change with temperature up to about 513 K.

From the point of view of the temperature stability of the electro-acoustic transducers it is better to use thin films of the second type for fabrication of such transducers.

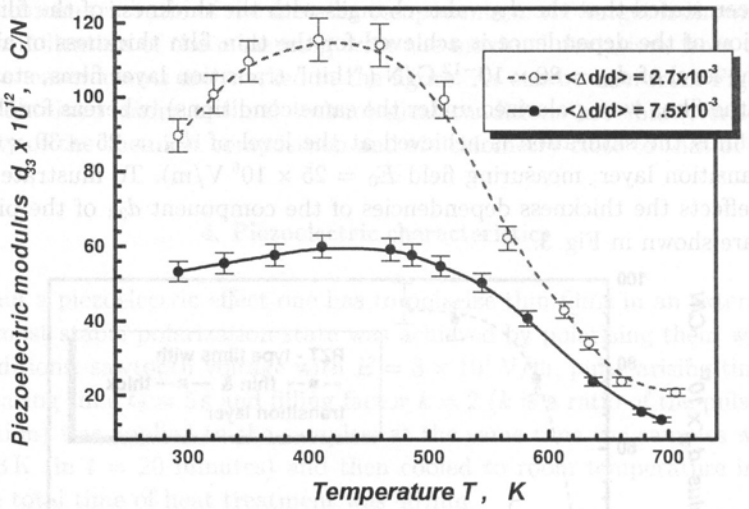

Fig. 4. Dependence of the piezoelectric coefficient d_{33} of the $Pb(Zr_{0.53}Ti_{0.45}W_{0.01}Cd_{0.01})O_3$ thin films versus temperature for films with different microdeformations $< \Delta d/d >$.

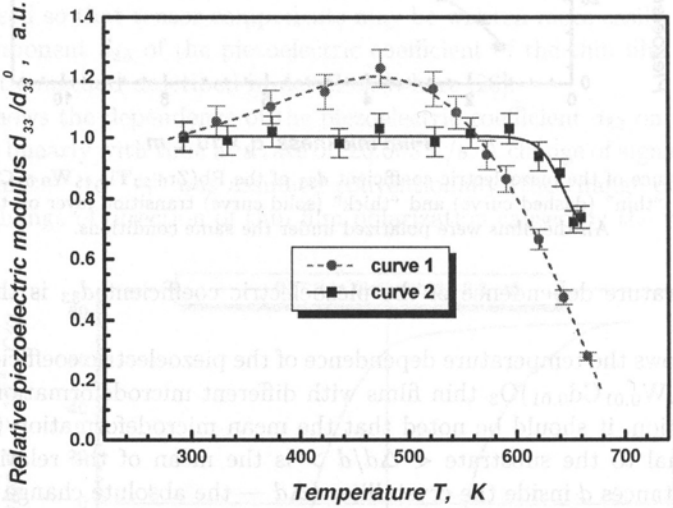

Fig. 5. Dependence of the piezoelectric coefficient d_{33} of PZT-type thin films with a thickness of 2.5 μm on temperature (curve 1) and dependence of d_{33} on temperature of primary heat treatment for measurements carried out at room temperature (curve 2).

However, it is worth noting that the thin films exhibit greater temperature stability of the piezoelectric coefficient than PZT ceramics do. This can be seen in Fig. 5 (curve 1). The $d_{33}(T)$ curve has a slight slope and there is no sharp peak near T_C (which appears for samples of ceramics). The increase in d_{33} with increasing T ends at a temperature $T \approx 593\,\mathrm{K}$. This is related to changes in $\varepsilon(T)$ and $P_S(T)$: the dielectric permittivity consistently increases in value while the spontaneous polarization consistently decreases

when temperature increases. Both effects are characteristic for ferroelectrics with a diffuse phase transition. Curve 2 in Fig. 5 shows the temperature stability of the thin film polarization state when the action time of the raised temperature is short. This curve was obtained as follows: the polarized sample was first heated to the designated temperature and kept at that temperature for 5 minutes and then cooled to room temperature; after that heat treatment the d_{33} was measured. It is worth noting, that rather a strong piezoelectric activity exists even after heating the sample to the Curie point.

5. Thin film sensor fabrication and characteristics

To build isotropic deformation sensors, the thin PZT-film of about 2.0 – 2.5 μm in thickness was deposited on stainless steel substrates. Disk-type aluminium electrodes were deposited on the upper side of the thin film by vacuum evaporation. These structures were cut into elements with the Al-electrode in the very centre. The thin film capacitors obtained (Fig. 6) were poled under experimentally chosen conditions.

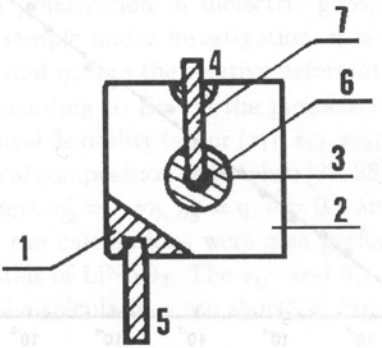

Fig. 6. Thin film isotropic sensor of dynamical deformation: diagram of sensor construction: 1 – substrate; 2 – upper surface of thin PZT film (not shaded); 3 – upper electrode; 7, 5 – electrical conductors welded on upper electrode (7) and substrate (5); 6 – silver drop or mark of point weld; 4 – electrical insulation of conductor (7) from substrate edge (1).

To obtain anisotropic deformation sensors, the PZT thin film was deposited on ceramic substrates (e.g. polycor). Planar interdigital Al-electrodes were deposited by photolithography on the upper side of the film. The dielectric gap width was equal to the width of a single "finger" of the electrode and was 12 μm, the length was 5 μm and the total number of "fingers" was 200 (Fig. 7).

In Fig. 8 the dependence of the piezoelectric signal V of the isotropic sensor on the value of the sum of the deformation tensor main components $\eta(1-\nu)$, where ν is the Poisson ration for steel ($\nu \approx 0.3$) and η is the relative deformation of the surface under investigations is presented [4]. One can see that the dependence is a linear one within the range of the investigated deformation. The lower limit of recorded relative deformation $\eta_{\min} = 10^{-9}$ is conditioned by the influence of acoustic noise, which can cause out-of-control deformation of the beam surface layer of $\gamma = 0.5 \times 10^{-10}$ order of magnitude. The upper limit of the recorded deformation $\eta_{\max} = 10^{-10}$ corresponds to

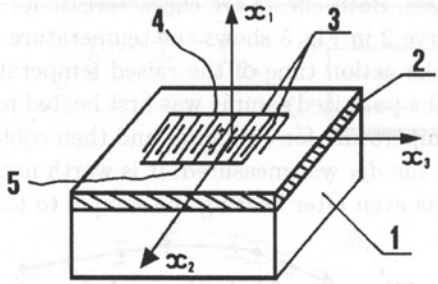

Fig. 7. Anisotropic sensor of dynamical deformation: 1 – polycor substrate; 2 – thin ferroelectric film; 3 – planar comb-shaped electrodes; 4, 5 – electrical conductors. The arrows show the directions of polarization in the dielectric gaps.

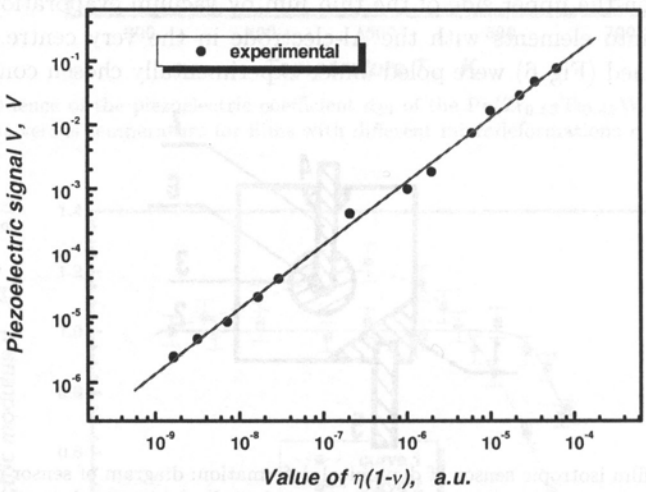

Fig. 8. Dependence of the piezoelectric signal V of isotropic sensor on the value of the sum of the deformation tensor main components $\eta(1-\nu)$.

the plastic deformation threshold of the beam material. The basic parameters of the isotropic ferroelectric thin film deformation sensors are presented in Table 2. The values of the particular parameters have been obtained by complex investigations of many sensors under both laboratory and industrial conditions.

Taking into account the assumptions we used in describing the isotropic deformation sensor [4] as well as considering the deformation of the thin film in the direction normal to the substrate surface, one can show that the intensity E_3 of the electric field in the sensor (along the X_3 axis) is:

$$E_3 = h_{31}\left[-\left(\frac{s_{12}s_{33}-s_{13}^2}{s_{11}s_{33}-s_{13}^2}+1\right)\left(\eta_2'\cos^2\phi+\eta_3'\sin^2\phi\right)\right.$$
$$\left.-\frac{s_{13}(s_{11}-s_{12})}{s_{11}s_{33}-s_{13}^2}\left(\eta_2'\sin^2\phi+\eta_3'\cos^2\phi\right)\right]-h_{33}\left(\eta_2'\sin^2\phi+\eta_3'\cos^2\phi\right), \qquad (1)$$

Table 2. Sensor parameters.

1. Sensitivity	η, V ..... 10^3
	μ, C ..... 10^{-6}
2. Range of deformation	$\Delta l/l$, ... $10^{-9} - 10^{-4}$
3. Range of frequency	Hz, ... $10^{-3} - 10^7$
4. Range of temperature	K, ... $77 - 573$
5. Electric capacitance	pF, ... 1000
6. Dimensions of an active element	mm^3, ... $2 \times 3 \times 0.1$
7. Mass	g, ... ≤ 0.01
8. Impact strength	m/s^2, ... 10^6
9. No time lag	

where s_{ij} are the elements of the mechanical compliance matrix, h_{ij} are the elements of the piezoelectric coefficient matrix, ϕ is the angle between the axis of the sensor (direction of the thin film polarization in dielectric gaps) and the main axis of the deformation tensor of the sample under investigation, η is the relative deformation in the superficial beam layer, and η'_{ij} are the relative deformation tensor components.

For estimation of E_3 according to Eq. (1) the piezoelectric constants (h_{31} and h_{33}) and elements of the mechanical flexibility tensor ($s_{11}, s_{12}, s_{13}, s_{33}$) for polarized PZT-type ceramics of the same chemical composition were taken [22, 28] together with the following values of the other parameters: $\eta'_2 = -\nu\eta$, $\eta'_3 = \eta$, $\nu = 0.3$ and $\eta = 5 \times 10^{-6}$. To compare with the PZT-type sensor the calculations were also performed for polarized $BaTiO_3$ ceramics and for monocrystals of $LiNbO_3$. The s_{ij}- and h_{ij}-parameters are summarised in Table 3. The results of the calculations are shown in Fig. 9.

Table 3. Piezoelectric and mechanical constants chosen for calculations.

Quantity	PZT (ceramics)	$BaTiO_3$ (ceramics)	$LiNbO_3$ (monocrystal)
h_{31}, V/m	-0.78×10^9	0.35×10^9	0.55×10^9
h_{33}, V/m	4.58×10^9	1.48×10^9	5.90×10^9
S^D_{33}, m^2/N	7.50×10^{-12}	6.73×10^{-12}	4.67×10^{-12}
S^D_{11}, m^2/N	10.40×10^{-12}	8.18×10^{-12}	5.15×10^{-12}
S^D_{13}, m^2/N	-2.40×10^{-12}	-1.95×10^{-12}	-1.28×10^{-12}
S^D_{12}, m^2/N	-4.70×10^{-12}	-2.98×10^{-12}	-0.53×10^{-12}

It is evident from both theoretical calculations and the experimental data given in Fig. 9 that: i) there is an angle $\phi = \phi_0$ for which there is no piezoelectric signal ($E_3(\phi_0) = 0$); ii) the intensity of the electric field E_3 for the $LiNbO_3$ sensor is greater than the $BaTiO_3$ sensor signal; the angle $\phi_0 = 64.53°$ for the $LiNbO_3$ sensor is greater than the angle $\phi_0 = 58.51°$ for the PZT sensor and $\phi_0 = 57.66°$ for the $BaTiO_3$ sensor; iii) experimental and theoretical values of E_3 differ considerably (E_3 exp. $\geq 70\% E_3$ theor.) whereas experimental and theoretical values of ϕ_0 are fairly similar (ϕ_0 exp. $\geq 95\% \phi_0$ theor.).

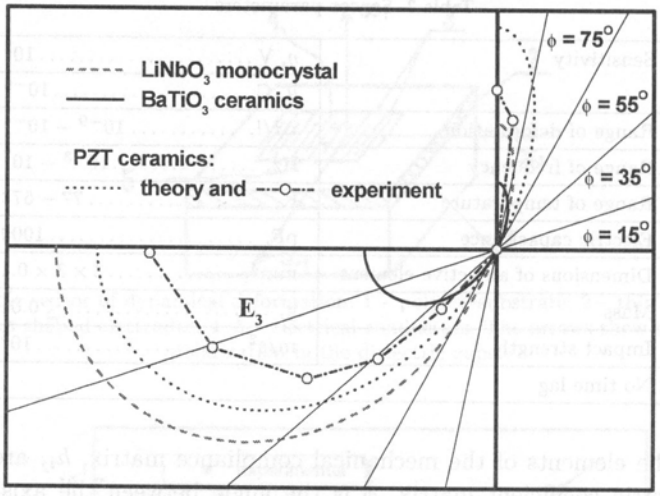

Fig. 9. Dependence of the anisotropic sensor signal E_3 on the angle ϕ between its axis and the main axis of the sample deformation tensor for $LiNbO_3$, $BaTiO_3$ and PZT-based sensors. The change in sign of E_3 should be interpreted as the change in polarity of the piezoelectric signal.

6. Conclusions

Polycrystalline ferroelectric thin films with the perovskite type structure and chemical composition $Pb(Zr_{0.53}Ti_{0.45}W_{0.01}Cd_{0.01})O_3$ have been fabricated by RF sputtering. The films exhibited slightly lower values of dielectric constant, residual polarization and piezoelectric coefficient $d_{33} = 80 \times 10^{-12}$ C/N, compared with ceramics of the same chemical composition. The thin films keep such a value of d_{33} up to the Curie point.

On the basis of the PZT-type thin films, isotropic and anisotropic piezoelectric sensors were built and investigated. The electrical signal of the isotropic sensors is proportional to the sum of the main components of the relative deformation tensor whereas the signal of the anisotropic sensors depends on the angle ϕ between the sensor axis and the main axis of the deformation tensor of the sample under investigation. The sensors are characterized by high stability of the generated signal.

Acknowledgements

The authors would like to thank the Committee for Scientific Research (KBN), Poland, for financial support under grant No. 7T08D 005 17.

References

[1] K. Okamoto, Y. Nasu and Y. Hamakawa, *Low-treshold-voltage thin-film electroluminescent devices*, IEEE Trans. Elec. Dev., **ED-28**, 6, 698–702 (1981).

[2] R. KHAMANKAR, J. KIM, B. JIANG, C. SUDHAMA, P. MANIAR, R. MOAZZAMI, R. JONES and J. LEE, *Impact of post processing damages on performance of high dielectric constant PLZT thin film capacitors for ULSI DRAM applications*, International Electron Devices Meeting, San Francisco, CA, December 11-14, 1994, IEDM Technical Digest, 337–340 (1994).

[3] R. WASER, *Recent trends in electroceramic thin films. Capacitors, pyroelectric sensors and piezoelectric devices*, [in:] Electroceramics V International Conference on Electronic Ceramics and Applications, J.L. BAPTISTA, J.A. LABRINCHA, P.M. VILARINHO [Eds.], University of Aveiro, Portugal 1996, 293–297.

[4] Z. SUROWIAK, D. CZEKAJ, A.A. BAKIROV and V.P. DUDKEVICH, *Dynamical deformation sensors based on thin ferroelectric PZT films*, Thin Solid Films, **256**, 226–233 (1995).

[5] D. CZEKAJ, Z. SUROWIAK, A.A. BAKIROV and V.P. DUDKEVICH, *Piezoelectric sensors of mechanical strains on the basis of the thin* $LiNbO_3$ *and* $BaTiO_3$ [in Polish], Akustyka Molekularna i Kwantowa, **15**, 43–57 (1994).

[6] N.F. FOSTER, *The deposition and piezoelectric characteristics of sputtered lithium niobate films*, J. Appl. Phys., **40**, 1, 420–423 (1969).

[7] J. DUDEK, *Piezoelectric acoustotransducers SAW on the basis of* $Pb(Zr,Ti)O_3$, The 8-th Piezoelectric Conference PIEZO'94, 5-7 October 1994, Zakopane, Poland, Proceedings, Tele & Radio Research Institute, 359–364 (1995).

[8] H. ADACHI, T. MITSUYA, O. YAMAZAKI and K. WASA, *Ferroelectric* $(Pb,La)(Zr,Ti)O_3$ *epitaxial thin films on sapphire grown by RF-magnetron sputtering*, J. Appl. Phys., **60**, 736–741 (1986).

[9] Z. SUROWIAK and V.P. DUDKEVICH, *Thin ferroelectric films* [in Polish], Wyd. Uniw. Śl., Katowice 1996, p. 331.

[10] P. MURALT, *PZT thin films for sensors and actuators*, [in:] Electroceramics V, International Conference on Electronic Ceramics and Applications, J.L. BAPTISTA, J.A. LABRINCHA, P.M. VILARINHO [Eds.], University of Aveiro, Portugal 1996, 11–18.

[11] B. WILLENG, M. KOHLI, K. BROOKS, P. MURALT and N. SETTER, *Pyroelectric thin film sensor arrays integrated on silicon*, Ferroelectrics, **201**, 147–156 (1997).

[12] J. KULEK, J.L. CHARTIER, R. LEBIHAN, L.M. HAFID and B. HILCZER, *Pyroelectric response and thermally stimulated current of PZT thin films*, Ferroelectric Letters, **22**, 83–88 (1997).

[13] D. BONDURANT and F. GNADINGER, *Ferroelectrics for nonvolatile RAMs*, IEEE Spectrum, **7**, 30–33 (1989).

[14] J.F. SCOTT and C.A. PAZ DE ARAUJO, *Ferroelectric memories*, Science, **246**, 1400–1405 (1989).

[15] J.F. SCOTT, *Ferroelectric memories*, Physics World, **2**, 46–50 (1995).

[16] A.C. PAZ DE ARAUJO, L.D. MCMILLAN, B.M. MELNIK and J.D. CUCHIARO, *Ferroelectric memories*, Integrated Ferroelectrics, **104**, 241–256 (1990).

[17] A.I. KINGON and S.K. STREIFFER, *Recent trends in electroceramic thin films: II. DRAMS, nonvolatile memories, and optical devices*, [in:] Electroceramics V, International Conference on Electronic Ceramics and Applications, J.L. BAPTISTA, J.A. LABRINCHA, P.M. VILARINHO [Eds.], University of Aveiro, Portugal 1996, 299–303.

[18] T. NAKAMURA, Y. NAKAO, A. KAMISAWA and H. TAKASU, *Ferroelectric memory FET with* Ir/IrO_2 *electrodes*, Integrated Ferroelectrics, **9**, 179–187 (1995).

[19] K.R. UDAYAKUMAR, J. CHEN, A.M. FLYNN, S.F. BART, L.S. TAVROV, D.J. EHRLICH, L.E. CROSS and R.A. BROOKS, *Ferroelectric thin films for piezoelectric micromotors*, Ferroelectrics, **160**, 347–356 (1994).

[20] W.Y. PAN, S. SUN and B.A. TUTTLE, *Electromechanical and dielectric instability induced by electric field cycling in ferroelectric ceramic actuators*, Smart Mater. Struct., **1**, 286–293 (1992).

[21] D.L. POLLA and L.F. FRANCIS, *Ferroelectric thin films in microelectromechanical systems applications*, MRS Bulletin, **21**, 7, 59–65 (1996).

[22] Y. XU, *Ferroelectric materials and their applications*, North–Holland, New York 1991, pp. 206–215.

[23] R. BRUCHHAUS, H. HUBER, D. PITZER and W. WERSING, *Deposition of ferroelectric PZT thin films by planar multi-target sputtering*, Ferroelectrics, **127**, 137–142 (1992).

[24] O. AUCIELLO, A.I. KINGON and S.B. KRUPANIDHI, *Sputter synthesis of ferroelectric films and heterostructures*, MRS Bulletin, **21**, 6, 25–30 (1996).

[25] Z. SUROWIAK, D. CZEKAJ, A.A. BAKIROV and V.P. DUDKEVICH, *Chemical composition and structure of thin PZT-type ferroelectric films* [in Polish], Archiwum nauki o materiałach, **16**, 1, 75–104 (1995).

[26] Z. SUROWIAK, D. CZEKAJ, A.M. MARGOLIN, E.V. SVIRIDOV, V.A. ALESHIN and V.P. DUDKEVICH, *The structure and the piezoelectric properties of thin* $Pb(Zr_{0.53}Ti_{0.45}W_{0.01}Cd_{0.01})O_3$ *films*, Thin Solid Films, **214**, 78–83 (1992).

[27] Z. SUROWIAK, D. CZEKAJ, A.A. BAKIROV, E.V. SVIRIDOV and V.P. DUDKEVICH, *The structure and dielectric properties of thin PZT-type ferroelectric films with a diffuse phase transition*, Integrated Ferroelectrics, **8**, 267–282 (1995).

[28] B. JAFFE, W.R. COOK and H. JAFFE, *Piezoelectric ceramics*, Academic Press, London 1971, 137–183.

ARCHIVES OF ACOUSTICS
24, 3, 391–399 (1999)

DIELECTRIC AND ELECTROSTRICTIVE PROPERTIES OF FERROELECTRIC RELAXORS

Z. SUROWIAK, E.G. FESENKO* and R. SKULSKI

University of Silesia, Faculty of Engineering
Department of Materials Science
(41–200 Sosnowiec, 2, Śnieżna St., Poland)
e-mail: surowiak@us.edu.pl

* Rostov State University,
PIEZOPRIBOR
(344–104 Rostov-on-Don, 10, Milchakova St., Russia)

On the basis of ferroelectric relaxors electrostrictive ceramics has been obtained. Searching for electrostrictive ceramic transducers with optimal electromechanical parameters include the following: 1) investigation of different types of complex oxides with the perovskite structure (OPS): ferroelectric, antiferroelectric, non-polar; 2) investigation of OPS with different degree of the cation order; 3) measurements of the electrostrictive coefficient (Q), Curie–Weiss constant (C), coefficient of linear thermal expansion (λ), polarization (P) and permittivity (ε); 4) X-ray structure analysis. The following rules have been stated out during the experimental investigations: 1) values of the electrostrictive coefficients (Q_{ijkl}) depend not only on the chemical constitution of OPS but, first of all, on the degree of cation order (i.e. the coefficients increase with an increase in the degree of cation order: non-ordered state — simple state — ordered state; 2) products of the hydrostatic electrostrictive coefficient (Q_h) and the Curie–Weiss (C) constant of all ferroelectric and antiferroelectric OPS are nearly equal; 3) value of the hydrostatic electrostrictive coefficient (Q_h) is nearly proportional to the linear thermal expansion coefficient square (λ^2). Taking into account the above mentioned rules the detailed and systematic investigations of OPS with non-ordered cations and high value of the Curie-Weiss constant (C) and permittivity (ε) were carried out. In such OPS high value of induced polarization leads to considerable electrostrictive deformation described by the M_{ijkl} tensor ($M_{ijkl} \approx Q_{ijkl}\varepsilon_r^2$). One can mention $PbNb_{2/3}Mg_{1/3}O_3$ and solid solution prepared on the basis of $PbNb_{2/3}Mg_{1/3}O_3$ as an example. Devices fabricated on the basis of electrostrictive ceramics provide a relative displacement of about 10^{-3} what is few times more than the one provided by devices on the basis of piezoelectric ceramics.

1. Introduction

Among ferroelectrics, *relaxors* are mainly characterized by:

1) a very broad permittivity (ε) vs. temperature peak;

2) hysteresis loops above the temperature T_m (the temperature at which the permittivity is a maximum, i.e., ε_m);

3) a frequency dependence of permittivity maximum ($\varepsilon_m(\omega)$) and of $T_m(\omega)$;

4) a depolarization temperature T_d (as defined in reference [1]) lower than the temperature T_m (for $\nu = 10^1 - 10^6$ Hz);

5) no evidence for any symmetry transformation;

6) when the temperature is higher than T_m, $\varepsilon(T)$ does not obey the Curie–Weiss law:

$$\varepsilon = \varepsilon_0 + \frac{C}{T - T_0} \approx \frac{C}{T - T_0}, \tag{1}$$

where C — the Curie–Weiss constant; T_0 — the Curie–Weiss temperature ($T > T_0$, T_0 is different from the Curie point T_c; in the case of the first-order phase transition, $T_0 < T_c$, while for the second-order phase transition $T_0 = T_c$); ε_0 — the temperature-independent term ε_0 can be neglected, because it is much smaller than the term $C/(T - T_0)$ when T is near T_0.

In fact, $\varepsilon(T)$ of the relaxors changes with T in the following manner:

$$\frac{1}{\varepsilon} - \frac{1}{\varepsilon_m} = C'(T - T_m)^n, \tag{2}$$

where C' — a constant, n — a constant ($1 < n < 2$).

It has been shown that the largest relative strains (η) of the electrostrictive nature take place in the case of the *ferroelectric relaxors* and of the *ferroelectrics with a diffuse phase transition*. The value of such strains ($\sim 10^{-3}$) may exceed relative strains of magnetostrictive or piezoelectric nature ($10^{-4} - 10^{-5}$).

When the electric field is applied to a dielectric material, it produces a strain proportional to the square of the field ($\eta \sim E^2$). This effect is called the *electrostrictive effect*. Electrostrictive effect is a quadratic effect and the electrostrictive strain is not related to the sign of the applied field. In fact, *electrostriction is a result of the polarization P induced by the applied field* and the electrostrictive strain is directly proportional to the square of the polarization ($\eta \sim P^2$). Unlike the piezoelectric effect, electrostriction may occur in all crystals whether or not the crystals have polarity.

In the case of ferroelectric crystal (e.g. $BaTiO_3$ in $T < T_c$) the electromechanical effect has a complex nature ($\eta(E)$ effect must be a function of the domain structure, the spontaneous (P_s) and induced (P_{ind}) polarizations, etc.).

In the case of a *centrosymmetric crystal* (e.g., barium titanate in its paraelectric state), the electrostrictive effect has rather simple form. In this case, the equations of state for stress (σ_{ij}) and for strain (η_{ij}) components can be written as:

$$\sigma_{ij} = c^P_{ijkl}\eta_{ij} + q_{ijkl}P_kP_l, \tag{3}$$

$$\sigma_{ij} = c^E_{ijkl}\eta_{ij} + m_{ijkl}E_kE_l, \tag{4}$$

$$\eta_{ij} = s^P_{ijkl}\sigma_{kl} + Q_{ijkl}P_kP_l, \tag{5}$$

$$\eta_{ij} = s^E_{ijkl}\sigma_{kl} + M_{ijkl}E_kE_l, \tag{6}$$

where $c^{P(E)}_{ijkl}$ — the elastic stiffness constants at constant electric field (the superscript E) or polarization (the superscript P), $s^{P(E)}_{ijkl}$ — the elastic compliance constants at constant E or P.

Equations (3) – (6) are called *elestrostriction equations*. In each of these equations, the first term on the right-hand side corresponds to Hooke's law and the second term to the electrostrictive effect. These equations define the electrostrictive coefficients Q, q, M and m. Each of the four electrostrictive coefficients is a fourth-rank tensor. Among these four coefficients, Q and M are most useful and its unit are $\mathrm{m}^4/\mathrm{C}^2$ and $\mathrm{C}^2/\mathrm{N}^2$ respectively. The relationship between Q_{ijkl} and M_{ijkl} is:

$$M_{ijkl} = \varepsilon_0^2 \left(\varepsilon_r^\sigma - 1\right)^2 Q_{ijkl}, \tag{7}$$

where ε_0 — the permittivity of free space ($\varepsilon_0 = 8.854 \cdot 10^{-12}\,\mathrm{F/m}$), ε_r^σ — the relative permittivity at stress σ = const., or $\sigma = 0$ (the superscript σ).

The aim of the present work was to obtain different types of complex oxides with the *perovskite* type structure (OSP) and with the *tetragonal tungsten bronze* type structure, to investigate of these ceramic materials (ferroelectric, antiferroelectric, non-polar) with different degree of the cation order and to search for electrostrictive ceramic transducers with optimal electromechanical parameters.

2. Methods for measuring the electrostrictive coefficients

Using the Voigt notation (with two subscripts to replace the four subscripts), Eq. (5) can be written as:

$$\eta_i = s_{ij}^P \sigma_j + Q_{ijkl} P_k P_l \qquad (i,j = 1,2,...,6; \quad k,l = 1,2,3). \tag{8}$$

Furthermore, upon stipulating that

$$Q_{i\mu} = Q_{ikl} \qquad (\text{for} \quad k = l), \tag{9}$$

and

$$Q_{i\mu} = 2Q_{ikl} \qquad (\text{for} \quad k \neq l), \tag{10}$$

Q_{ikl} becomes $Q_{i\mu}$ (with two subscripts). Thus, 81 components of the fourthrank tensor are reduced to 36 components. Due to the crystal's macroscopic symmetry, the number of independent components $Q_{i\mu}$ can furher be reduced. For centrosymmetric crystals (such as $\overline{4}3m$, 432, $m3m$, etc) as well as unpoled ceramics, the $Q_{i\mu}$ tensor is

	P_1^2	P_2^2	P_3^2	P_2P_3	P_1P_3	P_1P_2
η_1	Q_{11}	Q_{12}	Q_{12}	0	0	0
η_2	Q_{12}	Q_{11}	Q_{12}	0	0	0
η_3	Q_{12}	Q_{11}	Q_{11}	0	0	0
η_4	0	0	0	Q_{44}	0	0
η_5	0	0	0	0	Q_{44}	0
η_6	0	0	0	0	0	Q_{44}

(11)

In the present experiment with a sample in the zero-stress state ($\sigma_j = 0$), we obtain from Eqs. (8) and (11) relationships between components of strain (η_i) and components

of polarization (P) as follows:

$$\begin{aligned}
\eta_1 &= Q_{11}P_1^2 + Q_{12}P_2^2 + Q_{12}P_3^2,\\
\eta_2 &= Q_{12}P_1^2 + Q_{11}P_2^2 + Q_{12}P_3^2,\\
\eta_3 &= Q_{12}P_1^2 + Q_{12}P_2^2 + Q_{11}P_3^2,\\
\eta_4 &= Q_{44}P_2P_3,\\
\eta_5 &= Q_{44}P_3P_1,\\
\eta_6 &= Q_{44}P_1P_2.
\end{aligned} \tag{12}$$

These formulae are essential in the measurement of electrostrictive coefficients. Most of the practical electrostrictive materials are used in their paraelectric state, because in this state the remanent strain is avoidable. For studying the electrostrictive effect, direct and indirect methods have been designed.

In general, electrostrictive coefficients ($Q_{\lambda\mu}$) are obtained by measuring the electrostrictive strain directly. For example, if an electric field is applied in the direction 2 on a dielectric material with cubic symmetry (paraelectric phase), a transverse electrostrictive effect occurs, i.e., a strain develops along the direction 1. In this case the electrostriction equations (12) can be simplified to the form (transverse electrostrictive effect; $\eta_1 \perp P_2$):

$$\eta_1 = Q_{12}P_2^2, \tag{13}$$

where $\eta_1 = (\Delta l_1/l_1)$ — the strain in direction 1.

By applying an electric field on a sample, we can measure the strain η_1 and the polarization P_2 as a function of the applied field E. A plot of η_1 as a function of P_2^2 is a straight line with slope Q_{12}. The extension Δl_1 as a function of the applied field is measured by a micro-displace meter with an X-Y recorder, while the polarization P_2 as a function of the applied field is measured by a Sawyer–Tower circuit. If the strain is measured in the direction of the field, one obtains the longitudinal electrostrictive coefficient Q_{11} ($\eta_2 \parallel P_2$):

$$\eta_2 = Q_{11}P_2^2. \tag{14}$$

A plot of η_2 as a function of P_2^2 is a straight line with slope Q_{11}. The schematic diagram of a typical experimental set-up for direct measurement of the electrostrictive coefficients $Q_{\lambda\mu}$ has been shown in the book [2].

Block diagram of a set-up for indirect measurement of the electrostrictive coefficients has been shown in the paper [3].

According to thermodynamics, in the case of an isotropic material

$$(\partial\beta/\partial p_h)_T = 2Q_{11} + 4Q_{12} = 2Q_h, \tag{15}$$

where β — the impermeability, p_h — the hydrostatic pressure, Q_h — is defined as the electrostrictive coefficient under hydrostatic pressure.

As sample is inserted into a high-pressure container where it is subjected to a hydrostatic pressure p_h ($0 - 10^3$ MPa). The variation of β is measured as a function of p_h

under isothermal conditions. β is usually calculated from the dielectric permittivity ε using the following equations:

$$\beta_{mn} = (-1)^{m+n}\Delta^{\varepsilon}_{mn}/\Delta^{\varepsilon}, \tag{16}$$

$$\varepsilon_{mn} = (-1)^{m+n}\Delta^{\beta}_{mn}/\Delta^{\beta}, \tag{17}$$

where Δ^{ε} (or Δ^{β}) — an algebraic determinat of ε_{mn} or β_{mn} tensor, $\Delta^{\varepsilon}_{mn}$ (or Δ^{β}_{mn}) — represents a remanent subdeterminant in which the term ε_{mn} (or β_{mn}) is removed.

Q_h is then obtained from the slope of the β versus p_h curve. In practice, the hydrostatic pressure is raised to a maximum value in the beginning of the experiment and then allowed to drop gradually in steps. At each pressure step p_h, after the sample temperature becomes stable the sample capacity is measured by an *a.c.* bridge.

The method of indirect measurement has also been applied to a system under a uniaxial pressure. Thus, each independent component of the electrostrictive coefficient may be obtained separately. For example, if a stress σ_1 is applied in the direction 1, we obtain

$$2Q_{11} = -(\partial\beta_1/\partial\sigma_1). \tag{18}$$

For studying high-frequency piezoelectric and electrostrictive strains, a double-beam laser interferometr has been designed. This system is capable of resolving a displacement of 10^{-1}nm with the lock-in detection device and measuring strains up to the piezoelectric resonance frequencies using a digital oscilloscope. The interference of the sample bending in signal detection is effectively avoided. The schematic diagram of the double-beam laser interferometer along with the electronic accessories is shown in the paper [4].

3. Results of investigations and their interpretation

The following parameters are used for estimation of electric field induced electrostrictive deformations of dielectric and for practical estimation of usefulness of electrostrictive transducer:

1. Coefficients of electrostriction (M_{ij}, Q_{ij}):

$$M_{ij} = Q_{ij}\varepsilon_0^2\left(\varepsilon_r^{\sigma} - 1\right)^2, \tag{19}$$

where

$$M_{ij} = \left(\frac{\partial^2\eta_i}{\partial E_k \partial E_l}\right)_{\sigma,T}, \tag{20}$$

$$Q_{ij} = \left(\frac{\partial^2\eta_i}{\partial P_k \partial P_l}\right)_{\sigma,T}, \tag{21}$$

$$\varepsilon_r^{\sigma} = \frac{\varepsilon^{\sigma}}{\varepsilon_0}. \tag{22}$$

2. Hydrostatic coefficient of electrostriction:

$$Q_h = Q_{11} + 2Q_{12}. \tag{23}$$

3. Temperature coefficient of electrostriction

$$k_e = \frac{\Delta Q_{ij}}{\Delta T Q_{ij}} 100 \quad [\%\mathrm{K}^{-1}], \tag{24}$$

where

$$\Delta T = T_2 - T_1\,, \qquad \Delta Q_{ij} = |Q_{ij}(T_2) - Q_{ij}(T_1)|, \qquad Q_{ij} = Q_{ij}(T_{1/2}). \tag{25}$$

4. Linear expansion coefficient:

$$\lambda = \frac{\Delta x}{x_0 \Delta T} \quad [\mathrm{K}^{-1}]. \tag{26}$$

5. Curie–Weiss constant (C):

$$\varepsilon = \frac{C}{T - T_0}\,. \tag{27}$$

The values of M_{ij}, Q_{ij}, Q_h, ε_r^σ of electrostrictive materials used for production of electromechanical transducers (micromotors, micromanipulators etc.) should be as high as possible while values of λ and k_e should be as small as possible.

Ceramic compounds and ferroelectric solid solutions ($BaTiO_3$ (BT), $PbTiO_3$ (PT), $Pb(Mg_{1/3}Nb_{2/3})O_3$ (PMN), $Pb(Zn_{1/3}Nb_{2/3})O_3$ (PZN), $Pb(Sc_{1/2}Nb_{1/2})O_3$ (PSN), (x)PT-(1-x)PMN, $(Pb_{1-x}La_x)(Zr_yTi_{1-y})O_3$ (PLZT), $Sr_{5-x}Ba_xNb_{10}O_{30}$ (SBN)), antiferroelectric ($PbZrO_3$ (PZ), $Pb(Co_{1/2}W_{1/2})O_3$, (PCW), $Pb(Fe_{2/3}U_{1/3})O_3$ (PFU)) and non polar ($BaZrO_3$ (BZ), $(K_{3/4}Bi_{1/4})(Zn_{1/6}Nb_{5/6})O_3$ (KBiZnN)), of perovskite type structure (BT, PT, PMN, PZN, PSN, PLZT, PZ, PLW, PFU, BZ, KBiZnN) and of tetragonal bronze type structure (SBN), ordered, partially ordered and disordered of (A'A")(B'B")O_3, A(B'B")O_3 and another were the material of investigations.

Samples for investigations have been obtained by classic ceramic technology and by hot pressing method in conditions presented in our previous papers [e.g. 2]. Technological conditions substantially influence on the density of ceramics: from $\rho = (0.90 \div 0.93)\rho_{\mathrm{rtg}}$ (for classic technology) to $\rho > 0.96\rho_{\mathrm{rtg}}$ (for hot pressed ceramics). The increase of density influence on the value of dielectric permittivity at room temperature ($T_r = 293\,\mathrm{K}$) well as at T_m temperature. The degree of the diffusion of the phase transition (δ) in ferroelectric and antiferroelectric solid solutions decreases with increasing density (up to $\rho = 0.92\rho_{\mathrm{rtg}}$). For samples with $\rho > 0.92\rho_{\mathrm{rtg}}$ the degree of diffusion does not depends neither on conditions of deposition or on the method of sintering. In temperature range $T > T_m$ dielectric permittivity changes according to equation

$$1 - \varepsilon = \frac{1}{\varepsilon_m} + \frac{(T - T_m)^2}{2\varepsilon_m \delta}\,. \tag{28}$$

With increasing dielectric permittivity caused by increasing density of samples increase also the values of electrostriction coefficients M_{ij}.

Furthermore during the experimental investigations there were stated the following relations:

1) The values of electrostriction coefficients (Q_{ijkl}, Q_h) depend not only on the chemical composition of perovskite type oxides but first of all on the degree of ordering of

cations in solid solutions A(B'B")O_3 (i.e. increase after transition from disordered state through simple (ABO_3) to ordered state):

- simple compound (for example $BaTiO_3$) $:Q_h \approx 0.02\,\mathrm{m}^4/\mathrm{C}^2$;
- ordered solid solution (for example $Pb(Co_{1/2}W_{1/2})O_3$) $:Q_h \approx 0.027\,\mathrm{m}^4/\mathrm{C}^2$;
- partially ordered solid solution (for example $Pb(Sc_{1/2}Nb_{1/2})O_3$) $:Q_h \approx 0.008\,\mathrm{m}^4/\mathrm{C}^2$;
- disordered solid solution (for example $Pb(Mg_{1/3}Nb_{2/3})O_3$) $:Q_h \approx 0.006\,\mathrm{m}^4/\mathrm{C}^2$.

2) With increasing degree of ordering of cations in perovskite type oxides increases Q_h, while in ferroelectrics and antiferroelectrics decreases Curie–Weiss constant (C). The product of Curie–Weiss constant (C) and hydrostatic coefficient of electrostriction (Q_h) is approximately constant for all ferroelectric and antiferroelectrics perovskite type oxides:

$$Q_h \cdot C = (3.1 \pm 0.6) \cdot 10^3\,\mathrm{m}^4\mathrm{C}^{-2}\mathrm{K}. \tag{29}$$

This relation allows to estimate the value of Q_h for ferroelectrics and antiferroelectrics if the value of Curie–Weiss constant (C) is known (for example from the dependency $\varepsilon^{-1}(T)$ in temperatures higher than T_c (or T_m)):

- simple compound (for example $BaTiO_3$) $:C = 1.5 \cdot 10^5\,\mathrm{K}$,
- ordered solid solution (for example $Pb(Co_{1/2}W_{1/2})O_3$) $:C = 1.2 \cdot 10^5\,\mathrm{K}$,
- partially ordered solid solution (for example $Pb(Sc_{1/2}Nb_{1/2})O_3$ $:C = 3.5 \cdot 10^5\,\mathrm{K}$,
- disordered solid solution (for example $Pb(Mg_{1/3}Nb_{2/3})O_3$) $:C = 4.7 \cdot 10^5\,\mathrm{K}$.

3) The value of hydrostatic electrostriction coefficient is approximately proportional to square of linear expansion coefficient:

$$\begin{aligned} Q_h &\sim \lambda^2, \\ \lambda &= (3.8 \pm 0.4) \cdot 10^{-5} Q_h^{0.5} \quad [\mathrm{K}^{-1}]. \end{aligned} \tag{30}$$

In perovskite solid solution the value of λ decreases with increasing degree of disorder of cations:

- simple compound $:\lambda \approx 5.88 \cdot 10^{-6}\,\mathrm{K}^{-1}$,
- ordered solid solution $:\lambda \approx 6.72 \cdot 10^{-6}\,\mathrm{K}^{-1}$,
- partially ordered solid solution $:\lambda \approx 3.78 \cdot 10^{-6}\,\mathrm{K}^{-1}$,
- disordered solid solution $:\lambda \approx 3.36 \cdot 10^{-6}\,\mathrm{K}^{-1}$.

Very small value of λ in wide temperature range is typical for ferroelectric perovskite structure relaxors with low degree of ordering of cations. For such materials low value of hydrostatic electrostriction coefficient (Q_h) is also characteristic, independent on temperature. It means that it is not possible to obtain materials with high Q_h and low λ.

4) The highest stability of hydrostatic electrostriction coefficient (Q_h) is characteristic for ferroelectrics with diffused phase transition and ferroelectric relaxors. Estimated from Eq. (24) values k_e oscillated in the range from $0.4\%\,\mathrm{K}^{-1}$ for three component solid solution PMN-PT-BZN ($M_{13} \approx 12 \cdot 10^{-16}\,\mathrm{m}^2/\mathrm{V}^2$), to $3.5\%\,\mathrm{K}^{-1}$ for two component solid solution PMN-PT ($M_{13} \approx 0.2 \cdot 10^{-16}\,\mathrm{m}^2/\mathrm{V}^2$). In order to decrease the temperature coefficient of electrostriction (k_e) we should take into account that the increase of degree of diffusion of the phase transition leads to decrease of ε_r^σ and as a consequence to

decrease of the electrostriction coefficient M_{ij}. It means that it is not possible to obtain electrostrictive ceramics with high M_{ij} and simultaneously with low temperature coefficient k_e.

5) The value of the product $Q_{ij}\varepsilon_0^2(\varepsilon_r^\sigma - 1)^2 = M_{ij}$ used for estimation of the electrostrictive deformation is very high for ferroelectric relaxors i.e. solid solution with disordered structure. Such materials are obviously used as electrostrictive materials because in spite of their low Q_{ij} value their dielectric permittivity ε_r^σ in the surrounding of T_m temperature is very high (where T_m temperature in which dielectric permittivity reaches their maximal value). For example in pure PMN $\varepsilon_m = 16470$; $Q_{11} = 0.006\,\mathrm{m^4/C^2}$, $\varepsilon_0 = 8.854 \cdot 10^{-12}\,\mathrm{F/m}$, and as a result $M_{11} = 1.31 \cdot 10^{-16}\,\mathrm{m^2/V^2}$, however for solid solution 0.975 PMN – 0.025 PT: $\varepsilon_m = 19390$, $Q_{11} = 0.011\,\mathrm{m^4/C^2}$, and $M_{11} = 3.5 \cdot 10^{-16}\,\mathrm{m^2/V^2}$.

High values of M_{ij} electrostriction coefficients allows to obtain relative deformation of order $\eta \approx 10^{-3}$ in low electric fields.

The regularities in ε_r^σ, Q_{ij}, M_{ij}, k_e, λ and C related with different degree of cations ordering may be explained on the base of *ordered and disordered crystal structures model* for complex $A(B'_{1/2}B''_{1/2})O_3$ oxides. According to this model in ordered structure small B ions surrounded by bigger A and O ions have relatively small free space than in disordered structure. It leads to higher polarization related to the unit of electric field tension, and as a consequence to higher values of dielectric permittivity and Curie–Weiss constant. As a result the deformation related to the unit of polarization is smaller what gives smaller value of electrostriction coefficient Q_{ij}.

Regularities typical for ferroelectric relaxors presented in this work are in good agreement with results of investigations presented by another authors for example [5].

4. Conclusions

- In relaxor ferroelectrics and ferroelectrics with diffused phase transition (at $T > T_m$) the effect of electrostriction (deformation of the mechanically free sample ($\sigma_{\mathrm{ext}} = 0$) in external electric field ($\eta \sim E^2$) or appearance stresses proportional to the square of electric field ($\sigma \sim E^2$) in mechanically short circuited sample ($\eta = 0$)) are very high. The main cause of observed electromechanical effects is arising in investigated samples strong field induced polarization and as a result we can write that $\eta \sim P_{\mathrm{ind}}^2$ (for $\sigma_{\mathrm{ext}} = 0$) and $\sigma \sim P_{\mathrm{ind}}^2$ (for $(\eta = 0)$).
- Strong electrostrictive effect in ferroelectric relaxors and in ferroelectrics with diffused phase transition has wide practical applications.
- The electromechanical transducers based on electrostrictive ceramics can be applied in microengines, microactuators, micromanipulators, etc. One can mention the following unique advantage of electrostrictive ceramics namely:

1) high value of dielectric constant ($\varepsilon \approx 10^4$);

2) small coefficient of linear thermal expansion (λ);

3) independence of the deformation sign on direction of the external electric field intensity (simplified control of the deformation by electric field);

4) ability of reaching high tensile stresses ($< 4 \cdot 10^3\,\mathrm{N/cm^2}$);

5) high value of the relative strain ($\eta \approx 10^{-3}$);
6) low inertia (short turn on- and off-time: $\sim 10\,\mu s$);
7) small driving power;
8) absence of the remanent strain;
9) absence of the electromechanical hysteresis.

Acknowledgement

The authors would like to thank Committee for Scientific Research (KBN), Poland, for financial support under grant No 7 TO 8D 005 17.

References

[1] Z. SUROWIAK, R. SKULSKI and J. DUDEK, *The properties of the electromechanical transducers on the basis of electrostrictive ceramics*, [in:] Proc. of The XLIV Open Seminar on Acoustics, OSA'97, Gdańsk – Jastrzębia Góra (Poland), 15-18.09.1997. Ed. PTA Gdańsk. Vol. II, 1997, pp. 621–627.

[2] Y. XU, *Ferroelectric materials and their applications*, North–Holland, New York 1991, pp. 64–68.

[3] Z. SUROWIAK, *The electrostrictive properties of the ferroelectric ceramics* [in Polish], Molecular and Quantum Acoustics (Poland), **8**, 267–295 (1997).

[4] Z. SUROWIAK, J. RANACHOWSKI and A.E. PANICH, *Ceramic electrostrictive materials obtained on the basis of ferroelectrics* [in Polish], [in:] Advanced ceramics, technology and research methods, J. RANACHOWSKI [Ed.], IPPT PAN, Warszawa 1998, pp. 361–391.

[5] T.G. LUPEIKO *et al.*, *Electrostrictive properties of the* $(1\text{-}x)\,PbMg_{1/3}Nb_{2/3}O_3 - x\,PbTiO_3$ *ceramic materials* [in Russian], [in:] Piezoactive materials, A.E. PANICH [Ed.], RGU, Rostov-on-Don 1991, pp. 52–64.